CPMV as synthon and template in bionanotechnology

By

Alaa Ahmed Aljabali

This thesis is submitted in partial fulfilment of the requirements of the degree of
Doctor of Philosophy at the University of East Anglia
John Innes Centre, Norwich
September 2011

Statement

I hereby certify that the work contained within this thesis is my own original work, except where due reference is made to other contributing authors. This thesis is submitted for the degree of Doctor of Philosophy at the University of East Anglia and has not been submitted to this or any other university for any other qualification.

Alaa A. A. Aljabali

12/ 09 / 2011

Parts of the research described in this thesis have been published in the scientific literature as follows:

1 Shah S. N., Steinmetz N. F., Aljabali A. A. A., Lomonossoff G. P., Evans D. J.(2009) Environmentally benign synthesis of virus–templated, monodisperse, iron–platinum nanoparticles. Dalton Transactions 40; 8479–8480

2 Aljabali A. A. A., Barclay J. E., Butt J. N., Lomonossoff G. P., Evans D. J.(2010) Redox–active ferrocene–modified Cowpea mosaic virus nanoparticles. Dalton Transactions 39 7569–7574

3 Aljabali A. A. A., Sainsbury F., Lomonossoff G., Evans D. J.(2010) Cowpea mosaic virus unmodified empty virus–like particles can be loaded with metal and metal oxide. Small 6 818–821

4 Aljabali A. A. A., Barclay J. E., Lomonossoff G. P., Evans D. J.(2010) Virus templated metallic nanoparticles Nanoscale 2 2596–2600

5 Aljabali A. A. A., Shah S. N., Evans–Gowing R., Lomonossoff G. P., Evans D. J.(2011) Chemically–coupled–peptide promoted virus nanoparticle templated mineralization. Integrative Biology 3 119–125

6 Aljabali A. A. A., Lomonossoff G. P., Evans D. J.(2011) CPMV–polyelectrolyte–templated gold nanoparticles Biomacromolecules 12 2723–2728

7 Aljabali A. A. A., Barclay J. E., Cespedes O., Rashid A., Staniland S. S., Lomonossoff G. P., and Evans D. J., (2011) Charge modified Cowpea mosaic virus particles for templated mineralization. Advanced Functional Materials 21 21 4137-4142

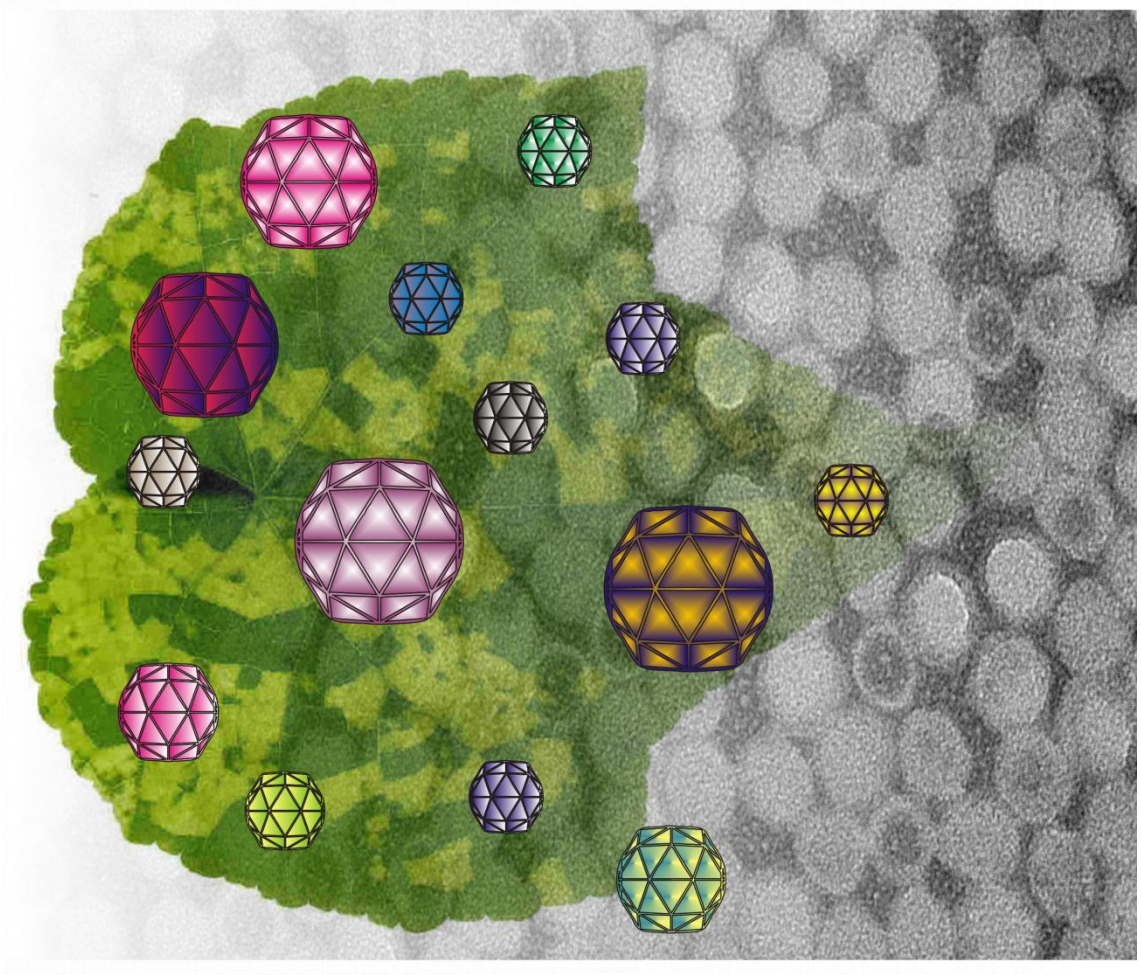

"Just as physicists recognize light either as electromagnetic waves or as particulate photons, depending on the context, so biologists can profitably regard viruses both as exceptionally simple microbes and as exceptionally complex chemicals"

R Dulbecco and HS Ginsberg, 1980. Virology (originally published as a section of Microbiology, 3rd. Edn., by Davis et al., Harper and Row, Hagerstown); p. 855.
URL http://www.mcb.uct.ac.za/tutorial/molechis.htm

Acknowledgments

My sincere gratitude goes to the Creator of the heavens and earths and what's in between; the Almighty God.

This dissertation would not have been possible without the supervision of Prof. David Evans, for his guidance, encouragement, always open door, and ready availability for discussion and support. He gave me the liberty to work independently and allowed me to explore my own ideas. Thank you!

I would also like to thank the other members of my supervisory committee: Prof. George Lomonossoff for his constructive comments throughout this research, for his support and for the parties my wife and I enjoyed in his house and with his family. Prof. Nick Brewin is thanked for his comments, suggestions and advice at the advisory panel.

I have been very fortunate to work in a very diverse and a world leading research centre (John Innes Centre– UK). I would like to thank all my colleagues in the Biological Chemistry Department for their support. In particular the "CPMV gang", super RA Keith Saunders, Pooja Saxena, Paolo Lenzi, Alberto Berardi, and Frank Sainsbury for their enormous help and sharing the morning coffee. My gratitude and special thanks to Mrs Elaine Barclay, "CPMV Queen", for her support in chemical material synthesis, CPMV inoculation and purification, and for her proof reading of this thesis.

Prof. Julea Butt for her support, time and allowing me to use her laboratory for the electrochemistry analysis, and my thanks extend to all of her lab members.

Kim Findlay, Sue Bunnewell and Grant Calder are thanked for training, support and advice in all sorts of microscopy–related matters.

I would like to thank my friends Mahmoud Al–Bassam and his family for the moral support and encouragement. Abdul Rashid is also thanked for help and support throughout my research degree.

My collaborators: Mr. Bertrand Leze, Mr. Graham Chilvers (UEA), Mr. Andrew Davis (JIC), and Mr Mike Ridout, Mr. Andrew Kirby (IFR), Dr's Sarah Staniland, Oscar Cespedes and

Neil Ranson (Leeds University), Prof. Quentin Pankhurst and his group (The Royal Institution of Great Britain), Dr. Pedro J. de Pablo (Universidad Autónoma de Madrid, Spain), and Prof. Nicole Steinmetz (Case Western Reserve University, USA) are thanked for fruitful collaborations and discussions.

I wish to thank my extended family: parents, brothers, sisters for their understanding, support and for their prayers during these years that I have spent away from them and in pursuit of my doctorate degree. I owe to my father and my beloved mother teaching me to value knowledge, honesty, virtues and humanity. I thank them for their never–ending unconditional love.

Finally, I am forever indebted to my in–laws and to my sweetheart wife Tala Zghoul for her sacrifice, patience, and love. My wife has been my source of strength that helped me to go through the PhD phase. Without her support and encouragement, this thesis would never have started much less finished. This thesis is dedicated to Tala and my unborn child.

CPMV for being the best collaborator.

This work was funded by the Biotechnology and Biological Sciences Research Council, U.K.

Abbreviations

“B”	Bottom component of CPMVwt
“M”	Middle component of CPMVwt
“T”	Top component of CPMVwt
°C	degree Celsius
µl	microlitre
µm	micrometre
1–D	one–dimensional
2–D	two–dimensional
3–D	three–dimensional
A	absorbance
A	adenine
A	ampere
A	surface area
Å	angstrom
a.a or aa	amino acid
AF	AlexaFluor
AFM	atomic force microscopy
Al_2O_3	aluminium oxide
Ala	alanine
APS	ammonium persulfate
Arg	arginine
Asp	aspartic acid
ATP	adenosine triphosphate
Au	from Latin: aurum "gold"
Au–CPMV	gold–coated CPMV particles
AuNP	gold nanoparticle
BIO	biotin
BMV	Brome mosaic virus
bp	base pairs
c	concentration
C	cytosine
Ca.	circa (from Latin, meaning "around")
CCMV	Cowpea chlorotic mottle virus
CdS	cadmium sulfide
CIV	Chilo iridescent virus
CM peptide	calcium molybdate peptide
CoPt	cobalt–platinum
CP	coat proteins
$CPMV_{Subscript}$	denotes molecules within or attached to the interior of the capsid
$CPMV_{wt}$	wild–type Cowpea mosaic virus
CsCl	caesium chloride
Cys	cysteine
d	length of light path (distance)
D	diffusion coefficient
DLS	dynamic light scattering
DMF	dimethylformamide
DMSO	dimethyl sulfoxide
DNA	deoxyribonucleic acid
Dox. or dox.	doxorubicin
E. coli	Escherichia coli

e.g.	from the latin "*exempli gratia*" means "for example,"
EDC	1–ethyl–3–[3–dimethylaminopropyl]carbodiimide hydrochloride
EDTA	ethylenediaminetetraacetic acid
EDXS	energy dispersive X–ray spectroscopy
ELD	electroless deposition
EMP	ethylmercury phosphate
E_p^a	anodic scans
E_p^c	cathodic scans
eVLPs	empty virus–like particles
fc	ferrocene
FC	field cooled
Fe_2O_3	hematite
Fe_3O_4	magnetite
FePt	iron–platinum
FITC–PAH	fluorescein isothiocyanate–labelled poly(allyl amine hydrochloride)
g	gram(s)
Gd^{3+}	gadolinium cations
GFP	green fluorescent protein
Glu	glutamic acid
GOX	glucose oxidase enzyme
HCRSV	Hibiscus chlorotic ringspot virus
HIV–1	Human immunodeficiency virus–1
HRP	horse radish peroxidase
Hsp	heat shock protein
i.s.	isomer shift
i_p^a	anodic peak current
i_p^c	cathodic peak current
IR	infra Red
JIC	John Innes Centre
K	Kelvin
kDa	kilodalton
KCl	potassium chloride
kDa	kilodalton
kg	kilogram
kV	kilovolt
l	litre
L subunit	large subunit
LbL	layer–by–layer
Ltd.	limited company
Lys	lysine
m	mass
M	molar
M13	M13 bacteriophage
mA	milliampere
MALDI–TOF	matrix assisted laser desorption/ionization time–of –flight
MAV	methyl(aminopropyl)viologen
MAX	maximum
MDa	million Dalton
mg	milligram
MHz	megahertz
min.	minute(s)
ml	millilitre
mm	millimetre
mM	millimolar
MS	mass spectrometry

MS2	Bacteriophage MS2
mV	millivolt
MWCO	molecular weight cut–off
NaCl	sodium chloride
NHS	*N*–hydroxysulfosuccinimide–*N*–hydroxysulfosuccinimide
nm	nanometre
NTA	nanoparticle tracking analysis
OAS	origin of assembly site
PAA	polyacrylic acid
^{PA}CPMV	Poly(allylamine)–CPMV
PAH	poly(allylamine hydrochloride)
PASA	polyanetholesulfonic acid
PBS	phosphate buffered saline
PDS	polydextran sulfate
*p*EAQ–HT	p Easy And Quick
PEG	polyethylene glycol
PGE	pyrolytic graphite edge
pH	negative logarithm to the base ten of the concentration of $[H]^+$ ions
p*I*	isoelectric point
PSA	polystyrenesulfonic acid
PSS	poly(styrenesulfonate)
PTA	phosphotungstic acid
q.s.	quadrupole splitting
QDs	quantum dots
R	radius
RCNMV	Red clover necrotic mosaic virus
RNA	ribonucleic acid
rpm	revolution per minute
RU	response units
s form	slow form
S subunit	small subunit
SA	Streptavidin
SATP or SATA	*N*–succinimidyl–*S*–acetylthiopropionate
SDS–PAGE	sodium dodecyl sulfate polyacrylamide gel electrophoresis
SEM	scanning electron microscopy
S_f	small fast subunit
SI	the International System of Units
SPDP	3–(2–pyridyldithio)propionate
SPR	surface plasmon resonance
S_s	small slow subunit
STM	scanning tunnelling microscopy
Sulfo–SFP	sulfo–succinimidyl 4–formylbenzoic acid (sulfo–SFB)
^{Superscript}CPMV	denotes molecules attached to the external surface of CPMV
T7	Bacteriophage T7
TB	blocking temperature
Tb^{3+}	terbium cations
TBSV	Tomato bushy stunt virus
TCEP	tris(2–carboxyethyl)phosphine hydrochloride
TEG	carboxylate terminated thioalkylated tetrathylene gylcol
TEM	transmission electron microscopy
Thr	threonine
TM	melting temperature
TMB	3,3',5,5'–Tetramethylbenzidine
TMV	Tobacco mosaic virus
TYMV	Turnip yellow mosaic virus

Tyr	tyrosine
U	unit(s)
UA	uranyl acetate
UV	ultra violet
V. unguiculata	*Vigna unguiculata*
v/v	volume per volume
VIS or vis	visible
VLP	virus–like particle
VNP(s)	virus nanoparticle(s)
vol.	volume
VPg	viral protein genome–linked
VSM	vibrating sample magnetometry
w/v	weight per volume
wt	wild–type
ZFC	zero field cooled
ZnS	zinc sulfide
ZP	zeta potential
ε	extinction coefficient
λ	wavelength
μA	microampere
μg	microgram
ν	scan rate

Abstract

Plant viruses are naturally occurring nanoparticles that are fascinating nanoscale platforms. The use of plant viruses as multifunctional nanoplatforms and as building blocks for nanotechnology provides unique advantages. The versatility of Cowpea mosaic virus (CPMV) to template metallic coatings and site–specific attachment of desired moieties was explored. CPMV's robustness, monodispersity, large–scale production, and amenability to chemical and genetic modification have enabled the research to be carried out as presented in this thesis.

CPMV capsid was utilised for the formation of a wide range of metallic coatings using both mineralization and metallization of the CPMV exterior. Moreover, CPMV's exterior was chemically modified with specifically designed functionalities (*i.e.* electroactive moieties, enzymes, peptides that favour certain types of mineralization, and therapeutic agents). The ability to utilise both the interior and exterior surface of CPMV empty virus–like particles (eVLPs) was explored. The use of eVLPs has broadened the range of potential applications of CPMV; for example, it is being investigated as a drug carrier. Most viruses contain pores in their capsid shell, through which small molecules can be loaded. Using this property, CPMV eVLPs were used as nanocontainers for drug encapsulation and for the formation of iron oxide nanoparticles, which are potentially useful as hyperthermia treatment agents. CPMV eVLP holds great potential to accurately deliver the treatment agents to the desired location and maintain the dose for an adequate duration. In addition, functionalised virus surface could selectively attach to specific cells and localise the bound drug. Thus, this could be explored as a drug delivery system without many of the limitations of synthetic nanoparticles. Polyelectrolyte coating of CPMV eVLPs has offered a workable loading and controlled release methodology. Collectively, this thesis describes covalent coupling of molecules to the exterior of CPMV, mineralization and metallization of CPMV exterior and mineralization within eVLPs.

Table of Contents

Acknowledgments....iv
Abbreviations....vi
Abstract....x
List of tables.... xxxvii
1 Literature review....1
1.1 Introduction....1
1.1.1 Bionanoparticles: Bio–inspired nanomaterials....3
1.1.2 Viruses....6
1.1.3 Why virus nanoparticles (VNPs)....6
1.1.4 Empty virus capsids–eVLPs....8
1.1.5 Biomineralization on viruses....11
1.1.6 Mineralization using phage display....14
1.1.7 Cowpea mosaic virus (CPMV)....15
1.1.8 Applications of viruses in nanotechnology....20
1.2 Summary....22
1.3 Aim and outline of this thesis....23
1.4 References:....24

2 General methods....33
2.1 Sodium phosphate buffer....33
2.2 Phosphate buffered saline (PBS)....33
2.2.1 Acetate buffer solution pH 5.3....33
2.2.2 Native gel electrophoresis....33
2.2.3 SDS–PAGE buffers....34
2.3 Virus propagation in *V. unguiculata*....34
2.4 CPMV purification....34
2.4.1 Agarose–gel electrophoresis....35
2.4.2 SDS–PAGE....35
2.5 Transmission electron microscopy (TEM)....36
2.6 UV–Vis Spectroscopy....36
2.7 Dynamic light scattering (DLS)....37
2.8 Nanoparticle tracking analysis (NTA)....37
2.9 Energy dispersive X–ray spectroscopy (EDXS)....37
2.10 Mössbauer analysis....38
2.11 Vibrating sample magnetometry (VSM) of $eVLP_{iron\ oxide}$ or iron oxide–CPMV....38
2.12 Immunological detection of CPMV coat proteins....39
2.12.1 Buffers and reagents....39
2.12.2 Immunological detection procedure....39
2.12.3 Immunological detection (dot blot):....39
2.13 Staining for cobalt and iron....40
2.14 Surface charge measurement....40
2.15 Carbodiimide method to generate $^{NHS\text{-}ester}$CPMV particles....40
2.16 SPDP method....41
2.17 Particle purification....42
2.17.1 Sucrose gradients....42
2.17.2 Size–exclusion chromatography....42
2.17.3 Ultrafiltration....42
2.17.4 Dialysis....43
2.18 References....43

3.1 Introduction....44
3.1.1 Peptides specificity for material synthesis (general insight)....45
3.1.2 Peptides for templated mineralization....46

3.1.3 Mineralization of chimaeric CPMV particles 47
3.1.4 Chemically–coupled–peptide–promoted mineralization 49
3.2 Experimental 50
3.2.1 Materials 50
3.2.2 Chimaeric CPMV preparation and mineralization 51
3.2.3 General method for chemical coupling of peptide to CPMV 51
3.2.4 Preparation of mineralized virus nanoparticles 52
3.2.5 $^{Peptide–CoPt}$CPMV quantification 53
3.2.6 External surface mineralization of amine–functionalised MWCNT 53
3.2.7 Scanning electron microscopy 54
3.3 Results and Discussion 54
3.3.1 Chimaera CPMV mineralization 54
3.3.2 ^{Peptide}CPMV conjugates 56
3.3.3 Mineralization of ^{Peptide}CPMV conjugates 59
3.3.4 Mineralization of $^{Peptide-CoPt}$MWCNT 69
3.4 Conclusions 71
3.5 References 72

4 Charge promoted mineralization 76
4.1 Introduction 76
4.2 Experimental 77
4.2.1 Materials 77
4.2.2 ^{Succinamate}CPMV 78
4.2.3 ^{Succinamate}CPMV quantification 78
4.2.4 Co–CPMV 79
4.2.5 Iron oxide–CPMV 79
4.2.6 Mössbauer spectroscopy analysis 79
4.2.7 Vibrating sample magnetometry (VSM) of iron oxide–CPMV 80
4.2.8 ^{Oligosaccharide}Metal–CPMV functionalisation 80
4.2.9 Au–CPMV functionalisation with cysteamine 80
4.2.10 MALDI–TOF mass spectrometry (MS) 80
4.2.11 CPMV–Poly(allylamine) hydrochloride (^{PA}CPMV) 81
4.2.12 Gold hydroxide solution 81
4.2.13 Gold coated CPMV nanoparticles (Au–CPMV) 81
4.2.14 Gold nanoparticle (AuNP) preparation 82
4.2.15 ^{PA}CPMV and pre–formed AuNP (Tessellated–spheres) 82
4.3 Results and Discussion 83
4.3.1 Charge promoted mineralization 83
4.3.2 ferroeneon oxide–CPMV functionalisation 92
4.4 CPMV–polyelectrolyte–templated gold nanoparticles 93
4.4.1 Polyelectrolyte adsorption onto CPMV surface 94
4.4.2 Conclusion 106
4.5 References 107

5 Electroless metal deposition on CPMV 110
5.1 Introduction 110
5.2 Experimental 111
5.2.1 Materials 111
5.2.2 Pre–activation of CPMV with palladium 111
5.2.3 ELD of metal coating 111
5.2.4 ELD of mixed metal coating 112
5.2.5 Purification of metallized particles 112
5.3 Results and discussion 113
5.3.1 $^{Pd2+}$CPMV activation 113

5.3.2 Metallization of CPMV....116
5.4 Conclusions....121
5.5 References....122

6 Empty Virus–like particles (eVLPs)....124
6.1 Introduction....124
6.1.1 CPMV eVLPs....125
6.2 Experimental....126
6.2.1 CPMV eVLP production....126
6.2.2 Encapsulation of cobalt within CPMV eVLPs ($VLPs_{cobalt}$)....127
6.2.3 Encapsulation of iron oxide within CPMV eVLPs ($VLP_{iron\ oxide}$)....128
6.2.4 Mössbauer analysis of $VLP_{iron\ oxide}$....128
6.2.5 Vibrating sample magnetometer (VSM) measurements of $VLP_{iron\ oxide}$....128
6.2.6 Staining for cobalt and iron within eVLPs....129
6.2.7 Biotinylation of eVLPs (^{Biotin}VLPs)....129
6.2.8 Surface plasmon resonance (SPR)....129
6.2.9 Infusion of rhodamine or doxorubicin into CPMV eVLPs....130
6.2.10 Gemcitabine and cisplatin loading....130
6.2.11 LBL formation onto $eVLPs_{drug}$....130
6.2.12 *In vitro* gemcitabine release and quantification....131
6.2.13 Internal chemistry (modifying internal cysteines)....132
6.2.14 ^{A20FMDV2}VLPs....132
6.2.15 ^{A20FMDV2}VLPs peptide quantification....133
6.3 Results and discussion....134
6.3.1 Internal mineralization of CPMV eVLPs....134
6.3.2 $VLPs_{iron\ oxide}$ as possible targeted hyperthermia therapeutics....145
6.4 Internal functionalisation of CPMV eVLPs....147
6.4.1 Results and discussion....148
6.5 Conclusions....164
6.6 References:....165

7 Electroactive CPMV nanoparticles....168
7.1 Introduction....168
7.1.1 Ferrocene functionalised CPMVwt particles (^{Fc}CPMV)....169
7.2 Materials and Methods....170
7.2.1 Materials....170
7.2.2 Methods: Coupling of ferrocene derivatives to CPMV....171
7.2.3 Electrochemical measurements....172
7.2.4 Methods: Coupling of ^{Fc}CPMV onto solid surfaces....173
7.3 Results and discussion....176
7.4 ^{Fc}CPMV Immobilisation on electrode surface....183
7.4.1 Coupling onto solid surfaces....184
7.4.2 Results and discussion of ^{Fc}CPMV onto solid surfaces....185
7.5 Conclusions....193
7.6 References:....195

8 ^{Enzyme}CPMV nanoparticles....198
8.1 Introduction....198
8.2 Materials and Methods....200
8.2.1 Materials....200
8.2.2 Enzyme activation (periodate method)....200
8.2.3 Enzyme–adipic acid dihydrazide (E–ADH)....200
8.2.4 ^{Enzyme}CPMV....201
8.2.5 Electrochemical measurements....203

8.2.6 HRP concentration using UV–vis analysis 204
8.3 Results and discussion 205
8.3.1 Enzyme oxidation (activation) with periodate 205
8.3.2 ^{Enzyme}CPMV 206
8.3.3 Enzyme quantification 211
8.3.4 $^{GOX–ADH}$CPMV and electrochemistry studies in solution 216
8.4 Conclusions 217
8.5 References: 219

9 Applications of chemical modifications 221
9.1 Introduction 221
9.1.1 Drug coupling and targeting on CPMV 221
9.2 Experimental 223
9.2.1 ^{A20FMDV2}CPMV particles 223
9.2.2 $^{Dox–NHS–ester}$CPMV 223
9.2.3 $^{Dox–BS3}$CPMV 224
9.2.4 $^{Dox–DTSSP}$CPMV 224
9.2.5 ^{Dox}CPMV quantification 225
9.2.6 $^{FA–NHS}$CPMV 226
9.2.7 $^{FA–NHS}$CPMV quantification 226
9.2.8 $^{Dox–NHS–ester}$CPMV^{FA} 227

9.3 Results and discussion 227
9.3.1 Attachment of targeting molecules 227
9.3.2 Chemical conjugation of doxorubicin 230
9.3.3 Conjugation of doxorubicin to CPMV capsid 230
9.3.4 ^{Dox}CPMV characterisation 230
9.4 Conclusion 234
9.5 References 236

10 Conclusions and future work 239

Appendix 243

List of figures xi

Figure 1.1– Structural illustration of some protein cages which have been used in bionanotechnology or biomedical applications. 4
Figure 1.2– Schematic illustration of the pH–induced dissociation–reformation process of apoferritin to form Prussian blue complex. 5
Figure 1.3– Cryo–transmission electron microscopy of vault particles 6
Figure 1.4– Scheme of the three important interfaces available for chemical and genetic manipulation in an assembled viral protein cage architecture. 8
Figure 1.5– Assembly of RCNMV VLPs around a gold nanoparticle via OAS templating. 10
Figure 1.6 – Proposed mechanism of VLP assembly from coat proteins (CP) 10
Figure 1.7– Peptides expressed in phage display and cell–surface display 14
Figure 1.8– The structure of Cowpea mosaic virus (CPMV) capsid and the asymmetric unit.. 16
Figure 1.9– Separation of the different components of Cowpea mosaic virus. 17
Figure 1.10– Schematic representation of the surface exposed addressable amines and carboxylates of the CPMV capsid. 19
Figure 2.1.–Derivatives of carboxylic acids can be prepared with EDC to generate active intermediates that react with amine containing molecules in the presence of NHS or Sulfo–NHS 41
Figure 3.1– Genetic insertion sites of peptide into the CPMV particle 49
Figure 3.2– Schematic representation of chemical coupling of peptides to CPMV capsid.. 50
Figure 3.3– Unstained TEM image of monodisperse FePt–coated chimaeric CPMV..……...57
Figure 3.4– Agarose gel electrophoresis of mineraliz CPMV particles. 57
Figure 3.5– UV–visible spectrum of doubly functionalised $^{Peptide–CoPt}CPMV^{DyLight594}$ particles.. 58
Figure 3.6– Native agarose gel electrophoresis of $^{Peptide–CoPt}CPMV^{DyLight594}$. 58
Figure 3.7– Unstained TEM image for unmodified CPMVwt particles incubated with equimolar quantities of $FeCl_3$ and H_2PtCl_6 in the presence of sodium borohydride.. 60
Figure 3.8– Unstained TEM image for $^{Peptide–ZnS}$CPMV incubated with equimolar quantities of $FeCl_3$ and H_2PtCl_6 in the presence of sodium borohydride.
Figure 3.9– Unstained TEM images for mineralized CPMV particles 62
Figure 3.10– EDX spectrum of mineralized particles ……62
Figure 3.11– Unstained TEM image of $^{Peptide–CoPt}$VLPs that have been mineralized both internally and externally. 63
Figure 3.12– Immunological detection of coat protein for eVLPs, $^{peptide–CoPt}$eVLPs and mineralized CoPt–eVLPs. 64
Figure 3.13– Native agarose gel for mineralized CPMV particles 65
Figure 3.14– Immunological detection of CPMVwt coat protein of mineralized particles..……..65
Figure 3.15– SDS–PAGE of mineralized CPMV particles 66
Figure 3.16– DLS data comparing CPMVwt and mineralized CPMV. 67
Figure 3.17– Zeta potential measurement of mineralized particles. 68
Figure 3.18– Negative image of a freeze–frame from nanoparticle tracking analysis for mineralized–CPMV……..68
Figure 3.19– SEM image of sputter–coated FePt–CPMV. 69
Figure 3.20– Demonstrating magnetic properties of FePt–CPMV prepared by the chemical modification route 69
Figure 3.21– Unstained TEM images of peptide–promoted mineralization of amine–functionalised MWCN 70
Figure 3.22– EDX spectrum of CoPt–mineralized MWCNT. 71

Figure 4.1– Schematic representation of the covalent modification of surface–exposed amines on the CPMVwt with succinamate..... 76
Figure 4.2– TEM images for ^{Succinamate}CPMV, unstained Co–CPMV and unstained iron oxide–CPMV particles..... 83
Figure 4.3– Unstained TEM of positive control of CPMVwt under identical mineralization conditions as those to form templated iron oxide–CPMV..... 83
Figure 4.4– Agarose gel electrophoresis of intact CPMV ,^{Succinamate}CPMV and mineralized–CPMV..... 85
Figure 4.5– EDX spectrum of mineralized–CPMV particles..... 85
Figure 4.6– Intact particles spotted on a nitrocellulose membrane probed with polyclonal antibodies raised against CPMV particles–dark spots show CPMV coat protein; (B) specific staining, 1–nitroso–2–naphthol to stain for cobalt and Prussian blue stain for iron..... 86
Figure 4.7– DLS and correlation plot for CPMVwt, Co–CPMV and iron oxide–CPMV particles..... 87
Figure 4.8– Zeta potential measurements of CPMVwt, ^{Succinamate}CPMV, Co–CPMV and iron oxide–CPMV..... 87
Figure 4.9– Frozen solution Mössbauer spectrum at 80 K of iron oxide–CPMV..... 88
Figure 4.10– Mössbauer spectrum of iron oxide–CPMV in the solid state 89
Figure 4.11– Mössbauer spectrum of bulk magnetite in the solid state at 80 K..... 89
Figure 4.12– Frozen solution Mössbauer spectrum at 80 K of reaction intermediate..... 90
Figure 4.13– Zero field cooled (ZFC) and field cooled (FC) magnetization curves..... 91
Figure 4.14– Mass spectrum of ^{Oligosaccharide} iron oxide–CPMV showing the corresponding peaks……...……..92
Figure 4.15– Schematic representation of the polyelectrolyte adsorption onto the CPMV capsid followed by the subsequent incubation with the gold solution to generate Au–CPMV..... 93
Figure 4.16– UV–vis absorption spectrum of CPMVwt and $^{FITC–PA}$CPMV (red line)..... 94
Figure 4.17– Agarose gel electrophoresis of ^{PA}CPMV and $^{FITC–PA}$CPMV..... 95
Figure 4.18– DLS of ^{PA}CPMV showing narrow size range..... 95
Figure 4.19– TEM images of ^{PA}CPMV, unstained Au–CPMV..... 95
Figure 4.20– Photographic images of gold coating reaction 96
Figure 4.21– UV–vis absorption spectrum of Au–CPMV 97
Figure 4.22– Unstained TEM images of Au–CPMV controls..... 98
Figure 4.23– Dynamic light scattering (DLS) comparing CPMVwt and Au–CPMV..... 99
Figure 4.24– Energy dispersive X–ray spectroscopy of Au–CPMV particles..... 99
Figure 4.25– Negative image of a freeze–frame from nanoparticle tracking analysis of Au–CPMV nanoparticles..... 100
Figure 4.26– Immunological detection of coat protein for CPMVwt, ^{PA}CPMV and Au–CPMV intact particles..... 100
Figure 4.27– Mass spectrum of ^{OLIGOSACCHARIDE}AU–CPMV..... 101
Figure 4.28– UV–vis absorption spectrum of Au–CPMV and $^{DyLight–594–Cysteamine}$Au–CPMV… 102
Figure 4.29– UV–visible spectrum of the tessellated–spheres 103
Figure 4.30– Tessellated–spheres formation..... 103
Figure 4.31– Scanning electron microscope and DLS analysis of the tessellated–spheres..... 103
Figure 4.32– Uranyl acetate stained TEM images for ^{PA}CPMV/AuNP control experiments… 104
Figure 5.1– TEM image of Pd^{2+}CPMV stained and unstained Pd^{0}–CPMV particles..... 113
Figure 5.2– DLS comparing CPMVwt and Pd^{0}–CPMV particles..... 113
Figure 5.3– EDX spectrum of Pd^{0}–CPMV metallized particles..... 114

Figure 5.4– Zeta potential measurement of Pd^{2+}CPMV particles and Pd^{0}–CPMV particles ... 114
Figure 5.5– Agarose gel of metallized CPMV particles 114
Figure 5.6– Unstained TEM images of metallized CPMV particles... 116
Figure 5.7– EDX spectrum of metallized CPMV particles. ... 116
Figure 5.8– Immunological detection of CPMV coat protein of metallized particles 117
Figure 5.9– Agarose gel of CPMV particles and metallized particles. ... 118
Figure 5.10– Negative image of a freeze–frame from nanoparticle tracking analysis for metallized–CPMV nanoparticles 118
Figure 5.11– AFM image for Ni–CPMV ... 118
Figure 6.1– Schematic representation of the production of eVLP using pEAQ–HT system.... 123
Figure 6.2– Cryo–EM reconstruction of CPMV particles. ... 124
Figure 6.3– UV–vis spectrum of CPMV eVLPs ... 125
Figure 6.4– Schematic representaion of cascade blue ethylenediamine coupled to the carboxylate groups on the virus capsid using the carbodiimide reaction... 131
Figure 6.5– Schematic representation of loading eVLPs with metal ions. ... 132
Figure 6.6– Unstained TEM images of internally mineralized $VLPs_{cobalt}$ and $VLPs_{iron\ oxide}$. 133
Figure 6.7– Negatively stained internally mineralized CPMV eVLPs.. ... 134
Figure 6.8– Metallic core analysis post protein capsid disruption. ... 135
Figure 6.9– DLS data of $VLPs_{cobalt}$ and $VLPs_{iron\ oxide}$. ... 135
Figure 6.10– Elemental energy–dispersive X–ray spectroscopy analysisof $VLPs_{cobalt}$ and $VLPs_{iron\ oxide}$. ... 136
Figure 6.11– Examples of zeta potential results for of $VLPs_{cobalt}$ and $VLPs_{iron\ oxide}$. ... 136
Figure 6.12– Gel electrophoresis analysis for internally mineralized CPMV eVLPs.. ... 137
Figure 6.13– Images of VLPs spotted on a nitrocellulose membrane probed with: polyclonal antibodies, 1–nitroso–2–naphthol to stain for cobalt and Prussian blue stain for iron.. ... 138
Figure 6.14– Sensogram showing the association and dissociation measurements of ^{Biotin}VLPs and $^{Biotin}VLPs_{cobalt}$ on a streptavidin–modified chip.. ... 139
Figure 6.15– AFM image for $^{Biotin}VLPs_{cobalt}$ on a SA–functionalised chip. ... 140
Figure 6.16– Illustration of one of 12 pentamers of CPMV at the five–fold axis.. ... 140
FIGURE 6.17– zero field cooled (ZFC) and field cooled (FC) OF $VLPs_{IRON\ OXIDE}$ PARTICLES.....141
Figure 6.18– Schematic illustration of the mechanism of hyperthermia treatment using iron oxide (CPMV $eVLPs_{iron\ oxide}$) ... 143
Figure 6.19– TEM images for stained $VLPs_{iron\ oxide}$ and $^{A20FMDV2}VLPs_{iron\ oxide}$ detected by streptavidin functionalised gold nanoparticles.. ... 145
Figure 6.20– TEM IMAGES FOR OF) STAINED $VLPs_{IRON\ OXIDE}$ AND $^{A20FMDV2}VLPs_{IRON\ OXIDE}$ 145
Figure 6.21– Chemical structures for rhodamine hydrochloride, doxorubicin, gemcitabine and cisplatin. ... 147
Figure 6.22– uv of $VLPs_{rhodamine}$ stained ... 148
Figure 6.23– TEM of $VLPs_{rhodamine}$ on a 1.2% agarose gel. ... 148
Figure 6.24– Wild–type and $VLPs_{RHODAMINE}$ ON A 1.2% AGAROSE GEL.. ... 148
Figure 6.25– eVLPs and $VLPs_{dox}$ on a 1.2% agarose gel... 150
Figure 6.26– labeling internal cysteines with sulfhydryl groups 151
Figure 6.27– The CPMV asymmetric unit with Cys postions. ... 152
Figure 6.28– Wild–type and $VLPs_{DyLight–488}$ migration on a 1.2% agarose gel... 152
Figure 6.29– UV–visible spectrum for $VLPs_{DyLight–488}$. ... 153
Figure 6.30– TEM image of $VLPs_{DyLight–488}$ in the presence of TCEP. 153

Figure 6.31– Schematic representation of the deposition of polycation/polyanion onto eVLPs 155
Figure 6.32– Charge reversal on alternate adsorption of polyelectrolyte on $^{(PAH/PSS)1-2}VLPs_{gemcitabine}$. 156
Figure 6.33– Stained TEM images of polyelectrolyte coated $VLPs_{drug}$. 156
Figure 6.34– Agarose gel electrophoresis of gemcitabine loaded VLPs. 157
Figure 6.35– Coomassie stained gel electrophoresis for $VLPs_{gemcitabine}$ 158
Figure 6.36– Elemental energy–dispersive X–ray spectroscopy analysis of $^{(PAH/PSS)2}VLPs_{gemcitabine}$ 159
Figure 6.37– Release studies using gel electrophoresis for $^{(PAH/PSS)2}VLPs_{gemcitabine}$. 160
Figure 6.38– $^{(PAH/PSS)2}TOP_{GEMCITABINE}$ drug release 161
Figure 7.1– ^{Fc}CPMV derivative nomenclature..... 168
Figure 7.2– Generating ^{SPDP}CPMV particles 170
Figure 7.3– Doubly–functionalised $^{Ferrocene\ carboxylic\ acid}CPMV^{azidopropylamine}$ particles.. 174
Figure 7.4– Transmission electron microscopy images of chemically modified ^{Ferrocene}CPMVparticles..... 175
Figure 7.5– DLS of ^{Ferrocene}CPMV……...……...……176
Figure 7.6– Wild–type and ^{Ferrocene}CPMV particles on a 1.2% agarose gel…..……..177
Figure 7.7– Cyclic voltammogram for some ^{Ferrocene}CPMV modified particles. 178
Figure 7.8– Randles–Sevcik equation..... 179
Figure 7.9– Addressable lysine residues on the exterior surface of the CPMV capsid with the separation distances.. 180
Figure 7.10– Schematic representation of FcC12 linker..... 181
Figure 7.11– Schematic of ^{Ferrocene}CPMV particles immobilised onto gold surface through cystamine SAM formed on Au surface. 183
Figure 7.12– Typical CV of a clean gold electrode in 0.1M H2SO4 at 100 mV s–1.. 184
Figure 7.13– Cyclic Voltamograms for the removal of cystamine SAM from the Au surface by the electroreduction…… 185
Figure 7.14– Ferrocenecarboxylic acid attached to cystamine functionalised Au surface. 184
Figure 7.15– CV scans of Au surface before and after attachment of ^{Fc6ac}CPMV particles. 186
Figure 7.16– Schematic illustration of carbon electrode functionalisation..... 188
Figure 7.17– CV scans for the confirmation of successful modification of PGE electrode before and after the modification……..189
Figure 7.18– CV scans for aminoferrocene conjugated to SAM layer formed via “click” chemistry reaction.. 190
Figure 7.19– CV scans for ^{Aminoferrocene}CPMV conjugated to PGE surface..... 191
Figure 8.1– Aldehyde groups generated on the enzyme surface can react with amine nucleophiles to form reversible Schiff base intermediates.. 200
Figure 8.2– Enzymes (HRP and GOX) activation by sodium metaperiodate 202
Figure 8.3– Wild–type and ^{Enzyme}CPMV particles separated on a 1.2% agarose gel 205
Figure 8.4–SDS–PAGE of $^{HRP–ADH}$CPMV particles..... 206
Figure 8.5– UV–vis spectrum for the fluorescently labelled HRP conjugated to CPMV particles……..…206
Figure 8.6–TEM image of $^{HRP–ADH}$CPMV particles stained with 2% UA..... 208
Figure 8.7– TEM images of $^{HRP–ADH}$CPMV particles stained with 1% $AgNO_3$ solution.. 218
Figure 8.8– Zeta potential measurement of $^{NHS–ester}$CPMV and $^{HRP–ADH}$CPMV particles..... 209
Figure 8.9– Calibration curve plotting known HRP concentrations against their corresponding absorbance at 450 nm..... 210

Figure 8.10– Agarose gel (1.2%) electrophoresis of $^{GOX–ADH}$CPMV particles visualised by ethidium bromide staining……..212
FIGURE 8.11– SDS–PAGE OF $^{GOX–ADH}$CPMV PARTICLES. 212
Figure 8.12– DLS data comparing CPMVwt and $^{GOX–ADH}$CPMV…….213
Figure 8.13– Calibration curve plotting known GOX concentrations against their corresponding absorbance at 571 nm..... 214
Figure 8.14– Current–potential profiles of $^{(Fc6ac)GOX–ADH}$CPMV. 215
Figure 9.1– A20FMDV2 peptide sequence for α5β3 integrin targeting.. 220
Figure 9.2– ^{DTSSP}CPMV particles…….223
Figure 9.3– 1.2% agarose gel electrophoresis for ^{A20FMDV2}CPMV particles. 226
Figure 9.4– Stained TEM image of ^{A20FMDV2}CPMV particles. 226
Figure 9.5– Illustration of the chemical coupling of Dox to the CPMV capsid. 228
Figure 9.6– Native 1.2% agarose gel electrophoresis of $^{Dox–NHS–ester}$CPMV particles. 229
Figure 9.7– UV–visible spectrum of $^{Dox–NHS–ester}$CPMV particles. 230
Figure 9.8– DLS data comparing CPMVwt and $^{Dox–NHS–ester}$CPMV..... 231
Figure 9.9– Stained TEM image of $^{Dox–NHS–ester}$CPMV particles. 231
Figure 9.10– Fluorescence analysis of $^{Dox–NHS–ester}$CPMV in Hela cells after 24 hours..... 232

List of tables

Table 1.1– Overview of the inorganic materials generated by peptides using viruses as templates. 15
Table 3.1– Examples of peptides known to direct the mineralization of inorganic nanomaterials.. 46
Table 3.2– Peptide sequences used for peptide–promoted mineralization.. 50
Table 3.3– Comparison between CPMV–templated FePt particles synthesised by either genetic insertion or chemical modification…… …..62
Table 3.4– Diameter and polydispersity measured by dynamic light scattering and zeta potential of CPMVwt and mineralized–CPMV nanoparticles……66
Table 4.1– Dynamic light scattering and zeta potential measurements.……84
Table 5.1– Pd^0–CPMV concentration and plating solution composition..... 111
Table 5.2– Diameter and polydispersity measured by dynamic light scattering of wild–type CPMV and metallized–CPMV..... 115
Table 5.3– Diameter and polydispersity measured by dynamic light scattering of wild–type CPMV and Co–CPMV nanoparticles on variation of incubation time with the ELD solution..... 119
Table 7.1– Diameter and polydispersity of ^{Ferrocene}CPMV 176
Table 7.2– Reduction potential (*E½*) of ferrocene and ^{Ferrocene}CPMV *vs* Ag/AgCl and the average number of ferrocenes per CPMV virion as calculated from the linear plots of current versus the square–root of the scan rate and 179

1 Literature review

1.1 Introduction

The great power of material manipulation at the nano scale lies in the resultant properties being unpredictably different from those observed at the macro scale. Nanotechnology is often described as a revolutionary new field of development with the potential to change lives and holds great promise in many areas. “Nano” science and technology promise and envisage futuristic applications from the ability to construct anything precisely by controlling the individual atoms or molecules; this prospect thrills the optimists as much as it frightens the pessimists. Nanotechnology offers ways to create smaller, cheaper, lighter and faster devices, which use fewer raw materials and consume less energy.

To attempt a short introduction to “nano” science and technology is an intimidating task. The field is incredibly broad and diverse. The SI prefix “nano” means a billionth (10^{-9}) part, thus a nanometre is a billionth of a metre. A common popular image of the nanometre is one eighty thousandth of the width of a human hair. “Nano” is used to refer to both science and technology; where “nanoscience” appears within a wide range of scientific fields (physics, chemistry, biology, and material science). However, “nanotechnology” has potential applications in a range of different disciplines (energy, transport, medicine, textiles and electronics).

According to the national nanotechnology initiative (www.nano.gov), an object is nanoscale when it is approximately in the 1–100 nm size range. In this size range, properties change because as things become very small, the surface shrinks less than their volumes, causing larger surface–to–volume ratios than for larger objects. A greater surface area can mean that nanomaterials have higher reactivity, conductivity and magnetic properties (Mansur, 2010).

Nanotechnology is not only featured in science fiction books or movies but also offers fascinating solutions to a number of practical problems. For example, nano–coated clothes can repel dirt and reduce the use of harmful chemicals, and mobile phones are becoming smaller and smaller but are growing cleverer, faster and cheaper.

Nanoscience is a multidisciplinary research area, which has the ability to tune physical, chemical, optical, magnetic and electronic properties on nanoparticles by adjusting the size and the shape of the nanoparticles. Nanoscale particles often exhibit properties distinct from those exhibited by larger objects of the same material. Properties such as colour, conductivity, and reactivity can all change at the nanoscale. A classic example of this is gold nanoparticles, which appear red (for particles less than 100 nm) (Sardar et al, 2009) and are more reactive compared to the inactive bulk material. In addition, the increase in surface area to volume ratio increases the reactivity of nanoparticles.

(Bio)nanotechnology or nano(bio)technology is a subset of nanotechnology; the words are synonymous. Bionanotechnology is atomic–level engineering and manufacturing using biological molecules or organisms for guidance. The integration of nanoparticles, which exhibit exceptional electronic, photonic, and catalytic properties, with biomaterials, which display unique recognition, catalytic and inhibition properties, has resulted in the production of new bionanomaterials with combined properties (Wu & Payne, 2004). The integration of the imparted functionalities in a defined arrangement on the bionanomaterials surface while preserving its integrity has great potential in the development of novel materials.

Two methods for the synthesis of miniaturised nanoscale structures and devices have been utilised by many research groups across the globe. The traditional method to synthesise such structures is a "top–down" approach involving miniaturisation processes or microfabrication: starting from large structures and by multiple etching processes generate the desired shape and structure. This approach has a size limitation of how small the structures could be miniaturised. Alternatively, "bottom–up" (enlargement strategy) which is starting with small scale materials and building something bigger offers better control over the size and shape of nanostructures depending on the building blocks available to start with.

Bionanotechnology does not only offer a unique and ideal way for the synthesis of well–defined nanostructures from the bottom–up but also adds specific functionalities that are positioned at precise locations and in defined distances across all particles. Bionanotechnology requires different scientific disciplines to contribute collectively toward the development of new

nanosystems to be used in nanomedicine and nanoelectronics. Biomolecules are considered as naturally occurring bionanoparticles and offer novel properties for the development of diagnostic, analytical and drug delivery systems (Niemeyer & Mirkin, 2004). As well as, providing scaffolds, which add structural support, and by their chemical composition, biomolecules offer ligand–binding sites to generate hybrid assemblies with the desired properties.

Physicist and Nobel Prize winner Richard Feynman planted the idea of "nano" in 1959. Feynman, in his influential speech "There's Plenty of Room at the Bottom", introduced the world to the wonders of "nanotechnology" through miniaturisation. The focus of Feynman's speech was about the field of miniaturization and his belief that man would create increasingly smaller and more powerful devices. Eric Drexler in "Engines of Creation" introduced for the first time the term "nanotechnology" (Drexler, 1986). Over the past two decades, nanotechnology has emerged as one of the most focused fields of research. Researchers are focused on exploiting the advances in nanotechnology for biomedical, environmental, and industrials applications.

1.1.1 Bionanoparticles: Bio–inspired nanomaterials

Bionanoparticles include protein cages, bacteria, DNA, liposomes, virus–like particles (VLPs) and viruses that are naturally occurring programmed self–assembled nanoparticles. They are robust, self–assembled architectures, less expensive to produce than inorganic materials, and can be relatively easily produced in large quantities. In particular, protein cages such as ferritin and some plant viruses have been extensively exploited as building blocks, templates and scaffolds in bionanotechnology (Douglas & Young, 2006; Fischlechner & Donath, 2007; Lee & Wang, 2006b). Figure 1.1 features examples of bionanoparticles, which may be used as constrained reaction containers, scaffolds for material synthesis, and multi–functional nanoparticles that could be constructed by modifying the external surface. Bionanoparticles modified with various ligands and moieties have generated new materials with

interesting properties, which have possible applications in the field of nanoscience. A wide library of such particles has been catalogued (Manchester & Steinmetz, 2009).

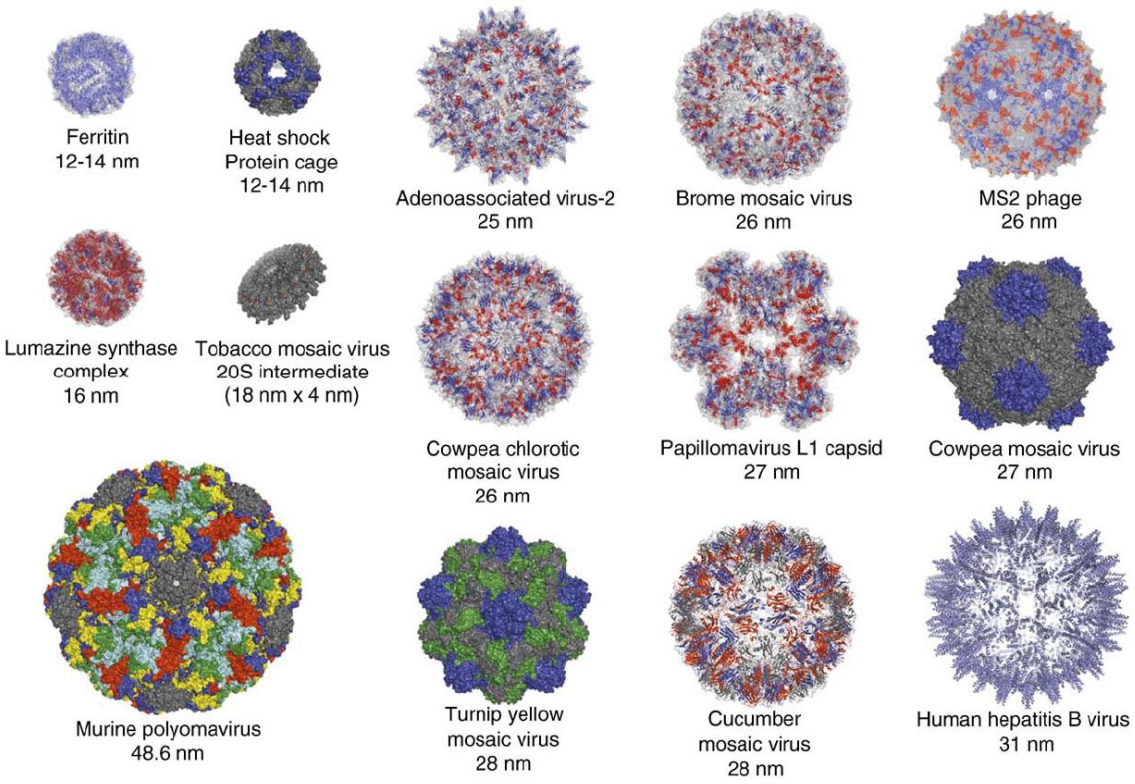

Figure 1.1– Structural illustration of some protein cages which have been used in bionanotechnology or biomedical applications. Reproduced from (Lee & Wang, 2006a).

Several examples of protein cages, which are capable of encapsulating molecules of interest, have been reported. Heat shock protein (Hsp), iron storage proteins (ferritin), and vaults are some examples. Each of these protein cages has particular properties (size, shape and function) that are suitable for many applications.

The iron storage protein ferritin is probably the most intensively studied and best understood model for encapsulation or material mineralization (Chasteen & Harrison, 1999). Ferritin comprises 24 subunits, of two types (H and L) that self–assemble to form a hollow cage structure of 12 nm in diameter. In the native ferritin form, iron is stored within an 8 nm diameter cavity (Andrews et al, 1992; Theil, 1987). In order to encapsulate molecules within ferritin, the internal cavity needs to be free of its iron core (apoferritin). A variety of apoferritin is

commercially available and has been used for material encapsulation, Figure 1.2, e.g. the formation of Prussian blue in ferritin (Dominguez–V & Colacio, 2003).

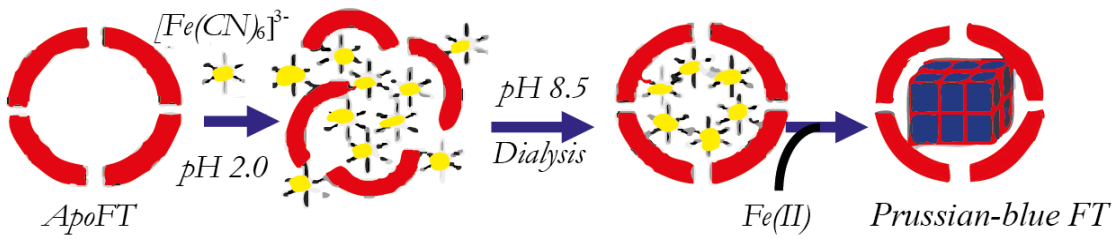

Figure 1.2– Schematic illustration of the pH–induced dissociation–reformation process of apoferritin to form Prussian blue complex. The protein is dissociated at pH 2.0 and after dialysis at pH 8.5 and the addition of Fe(II) Prussian blue is formed with the cavity. Reproduced from (Dominguez–V & Colacio, 2003).

Encapsulated chemicals within ferritin reported so far include: uranium (Hainfeld, 1992), copper (Ensign et al, 2004), manganese oxide (Meldrum et al, 1995), vanadium (Grady et al, 2000), beryllium (Price & Joshi, 1983), cadmium, zinc, nickel, magnesium (Pead et al, 1995), cobalt oxyhydroxide (Douglas & Stark, 2000), and iron phosphate, iron arsenate, iron vanadate and iron molybdate (Polanams et al, 2005). Other molecules also have been encapsulated within ferritin such as desferrioxamine B complex (DomInguez–V. & José M., 2004), Prussian blue (Dominguez–V & Colacio, 2003), and doxorubicin, an anticancer drug (Simsek & Kilic, 2005). Moreover, apo–ferritin protein is typically used for internal metal mineralization such as with cobalt oxide Co_3O_4 and Co(O)OH (Allen et al, 2003). Mann and co–workers showed formation of Fe_3O_4 (or γ–Fe_2O_3) under conditions of elevated temperature and pH (Douglas et al, 1995; Mann et al, 1993)

Heat shock protein (Hsp) forms a hollow spherical 24–subunit complex. The complex exhibits octahedral symmetry with an outer diameter of 120 Å and an inner diameter of 65 Å. Hsp was also used as template for external and internal modification and as a container for iron oxide encapsulation (Allen et al, 2003) and drug delivery systems (Flenniken et al, 2006).

Vaults are another type of self–assembled naturally occurring cellular protein nanocapsule, which are so–named as their morphology, with multiple arches, resembles that of cathedral ceilings (Kickhoefer et al, 2005). Vaults are found in high copy number in many

higher eukaryotes (including humans). Vaults are 13–MDa ribonucleoprotein particles with an internal volume of 5 x 107 $Å^3$. Vaults tend to have a hollow, barrel–like structure with two protruding caps and a thicker waist with overall dimensions of 420 x 420 x 750 Å as seen in Figure 1.3 (Kong et al, 2000). Due to the large structure, vault particles can encapsulate and accommodate large molecules such as green fluorescent protein (GFP) and luciferase (Kickhoefer et al, 2005).

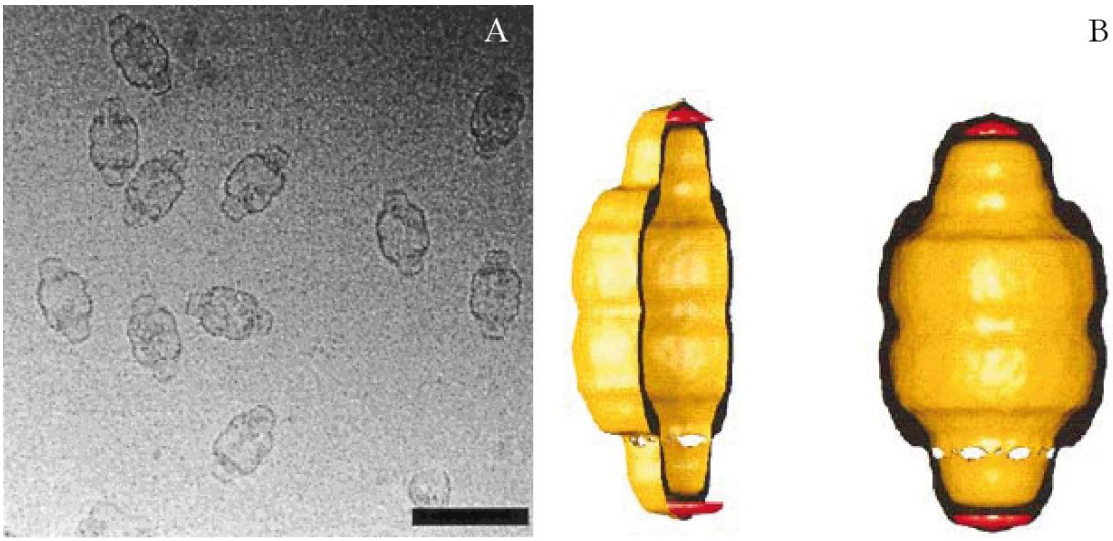

Figure 1.3– Cryo–transmission electron microscopy of vault particles. (A) cryo–EM. (B), half and full capsid images representing the inner and outer structure. The scale bar corresponds to 1000 Å. Reproduced from (Kong et al, 2000).

1.1.2 Viruses

The word virus is derived from Latin and means "poison". Viruses are obligate intracellular parasites, which only replicate within a host cell. Particles of simple (non–enveloped) virus typically consist of two components: one or more capsid proteins and the genome. The genome encodes the proteins necessary for the replication of the virus and the capsid protein(s), while the capsid is mainly for the protection of the genetic material. Virus capsids also have roles in host cell targeting and cell entry (Harrison, 1990). Virus particles typically represent very stable structures that have evolved to withstand a broad range of environments yet are sensitive enough to release their nucleic acid when they infect a susceptible cell (Liepold et al, 2005).

1.1.3 Why virus nanoparticles (VNPs)

Virus nanoparticles are no longer considered only as disease transmitting agents. All viruses encode, package, and transport viral nucleic acid. However, many virus coat proteins will assemble *in vitro* naturally or through genetic manipulation into non–infectious containers called virus–like particles (VLPs). Viruses can be found in a variety of distinct shapes (most commonly icosahedrons, spheres, and rod–shaped) though more complicated structures can be formed especially in the case of bacteriophage.

Material scientists view viruses as nanoscale building blocks and scaffolds. Their unique properties; ease of functionalisation, ability to self–assemble, monodispersity (every particle looks virtually identical in size and shape to all other particles), structural symmetry, stability over a wide range of pHs and temperatures, amenability to genetic and chemical modification, and diversity of sizes and shapes make them ideal work–horses with a variety of possible applications in nanotechnology. Besides, plant viruses are non–infectious towards organisms other than plants; therefore, they do not present any biological hazard. Fundamental research in the understanding of viruses as pathogens resulted in a wealth of information about their structure, stability, assembly, and physical and chemical properties. This knowledge, and the close collaboration between the fields of virology, material science and biomedical research, has pushed forward the use of VNPs in nanotechnology.

Viruses display a remarkable plasticity in their capsid structure and dynamics (coordinated assembly, disassembly, and their uniformity). Viruses can be produced in large scale at low cost in a relatively short time. Viruses have emerged as platforms for chemical manipulation with a range of applications from the creation of new materials to nanomedicine. Chemical or genetic manipulation makes it possible to attach new functions to protein cage architectures. This provides the possibility of arranging different chemical functionalities with nanometric precision.

Viruses offer three different surfaces that can be exploited: the exterior, the interior, and the interface between subunits (Figure 1.4). The inner cavity of the virus capsid is accessible to

small molecules and impermeable to larger ones, which allows the use of the interior space of the empty virus like particles (eVLPs) as nanotemplates and nanoreactors. Furthermore, the exterior surface is widely considered as a robust platform and is used for both chemical and genetic modification allowing multivalent ligand display. The viral architectural interface is crucial for the assembly and offers another route for the manipulation of the capsid architecture. Herein, the focus will be on the manipulation of the interior and the exterior of the viral capsid.

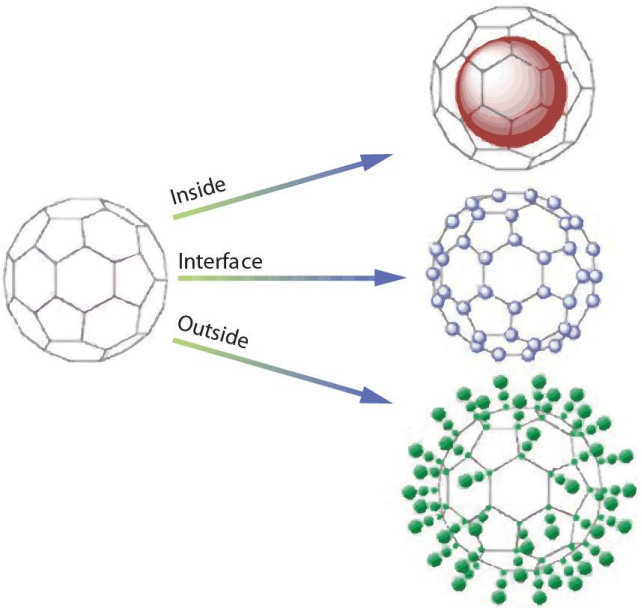

Figure 1.4– Scheme of the three important interfaces available for chemical and genetic manipulation in an assembled viral protein cage architecture. The interior, exterior and the interface have all been used for the construction of multifunctional viral–cage–based materials. Reproduced from (Douglas & Young, 2006).

1.1.4 Empty virus capsids–eVLPs

Virus–like particles (VLPs) resemble viruses, but are non–infections because they do not contain any viral genetic material. The expression of the virus structural proteins, can result in the self–assembly of VLPs. Libraries of virus platforms including; (CCMV) (Douglas & Young, 1998a), Tobacco mosaic virus (TMV) (Shenton et al, 1999), MS2 bacteriophage (Mastico et al, 1993; Wu et al, 1995) and polyoma virus–like particles (capsoids) (Abbing et al, 2004) have been used as constrained reaction vessels for packaging and nucleation sites for

mineralization (Douglas & Young, 1998a; Douglas & Young, 1999). In addition, intact enzymes have been encapsulated within the CCMV capsid (Comellas et al, 2007).

Therefore, many attempts to generate VLPs have been developed over the past three decades. *In vitro* assembly and re–assembly methods have been exploited for VLPs. Generally, particles are exposed to a disassembly buffer followed by dialysis against an assembly buffer. These disassembly approaches allow release of the nucleic acid and are used to generate VLPs or encapsulating materials of interest in the reassembly technique. VLPs of TMV and CCMV have been demonstrated to efficiently self–assemble *in vitro* (Miller et al, 2007). Alternatively, an alkaline hydrolysis method was developed to extract nucleic acid from T7 to generate ghost (empty) T7 particles (Liu et al, 2006a).

1.1.4.1 Entrapment of small molecules within VLPs

In many cases, the entrapment of small molecules within VLPs is dependent on the structural transitions of, for example, Brome mosaic virus (BMV), CCMV, and Red clover necrotic mosaic virus (RCNMV). The material is infused into particles when they are in the swollen "open" conformation. Dialysis against appropriate buffers allows reversible structural conformation to the "closed" form, taking with it whatever materials of interest are available in solution.

CCMV has been used as nanobuilding blocks (Wang et al, 2002d), for mineralization of iron oxide (Basu et al, 2003b), and as a host–guest encapsulation model of tungstate and vanadate (Douglas & Young, 1998a). The stability of the CCMV capsid is pH–dependent, which alters the opening of 60 separate pores of 2 nm each and exposes the interior to the surrounding medium. This conformation has been used to induce the formation of metal cores inside the CCMV capsid.

1.1.4.2 Encapsulation of preformed particles via templating

The decoration of preformed synthetic nanoparticles with origin of assembly site (OAS) that initiates coat protein monomer binding and leads to self–assembled VLPs with synthetic

nanoparticles within has been accomplished in RCNMV. Thiolated artificial OAS was attached to gold nanoparticles (Wu et al, 1995). OAS–gold nanoparticles were mixed with RCNMV coat protein monomers and templated in vitro self–assembly of VLPs around the gold nanoparticle, the process is depicted in Figure 1.5 (Loo et al, 2006). This approach was expanded to include encapsulation of QDs with sizes of 5, 10, and 15 nm (Loo et al, 2006; Loo et al, 2007).

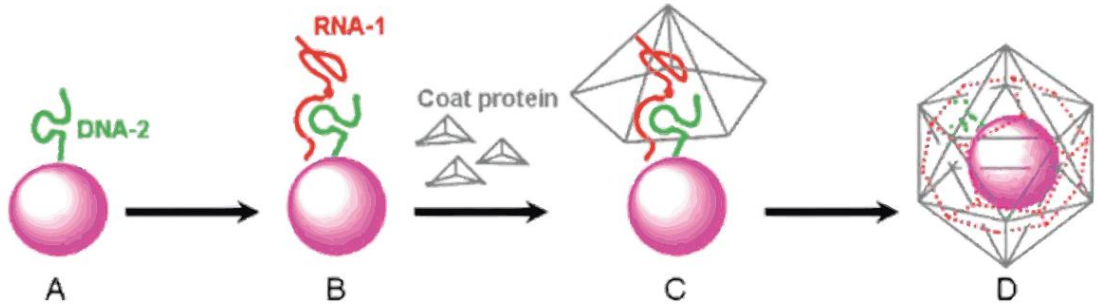

Figure 1.5– Assembly of RCNMV VLPs around a gold nanoparticle via OAS templating. (A) conjugation of nanoparticle with DNA–2; (B) addition of RNA–1, which interacts with DNA–2 to form the functional OAS; (C) the artificial OAS templates the assembly of coat protein; and (D) formation of virus–like particle with nanoparticle encapsulated. Reproduced from (Loo et al, 2006).

Alternatively, the nanoparticle is coated with negatively charged polymers to mimic RNA an approach, which was pioneered by Dragnea's group. Although citrate–stabilised gold nanoparticles resulted in encapsulated VLPs with preformed gold nanoparticles the process was not efficient (Dragnea et al, 2003). Alternatively, covalent functionalisation of nanoparticles with carboxylate–terminated polyethylene glycol (PEG) (Chen et al, 2006; Dixit et al, 2006) was used to mimic RNA nucleation and promote efficient *in vitro* self–assembly (Figure 1.6).

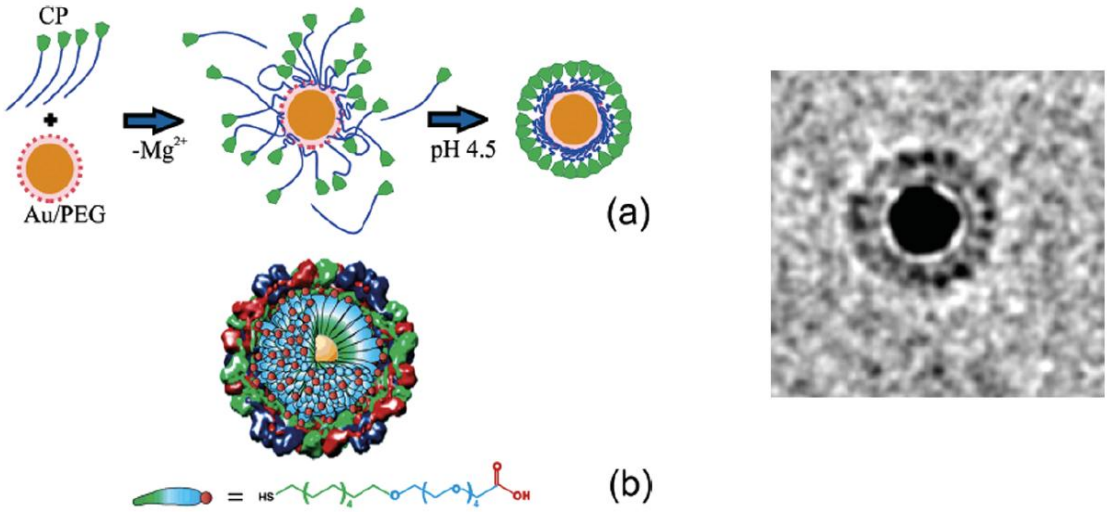

Figure 1.6 – Proposed mechanism of VLP assembly from coat proteins (CP). Electrostatic interaction leads to the formation of disordered protein–gold nanoparticle complexes. The second step is a crystallization phase in which the protein–protein interactions lead to the formation of a regular capsid. (b) Schematic depiction of the encapsidated nanoparticle functionalized with carboxyl–terminated TEG chains. Right: Cryo–EM micrograph of a single VLP. The protein structure coating the 12 nm diameter gold nanoparticle (black disk). Reproduced from (Chen et al, 2006).

1.1.4.3 Encapsulation during self–assembly

The self–assembly of a virus is initiated by electrostatic interactions between RNA and the protein subunits. In the case of CCMV, mixing the coat protein monomers with different sized polystyrene sulfonate (PSS) polymer to mimic the RNA resulted in two different size morphologies: 22 nm–sized particles generated by using PSS with molecular weight below 2 MDa; 27 nm–sized particles with PSS of 2 MDa or higher was used (Hu et al, 2008). Hibiscus chlorotic ringspot virus (HCRSV) particles have also been used to encapsulate negatively charged polymers including polystyrenesulfonic acid (PSA) and polyacrylic acid (PAA). Re–assembly yielded VLPs encapsulating the polymers. However, attempts to encapsulate neutral molecules such as fluorescein–labelled dextran failed, suggesting the encapsulation is based on electrostatic interactions (Ren et al, 2006b).

1.1.4.4 Infusion of materials into assembled eVLPs

Material encapsulation into assembled empty CCMV particles has triggered wide research interest. For example, pH–dependent gating of the CCMV pores (Douglas & Young, 1998a) controls the encapsulation of anionic polyanetholesulfonic acid (PASA) and polydextran sulfate (PDS). Small lanthanide molecules have been infused and entrapped into CPMVwt by taking advantage of the negatively charged RNA interaction with Gd^{3+} and Tb^{3+} cations (Prasuhn et al, 2007b). 80 ± 20 Gd^{3+} or Tb^{3+} ions can be encapsulated within CPMV particles (Prasuhn et al, 2007b). Similar approaches for lanthanide entrapment in CCMV have been reported (Allen et al, 2005b). In addition, a similar approach has been adopted to infuse fluorescent dyes and drugs within RCNMV (Loo et al, 2008).

1.1.5 Biomineralization on viruses

Biomineralization is defined as the formation, structure and properties of inorganic material intentionally formed in biological systems (Mann, 2001). Familiar examples of such structures include sand dollars and shells, as well as the human skeleton and teeth (Mann, 2001). Recently, interest from material scientists has focused on mimicking the methods that nature uses to create such inorganic materials. This process is called biomimetics. Biomimetics may also include materials that resemble the structure or properties of materials produced by biological entities (Mann, 1996; Mann, 2001). Biomineralization techniques can create incredibly precise and complicated structures under ambient conditions such as such as platinum, gold, and silicon dioxide (Sarikaya, 2003).

Over the past few decades, biological hard tissues have been an inspiration for the engineering and design of inorganic structures with controlled structure and properties. Biomineralization seeks to understand the mechanism by which biosystems can uptake elements from its surroundings, and organise them into complex highly ordered structures of defined functionality (Mann, 1996; Seeman & Belcher, 2002; Tamerler et al, 2010). Although these materials provide essential life function for many organisms (Weiner & Traub, 1992), their

unique properties and inherently precise control have generated much attention from material scientists. Furthermore, biomineralization reactions proceed under aqueous conditions at ambient temperature; for example, the organisation of a lipid–based closed membrane incorporating a magnetic nanoparticle that forms within the bacteria *Aquaspirillum magnetotacticium*. The magnetite (Fe_3O_4) aligns inside the bacteria to create a magnetic field large enough to sense the earth's magnetic field (0.5 Gauss). The Fe_3O_4 is formed as perfect cubo–octahedral single crystals, about 35–120 nm in diameter, each having a superparamagnetic domain and the particles are aligned with respect to each other in order to maximise magnetic field sensing that allows the cell to have a directional mobility (Schuler, 2002; Staniland, 2007).

The successful isolation of protein sequences that play a role in the biomineralization process has provided some insight in understanding the mechanisms behind biomineralization. However, the complexity of natural systems has hindered the complete understanding of the biomineralization process. The exploitation of the tremendous advantages of biomineralization; a rapid method for utilising functional, material–specific peptides is needed to be developed for applications in semiconductors, conductors and magnetic materials synthesis.

1.1.5.1 Mineralization using natural properties of VNPs

Almost all of the adopted biological systems for templated mineralization are based around the natural properties of the VNPs. The first system to be used was CCMV using its pH–dependent gating system. The mineralization reaction within CCMV is electrostatically driven. The interior is highly positively charged and therefore provides an interface for inorganic nucleation. The negatively charged WO_4^- and VO_3^- anions interact with the interior capsid surface via electrostatic interactions (Douglas & Young, 1998b). The same principle was used to generate titanium oxide (TiO_2) (Klem et al, 2008) and Prussian Blue nanoparticles (de la Escosura et al, 2008). Furthermore, the substitution of all the basic residues on the N–terminus of the coat protein with negatively charged amino acid Glu (Brumfield et al, 2004) resulted in

the mutant favouring interaction with ferrous and ferric ions leading to the formation of iron oxide (Fe_2O_3) within the capsid.

Empty T7 ghost particles were filled with metallic cobalt (Liu et al, 2006b). Similarly, the high charge density on the interior surface of ferritin leads to the nucleation of soluble Fe(II), which is subsequently oxidized, resulting in encapsulated iron oxide (Fe_2O_3) nanoparticles (Uchida et al, 2007).

The exterior and interior of TMV was utilised for inorganic material synthesis via metal electroless deposition (ELD). The interior surface of TMV is predominantly carboxylic acids, hence the capsid interior is negatively charged under physiological conditions, whereas the exterior surface exhibits positive charge (Namba & Stubbs, 1986). The exterior of TMV was coated with PbS, CdS, amorphous iron oxide, silica (Shenton et al, 1999), platinum, gold, and silver incorporated inside the central channel (Bromley et al, 2008; Dujardin et al, 2003a). The differential nucleation is electrostatically driven and resulted from the difference in surface charge. In addition, TMV particles were engineered to encode unique cysteine residues (TMV1cys); this allowed the assembly of TMV1cys onto a gold patterned surface, the particles assembled in a vertically oriented fashion. The subsequent ELD resulted in uniform metal coatings up to 40 nm thick (Royston et al, 2007).

1.1.6 Mineralization using phage display

Many biological processes in biosystems rely on specific, protein–ligand interactions. Biomineralization is no different in that the inorganic substrate serves as the ligand, and highly specific peptides dictate the organization and construction of the inorganic structure. Combinatorial screening is a routinely used technique for isolating peptides that exhibit the necessary affinity for specific targets; in this case an inorganic substrate. The research team led by Belcher developed the use of phage display screening and selection to identify peptide sequences that bind and nucleate specific inorganic materials (Mao et al, 2004; Seeman & Belcher, 2002; Whaley et al, 2000). Insertion of nucleic acid sequences into certain proteins (PIII (peptide displayed on the end structure) or PVIII (throughout the body) within a phage

genome (M13) (Figure 1.7) generated phage that present the peptides of interest on their surfaces (Kwon et al, 2009). Peptide–M13 then binds to the substrate (e.g., gold or platinum). Stringent washing steps are used to remove phage lacking surface peptides that strongly interact with the inorganic material. The eluted phages are cultured and the cycle repeated until only phage with high affinity to the specific inorganic surface remains.

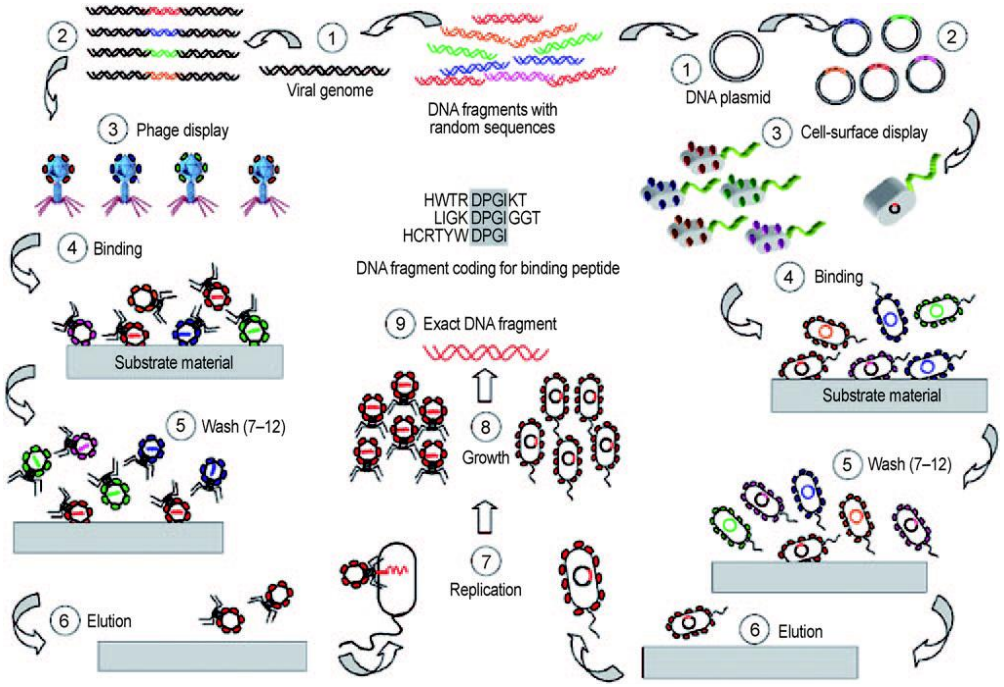

Figure 1.7– Peptides expressed in phage display and cell–surface display. This figure is reproduced from (Kwon et al, 2009).

A variety of peptides that are specific for binding to different materials are summarised in Table 1.1. The peptides are highly selective and the binding motif is small; the selected peptides are typically from (7–11)–mer libraries. Besides, dual peptides have been engineered on PVIII specific for ZnS and CdS. When the M13 was incubated with both Zn(II) and Cd(II) in the presence of sulfide anions the M13 particles nucleated both CdS and ZnS nanocrystals with a random distribution such that both CdS and ZnS nanocrystals appeared on the same phage constructs (Mao et al, 2003).

Viruses	Material	Synthesis mechanism	Reference
CPMV (exterior)	Silica (SiO_2)	Peptide–mediated synthesis (YSDQPTQSSQRP)	(Steinmetz et al, 2009c)
CPMV (exterior)	CoPt, FePt and ZnS	Chemical conjugation of peptide–mediated synthesis (see chapter 3)	(Aljabali et al, 2011)
CPMV (exterior–Chimaera)	FePt	Peptide–mediated synthesis (HNKHLPSTQPLA)	(Shah et al, 2009b)
M13 (exterior–Chimaera)	ZnS	Peptide–mediated synthesis (CNNPMHQNC)	(Mao et al, 2004)
M13 (exterior)	CdS	Peptide–mediated synthesis (SLTPLTTSHLRS)	(Mao et al, 2004)
M13 (exterior)	FePt	Peptide–mediated synthesis (HNKHLPSTQPLA)	(Reiss et al, 2004b)
M13 (exterior)	CoPt	Peptide–mediated synthesis (CNAGDHANC)	(Mao et al, 2004; Reiss et al, 2004b)
M13 (exterior)	Co^{2+}	Peptide–mediated synthesis (EPGHDAVP)	(Lee et al, 2006)
M13 (exterior)	Gold	Peptide–mediated synthesis (VSGSSPDS)	(Khalil et al, 2007; Nam et al, 2006)
M13 (exterior)	Co_3O_4	Peptide–mediated synthesis (EEEE)	(Khalil et al, 2007; Nam et al, 2008)
M13 (exterior)	CoPt	Peptide–mediated synthesis (CNAGDHANC)	(Reiss et al, 2004b)
T7 (interior)	Cobalt	Electrostatically driven synthesis	(Liu et al, 2006b)

Table 1.1 – Overview of the inorganic materials generated by peptides using viruses as templates.

1.1.7 Cowpea mosaic virus (CPMV)

CPMV is a non–enveloped plant mosaic virus, which is the type member of the comovirus genus of the family Comoviridae (Lin & Johnson, 2003). The virus is normally propagated in *Vigna unguiculata*, commonly known as cowpeas or black–eyed peas or beans. The virus is introduced into the plant by means of mechanical inoculation, which results in mosaic and yellowing symptoms of the leaves. CPMV is considered one of the best investigated viruses and is widely used in bionanotechnology (Evans, 2010; Sainsbury et al, 2010).

CPMV capsids have pseudo T=3 icosahedral symmetry and a diameter of approximately 28 nm. The CPMV capsid structure comprises 60 small coat proteins (S, domain A) which folds into one jelly roll β–sandwich arranged as 12 pentamers at the 5–fold axis and 60 large coat proteins (L, domains B and C) arranged as trimers at the 3–fold axis and fold into two jelly roll β–sandwich domains. The three domains form the asymmetric unit (Figure 1.8). The crystal structure is known to 2.8 Å resolution (Lin et al, 1999b). CPMV is a single stranded positive–sense bipartite RNA virus. Both of the separately encapsidated RNA segments are

required for infection (Bruening & Agrawal, 1967; Liu & Lomonossoff, 2002; van Kammen, 1967). However, it was later demonstrated that RNA–1 is independently capable of replicating CPMV particles in protoplasts (Goldbach et al, 1980). RNA–1 encodes the virus replication machinery (Goldbach et al, 1980) as well as the virus proteinase and the viral protein genome–linked (VPg), which plays an essential role in initiating RNA synthesis. On the other hand, the smaller RNA–2 encodes the movement protein and the two–capsid proteins.

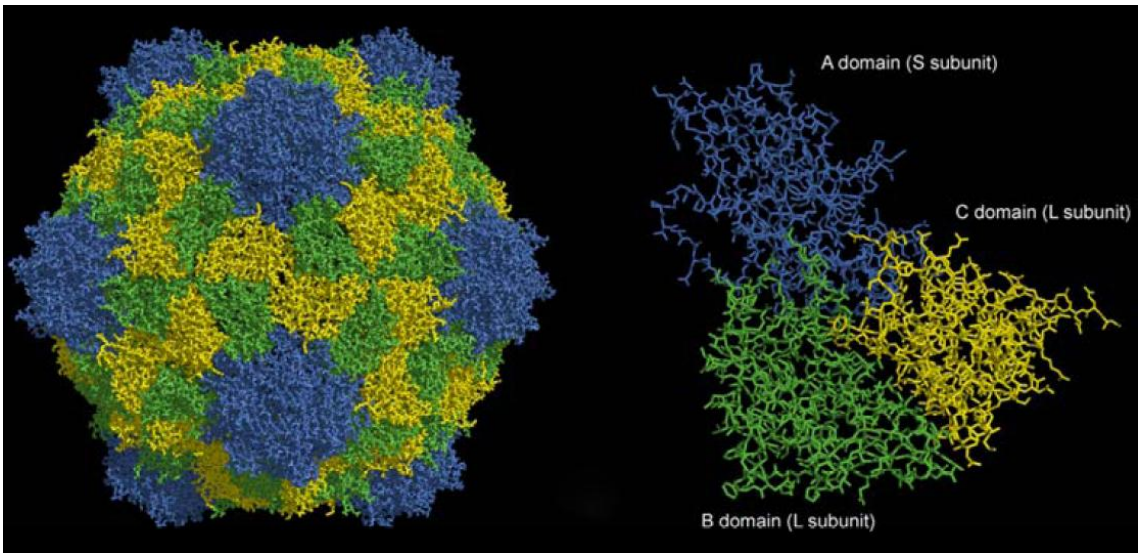

Figure 1.8– The structure of Cowpea mosaic virus (CPMV) capsid and the asymmetric unit. CPMV capsid is comprised of small (S) and large (L) protein. The A domain (in blue), B domain (in green) and C domain (in yellow).

CPMV particles produced during the infection process can be separated into three components on caesium chloride density gradients. These have identical protein compositions, but differ in their RNA contents (Bruening & Agrawal, 1967). The three centrifugal components are termed top (T), middle (M), and bottom (B) and contain no RNA, RNA–2, and RNA–1, respectively as shown in Figure 1.9–A (Bruening & Agrawal, 1967; Lomonossoff & Johnson, 1991a; van Kammen, 1967).

The three components generated during CPMV infection also exist as two electrophoretic forms, slow and fast (Figure 1.9–B) (Semancik, 1966). The slow form can be converted to the fast form by proteolytic cleavage at the carboxyl (C)–terminus of the S protein (Kridl & Bruening, 1983; Niblett & Semancik, 1969b). The conversion occurs naturally during infection, with the fast (C–terminally processed) form of the S protein (S_f) predominating at

later times (Niblett & Semancik, 1969b). Cleavage of the S protein was shown to occur after Leu189 of the S protein resulting in the loss of the carboxyl–terminal 24 amino acids (Taylor et al, 1999).

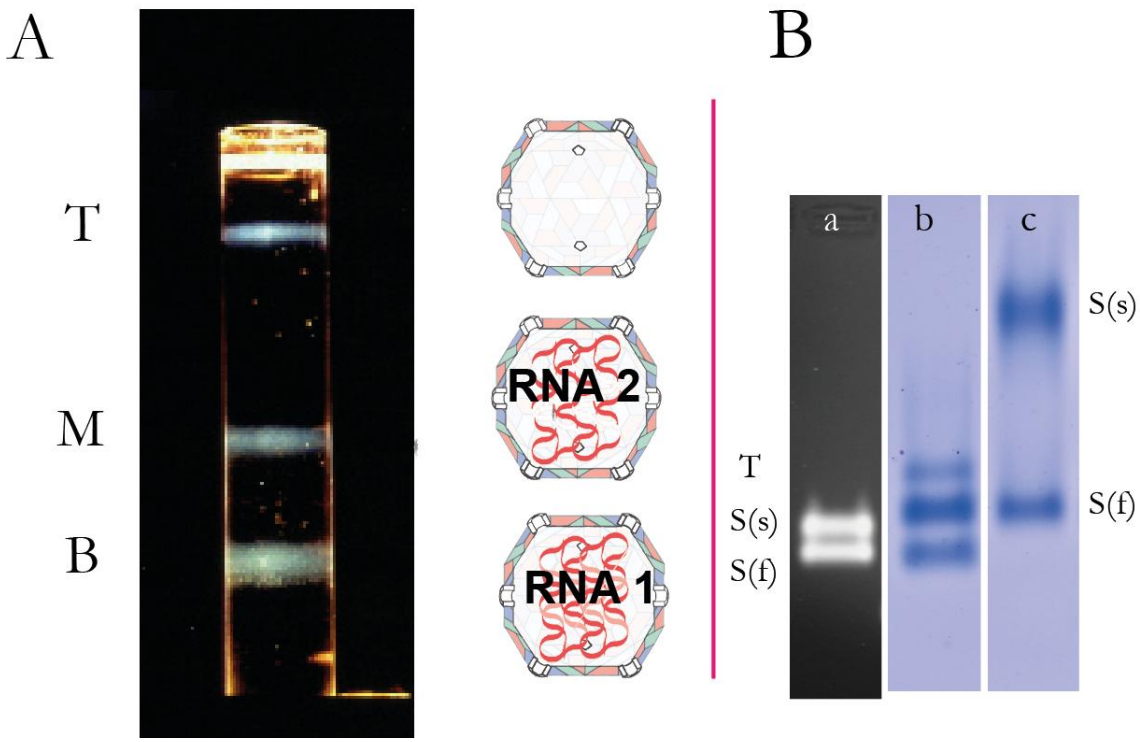

Figure 1.9– Separation of the different components of Cowpea mosaic virus. (A) In a caesium chloride gradient by ultracentrifugation, (B) different electrophoretic forms of particles containing the different forms of the S subunit, the slow (s) and the fast (f), separated on agarose gel electrophoresis: (a) ethidium bromide stained (b) and (c) are Coomassie stained, mobility shift from the s to the f form is due to carboxy–terminal cleavage of 24 amino acids of the S subunit. Caesium chloride gradient photographic image courtesy of Dr. Keith Saunders.

As the importance of eVLPs is apparent, some attempts to inactivate or eliminate the viral RNA within CPMV capsids have been reported including UV irradiation (254 nm) using a dosage of 2.0–2.5J/cm^2. The inactivated particles were deemed as non–infectious to plants. However, particles remained intact and maintained chemical reactivity (Rae et al, 2008). Moreover, the RNA content remains encapsidated so that the internal cavity of the particles is not accessible for material loading. Additionally, alkaline hydrolysis was used to generate artificial empty CPMV particles (Ochoa et al, 2006). This approach was very difficult to reproduce in our laboratory and the majority of the particles remain intact during the disassembly step. In addition, these processes risk altering the structural properties of the particles and generally do not actually remove RNA from the particles.

1.1.7.1 CPMVwt exploitable surface

The structure of CPMV is known to near atomic resolution (Lin et al, 1999a). The particles have an average diameter of 28 nm diameter as confirmed by X–ray diffraction analysis (Lin et al, 1999b) and the capsid protein is 3.9 nm thick. The capsid of CPMV is comprised of 60 copies of the L and S coat proteins. As a result, the external surface of a virus capsid consists of highly symmetrical and repetitive amino acids such as glutamate, aspartate, arginine and lysine. These functional groups have been exploited to serve as a template for nanoparticle synthesis. The surface–exposed amino acids have served as targets for bioconjugation chemistry since 2002 when, for the first time, CPMV was considered as an addressable nanobuilding block (Wang et al, 2002d).

The functional groups ($–NH_2$ or –COOH) on the surface offer a precise addressable site and are the most frequently used for chemical modification. This can be achieved using various techniques of covalent coupling (Aljabali et al, 2010a; Evans, 2010; Hermanson, 2008; Laufer et al, 2009; Meunier et al, 2004; Pokorski & Steinmetz, 2011; Steinmetz et al, 2011) and by "click" chemistry (Manchester & Singh, 2006). Both wild–type and genetic variants of CPMV have been used as scaffolds for chemical modification; early investigations of the chemical reactivity of CPMVwt was aimed at lysine– and cysteine–selective derivatives (Wang et al, 2002). The X–ray structure and coordinates of CPMV (VIPER database) indicated the presence of five solvent–exposed Lys per asymmetric unit, which equates to 300 exposed Lys side chains per CPMV particle, (Figure 1.10) (Chatterji et al, 2004). Four of the five solvent–exposed Lys have been modified with different moieties (Aljabali et al, 2010a; Steinmetz et al, 2006d). In a proof–of–concept study on CPMV, single, double, triple, and quadruple Lys–minus mutants, in which the addressable lysines were sequentially replaced with arginines, were generated and chemical labelling efficiency was measured. The studies indicated that all of the five Lys are available for functionalisation; the degree of labelling efficiency varies between the different sites, and normally only four per subunit are modified. The most reactive groups were found to be Lys 38 on the S protein and Lys 99 on L (Chatterji et al, 2004).

Additionally, carboxylates derived from Asp and Glu have been utilized. Chemical attachment of amine–containing compounds can be achieved by making use of the coupling reagents EDC and NHS. A fundamental problem with this strategy is that interparticle linkage can occur; this can be reduced by using short linkers. 180 surface addressable carboxylates per virion have been modified with different moieties (Aljabali et al, 2010a; Steinmetz et al, 2006c).

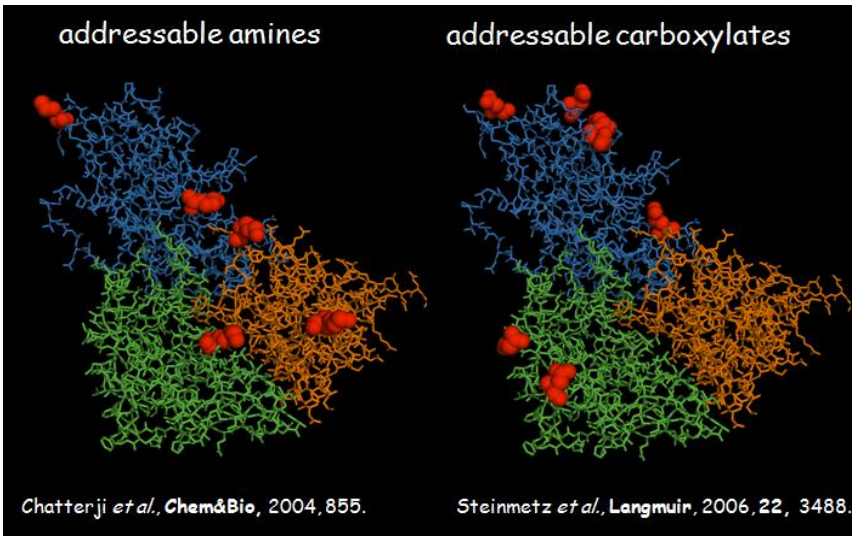

Figure 1.10– Schematic representation of the surface exposed addressable amines and carboxylates of the CPMV capsid.

The aromatic group of Tyr side chains also provides a possible target for chemical modification. However, the aromatic group is only moderately reactive and to achieve bioconjugation the tyrosine phenol has to be oxidised by one electron with, for example, peracid or persulfate reagents mediated by nickel complex of the Gly–Gly–His (GGH) tripeptide (Manchester & Steinmetz, 2009). Commercial reagents for this reaction are typically not available; therefore, the starting materials and coupling reagents must be chemically synthesized. The most common reaction utilizing Tyr side chains on viruses is diazonium coupling and this has been widely used on MS2 and TMV (Kovacs et al, 2007; Schlick et al, 2005a). CPMV particles display two accessible Tyr side chains located in the S subunit, which are available for chemical modification. In a proof–of–concept study, fluorescein has been covalently attached to CPMV Tyr side chains (Meunier et al, 2004).

Thiols derived from Cys side chains are typically not found in the free reactive form on the solvent–exposed surface of viruses, whereas, Cys side chains have been identified on the interior solvent–exposed surface of CPMV (Wang et al, 2002c; Wang et al, 2003a). Thiols are nevertheless useful groups to use for bioconjugation, therefore a range of viruses have been generated via genetic modification to add Cys side chains. Cys–added versions of CCMV, CPMV, FHV, MS2, TMV, and M13, for example, are available (Destito et al, 2009; Khalil et al, 2007; Klem et al, 2003; Kreppel et al, 2005; Miller et al, 2007; Peabody, 2003; Wang et al, 2002b(Wu et al, 1995).

1.1.8 Applications of viruses in nanotechnology

The use of viruses in nanotechnology offers the prospect of rich and diverse technological advancements. As mentioned earlier, the outer surface of a virus capsid can be exploited as a nucleation site for growth of nanoparticles. For example, the deposition of Pt^{2+} ions on the TMV capsid to form nanoparticles with an average diameter of 10 nm (Gorzny et al, 2008; Tseng et al, 2006). When TMV–Pt was placed between two aluminium electrodes, a unique memory effect was observed in which the RNA and the TMV capsid acted as charge donor and energy barrier, respectively. When current was applied, the charge transferred from the aromatic rings such as guanine in the RNA and was trapped in the Pt nanoparticles. The reversible charge transfer and charge trapped process created a memory device. Similarly, another memory device was designed using CPMV with the exterior of the capsid modified with quantum dots (QD) (Portney et al, 2007). The ZnS capped layer of the QD acted as a charge store while the aromatic residues (tryptophan) on the CPMV capsid acted as a charge transport. Ferromagnetic materials play an important role in the development of high–density storage devices, e.g. a computer disk contains a two–dimensional (2–D) ferromagnetic thin film, where information is stored. Ferromagnetic nanoparticles like FePt and CoPt (Sun et al, 2004) emerged as potential high–density storage media. Therefore, the ability to generate highly monodisperse FePt– and CoPt–CPMV might be an alternative route to synthesise these particles (Aljabali et al, 2011). However, the properties of such particles are yet to be established.

Throughout this thesis, many VNPs are used to synthesise magnetic and metallic nanoparticles of various shapes. Besides, hollow metallic nanoparticles and nanoshells, which can differ in their properties, might hold great potential in nanomaterial development. Furthermore, viruses are considered as naturally biocompatible and biodegradable, which is particularly important for medical applications. Plant viruses are less likely to interact with human receptors and the virus replication or gene expression is not supported in mammalian systems (Koudelka & Manchester, 2010; Steinmetz et al, 2011). Although foreign proteins have the potential to cause an immune response, there is currently no evidence to assume the immunogenicity of plant viruses induced in mice.

Nanoparticles and VNPs are currently under investigation in the field of nanomedicine (broadly defined as the application of nanotechnology to medicine) and with the aim of controlling drug delivery and targeting to cancerous cells. Tumours have numerous traits that make their treatment daunting. These traits include self–sufficiency, the ability to evade programmed cell death, limitless potential to replicate, and the ability to invade tissues and form metastases that can induce the growth of blood vessels to support them (Ptak et al, 2010). Therefore, nanotechnology has the capacity to deal with the complexity of cancer, by providing tools to diagnose cancer and deliver therapeutics to specific targets whilst sparing normal cells by using different targeting agents by using agents that specifically guide molecules to the diseased cells.

VNPs are less likely to interact specifically with the mammalian system and therefore are less likely to cause potential side effects (Koudelka et al, 2009). For CPMV it was shown that, even up to dosages of 10^{16} CPMV particles/kg body weight, no apparent toxic side effects were observed in mice (Singh et al, 2007). It has been reported that CPMV and CCMV have a broad biodistribution and were detected in a wide variety of tissues throughout the body with no apparent toxic effects (Kaiser et al, 2007; Rae et al, 2005). CPMV particles mostly accumulated in the liver and spleen (Singh et al, 2007). Additionally, VNPs can be PEGylated (modified with polyethylene glycol, PEG) to reduce the immunogenicity (Destito et al, 2007; Lewis et al, 2006b; Steinmetz & Manchester, 2009).

VNPs have been modified with fluorophores, QDs, metallic nanoparticles, and gadolinium (Gd) complexes have been developed for *in vivo* imaging agents (Manchester & Steinmetz, 2009; Singh et al, 2006; Steinmetz & Evans, 2007; Steinmetz et al, 2009a). ^{Fluorescent}CPMV particles allowed high–resolution imaging of major blood vessels to a depth of up to 500 μm in comparison to fluorescent–labelled nanospheres (Lewis et al, 2006a). Furthermore, It has been shown that Gd^{3+} ions can be covalently attached to the exterior or interior surface of CPMV or electrostatically interacted with the encapsidated RNA molecules (Allen et al, 2005; Anderson et al, 2006; Hooker et al, 2007a; Prasuhn et al, 2007a) indicating that VNPs could serve as excellent candidates for magnetic resonance imaging (MRI) contrast agents.

1.2 Summary

In this chapter, many different examples of protein–based nanomaterials have been described. The natural, self–assembling properties of viruses, including monodisperse structure, amenable to chemical or genetic modification, as well as ease of production make them ideal templates for a variety of applications in nanotechnology. The monodispersity of the generated nanoparticles within the protein cages is another attractive property as the particles size is confined by the coat protein. As viruses exist in diverse sizes and shapes, this enables the formation of a wide range of nanoparticles. Broad ranges of mineralization and metal deposition techniques have been discussed. The interior of protein cages has also been used for biomineralization reactions. CPMV and CPMV eVLPs are the focus of this thesis for new material synthesis and imparting new functionalities.

1.3 Aim and outline of this thesis

The aim of the work presented in this thesis is to develop CPMV as a template for material synthesis and for biomedical applications. The chemical coupling of peptides that favour certain types of mineralization was proven to be a very successful way in generating

valuable metallic coatings in a range not otherwise been possible to produce. The following questions are addressed:

1 Can CPMV be used as a template for mineralization and metallization processes to generate monodisperse metallic nanoparticles?

2 Can charge alone initiate the mineralization of CPMV particles?

3 Can polyelectrolyte coated CPMV particles template mineralization?

4 Is it possible to develop ^{Ferrocene}CPMV as a nanoelectronic device or component?

5 What is the effect of the linker length on the number of moieties bound to the virus capsid?

6 Can a monolayer of ^{Ferrocene}CPMV be assembled on an electrode surface?

7 Is it possible to generate ^{Enzyme}CPMV nanoparticles?

8 Can CPMV eVLPs be used to encapsulate magnetic materials?

9 Can CPMV eVLPs be developed as drug carriers for targeted therapy?

1.4 References:

Abbing A, Blaschke UK, Grein S, Kretschmar M, Stark CMB, Thies MJW, Walter J, Weigand M, Woith DC, Hess J, Reiser COA (2004) Efficient intracellular delivery of a protein and a low molecular weight substance via recombinant polyomavirus–like particles. *Journal of Biological Chemistry* **279:** 27410–27421

Aljabali AAA, Barclay JE, Butt JN, Lomonossoff GP, Evans DJ (2010) Redox–active ferrocene–modified Cowpea mosaic virus nanoparticles. *Dalton Transactions* **39:** 7569–7574

Aljabali AAA, Shah SN, Evans–Gowing R, Lomonossoff GP, Evans DJ (2011) Chemically–coupled–peptide–promoted virus nanoparticle templated mineralization. *Integrative Biology* **3:** 119–125

Allen M, Bulte JW, Liepold L, Basu G, Zywicke HA, Frank JA, Young M, Douglas T (2005) Paramagnetic viral nanoparticles as potential high–relaxivity magnetic resonance contrast agents. *Magn Reson Med* **54:** 807–812

Allen M, Willits D, Young M, Douglas T (2003) Constrained synthesis of cobalt oxide nanomaterials in the 12–subunit protein cage from Listeria innocua. *Inorganic Chemistry* **42:** 6300–6305

Anderson EA, Isaacman S, Peabody DS, Wang EY, Canary JW, Kirshenbaum K (2006) Viral nanoparticles donning a paramagnetic coat: conjugation of MRI contrast agents to the MS2 capsid. *Nano Lett* **6:** 1160–1164

Andrews SC, Harrison PM, Yewdall SJ, Arosio P, Levi S, Bottke W, von Darl M, Briat J, Laulhère J, Lobreaux S (1992) Structure, function, and evolution of ferritins. *Journal of Inorganic Biochemistry* **47:** 161–174

Anobom CD, Albuquerque SC, Albernaz FP, Oliveira AC, Silva JL, Peabody DS, Valente AP, Almeida FCL (2003) Structural studies of MS2 bacteriophage virus particle disassembly by nuclear magnetic resonance relaxation measurements. *Biophys J* **84:** 3894–3903

Basu G, Allen M, Willits D, Young M, Douglas T (2003) Metal binding to cowpea chlorotic mottle virus using terbium(III) fluorescence. *J Biol Inorg Chem* **8:** 721 – 725

Bromley KM, Patil AJ, Perriman AW, Stubbs G, Mann S (2008) Preparation of high quality nanowires by tobacco mosaic virus templating of gold nanoparticles. *J Mater Chem* **18:** 4796–4801

Bruening G, Agrawal HO (1967) Infectivity of a mixture of cowpea mosaic virus ribonucleoprotein components. *Virology* **32:** 306–320

Brumfield S, Willits D, Tang L, Johnson JE, Douglas T, Young M (2004) Heterologous expression of the modified coat protein of Cowpea chlorotic mottle bromovirus results in the assembly of protein cages with altered architectures and function. *J Gen Virol* **85:** 1049–1053

Chasteen ND, Harrison PM (1999) Mineralization in Ferritin: An Efficient Means of Iron Storage. *Journal of Structural Biology* **126:** 182–194

Chatterji A, Ochoa W, Paine M, Ratna BR, Johnson JE, Lin T (2004) New addresses on an addressable virus nanoblock: uniquely reactive Lys residues on cowpea mosaic virus. *Chem Biol* **11:** 855–863

Chen C, Daniel MC, Quinkert ZT, De M, Stein B, Bowman VD, Chipman PR, Rotello VM, Kao CC, Dragnea B (2006) Nanoparticle–templated assembly of viral protein cages. *Nano Letters* **6:** 611–615

Comellas M, Engelkamp H, Claessen VI, Sommerdijk AJM, Rowan AE, Christianen PCM, Maan JC, Verduin BJM, Cornelissen JJLM, Nolte RJM (2007) A virus–based single–enzyme nanoreactor. *Nat Nano* **2:** 635–639

de la Escosura A, Nolte RJM, Cornelissen JJLM (2009) Viruses and protein cages as nanocontainers and nanoreactors. *Journal of Materials Chemistry* **19:** 2274–2278

de la Escosura A, Verwegen M, Sikkema FD, Comellas–Aragones M, Kirilyuk A, Rasing T, Nolte RJ, Cornelissen JJ (2008) Viral capsids as templates for the production of monodisperse Prussian blue nanoparticles. *Chemical communications (Cambridge, England)***:** 1542–1544

Destito G, Schneemann A, Manchester M (2009) Biomedical nanotechnology using virus–based nanoparticles. *Curr Top Microbiol Immunol* **327:** 95–122

Destito G, Yeh R, Rae CS, Finn MG, Manchester M (2007) Folic acid–mediated targeting of cowpea mosaic virus particles to tumor cells. *Chemistry & Biology* **14:** 1152–1162

Dixit SK, Goicochea NL, Daniel MC, Murali A, Bronstein L, De M, Stein B, Rotello VM, Kao CC, Dragnea B (2006) Quantum dot encapsulation in viral capsids. *Nano Letters* **6:** 1993–1999

Dominguez–V JM, Colacio E (2003) Nanoparticles of Prussian blue ferritin: A new route for obtaining nanomaterials. *Inorganic Chemistry* **42:** 6983–6985

DomInguez–V., M.. J (2004) Iron(III) complexation of Desferrioxamine B encapsulated in apoferritin. *Journal of Inorganic Biochemistry* **98:** 469–472

Douglas T, Dickson DPE, Betteridge S, Charnock J, Garner CD, Mann S (1995) Synthesis and Structure of an Iron(Iii) Sulfide–Ferritin Bioinorganic Nanocomposite. *Science* **269:** 54–57

Douglas T, Stark T (2000) Nanophase Cobalt Oxyhydroxide Mineral Synthesized within the Protein Cage of Ferritin. *Inorganic Chemistry* **39:** 1828–1830

Douglas T, Young M (1998a) Host–Guest encapsulation of materials by assembled virus protein cages. *Nature* **393:** 152–155

Douglas T, Young M (1999) Virus particles as templates for materials synthesis. *Advanced Materials* **11:** 679–681

Douglas T, Young M (2006) Viruses: Making friends with old foes. *Science* **312:** 873–875

Dragnea B, Chen C, Kwak ES, Stein B, Kao CC (2003) Gold nanoparticles as spectroscopic enhancers for in vitro studies on single viruses. *Journal of the American Chemical Society* **125:** 6374–6375

Drexler KE (1986) Engines of Creation: The Coming Era of Nanotechnology New York: Anchor Books.

Dujardin E, Peet C, Stubbs G, Culver JN, Mann S (2003) Organisation of metallic nanoparticles using Tobacco mosaic virus. *Nano Lett* **3:** 413–417

Ensign D, Young M, Douglas T (2004) Photocatalytic synthesis of copper colloids from CuII by the ferrihydrite core of ferritin. *Inorg Chem* **43:** 3441–3446

Evans DJ (2010) Bionanoscience at the plant virus–inorganic chemistry interface. *Inorganica Chimica Acta* **363:** 1070–1076

Fischlechner M, Donath E (2007) Viruses as building blocks for materials and devices. *Angew Chem–Int Edit* **46:** 3184–3193

Flenniken ML, Willits DA, Harmsen AL, Liepold LO, Harmsen AG, Young MJ, Douglas T (2006) Melanoma and Lymphocyte Cell–Specific Targeting Incorporated into a Heat Shock Protein Cage Architecture. *Chemistry & Biology* **13:** 161–170

Goldbach R, Rezelman G, Vankammen A (1980) Independent Replication and Expression of B–Component Rna of Cowpea Mosaic–Virus. *Nature* **286:** 297–300

Grady JK, Shao J, Arosio P, Santambrogio P, Chasteen ND (2000) Vanadyl(IV) binding to mammalian ferritins. An EPR study aided by site–directed mutagenesis. *Journal of Inorganic Biochemistry* **80:** 107–113

Hainfeld JF (1992) Uranium–Loaded Apoferritin with Antibodies Attached – Molecular Design for Uranium Neutron–Capture Therapy. *P Natl Acad Sci USA* **89:** 11064–11068

Harrison SC (1990) Principles of Virus Structure" in Fundamental Virology, 2nd Ed edn. NY: Raven Press,.

Hermanson TG (2008) *Bioconjugate Techniques*, second edn. London: Academic Press.

Hooker JM, Datta A, Botta M, Raymond KN, Francis MB (2007) Magnetic resonance contrast agents from viral capsid shells: a comparison of exterior and interior cargo strategies. *Nano Lett* **7:** 2207–2210

Hu YF, Zandi R, Anavitarte A, Knobler CM, Gelbart WM (2008) Packaging of a polymer by a viral capsid: The interplay between polymer length and capsid size. *Biophys J* **94:** 1428–1436

Kaiser CR, Flenniken ML, Gillitzer E, Harmsen AL, Harmsen AG, Jutila MA, Douglas T, Young MJ (2007) Biodistribution studies of protein cage nanoparticles demonstrate broad tissue distribution and rapid clearance in vivo. *Int J Nanomedicine* **2:** 715–733

Khalil AS, Ferrer JM, Brau RR, Kottmann ST, Noren CJ, Lang MJ, Belcher AM (2007a) Single M13 bacteriophage tethering and stretching. *Proceedings of the National Academy of Sciences of the United States of America* **104:** 4892–4897

Kickhoefer VA, Garcia Y, Mikyas Y, Johansson E, Zhou JC, Raval–Fernandes S, Minoofar P, Zink JI, Dunn B, Stewart PL, Rome LH (2005) Engineering of vault nanocapsules with enzymatic and fluorescent properties. *Proc Natl Acad Sci U S A* **102:** 4348–4352

Kammen V A (1967) Purification and properties of the components of cowpea mosaic virus. *Virology* **31:** 633-642

Klem MT, Willits D, Young M, Douglas T (2003) 2–D array formation of genetically engineered viral cages on Au surfaces and imaging by atomic force microscopy. *J Am Chem Soc* **125:** 10806–10807

Klem MT, Young M, Douglas T (2008) Biomimetic synthesis of –TiO2 inside a viral capsid. *J Mater Chem* **18:** 3821 – 3823
Kong LB, Siva AC, Kickhoefer VA, Rome LH, Stewart PL (2000) RNA location and modeling of a WD40 repeat domain within the vault. *RNA* **6:** 890–900

Koudelka KJ, Destito G, Plummer EM, Trauger SA, Siuzdak G, Manchester M (2009) Endothelial Targeting of Cowpea Mosaic Virus (CPMV) via Surface Vimentin. *Plos Pathog* **5**

Koudelka KJ, Manchester M (2010) Chemically modified viruses: principles and applications. *Current Opinion in Chemical Biology* **14:** 810–817

Kovacs EW, Hooker JM, Romanini DW, Holder PG, Berry KE, Francis MB (2007) Dual–surface–modified bacteriophage MS2 as an ideal scaffold for a viral capsid–based drug delivery system. *Bioconjug Chem* **18:** 1140–1147

Kreppel F, Gackowski J, Schmidt E, Kochanek S (2005) Combined genetic and chemical capsid modifications enable flexible and efficient de– and retargeting of adenovirus vectors. *Mol Ther* **12:** 107–117

Kridl JC, Bruening G (1983) Comparison of capsids and nucleocapsids from cowpea mosaic virus–infected cowpea protoplasts and seedlings. *Virology* **129:** 369–380

Kwon YW, Lee CH, Choi DH, Jin J (2009) Materials science of DNA. *Journal of Materials Chemistry* **19:** 1353–1380

Laufer B, Steinmetz NF, Hong V, Manchester M, Kessler H, Finn MG (2009) Guiding VLp's the Right Way: Coating of Virus–like Particles with Peptidic Integrin Ligands. *Biopolymers* **92:** 323–323

Lee LA, Wang Q (2006b) Adaptations of nanoscale viruses and other protein cages for medical applications. *Nanomedicine: Nanotechnology, Biology and Medicine* **2:** 137–149

Lee SK, Yun DS, Belcher AM (2006) Cobalt ion mediated self–assembly of genetically engineered bacteriophage for biomimetic Co–Pt hybrid material. *Biomacromolecules* **7:** 14–17

Lewis JD, Destito G, Zijlstra A, Gonzalez MJ, Quigley JP, Manchester M, Stuhlmann H (2006a) Viral nanoparticles as tools for intravital vascular imaging. *Nat Med* **12:** 354–360

Liepold LO, Revis J, Allen M, Oltrogge L, Young M, Douglas T (2005) Structural transitions in Cowpea chlorotic mottle virus (CCMV). *Physical biology* **2:** S166–172

Lin T, Chen Z, Usha R, Stauffacher CV, Dai J, Schmidt T, Johnson JE (1999a) The Refined Crystal Structure of Cowpea Mosaic Virus at 2.8 Å Resolution. *Virology* **265:** 20–34

Lin T, Johnson JE (2003) Structures of picorna–like plant viruses: implications and applications. *Advances in virus research* **62:** 167–239

Lin TW, Chen ZG, Usha R, Stauffacher CV, Dai JB, Schmidt T, Johnson JE (1999b) The refined crystal structure of cowpea mosaic virus at 2.8 angstrom resolution. *Virology* **265:** 20–34

Liu C, Chung S, Jin Q, Sutton A, Yan F, Hoffmann A, Kay BK, Bader SD, Makowski L, Chen L (2006a) Magnetic viruses via nano–capsid templates. *J Magn Magn Mater* **302:** 47–51

Liu CM, Chung S–H, Jin Q, Sutton A, Yan F, Hoffmann A, Kay BK, Bader SD, Makowski L, Chen L (2006b) Magnetic viruses via nano–capsid templates. *Journal of Magnetism an Magnetic Materials* **302:** 47–51

Liu L, Lomonossoff GP (2002) Agroinfection as a rapid method for propagating Cowpea mosaic virus–based constructs. *Journal of Virological Methods* **105:** 343–348

Lomonossoff GP, Johnson JE (1991) The Synthesis and Structure of Comovirus Capsids. *Progress in Biophysics & Molecular Biology* **55:** 107–137

Loo L, Guenther RH, Basnayake VR, Lommel SA, Franzen S (2006) Controlled encapsidation of gold nanoparticles by a viral protein shell. *Journal of the American Chemical Society* **128:** 4502–4503

Loo L, Guenther RH, Lommel SA, Franzen S (2007) Encapsidation of nanoparticles by red clover necrotic mosaic virus. *Journal of the American Chemical Society* **129:** 11111–11117

Loo L, Guenther RH, Lommel SA, Franzen S (2008) Infusion of dye molecules into Red clover necrotic mosaic virus. *Chem Commun***:** 88–90

Manchester M, Singh P (2006) Virus–based nanoparticles (VNPs): platform technologies for diagnostic imaging. *Advanced drug delivery reviews* **58:** 1505–1522

Manchester M, Steinmetz NF (2008) *Viruses and Nanotechnology*, Vol. 327, Berlin Heidelberg: Springer Verlag.

Manchester M, Steinmetz NF. (2009) Viruses and nanotechnology. *Current Topics in Microbiology and Immunology*,. Springer Berlin Heidelberg, Berlin, Heidelberg.

Mann S (1996) *Biomimetic materials chemistry*, New York: VCH.

Mann S (2001) Biomineralization: Principals and Concepts in Bioinorganic Materials Chemistry, Vol. 3: Oxford University Press.

Mann S, Archibald DD, Didymus JM, Douglas T, Heywood BR, Meldrum FC, Reeves NJ (1993) Crystallization at Inorganic–Organic Interfaces–Biominerals and Biomimetic Synthesis. *Science* **261:** 1286–1292

Mansur HS (2010) Quantum dots and nanocomposites. *Wiley Interdiscip Rev Nanomed Nanobiotechnol* **2:** 113–129

Mao C, Flynn CE, Hayhurst A, Sweeney R, Qi J, Georgiou G, Iverson B, Belcher AM (2003) Viral assembly of oriented quantum dot nanowires. *Proceedings of the National Academy of Sciences of the United States of America* **100:** 6946–6951

Mao C, Solis DJ, Reiss BD, Kottmann ST, Sweeney RY, Hayhurst A, Georgiou G, Iverson B, Belcher AM (2004) Virus–based toolkit for the directed synthesis of magnetic and semiconducting nanowires. *Science* **303:** 213–217

Meldrum FC, Douglas T, Levi S, Arosio P, Mann S (1995) Reconstitution of manganese oxide cores in horse spleen and recombinant ferritins. *Journal of Inorganic Biochemistry* **58:** 59–68

Meunier S, Strable E, Finn MG (2004) Crosslinking of and coupling to viral capsid proteins by tyrosine oxidation. *Chemistry & biology* **11:** 319–326

Miller RA, Presley AD, Francis MB (2007) Self–assembling light–harvesting systems from synthetically modified tobacco mosaic virus coat proteins. *J Am Chem Soc* **129:** 3104–3109

Nam KT, Kim DW, Yoo PJ, Chiang CY, Meethong N, Hammond PT, Chiang YM, Belcher AM (2006) Virus–enabled synthesis and assembly of nanowires for lithium ion battery electrodes. *Science* **312:** 885–888

Nam KT, Wartena R, Yoo PJ, Liau FW, Lee YJ, Chiang YM, Hammond PT, Belcher AM (2008) Stamped microbattery electrodes based on self–assembled M13 viruses. *P Natl Acad Sci USA* **105:** 17227–17231

Namba K, Stubbs G (1986) Structure of tobacco mosaic virus at 3.6 A resolution: implications for assembly. *Science* **231:** 1401–1406

Niblett CL, Semancik JS (1969) Conversion of the electrophoretic forms of cowpea mosaic virus in vivo and in vitro. *Virology* **38:** 685–693

Niemeyer CM (2001) Nanoparticles, Proteins, and Nucleic Acids: Biotechnology Meets Materials Science. *Angewandte Chemie International Edition* **40:** 4128–4158

Niemeyer CM, Mirkin CA (2004) *Nanobiotechnology: concepts, applications and perspectives*, Weinheim, Chichester: Wiley–VCH ; John Wiley.

Mastico RA, Talbot SJ, Stockley PG (1993) Multiple presentation of foreign peptides on the surface of an RNA-free spherical bacteriophage capsid. *J Gen Virol* **74 (Pt 4):** 541-548

Ochoa WF, Chatterji A, Lin T, Johnson JE (2006) Generation and Structural Analysis of Reactive Empty Particles Derived from an Icosahedral Virus. *Chemistry & Biology* **13:** 771–778

Peabody DS (2003) A Viral Platform for Chemical Modification and Multivalent Display. *J Nanobiotechnology* **1:** 5

Pead S, Durrant E, Webb B, Larsen C, Heaton D, Johnson J, Watt GD (1995) Metal ion binding to apo, holo, and reconstituted horse spleen ferritin. *Journal of Inorganic Biochemistry* **59:** 15–27

Pokorski JK, Steinmetz NF (2011) The Art of Engineering Viral Nanoparticles. *Molecular Pharmaceutics* **8:** 29–43

Polanams J, Ray AD, Watt RK (2005) Nanophase iron phosphate, iron arsenate, iron vanadate, and iron molybdate minerals synthesized within the protein cage of ferritin. *Inorganic Chemistry* **44:** 3203–3209

Porta C, Spall VE, Lin TW, Johnson JE, Lomonossoff GP (1996) The development of cowpea mosaic virus as a potential source of novel vaccines. *Intervirology* **39:** 79–84

Porta C, Spall VE, Loveland J, Johnson JE, Barker PJ, Lomonossoff GP (1994) Development of Cowpea Mosaic–Virus as a High–Yielding System for the Presentation of Foreign Peptides. *Virology* **202:** 949–955

Portney NG, Tseng RJ, Destito G, Strable E, Yang Y, Manchester M, Finn MG, Ozkan M (2007) Microscale memory characteristics of virus–quantum dot hybrids. *Appl Phys Lett* **90:**1–3

Prasuhn DE, Jr., Yeh RM, Obenaus A, Manchester M, Finn MG (2007a) Viral MRI contrast agents: coordination of Gd by native virions and attachment of Gd complexes by azide–alkyne cycloaddition. *Chem Commun***:** 1269–1271

Prasuhn DE, Yeh RM, Obenaus A, Manchester M, Finn MG (2007b) Viral MRI contrast agents: coordination of Gd by native virions and attachment of Gd complexes by azide–alkyne cycloaddition. *Chem Commun***:** 1269–1271

Price DJ, Joshi JG (1983) Ferritin. Binding of beryllium and other divalent metal ions. *J Biol Chem* **258:** 10873–10880

Ptak K, Farrell D, Panaro NJ, Grodzinski P, Barker AD (2010) The NCI Alliance for Nanotechnology in Cancer: achievement and path forward. *Wiley Interdisciplinary Reviews: Nanomedicine and Nanobiotechnology* **2:** 450–460

Rae C, Koudelka KJ, Destito G, Estrada MN, Gonzalez MJ, Manchester M (2008) Chemical addressability of ultraviolet–inactivated viral nanoparticles (VNPs). *PLoS One* **3:** e3315

Rae CS, Khor IW, Wang Q, Destito G, Gonzalez MJ, Singh P, Thomas DM, Estrada MN, Powell E, Finn MG, Manchester M (2005) Systemic trafficking of plant virus nanoparticles in mice via the oral route. *Virology* **343:** 224–235

Reiss BD, Mao C, Solis DJ, Ryan KS, Thomson T, Belcher AM (2004) Biological routes to metal alloy ferromagnetic nanostructures. *Nano Lett* **4:** 1127–1132

Ren YP, Wong SM, Lim LY (2006) In vitro–reassembled plant virus–like particles for loading of polyacids. *Journal of General Virology* **87:** 2749–2754

Royston E, Ghosh A, Kofinas P, Harris MT, Culver JN (2007) Self-Assembly of Virus-Structured High Surface Area Nanomaterials and Their Application as Battery Electrodes. *Langmuir* **24:** 906-912

Sainsbury F, Cañizares MC, Lomonossoff GP (2010b) Cowpea mosaic Virus: The Plant Virus–Based Biotechnology Workhorse. *Annual Review of Phytopathology* **48:** 437–455

Sainsbury F, Thuenemann EC, Lomonossoff GP (2009) pEAQ: versatile expression vectors for easy and quick transient expression of heterologous proteins in plants. *Plant Biotechnol J* **7:** 682–693

Sardar R, Funston AM, Mulvaney P, Murray RW (2009) Gold nanoparticles: past, present, and future. *Langmuir* **25:** 13840–13851

Sarikaya M, Tamerler, C., Jen, A. K. Y., Schulten, K., Baneyx, F. (2003) Molecular biomimetics: nanotechnology through biology. *Nature Materials* **2:** 577–585

Schlick TL, Ding Z, Kovacs EW, Francis MB (2005) Dual–surface modification of the tobacco mosaic virus. *J Am Chem Soc* **127:** 3718–3723

Schuler D (2002) The biomineralization of magnetosomes in Magnetospirillum gryphiswaldense. *Int Microbiol* **5:** 209–214

Seeman NC, Belcher AM (2002) Emulating biology: Building nanostructures from the bottom up. *P Natl Acad Sci USA* **99:** 6451–6455

Semancik JS (1966) Studies on electrophoretic heterogeneity in isometric plant viruses. *Virology* **30:** 698–704

Shah SN, Steinmetz NF, Aljabali AAA, Lomonossoff GP, Evans DJ (2009) Environmentally benign synthesis of virus–templated, monodisperse, iron–platinum nanoparticles. *Dalton Transaction* **40:** 8479–8480

Shenton W, Douglas T, Young M, Stubbs G, Mann S (1999a) Inorganic–organic nanotube composites from template mineralization of tobacco mosaic virus. *Advanced Materials* **11:** 253–55

Simsek E, Kilic MA (2005) Magic ferritin: A novel chemotherapeutic encapsulation bullet. *J Magn Magn Mater* **293:** 509–513

Singh P, Gonzalez MJ, Manchester M (2006) Virsues and their uses in nanotechnology. *Drug development research* **67:** 23–41

Singh P, Prasuhn D, Yeh RM, Destito G, Rae CS, Osborn K, Finn MG, Manchester M (2007) Bio–distribution, toxicity and pathology of cowpea mosaic virus nanoparticles in vivo. *J Control Release* **120:** 41–50

Staniland SS (2007) Magnetosomes: Bacterial Biosynthesis of Magnetic Nanoparticles and Potential Biomedical Applications. In *Nanotechnologies for the Life Sciences*. Wiley–VCH Verlag GmbH & Co. KGaA

Steinmetz NF, Cho CF, Ablack A, Lewis JD, Manchester M (2011) Cowpea mosaic virus nanoparticles target surface vimentin on cancer cells. *Nanomedicine* **6:** 351–364

Steinmetz NF, Evans DJ (2007) Utilisation of plant viruses in bionanotechnology. *Org Biomol Chem* **5:** 2891–2902

Steinmetz NF, Lin T, Lomonossoff GP, Johnson JE (2009a) Structure–based engineering of an icosahedral virus for nanomedicine and nanotechnology. *Curr Top Microbiol Immunol* **327:** 23–58

Steinmetz NF, Lomonossoff GP, Evans DJ (2006a) Cowpea Mosaic Virus for Material Fabrication: Addressable Carboxylate Groups on a Programmable Nanoscaffold. *Langmuir* **22:** 3488–3490

Steinmetz NF, Lomonossoff GP, Evans DJ (2006b) Decoration of Cowpea mosaic virus with multiple, redox–active, organometallic complexes. *Small* **2:** 530–533

Steinmetz NF, Manchester M (2009) PEGylated Viral Nanoparticles for Biomedicine: The Impact of PEG Chain Length on VNP Cell Interactions In Vitro and Ex Vivo. *Biomacromolecules* **10:** 784–792

Steinmetz NF, Shah SN, Barclay JE, Rallapalli G, Lomonossoff GP, Evans DJ (2009b) Virus–templated silica nanoparticles. *Small* **5:** 813–816

Sun XC, Huang YH, Nikles DE (2004) FePt and CoPt magnetic nanoparticles film for future high density data storage media. *Int J Nanotechnol* **1:** 328–346

Tamerler C, Khatayevich D, Gungormus M, Kacar T, Oren EE, Hnilova M, Sarikaya M (2010) Molecular biomimetics: GEPI–based biological routes to technology. *Peptide Science* **94:** 78–94

Taylor KM, Spall VE, Butler PJ, Lomonossoff GP (1999) The cleavable carboxyl–terminus of the small coat protein of cowpea mosaic virus is involved in RNA encapsidation. *Virology* **255:** 129–137

Theil EC (1987) Ferritin: Structure, Gene Regulation, and Cellular Function in Animals, Plants, and Microorganisms. *Annual Review of Biochemistry* **56:** 289–315

Uchida M, Klem MT, Allen M, Suci P, Flenniken M, Gillitzer E, Varpness Z, Liepold LO, Young M, Douglas T (2007a) Biological containers: Protein cages as multifunctional nanoplatforms. *Advanced Materials* **19:** 1025–1042

Uchida M, Klem MT, Allen M, Suci P, Flenniken ML, Gillitzer E, Varpness Z, Liepold LO, Young M, Douglas T (2007b) Biological containers: Protein cages as multifunctional nanoplatforms. *Adv Mater* **19:** 1025–1042

van Kammen A (1967) Purification and properties of the components of cowpea mosaic virus. *Virology* **31:** 633–642

Wang Q, Lin T, Johnson JE, Finn MG (2002a) Natural supramolecular building blocks: Cysteine–added mutants of cowpea mosaic virus. *Chem Biol* **9:** 813–819

Wang Q, Lin T, Tang L, Johnson JE, Finn MG (2002b) Icosahedral virus particles as addressable nanoscale building blocks. *Angew Chem Int Ed* **41:** 459–462

Wang Q, Raja KS, Janda KD, Lin T, Finn MG (2003) Blue fluorescent antibodies as reporters of steric accessibility in virus conjugates. *Bioconjug Chem* **14:** 38–43

Weeks, Alcamo (2008) *Microbes and Society*, Vol. 2nd London: Jones and Bartlett Publishers International

Weiner S, Traub W (1992) Bone structure: from angstroms to microns. The FASEB journal : official publication of the Federation of American Societies for Experimental Biology **6:** 879–885

Whaley SR, English DS, Hu EL, Barbara PF, Belcher AM (2000) Selection of peptides with semiconductor binding specificity for directed nanocrystal assembly. *Nature* **405:** 665–668

Wu LQ, Payne GF (2004) Biofabrication: using biological materials and biocatalysts to construct nanostructured assemblies. *Trends in biotechnology* **22:** 593–599

Wang Q, Kaltgrad E, Lin T, Johnson JE, Finn MG (2002) Natural supramolecular building blocks. Wild-type cowpea mosaic virus. *Chem Biol* **9:** 805-811

Wu M, Brown WL, Stockley PG (1995) Cell-Specific Delivery of Bacteriophage-Encapsidated Ricin A Chain. *Bioconjugate Chemistry* **6:** 587-595

Mastico RA, Talbot SJ, Stockley PG (1993) Multiple presentation of foreign peptides on the surface of an RNA-free spherical bacteriophage capsid. *J Gen Virol* **74 (Pt 4):** 541-548

Royston E, Ghosh A, Kofinas P, Harris MT, Culver JN (2007) Self-Assembly of Virus-Structured High Surface Area Nanomaterials and Their Application as Battery Electrodes. *Langmuir* **24:** 906-912

Wang Q, Kaltgrad E, Lin T, Johnson JE, Finn MG (2002) Natural supramolecular building blocks. Wild-type cowpea mosaic virus. *Chem Biol* **9:** 805-811

Wu M, Brown WL, Stockley PG (1995) Cell-Specific Delivery of Bacteriophage-Encapsidated Ricin A Chain. *Bioconjugate Chemistry* **6:** 587-595

2 General methods

2.1 Sodium phosphate buffer

1 litre of 0.2 M Na_2HPO_4 (27.0 g) and 1 litre of 0.2 M NaH_2PO_4 (28.39 g) were prepared in Milli–Q water and autoclaved before mixing. To prepare 0.1 M buffer solution; 305 ml of Na_2HPO_4 solution and 195 ml of NaH_2PO_4 solution was added to 500 ml Milli–Q water that gave a pH of 7.0.

2.2 Phosphate buffered saline (PBS)

To make 1 litre of 1 x PBS mix 140 mM NaCl, 27 mM KCl, 80 mM Na_2HPO_4 and 15 mM of KH_2PO_4. The pH was adjusted to 7.4 with HCl, and the buffer was autoclaved before use.

2.2.1 Acetate buffer solution pH 5.3

1 litre of 0.1 M acetic acid and 1 litre of 0.1 M sodium acetate (tri–hydrate) (13.6 g) were prepared in Milli–Q water and autoclaved before mixing. To prepare 0.1 M buffer solution with pH of 5.3; 357 ml of 0.1 M acetic acid solution and 643 ml of 0.1 M sodium acetate solution mixed together to give pH of 5.3.

2.2.2 Native gel electrophoresis

2.2.2.1 Buffers and solutions

10X TBE buffer	900 mM tris–base; 900 mM boric acid; 25 mM ethylenediaminetetraacetic acid (EDTA); made up with MilliQ water to 1000 ml
Coomassie staining solution	50 % (v/v) methanol; 10 % (v/v) acetic acid; 0.25 % (w/v) Coomassie Brilliant Blue G–250 in Milli–Q water
Destaining solution for native gel	50 % (v/v) methanol; 10 % (v/v) acetic acid in MilliQ water

2.2.3 SDS–PAGE Buffers

Running buffer (RunBlue, Expedeon)	30 ml of 20x SDS RunBlue buffer in 600 ml Milli–Q water
Coomassie staining solution	20 ml of Instant blue ready to use (Expedeon) for ~ 30 minutes.
Coomassie destaining solution	See section 2.4.1

2.3 Virus propagation in *V. unguiculata*.

Approximately 10–12 days after sowing, the plants were infected with CPMV by mechanical inoculation as follows. The leaves were treated with Carborundum (silicon carbide abrasive). The inoculation of the primary leaves was performed by using 50 µl per leaf of purified CPMV virions of 0.1 mg ml^{-1} particles suspended in 10 mM sodium phosphate buffer pH 7.0. The leaves were washed with tap water after inoculation of the plants to remove the Carborundum. 11–12 days after infection, the symptomatic leaves were harvested and stored at –20 °C prior to use. Plants were grown under the following conditions: supplementary lighting for 16 hours a day with temperature set points 25 °C at day and 22 °C at night. Plants were maintained by the horticultural services of JIC.

2.4 CPMV purification

CPMV was purified from infected leaves using a modified protocol (http://www.dpvweb.net/dpv/showdpv.php?dpvno=378). Leaf tissue was homogenized, using an electrical blender, with 100 mM sodium phosphate buffer pH 7.0, and then squeezed through two layers of muslin and centrifuged at 9000 rpm for 20 min in a FAS–14C rotor. The supernatant fluid was kept and stirred for 5–10 minutes at 4 °C with 0.7 volumes of 1:1 (v: v) chloroform/n–butanol. After centrifugation at 6000 rpm in FAS–14C rotor for 20 min at 4 °C, the clear aqueous layer was removed and incubated with 0.25 of the volume with 20% (w/v) PEG/1M NaCl overnight at 4° C. The solution was then centrifuged at 15000 rpm for 20 min and the pellet was recovered with 9 ml of 10 mM sodium phosphate buffer pH 7.0. The solution was spun at 9000 rpm for 20 minutes, the pellet was suspended and the solution was

ultracentrifuged for 2.5 hours at 36 000 rpm at 4 °C in a T–1270 rotor (Beckman, USA). The pellet was resuspended in a small volume of 10 mM sodium phosphate buffer. The suspension was centrifuged at 14000 rpm for 15 min at ambient temperature, and the supernatants were pooled and dialysed against 10 mM sodium phosphate buffer using 100 kDa MWCO cassettes (Spectrum laboratories). The clear virus pellet was again suspended in 10 mM sodium phosphate buffer and centrifuged at 14000 rpm for 15 min to remove possible contaminants. The final virus samples were stored at 4 °C in 10 mM sodium phosphate buffer prior to use. Virus concentration was measured by using an extinction coefficient of 8.1 ml mg^{-1} cm^{-1} at 260 nm. The yields obtained were about 1–1.3 g of virions per kg–infected leaves.

2.4.1 Agarose–gel electrophoresis

5–10 µg of CPMV particles suspended in 10 mM sodium phosphate buffer pH 7.0 with 2 µl of loading dye (Coomassie staining solution or MBI Fermentas dye) were analysed on 1.2 % (w/v) agarose gels in TBE using an electric field of 1–5 V cm^{-2} for 1–2 hours. For ethidium bromide staining (nucleic acid staining) 0.1 µg/ ml ethidium bromide (4–5 µl) in 1x TBE buffer was added to the gel. Particles were visualised on a UV transilluminator at 302 nm using Gene Genius Bio Imaging System with Gene Snap software (Syngene). For coat protein, visualisation gels were stained with Coomassie solution overnight. Gel images were recorded using a camera or scanner.

2.4.2 SDS–PAGE

2.4.2.1 SDS–PAGE procedure

Sodium dodecyl sulfate polyacrylamide gel electrophoresis (SDS–PAGE) was performed on 5–10 µg of virus in 10 mM sodium phosphate buffer pH 7.0 mixed with 3 µL of 4x RunBlue LDS Sample Buffer (Expedeon). Samples were heated for 5–10 minutes at 100 ºC in a thermoblock in order to denature the protein. In the case of the mineralized particles, they were heated for 20 minutes with 10% sodium dodecyl sulfate. The samples were analysed on 12

% TEO–CI SDS RunBlue precast gels (Expedeon) under non–reducing conditions at 180 V for 30–70 minutes using 600–700 ml of 20:1 dilution of 20x RunBlue SDS Running Buffer (Expedeon). The bands when stained with 20 ml of InstantBlue (Expedeon) were visible after a few minutes. Gels were washed with Milli–Q water prior to imaging.

2.5 Transmission electron microscopy (TEM)

Purified particles were transferred into MilliQ water using 100 kDa cut–off columns (Millipore). 5–10 µl of 0.1 mg ml^{-1} particles were allowed to settle briefly (1 minute) onto pyroxylin and carbon–coated copper grids (400 mesh, Agar Scientific), and then blotted dry with filter paper; grids were then washed with Milli–Q water. For negative staining 2% (w/v) uranyl acetate was used, the excess solution was removed with filter paper and the grids left to air dry until needed. Grids were viewed at 200 Kv in an FEI Tecnai20 TEM (FEI UK Ltd, Cambridge) and images were obtained using a bottom–mounted AMT XR60 CCD camera (Deben UK Ltd, Bury St. Edmunds).

2.6 UV–Vis Spectroscopy

Virion (CPMV or eVLP) concentration was determined by photometrical measurement using either a Perkin Elmer Lambda 25 UV–VIS spectrophotometer with UVWINLab Software or a NanoDrop® ND–1000 spectrophotometer and ND–1000 software at room temperature by using a 1 cm quartz cuvette (light path: 1 cm).

CPMV particles have an absorption maximum at a wavelength of $\lambda = 260$ nm (derived from the encapsidated RNA molecules) with molar extinction coefficient of $\varepsilon = 8.1$ ml mg^{-1} cm^{-1}. CPMV eVLPs have an absorption maximum at $\lambda = 280$ nm with molar extinction coefficient of $\varepsilon = 1.28$ ml mg^{-1} cm^{-1} as determined by (van Kammen, 1967). The law of Beer Lambert can be used to calculate the concentration:

$$A = c\ d\ \varepsilon$$

Where; A is the absorbance, c is the concentration of the particles in mg ml^{-1}, d is the length of the light path in cm and ε the molar extinction coefficient in ml mg^{-1} cm^{-1}.

2.7 Dynamic light scattering (DLS)

DLS was measured on a DynaPro Titan, Wyatt Technology Corporation (laser wavelength 830 nm, scattering angle 20 º) with Dynamics software Version 6.9.2.11. Particles at a concentration of 0.5–1 mg^{-1} cm^{-1} in 10 mM sodium phosphate buffer pH 7.0 were filtered through 0.1–0.4 micron filters (Millipore) prior to analysis. Four independent measurements were performed; each single measurement presents an average of ten measurements. Data were recorded at 20 °C. DLS determines the hydrodynamic diameter and refers to how a particle diffuses within a fluid by recording the laser scattering from the particles. The particles undergo Brownian motion leading to time-dependent fluctuation. The diameter obtained by this technique is that of a sphere that has the same translational diffusion coefficient as the particle being measured. The translational diffusion coefficient will depend not only on the size of the particle "core", but also on any surface structure, as well as the concentration and type of ions in the medium. This means that the size can be larger than that measured by electron microscopy.

2.8 Nanoparticle tracking analysis (NTA)

A NanoSight LM 10 instrument was used for NTA (ca. 80–micron wide 640 nm wavelength laser beam; cell depth 0.5 mm; cell volume ca. 0.25 ml). Samples for NTA were prepared with 300 µl (0.2–0.5 mg^{-1} cm^{-1}) of mineralized–CPMV particles suspended in 10 mM sodium phosphate buffer pH 7.0 and analysed by recording a 30–second video of the nanoparticles' motion when illuminated by laser light mounted under the microscope objective lens. The particle movement was tracked using conventional CCD camera, operating at 30 frames per second. NTA is a method for visualizing and analyzing particles in liquids that relates the rate of Brownian motion to particle size. The rate of movement is related only to the

viscosity and temperature of the liquid, it is not influenced by particle density or refractive index. NTA allows the determination of a size distribution profile of small particles (10-1000nm) in liquid suspension.

2.9 Energy dispersive X–ray spectroscopy (EDXS)

An Oxford Instruments INCA Energy 200Premium is attached to a TEM or JEOL JSM 5900LV scanning electron microscope (SEM). EDXS works by detecting X–rays that are produced by the sample of interest in an electron beam. The electron beam excites the atoms in the sample that subsequently produce X–rays to discharge the excess energy. The energy of the X–rays is characteristic of the atoms that produced them giving a spectral pattern. EDXS is an analytical technique used for the elemental analysis or chemical characterization of a sample. It relies on the investigation of an interaction of some source of X-ray excitation and a sample. Its characterization capabilities are due in large part to the fundamental principle that each element has a unique atomic structure allowing X-rays that are characteristic of an element's atomic structure to be identified uniquely from one another.

2.10 Mössbauer analysis

Mössbauer spectra were recorded in zero magnetic field at 80 or 298 K on an ES–Technology MS–105 Mössbauer spectrometer with a 100 MBq ^{57}Co source in a rhodium matrix at ambient temperature. Spectra were referenced against a 25 μm iron foil at 298 K and spectrum parameters were obtained by fitting with Lorentzian curves (errors < ± 0.02 mms^{-1}; half–width–at–half–maxima 0.21–0.26 mms^{-1}). Samples of iron oxide–CPMV were prepared as above except $^{57}FeCl_3$ was used that had been enriched with ^{57}Fe (95.4% enriched metal powder, Isoflex, Russia) (Oganesyan et al, 2004). Spectra were recorded either as frozen solutions or in the solid state. Prof. Dave Evans and Mrs Elaine Barclay conducted experiments.

Mössbauer spectroscopy probes tiny changes in the gamma energy levels of an atomic nucleus in response to its environment. Mössbauer spectroscopy is limited by the need for a suitable gamma-ray source. Usually, this consists of a radioactive parent that decays to the

desired isotope. For example, the source for ^{57}Fe consists of ^{57}Co, which decays by electron capture to an excited state of ^{57}Fe, then subsequently decays to a ground state emitting the desired gamma-ray.

2.11 Vibrating sample magnetometry (VSM) of $eVLP_{iron\ oxide}$ or iron oxide–CPMV

Magnetic measurements were made on 1.65 mg of dried sample of $eVLP_{iron\ oxide}$ or 2 mg of iron oxide–CPMV, using a vibrating sample magnetometer (VSM) from Oxford Instruments operating at temperatures from 4 to 275 K, and fields of up to 5 Tesla. The typical noise level was below 10 microemu, and the maximum sample moment at low temperatures was of the order of 25 memu. VSM was operated at 55 Hz with vibration amplitude of 1.5 mm. The temperature was changed with a heating resistor and a needle valve that allows the flow of helium from the cryostat into the sample space. The temperature was controlled through a PID loop feedback, providing stability better than 10 mK at low temperatures. (The magnetic measurements were conducted as a collaborative project with Drs. Oscar Céspedes and Sarah Staniland, School of Physics and Astronomy, University of Leeds, United Kingdom).

A sample is placed inside a uniform magnetic field to magnetize the sample. The sample is then physically vibrated sinusoidally, typically through the use of a piezoelectric material. The induced voltage in the pickup coil is proportional to the sample's magnetic moment, but does not depend on the strength of the applied magnetic field. In a typical setup, the induced voltage is measured through the use of a lock-in amplifier using the piezoelectric signal as its reference signal. By measuring in the field of an external electromagnet, it is possible to obtain the hysteresis curve of a material.

2.12 Immunological detection of CPMV coat proteins

2.12.1 Buffers and reagents

Solution	Composition
10x PBS	1.37 M NaCl; 27 mM KCl; 81 mM Na_2HPO_4; 15 mM KH_2PO_4 in MilliQ water; pH 7.0
1x PBST	0.05 % (v/v) Tween–20 (Sigma Aldrich) in 1x PBS
1x PBSTM	5% (w/v) dry milk (Marvel) in 1x PBST

2.12.2 Immunological detection procedure

Step	Reagents	Time/temperature
Blocking	1x PBSTM	2 hours at ambient temperature or overnight at 4 °C
1st antibody	anti–CPMV antibody/1:1000 in 1x PBSTM (20 µl of G49 in 20 ml) freshly prepared	3 hours at ambient temperature while gently shaking
2nd antibody	anti–rabbit IgG–HRP/1:2000 in 1x PBSTM (2 µl)	2 hours at ambient temperature while gently shaking
After each step, the membranes were washed three times for approximately 15 min each run with 1x PBST at ambient temperature on a shaker. After the 2nd antibodies addition the membranes were washed once with 1x PBST and twice with 1x PBS		

2.12.3 Immunological detection (Dot blot):

For protein detection, 10 µg of intact wild–type CPMV (positive control) and any materials to be tested suspended in 10 mM phosphate buffer, were spotted onto a nitrocellulose membrane (Amersham) and air dried for 30 minutes. Nonspecific binding sites were blocked using a solution consisting of 5% (w/v) skim–milk powder in phosphate buffered saline (PBS) plus 0.025% (v/v) Tween–20. The membrane was then probed with a polyclonal antibody specific to CPMV (G49) followed by a horseradish peroxdiase–conjugated anti–rabbit antibody. Both antibodies were diluted (1:1000) in blocking solution. Signals were generated by chemiluminescence using a SuperSignal West Dura substrate kit (Thermo Scientific) and captured on film (HyperfilmTM ECL, Amersham Biosciences) which was developed using a Curix 60 film processor (Agfa Gevaert).

2.13 Staining for cobalt and iron

4 µg each of eVLP, $eVLP_{cobalt}$, $eVLP_{iron\ oxide}$, Co-CPMV and iron oxide–CPMV suspended in 10 mM sodium phosphate buffer, were spotted onto a nitrocellulose membrane (Amersham) and air dried for 30 minutes. The membranes were then probed for cobalt and iron using the appropriate stain.

Cobalt stain: 20 mM 1–nitroso–2–naphthol in 1:1 (v/v) methanol/MilliQ water followed by destaining with 10 mM NaOH (Douglas & Stark, 2000).

Prussian Blue stain: Equal volumes of 20% hydrochloric acid in MilliQ water and 10% potassium ferrocyanide in MilliQ water were mixed just prior to use and incubated with the membrane.

2.14 Surface charge measurement

Zeta potential was measured on a Malvern Instruments Zetasizer–Nano ZS where 1 ml of 0.5 mg ml^{-1} particles was suspended in 10 mM sodium phosphate buffer pH 7.0. Zeta cells were equilibrated at 21°C before recording three measurements each of 12 runs. The data were fitted using the Smoluchowski approximation assuming a Henry's function f(Ka) of 1.5. The electrophoretic mobility is converted to the zeta potential using the Henry equation (Zhang et al, 2008). Zeta potential determinations were based on the electrophoretic mobility of the nanoparticles by applying an external current.

The Zeta potential of dispersion is measured by applying an electric field across the dispersion. Particles within the dispersion with a zeta potential will migrate toward the electrode of opposite charge with a velocity proportional to the magnitude of the zeta potential. Zeta potential is electric potential in the interfacial double layer (DL) at the location of the slipping plane versus a point in the bulk fluid away from the interface. A value of 25 mV (positive or negative) can be taken as the arbitrary value that separates low-charged surfaces from highly-charged surfaces. The significance of zeta potential is that its value can be related to the stability

of colloidal dispersions. The zeta potential indicates the degree of repulsion between adjacent, similarly charged particles in dispersion (Malvern Instruments catalogue).

2.15 Carbodiimide method to generate O–succinimide esterified CPMV particles

Carboxylic acid groups were activated by the carbodiimide method using EDC and NHS or sulfo–NHS as depicted in Figure 2.1. CPMV particles in either 10 mM or 0.1M sodium phosphate buffer pH 7.4 or any other carboxylic acid–containing moieties were incubated with a freshly prepared Milli–Q water solution of EDC (1 molar equivalent) for 5 minutes followed by the addition of a freshly prepared dimethylsulfoxide solution of NHS (4 molar equivalents). The reaction was allowed to proceed for 2 hours at room temperature with gentle stirring. The resulted O–succinimide esterified CPMV particles were purified by any of the methods described below. Further information about the carbodiimide method is provided in (Gillitzer et al, 2002; Hermanson, 2008).

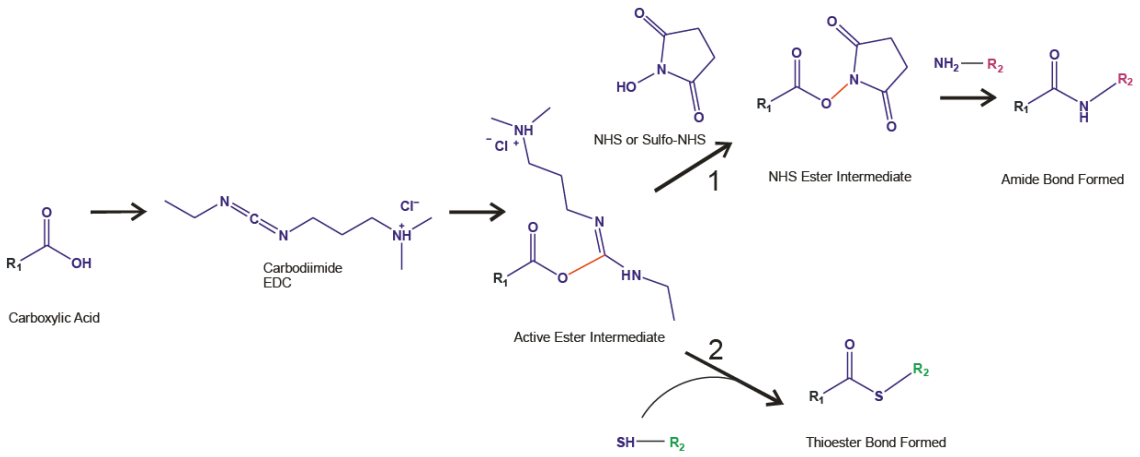

Figure 2.1– Derivatives of carboxylic acids can be prepared with EDC to generate active intermediates that react with amine containing molecules in the presence of NHS or Sulfo–NHS to generate peptide bond route (1). Alternatively, thiolated or cysteine containing molecules could be used with the active ester intermediate to generate thioester bond.

2.16 SPDP method

CPMV particles (10 – 20 mg ml^{-1}), suspended in 10 mM sodium phosphate buffer pH 7.0, were incubated with a solution of SPDP (1000 molar excess) in dimethylsulfoxide (DMSO), the final concentration of DMSO was adjusted to 20% (v/v). The reaction was stirred

gently overnight at 4 °C. The modified CPMV particles were dialyzed using 100 kDa molecular weight cut–off membranes against 10 mM sodium phosphate buffer for 24–36 hours and then concentrated using 100 kDa cut–off columns. $^{3\text{–(2–pyridyldithio)propionate}}$CPMV modified particles were incubated overnight at 4 °C with thiol– or cysteine–containing molecules (1000 molar excess) in either DMSO or DMF; the final concentration of organic solvent was adjusted to 20% (v/v). $^{\text{Thiol–containing molecules}}$CPMV particles were purified by gel filtration (Sephacryl S–500 column) and the eluted fractions were collected and concentrated on 100 kDa cut–off columns. The recovered yield of virions was about 60–70 % of starting materials. The modified particle integrity was established by agarose gel electrophoresis, TEM and DLS.

2.17 Particle purification

2.17.1 Sucrose gradients

Sucrose solutions of 50%, 40%, 30%, 20%, and 10% (w/v) in 10 mM sodium phosphate buffer pH 7.4 were prepared and used within 2 weeks. Gradients were prepared by underlying sucrose solutions of decreasing density (175 or 500 µl) in a centrifuge tube of (2.1 ml or 5 ml, respectively) and carefully overlaying the sample to fill the tube (normally 300–500 µl). Gradients were ultracentrifuged in a swing–out rotor (AH–650) and centrifuged at 137000 g for 1.5–2.5 hours at 4 ºC; 175–300 µl fractions containing modified particles were collected and buffer exchanged for 10 mM sodium phosphate buffer pH 7.4.

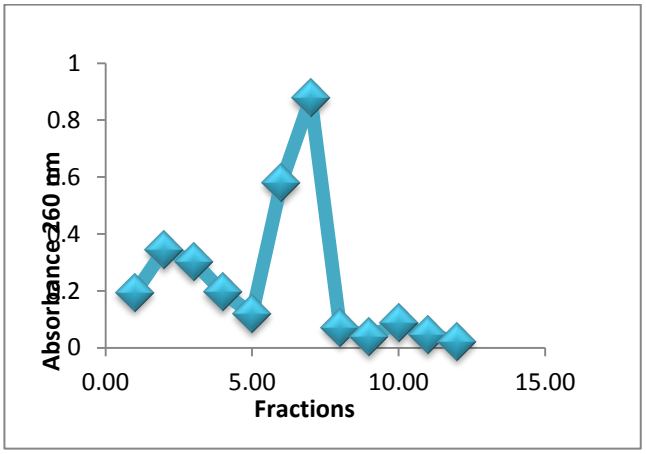

Figure 2.2– An example of sucrose gradient profile for modified CPMV particles. Number of fractions 5-8 contains the modified particles. 2.1 ml sucrose gradient and 175 µl fractions.

2.17.2 Size–exclusion chromatography

Low molecular weight impurities are retarded in the gel filtration matrix, while virus particles eluted first from the column. Gel filtration (AKTA Purifier–900) on a Sephacryl S–500 column (GE Healthcare) and PD–10 desalting columns (Amersham) were used according to the manufacturer's instruction and were pre–equilibrated with 10 mM sodium phosphate buffer unless otherwise indicated.

2.17.3 Ultrafiltration

Ultrafiltration was used as a method for purification and concentration of virus particles. Samples were applied to various volume tubes (500 µl – 15 ml) of 100, 300, and 10000 kDa molecular–weight cut–off columns (Microcon, Amicon Millipore, and Sartorius Stedim) and centrifuged. The particles are retained on the filter of these tubes while the buffer and small impurities pass through the membrane. This is a very efficient method in virus concentration. Specific details are provided in each Chapter.

2.17.4 Dialysis

This method is very efficient in buffer exchange and particle purification. The semi–permeable membrane retains the particles within, while small molecules diffuse to the lower concentration in the buffer reservoir, and *vice versa*. Slide–A–Lyzer cassettes (Pierce), Float–A–Lyze tubing, and Snakeskin tubing have been used throughout the research. Specific details are provided in each Chapter.

2.18 References

Douglas T, Stark T (2000) Nanophase Cobalt Oxyhydroxide Mineral Synthesized within the Protein Cage of Ferritin. Inorganic Chemistry 39: 1828–1830

DPVweb. Zhejiang Academy of Agricultural Sciences, Hangzhou, People's Republic of China, Hangshou, Vol. 2011. An open access internet resource on plant viruses and virus diseases.

Gillitzer E, Willits D, Young M, Douglas T (2002) Chemical modification of a viral cage for multivalent presentation. Chem Commun: 2390–2391

Hermanson TG (2008) Bioconjugate Techniques, second edn. London: Academic Press.

Oganesyan VS, Barclay JE, Hardy SM, Evans DJ, Pickett CJ, Jayasooriya UA (2004) Nuclear inelastic scattering spectroscopy of iron–sulfur cubane compounds. Chem Commun: 214–215

Kammen VA (1967) Purification and properties of the components of cowpea mosaic virus. *Virology* **31:** 633-642

Zhang Y, Yang M, Portney NG, Cui DX, Budak G, Ozbay E, Ozkan M, Ozkan CS (2008) Zeta potential: a surface electrical characteristic to probe the interaction of nanoparticles with normal and cancer human breast epithelial cells. Biomed Microdevices 10: 321–328

3 Chemically–coupled– of peptide promoted mineralization

3.1 Introduction

When a biomolecule inorganic material interaction is accomplished with molecular specificity, it leads to the formation of controlled structures and functions. Molecular specificity of probe–target interactions, e.g., ligand–receptor, antigen–antibody, is always based on specific peptide molecular recognition (Tamerler et al, 2010). The exploitation of peptide–material interaction as a tool for novel nanomaterial synthesis has been fuelled by the availability of short peptides that are specific to a variety of inorganic materials. Such peptides can selectively bind, interact with and direct the formation of inorganic materials.

Much effort has been invested by many groups around the globe in understanding protein recognition of, and binding to, inorganic materials (Descalzo et al, 2006; Flynn, 2003; Merzlyak & Lee, 2006; Tamerler & Sarikaya, 2009). The main challenge remains to establish sequence–reactivity relationships from peptides either isolated from biological sources or generated by combinatorial peptide libraries (Tan et al, 2010). In addition, the abundance of neutral amino acid (e.g., glycine, alanine, valine, leucine and isoleucine) sequences in the peptides is poorly understood and is thought not to be charge related. Despite this, the gained insight allowed the making of practical materials using peptides engineered to bionanoparticles (Flynn et al, 2003a; Mao et al, 2004; Shah et al, 2009a; Steinmetz. N. F. et al, 2009). Moreover, it enhanced the general understanding of the importance of sequence and the composition of the peptides on nanoparticle formation.

The preparation of nanoparticles with controlled size and composition is of major fundamental and technological interest (Sun, 2000). For example, mixed–metal nanoparticles, such as those of FePt and CoPt, have been identified as important materials for use in catalysis and in ultra–high density magnetic storage devices (Hyeon, 2003), and semiconducting zinc sulfide nanoparticles promise applications in a range of optoelectronic devices, such as solar cells (Chen & Lockwood, 2002; Gao et al, 2004). To be useful, the size and size distribution of

the nanoparticle needs to be accurately controlled (Nanda, 2000; Sun, 2006). Further, hollow nanospheres may have many applications in, for example, catalysis, where a hollow nanosphere has potentially a higher catalytically active surface area than its solid analogue and consumes less of the costly and limited metal resources in its synthesis (Liang, 2004).

3.1.1 Peptides specificity for material synthesis (general insight)

Screening peptide libraries for sequences that might be useful in the synthesis of interesting materials has resulted in gigantic databases. Displaying random peptides on the surface of filamentous phage began with G. P. Smith, who showed that fragments of a target protein could be fused to the pIII protein of the filamentous bacteriophage M13 and the resulting particles captured by immobilized antibodies against the target protein (Scott & Smith, 1990; Smith & Scott, 1993). Peptide libraries expanded by size and included various screening approaches. However, peptide affinity toward its binding target remains vital for peptide selection. Some peptides have been used as molecular templates to synthesis inorganic materials and others have been used to synthesise the inorganic material that they were selected against (Slocik & Naik, 2006).

Peptides which bind to inorganic materials were first identified by Brown, who isolated peptides that selectively adhere to Fe_2O_3 surfaces (Brown, 1992). This was the first demonstration of the selectivity of a peptide, which could bind to Fe_2O_3 but not Cr_2O_3 or Fe_3O_4 (Brown, 1992). Multiple copies of the peptides were expressed on the surface of genetically modified *E. coli*. Belcher and co–workers further developed Brown's pioneering work using a combinatorial phage–display library to identify peptides with sequences that specifically bind/interact with inorganic material (Whaley et al, 2000). After sequential washes to remove weak binding or non–bound sequences, the bacteriophage presenting the remaining peptide sequences were amplified in *E.coli* and the peptides with the highest affinity for the target material were selected and used (See Introduction chapter). The screening approach to identify substrate–specific binding peptides and the use of bionanoparticles is no longer restricted to

native mineralization conditions. Peptides can also be engineered as scaffolds and templates for hybrid structure formation (Tamerler et al, 2010). Peptides with affinity for several inorganic materials have been identified using the phage–display method and some examples are shown in Table 3.1. For example, Naik and colleagues identified peptides, which possess affinity for the surface of silica (Naik et al, 2002a). This finding, that peptides specifically bind to inorganic material and may initiate or control the formation of the same material has advanced the synthesis of new materials (Baeuerlein, 2004).

Peptide sequences	**Inorganic materials**	**Salt**
AYSSGAPPMPPF	Ag nanoparticles	$AgNO_3$
	Au nanoparticles	$HAuCl_4$
NPSSLFRYLPSD	Ag nanoparticles	$AgNO_3$
AHHAHHAAD	Au nanoparticles	$ClAuPMe_3$
HYPTLPLGSSTY	CoPt nanoparticles	$(NH4)_2PtCl_6$ + $Co(CH_3COO)_2$
HNKHLPSTQPLA	FePt nanoparticles	$FeCl_2$ + H_2PtCl_6
VCATCEQIADSQHRSHRQMV	ZnS nanoparticles	Zinc 2,9,16,23–tetrakis(phenylthio)–29–H,31H–phthalocyanine + Na_2S
NNPMHQN	ZnS nanoparticles	$ZnCl_2$ + Na_2S

Table 3.1– Examples of peptides known to direct the mineralization of inorganic nanomaterials. The peptide sequences revealed that, in some cases, the same sequence could interact/promote for two different materials or two different sequences could interact/promote for the same material. The data is adapted from (Chun–Long & Nathaniel, 2010).

3.1.2 Peptides for templated mineralization

Viruses assemble to give high precision architectures of simple symmetry; this allows identical subunits to come together with a maximum number of non–covalent interactions, which in turn form the largest cavity from the least number of subunits (this only applies to spherical symmetries). Currently, there is a growing library of virus and protein virus architectures, which provide different functionalities for the synthesis of magnetic particles, imaging agents, and cell specific targeting agents, and for gene therapy and drug encapsulation (Manchester & Steinmetz, 2009). The exploitation of biomaterials for chemical design has become an important area of materials science (Evans, 2008). For example, bacteriophage and

plant viruses provide a variety of morphologies and are robust enough to support reactions to produce new organic and inorganic materials (Flynn et al, 2003a; Shenton et al, 2001). The bacteriophage M13 can template mineralization of several materials (Mao et al, 2004), and has been utilised, for example, in the development of lithium ion battery electrodes (Nam et al, 2006). In addition, the exterior and interior of the rod–shaped plant virus Tobacco mosaic virus has been utilised for material synthesis (Kind, 1998; Royston et al, 2006; Royston et al, 2009).

Although peptides are not complicated molecules, they still encode unique recognition properties. Tan et al (2010) showed that the 20 amino acids have different reduction capabilities of gold solution, with tryptophan being the fastest reducing agent. However, peptides gave a different faster rate reaction than a mixture of free amino acids with the same overall composition because the amino acid residues acted collectively (Tan et al, 2010).

Although the origin of peptide specificity toward target material not fully understood, the fact of peptide selectivity is well established. The literature is full of examples of the ability of certain peptides to direct the formation of inorganic materials such as gold and silver (Brown et al, 2000; Naik et al, 2002b), $CaCO_3$ (Li et al, 2002), CdS (Flynn et al, 2003c) and many more. Flynn et. al. have also utilised this method to identify peptides which induce synthesis of ZnS. Their work demonstrated for the first time that phage–display peptides were essential to both bind to and induce the precipitation of inorganic material (Flynn, 2003). Ahmad et. al. determined calcium molybdate (CM) peptides (AAPNSPWYAYEY, SWSPAFFMQNMP, YESIRIGVAPSQ and DSYSLKSQLPRQ) that induce the precipitation of $CaMoO_4$ from an aqueous precursor solution. Any changes in the peptide sequence or even reordering the amino acids in these peptides had an impact on the yield of the precipitated $CaMoO_4$ (Ahmad, 2006).

3.1.3 Mineralization of chimaeric CPMV particles

CPMV particles have the characteristics of an ideal nanotemplate in terms of their size (~ 28 nm diameter) and their regular symmetric structure. The structure of the virus particle is known to near atomic resolution and its genetic, biological and physical properties are well–

characterised (Lin & Johnson, 2003; Lomonossoff & Johnson, 1991b). Functional groups on the exterior surface of the virion make CPMV a useful nanoscaffold allowing attachment of a multitude of different moieties (Aljabali et al, 2010a; Steinmetz & Evans, 2007; Steinmetz et al, 2006d).

The term virus chimaera refers to genetically modified virus particles. Chimaeric virus technology allows multiple genetic deletion or insertions of foreign sequences into the coat protein sequence; an important advantage over synthetic nanoparticles. Short peptide sequences can be introduced into surface loops that alter the particle surface properties. To display the insertion of a peptide that selectively promotes mineralization is a very attractive methodology for the development of nanomaterials.

The first approach to displaying inserted peptides on the surface of CPMV involved the use of infectious cDNA clones to modify the capsid surface, thereby allow the presentation of foreign peptides on the external CPMV surface (Dessens & Lomonossoff, 1993; Lin et al, 1996; Lomonossoff, 1996). It has been established that additional amino acids can be inserted into the highly surface exposed βB–βC loop of the small subunit of CPMV as shown in (Figure 3.1). CPMV–based chimaeric virus technology was then adapted for the environmentally benign synthesis of virus–templated monodisperse silica (Steinmetz et al, 2009b) and amorphous iron–platinum nanoparticles (Shah et al, 2009a).

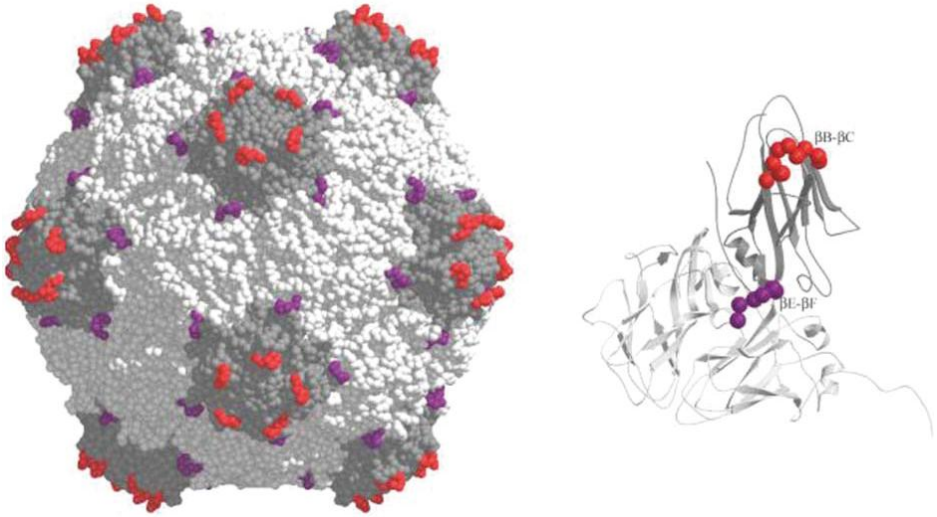

Figure 3.1– Genetic insertion sites of peptide into the CPMV particle. (Left) Space filling model of CPMV, with the insertion site βB–βC of small subunit (red) and βE–βF (purple) on ribbon diagram of CPMV asymmetric unit.

Despite success with chimaeric CPMV for mineralization with silica and iron–platinum, the expression, propagation, isolation and purification of chimaeric CPMVs can be problematic. The chimaeras can revert to wild–type as the inserts, in some cases, are not well tolerated (Porta et al, 2003). In addition, the genetic stability of chimaeras and there is the potential for reversion to wild–type is another disadvantage; this was found in the case of a chimaera with a peptide insert designed to promote mineralization with CoPt. In some cases, the appropriate chimaera cannot be produced at all, as was found in the case of a chimaera that presented a peptide designed to direct mineralization with ZnS. This was the driving force behind the search for seeking alternative routes for the presentation of peptides on the surface of CPMV.

3.1.4 Chemically–coupled–peptide–promoted mineralization

To avoid the lengthy process of generating chimaeric CPMV particles, and to avoid some of the aforementioned disadvantages of the genetic engineering route, the possibility of chemically attaching peptides that promote specific mineralisation to the surface of CPMV particles was investigated. It was found that the appropriate N–protected peptides with the shown sequence in, Table 3.2 can be easily chemically coupled to lysine residues on the surface

of wild–type CPMV. The ^{Peptide}CPMV conjugate can then template the directed and controlled fabrication of monodisperse nanoparticles, of approximately 32 nm diameter, at ambient temperature and pressure in aqueous solution. The reaction scheme is depicted in Figure 3.2.

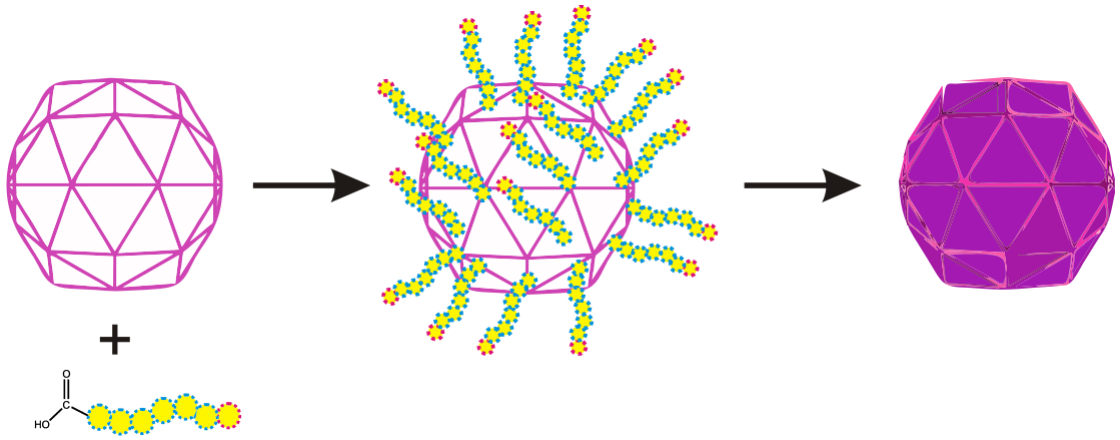

Figure 3.2– Schematic representation of chemical coupling of peptides to CPMV capsid (^{Peptide}CPMV). The red ring on the peptide representation depicts the protected N–terminus that prevents peptide self–aggregation. The numbers of peptides bound to the virus capsid were quantified to be 180 per virus.

Peptide Sequence	Material selectivity
(Cbz)–CNAGDHANC	Peptide–CoPt
(Cbz)–CNAHDGANC	peptide'CoPt (reversed sequence)
(Cbz)–HNKHLPSTQPLA	Peptide–FePt
(Cbz)–CNNPMHQNC	Peptide–ZnS

Table 3.2– Peptide sequences used for peptide–promoted mineralization. (Cbz) denotes a carboxybenzyl group coupled to the N– terminus to prevent self–aggregation. The subscript refers to the specific peptide sequence (un–mineralized). Peptide'CoPt refers to the reverse sequence of Peptide–CoPt. Peptide sequences are generated from http://www.phagedisplay.net/

3.2 Experimental

3.2.1 Materials

The N–protected peptides carboxybenzyl (Cbz)–CNAGDHANC (peptide–CoPt), Cbz–CNAHDGANC (peptide'CoPt), Cbz–HNKHLPSTQPLA (peptide–FePt) and Cbz–CNNPMHQNC (peptide–ZnS) were purchased from GeneCust, Luxembourg. All general reagents were bought from Sigma–Aldrich UK and used without further purification. 1–ethyl–3–(3–dimethlyaminopropyl) carbodiimide hydrochloride (EDC) was purchased from

Novabiochem and *N*–hydroxysuccinimide (NHS) from Fluka. Nanocyl S.A., Belgium, supplied amine–functionalised short, thin, multiwall carbon nanotubes (MWCNT), 95% C purity, with average diameter of 9.5 nm and average length of 1 µm.

3.2.2 Chimaeric CPMV preparation and mineralization

Oligonucleotides encoding the peptide of interest, flanked by appropriate restriction sites (NheI and AatII), were cloned into the CPMV RNA2–based vector. In a second cloning step, the chimaeric sequence was cloned via the enzymes BamHI and EcoRI into the CPMV RNA–2 based binary vector pBinP–NS1 (The chimaeric particles were prepared by Drs. Nicole Steinmetz and Sachin Shah). The resulting recombinant, termed pBin–NS1–FEPT, was used to agroinoculate cowpea plants in the presence of the full–length clone of RNA–1. Chimaeric particles were extracted as described for the wild–type and used for the mineralization process (Shah et al, 2009a; Steinmetz. N. F. et al, 2009).

3.2.3 General method for chemical coupling of peptide to CPMV

The carboxylic acid terminus of the peptide was activated by the carbodiimide method using EDC and NHS (see scheme in section 2.15). Cbz–peptide in Milli–Q water (Millipore) was incubated with a freshly prepared Milli–Q water solution of EDC (1 molar equivalent) for 5 minutes followed by the addition of a freshly prepared solution of NHS in DMSO (4 molar equivalents). The reaction was allowed to proceed for 2 hours at room temperature with gentle stirring. The activated peptide was then added to a solution of CPMVwt in 10 mM sodium phosphate buffer pH 7.0 in a molar ratio of 2000:1, the reaction was incubated at 4 ºC overnight with gentle stirring. The resultant ^{Peptide}CPMV conjugate was purified by gel filtration (AKTA Purifier–900) on a Sephacryl S–500 column (GE Healthcare). Fractions containing only the ^{Peptide}CPMV conjugate were pooled, concentrated using 100 kDa cut–off membranes (Millipore), and analysed by native agarose gel electrophoresis and TEM to ensure the presence and integrity of the modified CPMV particles. The ^{Peptide}CPMV conjugate concentration was

determined by UV–visible spectrophotometry; the yield of ^{Peptide}CPMV conjugate was between 70–90% based on the initial virus concentration. ^{Peptide}top component (naturally occurring eVLPs) conjugate was prepared by the same method and in similar yield.

3.2.4 Preparation of mineralized virus nanoparticles

To ^{Peptide}CPMV (400 µl of 10 mg ml^{-1}) in 10 mM sodium phosphate buffer pH 7.0 was added, with constant stirring, over 10 min at room temperature either: (a) a 1:1:1 mixture of $CoCl_2$ (0.05 mol dm^{-3}), H_2PtCl_6 (0.05 mol dm^{-3}) and $NaBH_4$ (0.1 mol dm^{-3}) each in Milli–Q water (400 µl); (b) a 1:1:1 mixture of $FeCl_3$ (0.05 mol dm^{-3}), H_2PtCl_6 (0.05 mol dm^{-3}) and $NaBH_4$ (0.1 mol dm^{-3}) each in Milli–Q water (400 µl); or (c) a 1:1 mixture of $ZnCl_2$ (0.05 mol dm^{-3}) and Na_2S (0.05 mol dm^{-3}) each in Milli–Q water (400 µl). The mixture was incubated, with gentle stirring at ambient temperature, for 40–48 hours. The FePt–CPMV, CoPt–CPMV and ZnS–CPMV nanoparticles (this nomenclature refers to externally coated particles with the corresponding metals), respectively, were recovered by centrifugation at 14000 rpm (bench top centrifuge, Eppendorf) for 20 minutes. The supernatant containing the mineralized–CPMV nanoparticles was further purified using 100 kDa cut–off columns and washed several times with Milli–Q water to remove all excess reagents. The yield of nanoparticles was 70–80% as determined by UV–visible spectrophotometry based on the initial virus concentration. The method can be scaled up at least two–and–a–half fold; at larger scales a combination of dialysis (100 kDa membrane) and sucrose gradient (2.1 ml 10–50% sucrose gradients centrifuged at 137000 g for 1.5 hours at 4 ºC as described in section 2.17.1. Fractions containing mineralized particles were collected and dialysed against 10 mM sodium phosphate buffer pH 7.0 for 15 hours). The integrity, characterisation and composition of the mineralized–CPMV nanoparticles were determined by TEM, EDXS, NTA, DLS and zeta potential measurements.

^{Peptide}top component mineralization: top component (naturally occurring eVLPs) (400 µg/ml, 500 µl) was incubated with cobalt and platinum salts and a reductant as described for the wild–type particles. The same purification steps were followed as above.

3.2.5 $^{Peptide–CoPt}$CPMV quantification

The number of peptides per particle was determined for $^{Peptide–CoPt}$CPMV conjugate as follows. $^{Peptide–CoPt}$CPMV in 10 mM sodium phosphate buffer pH 7 was reacted with a 2000 molar excess of NHS ester–activated amine specific dye, DyLight594, in DMSO. The DMSO level was adjusted to 20% (v/v) and the reaction left to proceed at 4 °C overnight while gently stirring. The doubly functionalised particles were purified on a PD–10 column equilibrated with 10 mM sodium phosphate buffer pH 7.0, and eluted samples were concentrated on 100 kDa cut–off columns before being layered onto 5 ml 10%–50% sucrose gradients. The gradients were centrifuged at 137000g for 1 to 1.5 hours at 4 °C as described in section 2.17.1. After further concentration on 100 kDa cut–off columns, the number of free reactive lysines was calculated, from the absorbance spectrum (Figure 3.5), to be ~ 66 per virion. .

3.2.6 External surface mineralization of amine–functionalised MWCNT

Cbz–CNAGDHANC (peptide–CoPt; 1.0 mg ml^{-1}) was activated with a freshly prepared solution of EDC (1 molar equivalent) in Milli–Q water for 5 minutes followed by the addition of a freshly prepared DMSO solution of NHS (4 molar equivalents). The reaction was allowed to proceed for 2 hours at room temperature with gentle stirring. The solution of activated peptide–CoPt was added to a suspension of amine surface–functionalised, short, thin, multiwall carbon nanotubes (MWCNT; 0.30 mg) in Milli–Q water (1 ml) and then gently stirred at 4 ºC overnight. The resultant peptide–functionalised MWCNT ($^{Peptide–CoPt}$MWCNT) was purified on a 100 kDa cut–off column. A suspension of $^{Peptide–CoPt}$MWCNT (100 µl) was treated with a 1:1:1 mixture of $CoCl_2$ (0.05 mol dm^{-3}), H_2PtCl_6 (0.05 mol dm^{-3}) and $NaBH_4$ (0.1 mol dm^{-3}) each in Milli–Q water (500 µl). The reaction was allowed to proceed at ambient temperature with gentle stirring. After 24 hours the reaction mixture was centrifuged at 14000 rpm (bench top) for 10 minutes, the pellet was re–suspended in Milli–Q water and purified further on a 100 kDa cut–off column and washed thoroughly with Milli–Q water. TEM examination showed partial

mineralization of the nanotube external surface. The process described above was repeated sequentially over each of seven days to give external surface–mineralized MWCNT.

3.2.7 Scanning electron microscopy

FePt–CPMV coated particles were air–dried on a freshly prepared mica surface. The surface was mounted onto an aluminium pin stub using double–sided adhesive carbon discs (Agar Scientific Ltd). The stubs were then sputter–coated with approximately 10–15 nm platinum in a high–resolution sputter coater (Agar Scientific Ltd) and transferred to a Zeiss Supra 55 VP FEG scanning electron microscope (Zeiss SMT). The samples were viewed at 3 kV with 5mm inLens signal.

3.3 Results and Discussion

3.3.1 Chimaera CPMV mineralization

The previously defined dodecapeptide sequence HNKHLPSTQPLA (Reiss et al, 2004a) was inserted by a well–established cloning method between alanine–22 and proline–23 in the βB–βC loop of the small subunit of CPMV and the chimaeric $CPMV_{FePt}$ construct was introduced into cowpea plants by agroinoculation. The extracted and purified chimaeric $CPMV_{FePt}$ presents 60 copies of the inserted peptide, was incubated with iron and platinum precursors and, after reduction with borohydride, generated monodisperse FePt coated CPMV chimaeric particles as confirmed by TEM (Shah et al 2009a) (Figure 3.3). The DLS was also consistent with monodisperse nanoparticles of ~ 30 nm diameter; this implies an FePt coating of approximately 1 nm on each particle.

Zeta potential is the electrostatic potential that exists at the shear plane of a particle, which is related to both surface charge and the surrounding environment (Zhang et al, 2008). The instrument measures the electrophoretic mobility (or zeta potential) by applying an external

current in liquid suspensions. Zeta potential values have regularly been used as an indicator of the stability of colloidal particles. The higher the absolute values, the higher the net electrical charge on the particle surface and, therefore, the larger the electrical repulsion between particles. The suggested theoretical limit of stability is $\left|25\right|$ mV. Particles are considered to exist as stable colloids if their zeta potential is higher than 25 mV or lower than –25 mV. The zeta potential of chimaeric $CPMV_{FePt}$ of –49.6 mV in buffer indicated that the colloid has good stability and no propensity to aggregate. For a detailed discussion of these results, see (Shah et al, 2009a).

The inserted peptide showed specificity for the target material and the chimaeric CPMV particles acted as a template for metal deposition. The chimaeric particle does not generate a metallic coating when incubated with metals other than the ones the peptide sequence favours. For example, chimaeric $CPMV_{FePt}$ when treated with reagents for cobalt or zinc sulfide did not generate mineralized particles. The peptide exhibited control over the mineralization process; CPMVwt particles (genetically unmodified) showed no templated mineralized particles but, rather, the non–specific formation of nanoparticles with a wide size distribution as shown by TEM (data not shown). These findings suggested that nanoparticles of desired composition and size could be produced by engineering viral particles with specific peptides selected through phage display. Furthermore, silica coated CPMV particles had been generated following the same approach as described above (Steinmetz et al, 2009b).

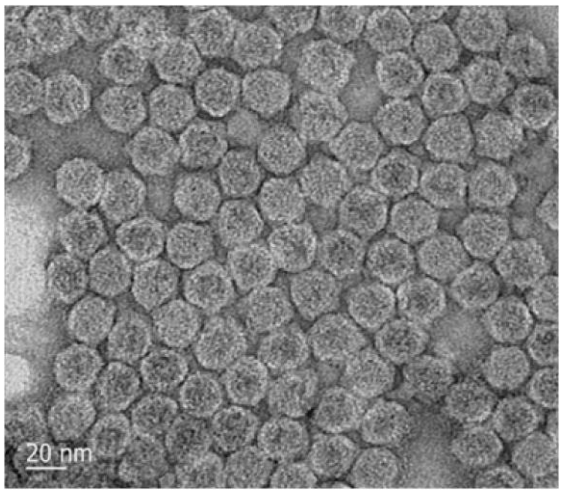

Figure 3.3– Unstained TEM image of monodisperse FePt–coated chimaeric CPMV particles. Reproduced from (Shah et al, 2009a).

3.3.2 ^{Peptide}CPMV conjugates

Peptides previously identified by using phage–display that specifically direct mineralization by CoPt (Cbz–CNAGDHANC), FePt (Cbz–HNKHLPSTQPLA), and ZnS (Cbz–CNNPMHQNC) as shown in Table 3.2 were chosen (Mao et al, 2004; Reiss et al, 2004a). To prepare ^{Peptide}CPMV conjugates, the carboxyl–terminus of the relevant peptide was first pre–activated by conversion to the *O*–succinimide active ester, the simplified reaction scheme is shown in Figure 3.2 and the chemical scheme is depicted in section 2.13. Reaction of the peptide ester with surface amines, derived from lysine groups exposed on the external surface of wild–type CPMV, generated ^{Peptide}CPMV conjugates in 70–90% recovered yield based on the initial virus concentration.

The integrity of the modified particles was confirmed by TEM (data not shown) and agarose gel electrophoresis. Figure 3.4 shows an ethidium bromide stained agarose gel of CPMVwt, a positive control of *O*–succinimide esterified CPMV and the three ^{Peptide}CPMV conjugates. According to their migration in an electric field towards the anode, intact virions of CPMVwt can be separated into a higher– and lower–mobility form, depending on their RNA content. The *O*–succinimide esterified CPMV particles migrate more slowly toward the anode than wild–type and each of the three ^{Peptide}CPMV conjugates.

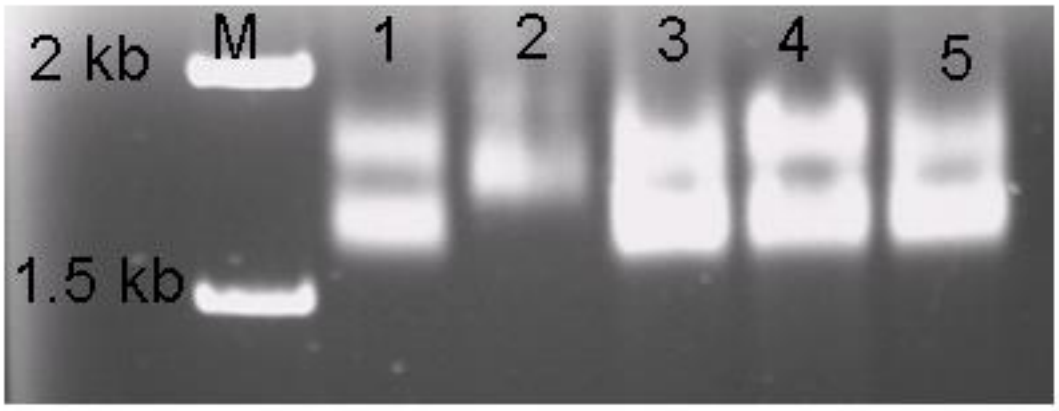

Figure 3.4– Agarose gel (1.2%) electrophoresis of CPMV particles visualised by ethidium bromide staining. M represents a 1–kbp DNA ladder. Lane 1, wild–type CPMV; 2, $^{NHS–ester}$CPMV; 3, $^{Peptide–CoPt}$CPMV; 4, $^{Peptide–FePt}$CPMV; 5, $^{Peptide–ZnS}$CPMV.

The number of peptides per virus particle was determined for $^{Peptide–CoPt}$CPMV conjugate. $^{Peptide–CoPt}$CPMV in sodium phosphate buffer pH 7.0 was reacted with an excess of NHS ester–activated amine specific dye, DyLight594. The doubly functionalised particles $^{Peptide–CoPt}$CPMV^{DyLight594} were purified rigorously (as described in section 2.17) and the number of free reactive lysines was calculated, from the absorbance spectrum Figure 3.5, to be on average ~66 ± 4 per virion. This equates to approximately 180 peptides [maximum addressable amines (240) – free amines remaining in conjugate (66) = 170–174] being bound to each CPMV virus particle; whereas in the case of genetically engineered chimaera the total number of peptides was 60 per virus. The ^{Peptide}CPMV conjugates were found to be monodisperse by DLS and the particle size did not increase significantly compared to wild–type.

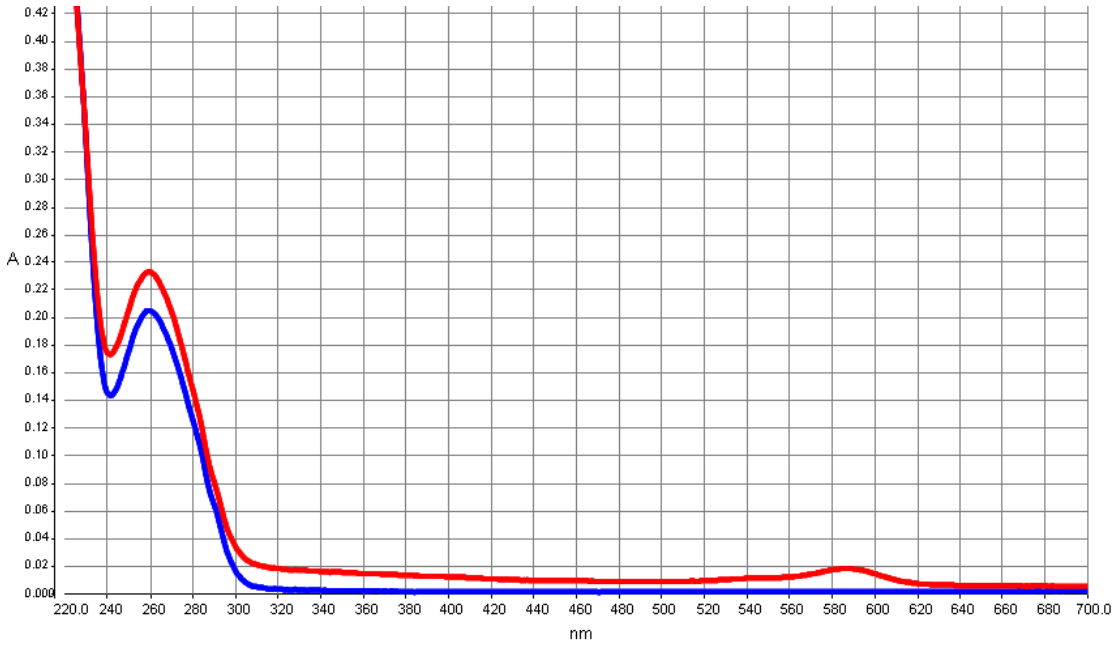

Figure 3.5– UV–visible spectrum of doubly functionalised $^{Peptide–CoPt}$CPMV particles. CPMVwt (blue line) and $^{Peptide–CoPt}$CPMV^{DyLight594} (red line). The number of peptides bound to the virus capsid was 174 peptide/virus, which means 3 of the 4 regularly addressable lysine are coupled to peptide.

The integrity of the doubly–functionalised particles was confirmed by agarose gel electrophoresis. Unstained native agarose gel electrophoresis revealed a visible fluorescent band as a result of the fluorescently labelled ^{PeptideCoPt}CPMV^{DyLight594} virus capsid and also revealed that no free dyes are present in the sample (Figure 3.6–A). In addition, staining with both

ethidium bromide and Coomassie blue confirmed the integrity of the intact particles (Figure 3.6–B and C, respectively).

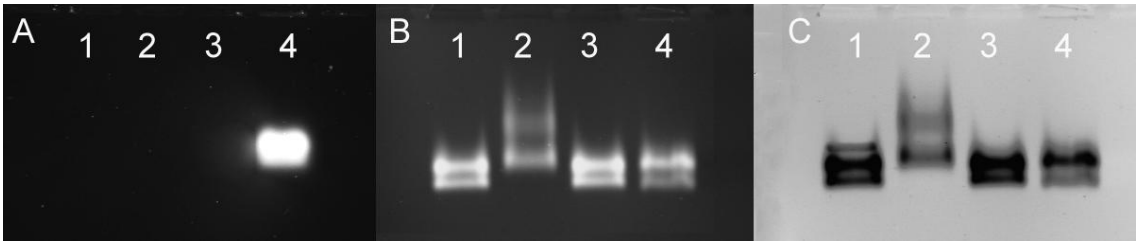

Figure 3.6– Native 1.2% agarose gel electrophoresis (A) unstained; (B) ethidium bromide stained; (C) Coomassie blue stained. Lane 1, wild–type CPMV; 2, $^{\text{NHS–ester}}$CPMV; 3, $^{\text{Peptide–CoPt}}$CPMV conjugate; 4, $^{\text{Peptide–CoPt}}$CPMV$^{\text{DyLight594}}$ conjugate.

3.3.3 Mineralization of $^{\text{Peptide}}$CPMV conjugates

Reaction of $^{\text{Peptide}}$CPMV conjugates with reagents for mineralization produced monodisperse nanoparticles. For example, treatment of $^{\text{Peptide–CoPt}}$CPMV in buffer with an equimolar mixture of cobalt(II)chloride and hexachloroplatinic acid together with two molar equivalents of sodium borohydride reductant, within 48 hours, generated virus–templated CoPt–CPMV particles. A similar approach was used to prepare FePt–CPMV nanoparticles using iron(III)chloride and hexachloroplatinic acid. For ZnS–CPMV, the reagents used were zinc chloride and sodium sulfide in an equimolar ratio. After purification, the mineralized particles were obtained in 70–80% recovered yield based on the initial virus concentration. This protocol requires neither high temperature nor pressure, is performed in aqueous buffer, and produces little waste so is environmentally benign. It has been found that this process can be readily scaled–up to 10 mg ml^{-1} of virus particles. The $^{\text{Peptide}}$CPMV conjugates are specific to their corresponding mineralization process. CPMVwt, when incubated under identical conditions with the reagents for mineralization did not mineralize; no monodisperse, templated nanoparticles were formed but some non–specific mineralization and bulk precipitation was observed (Figure 3.7). Similarly, the peptide alone does not promote formation of monodisperse nanoparticles.

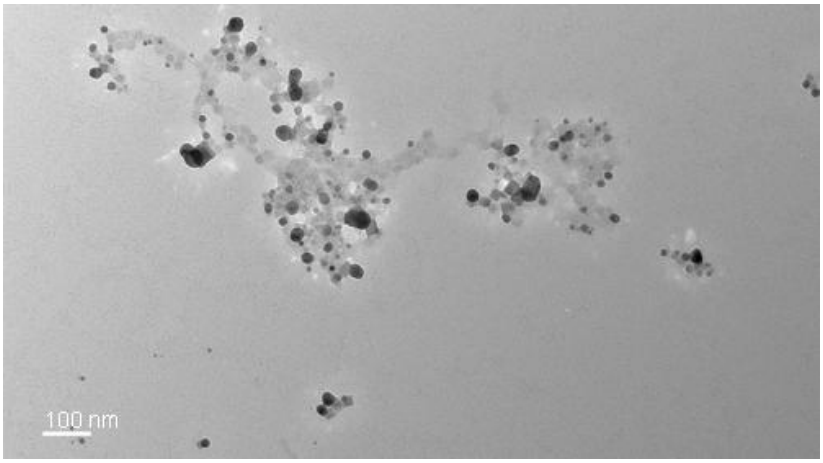

Figure 3.7– Unstained TEM image for unmodified CPMVwt particles incubated with equimolar quantities of $FeCl_3$ and H_2PtCl_6 in the presence of sodium borohydride. The apparent virus particle is possibly because of platinum staining.

When the conjugate that is specific for directed CoPt mineralization $^{Peptide–CoPt}$CPMV was reacted with the reagents for mineralization with FePt or ZnS, and *vice versa*, there was no evidence for templated–mineralization observed by TEM. This is direct evidence and demonstration of the selectivity of the peptides. Figure 3.8 shows the selectivity of $^{Peptide–ZnS}$CPMV, when incubated with Fe and Pt salt precursors only non–specific and bulk precipitation was observed.

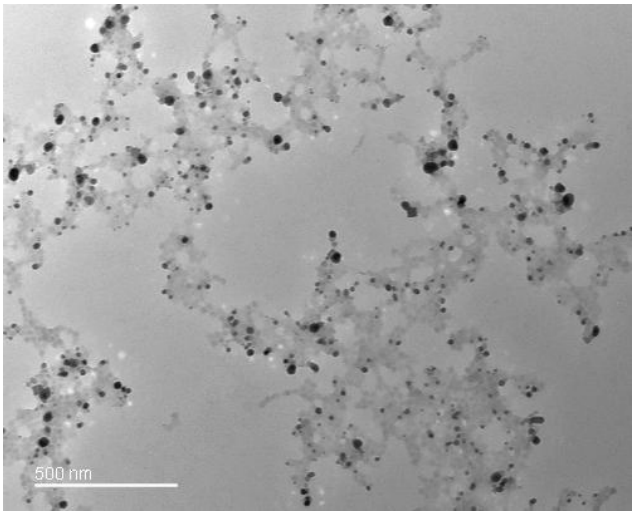

Figure 3.8– Unstained TEM image for $^{Peptide–ZnS}$CPMV incubated with equimolar quantities of $FeCl_3$ and H_2PtCl_6 in the presence of sodium borohydride. The black spheres are believed to be iron–platinum either as an alloy or as separate metals.

In the case of $^{Peptide–CoPt}$CPMV, the mineralization occurs irrespective of the C– to N–terminus ordering of the peptide; that is, peptide can be bound by the C–terminus carboxylate to amine groups on the virus surface as Cbz–CNAGDHANC or Cbz–CNAHDGANC without the mineralization process being affected. TEM images (data not shown) are very similar to those obtained in Figure 3.9.

The unstained TEM images for CoPt–CPMV, Figure 3.9–A, FePt–CPMV, Figure 3.9–B, and ZnS–CPMV, Figure 3.9–C, reveal dense, mineralized nanoparticles of *ca.* 32 nm, which is in agreement with the particle size measured by DLS (Table 3.4). Wild–type CPMV when treated under identical mineralization conditions and after purification cannot be visualised in an unstained TEM image and can only be seen after negative staining with uranyl acetate. These images are similar to those previously observed for templated mineralized–CPMV particles prepared using CPMV–chimaeras (Shah et al, 2009a) and confirm that the ^{Peptide}CPMV conjugates direct templated surface mineralization. Comparison between the two approaches is summarised in Table 3.3.

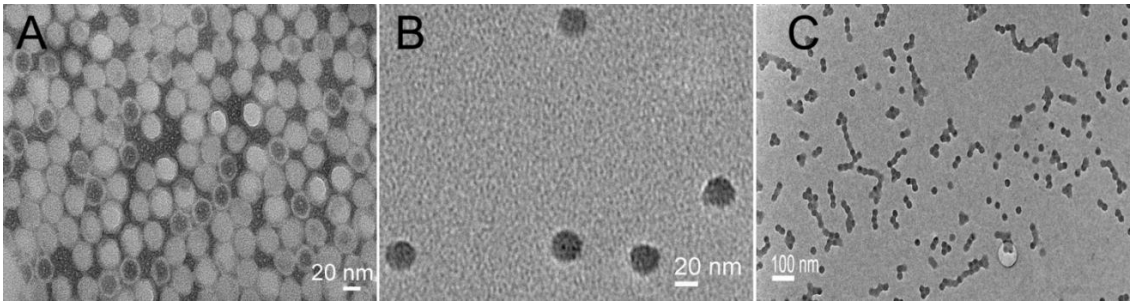

Figure 3.9– Unstained TEM images for mineralized CPMV particles. (A) CoPt–CPMV mineralized particles, (B) FePt–CPMV mineralized particles and (C) ZnS–CPMV mineralized particles.

FePt coated particles	Chimaeric mineralization	Chemical modification
Diameter	30.0 ± 0.2 nm	32.0 ± 0.5 nm
Zeta potential	– 49.6 ± 1.0 nm	– 60.3 ± 1.9 nm
Yield	Very low	Depending on starting material, with 80% recovery

Table 3.3– Comparison between CPMV–templated FePt particles synthesised by either genetic insertion or chemical modification.

Elemental analysis using EDXS confirmed that cobalt and platinum, iron and platinum, and zinc and sulfur coated the external surfaces of CoPt–, FePt– and ZnS–CPMV nanoparticles, respectively, Figure 3.10.

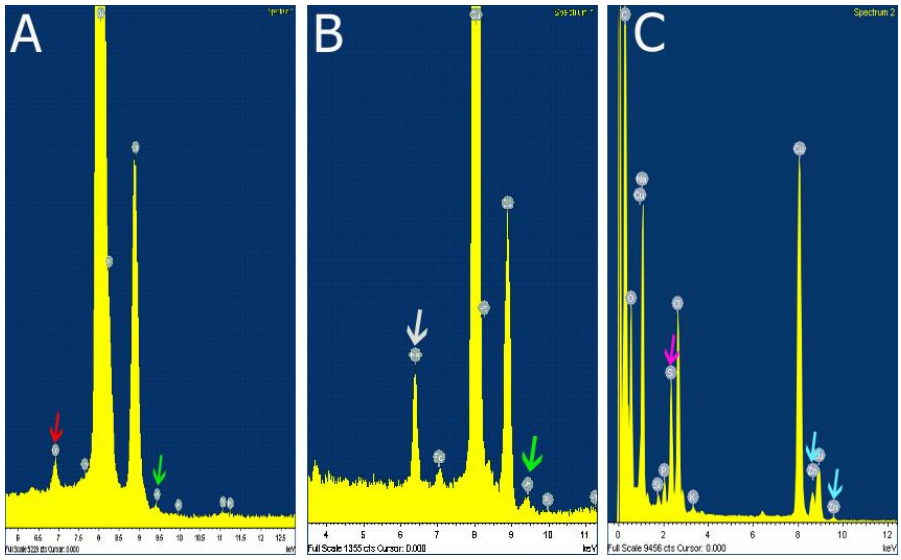

Figure 3.10– EDX spectrum of mineralized particles. (A) CoPt–CPMV, (B) FePt–CPMV and (C) ZnS–CPMV. Major peaks for each metal indicated with arrows; red for cobalt, green for platinum, white for iron, pink for zinc and blue for sulphide.

Electron microscopy revealed two distinct morphologies in the unstained TEM image of CoPt–CPMV, Figure 3.9–A. One is as expected for an externally mineralized virus capsid but the other, with a darker core, is similar to that observed for internally–mineralized CPMV empty (devoid of RNA) virus–like particles (eVLPs) in which the internal cavity contains cobalt or iron oxide metals (Aljabali et al, 2010c). During a normal plant infection with wild–type CPMV, up to 10% of the virions isolated are devoid of RNA. It is proposed that the particles exhibiting the darker core are naturally occurring eVLPs that have been loaded with cobalt or cobalt/platinum as well as being externally mineralized because of the peptide bound to the exterior of the particles.

To support the proposed hypothesis, naturally occurring eVLPs (top component) that have been chemically modified to display peptide–CoPt on their outer surface, showed a similar morphology in the TEM to the CoPt–CPMV, Figure 3.11, when mineralized with

cobalt/platinum. Later studies on the mineralization of the eVLPs confirmed the ability to internally mineralize the cavity of the eVLPs without the need for any further modification; this will be discussed in Chapter 6.

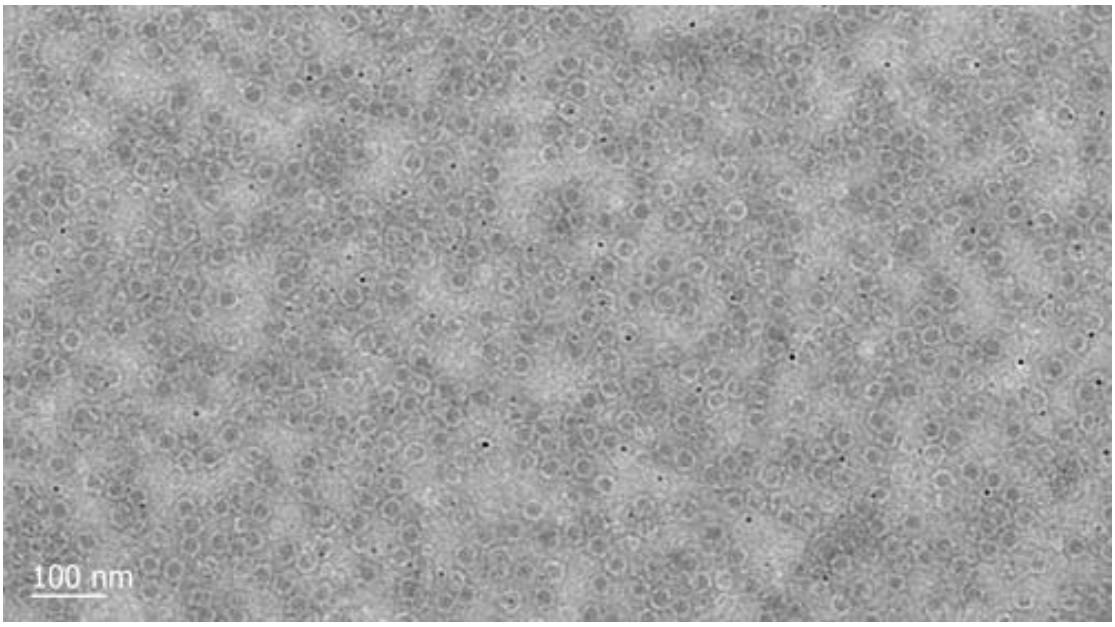

Figure 3.11– Unstained TEM image of $^{Peptide–CoPt}$VLPs that have been mineralized both internally and externally. The black spots are non–templated CoPt nanoparticles that remained in the sample after purification.

Further, immunological detection (as described in section 2.12) shows the presence of accessible coat protein for eVLPs and $^{Peptide–CoPt}$eVLPs but not for externally mineralized particles as shown in Figure 3.12. This is consistent with the two observed morphologies being indeed for both internal and external mineralization.

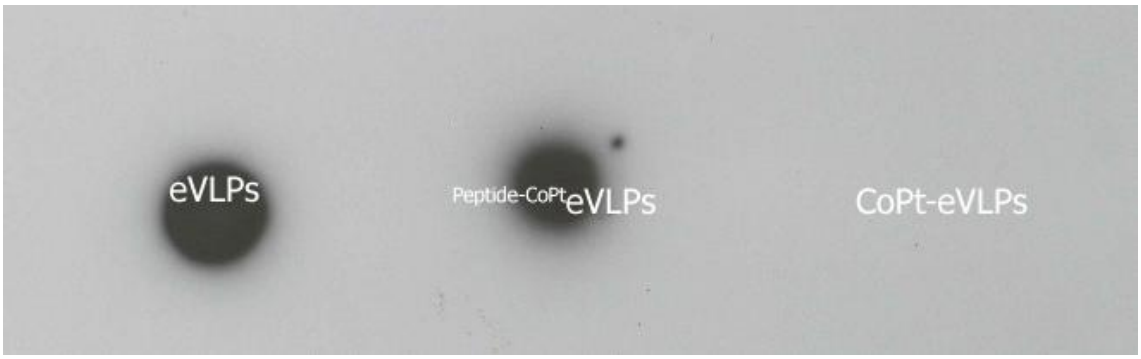

Figure 3.12– Immunological detection of coat protein for eVLPs, $^{peptide–CoPt}$eVLPs that reveal accessibility to the coat protein. However, mineralized CoPt–eVLPs were not detected immunologically.

Analysis of the mineralized CoPt–eVLP particles using agarose gel electrophoresis cannot differentiate between the two morphologies, as the eVLPs that are both externally and internally mineralized do not contain encapsidated RNA, which would stain with ethidium bromide.

Characterisation of CPMV mineralized particles using agarose gel electrophoresis was performed. For CoPt–CPMV stained with ethidium bromide some fluorescent intensity was observed from a band of different mobility to wild–type and to $^{Peptide–CoPt}$CPMV conjugate (Figure 3.13–A), suggesting that the CoPt–CPMV surface has some limited porosity sufficient to allow intercalation of ethidium bromide with the encapsulated RNA. For FePt–CPMV and ZnS–CPMV, less intense fluorescence is observed implying that there is less surface porosity after mineralization. However, when the gel is stained with Coomassie blue, Figure 3.13–B, no colouration is observed for each of the mineralized samples, this is consistent with the virus protein surface not being accessible to the stain as it is coated with mineral.

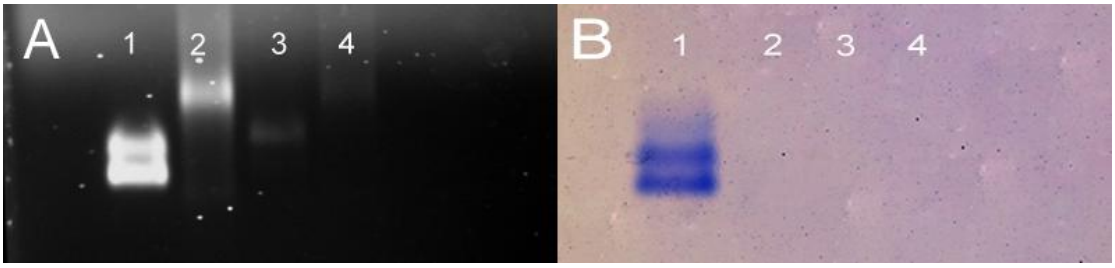

Figure 3.13– Native 1.2% agarose gel for mineralized CPMV particles. Stained with (A) ethidium bromide and (B) coomassie Blue. Lane 1, CPMVwt; 2, CoPt–CPMV; 3, FePt–CPMV; 4, ZnS–CPMV.

In addition, the CPMV coat protein of CoPt–CPMV, FePt–CPMV and ZnS–CPMV was not detected immunologically (Figure 3.14). Only in the case of CPMVwt was a signal obtained, confirming the presence of CPMV coat protein; for the mineralized particles, the coat protein was not accessible to the antibody presumably due to the mineral coating.

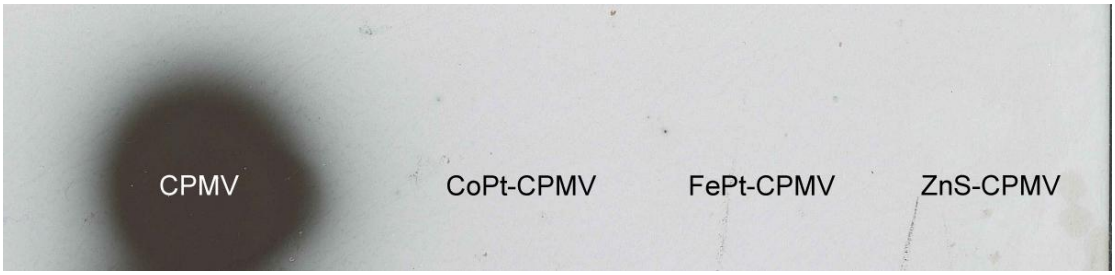

Figure 3.14– Immunological detection of CPMVwt coat protein of mineralized particles spotted on a nitrocellulose membrane probed with polyclonal antibodies raised against CPMV. Only CPMVwt gave a detectable signal.

Further support for the deposition of a robust mineral shell on the external surface is provided by comparison of the SDS–PAGE of mineralized and non–mineralized CPMV particles (Figure 3.15). Even under harsh denaturing conditions, such as with sodium dodecyl sulfate at 100 ºC for 20 minutes, there is only very partial release of coat proteins on denaturation of the mineralized–CPMV particles as shown by the near absence of coat protein on the SDS–PAGE gel. This is what would be expected if the denaturing agent either is unable to penetrate the mineral coat and/or the coat protein cannot be released from the mineralized shells.

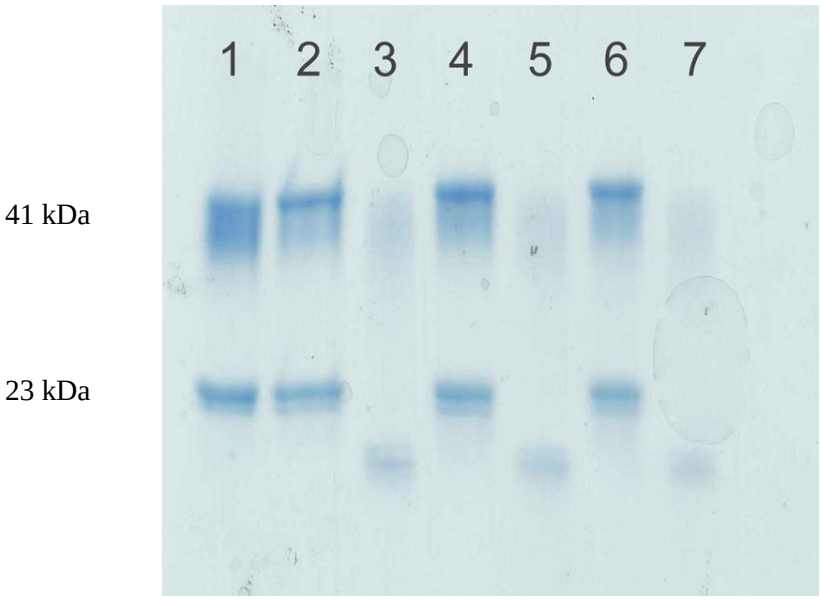

Figure 3.15– SDS–PAGE of mineralized CPMV particles. There is only very partial release of coat protein on denaturation of the mineralized–CPMV particles as shown by the near absence of coat proteins on the SDS–PAGE gel. Lane 1, CPMVwt; 2, $^{Peptide–CoPt}$CPMV; 3, CoPt–CPMV; 4, $^{Peptide–FePt}$CPMV; 5, FePt–CPMV; 6, $^{Peptide–ZnS}$CPMV; 7, ZnS–CPMV. Lanes 2, 4 and 6 are before mineralization whereas lanes 3, 5 and 7 are after mineralization.

The results of DLS and zeta potential measurements for the mineralized nanoparticles are shown in Table 3.4 (and detailed graphs are shown in Figure 3.16). The particle size in buffer as measured by DLS shows an increase in average hydrodynamic diameter to *ca.* 32 nm following mineralization. Prior to peptide–modification and mineralization, CPMV has a diameter of *ca.* 28 nm, implying that the coating on each particle is approximately 2 nm. This contrasts with a coating of 1 nm observed when FePt is templated on chimaeric $CPMV_{FePt}$ (Shah et al, 2009a). The coating thickness is significantly greater than the atomic diameter of individual metal atoms (0.25–0.27 nm) and the length of the coupled–peptide (ca. 1.00 – 1.50 nm).

	DLS diameter (nm)	**Polydispersity (%)**	**Zeta potential (mV)**
CPMVwt	27.4 ± 0.5	14.0	–12.3 ± 1.5
CoPt–CPMV	31.8 ± 0.5	16.7	–39.1 ± 2.1
FePt–CPMV	32.0 ± 0.2	20.9	–60.3 ± 1.9
ZnS–CPMV	30.8 ± 0.4	15.0	–22.2 ± 3.3

Table 3.4– Diameter and polydispersity measured by dynamic light scattering and zeta potential of CPMVwt and mineralized–CPMV nanoparticles.

The DLS polydispersity indicates that, by this criterion (see chapter 2) and in agreement with the observed TEM images, the particles are monodisperse and that the coated CPMV particles are uniformly mineralized on their outer surfaces.

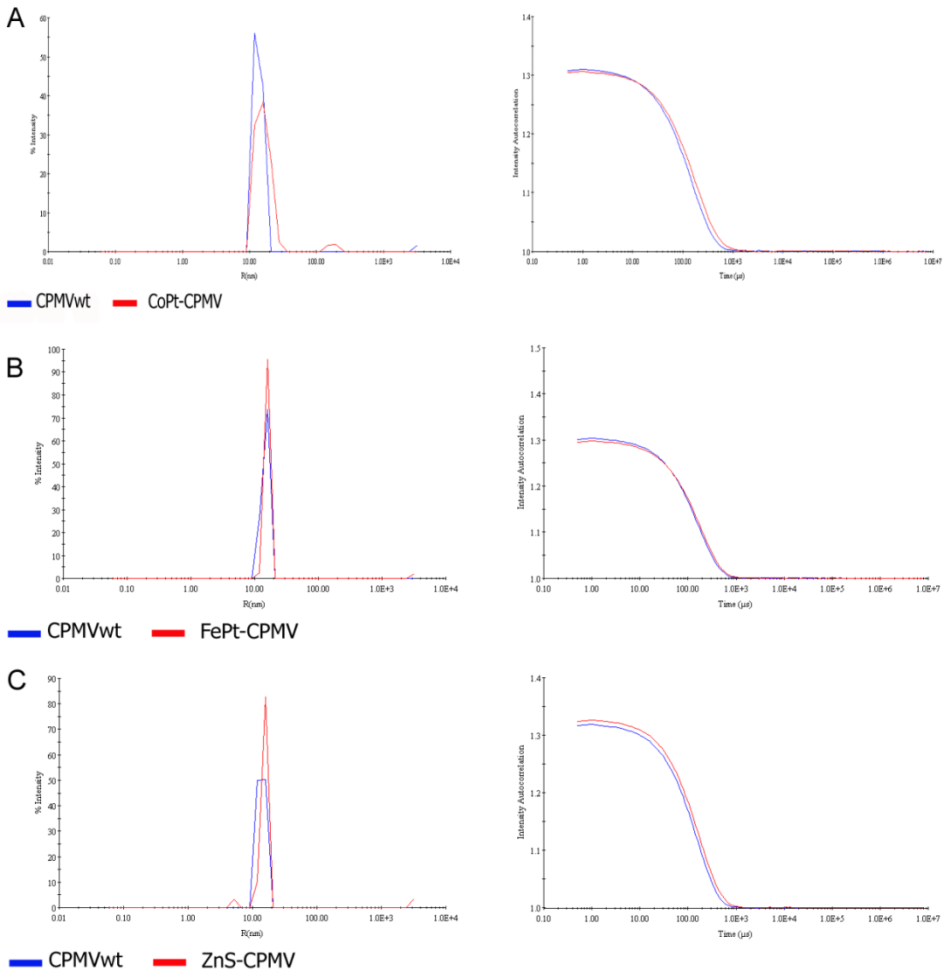

Figure 3.16– DLS data comparing CPMVwt and mineralized particles (A) CoPt–CPMV (B) FePt–CPMV (C) ZnS–CPMV.

The zeta potential for suspensions of the mineralized particles in buffer are considerably more negative than that for CPMVwt (Figure 3.17), of *ca.* – 12 mV, and show that the colloids have good stability and no propensity to aggregate. Particles were stable over 2–3 months. Zeta potential values are summarised in Table 3.4.

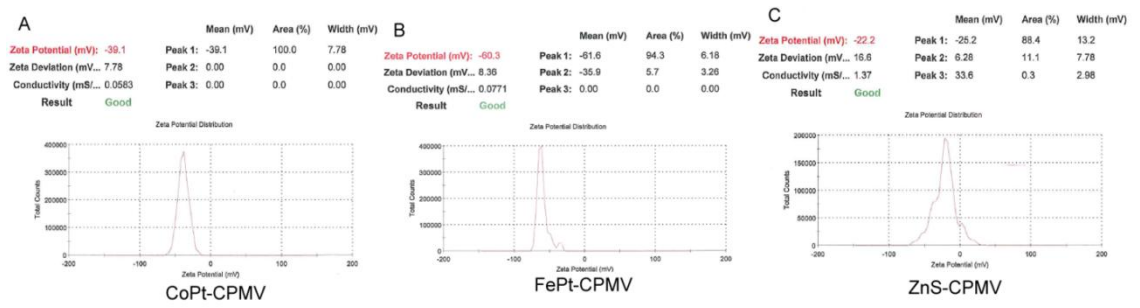

Figure 3.17– Zeta potential measurement of mineralized (A) CoPt–CPMV (B) FePt–CPMV and (C) ZnS–CPMV particles.

Nanoparticle tracking analysis (Figure 3.18), based on laser light scattering microscopy, was also consistent with mineralization of the virus. For each of the mineralized virus particles there was a significant increase in the relative refractive index compared with wild–type and with ^{Peptide}CPMV conjugates. The analysis is also consistent with the mineralized particles being monodisperse as indicated by the particle size distribution; although for ZnS–CPMV there was a little non–specific aggregation under the measurement conditions employed.

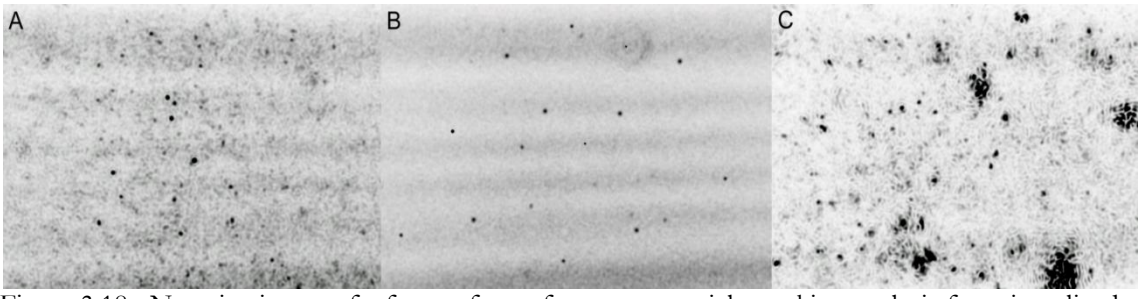

Figure 3.18– Negative image of a freeze–frame from nanoparticle tracking analysis for mineralized–CPMV nanoparticles. Showing that the particles appear individually as point scatterers under Brownian motion with a high refractive index. (A) CoPt–CPMV; (B) FePt–CPMV; (C) ZnS–CPMV.

The scanning electron micrograph of FePt–CPMV (Figure 3.19) provides further evidence that the templated nanoparticles retain their integrity and monodispersity.

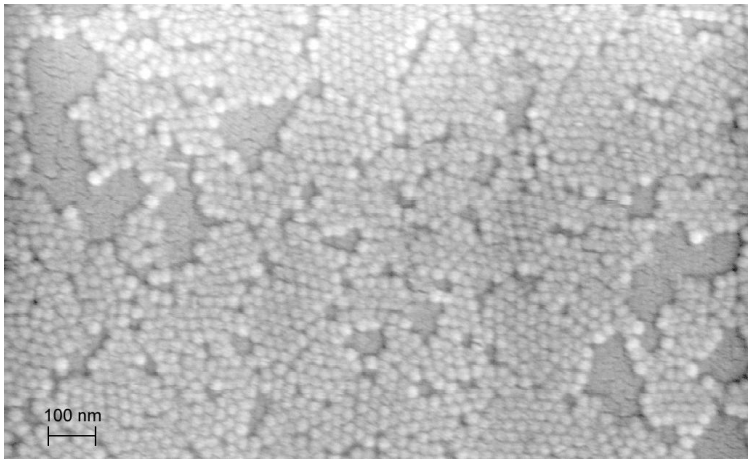

Figure 3.19– SEM image of sputter–coated FePt–CPMV deposited on a mica surface.

Finally, the magnetic properties for the chimaeric–templated particles could not be obtained because of the low amount of the mineralized particles obtained. However, in order to demonstrate that the FePt–CPMV possesses magnetic properties, a large sample of mineralized FePt–CPMV (115 mg ml^{-1}, 200 µl) was prepared by the chemical modification route and placed beside an external magnet as shown in Figure 3.20. Immediately, a progressive migration of the dark nanoparticles towards the magnet was observed. It was very difficult to demagnetise the particles maybe as a result of ferromagnetic properties. Particles remained in pellet form or as large aggregates as confirmed by TEM, Figure 3.20–C.

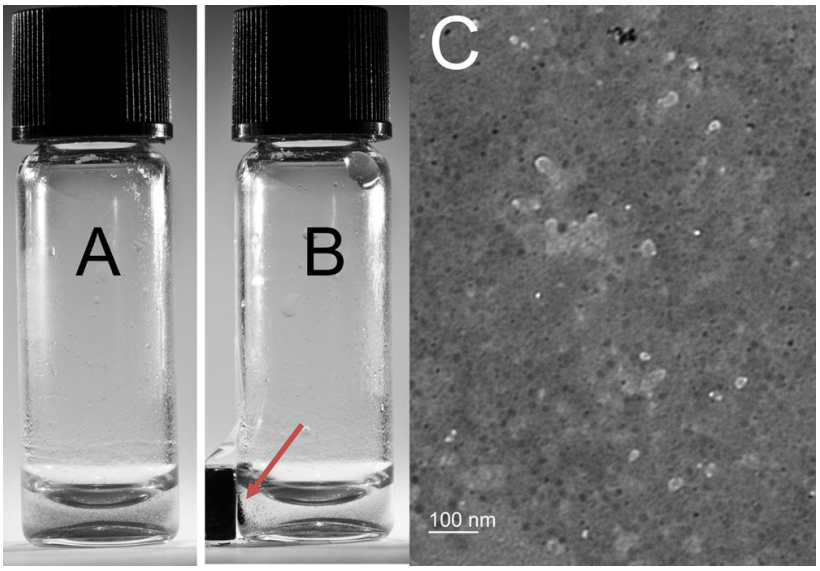

Figure 3.20– Demonstrating magnetic properties of FePt–CPMV prepared by the chemical modification route. (A) (115 mg ml^{-1}, 200 µl) FePt–CPMV particles suspended in 100 mM sodium phosphate buffer pH 7.0. (B) The same sample after 1 minute of exposure to the magnetic field, and (C) is the corresponding TEM from the accumulated pellet in (B). Arrow indicates particle attracted to the external magnet.

3.3.4 Mineralization of peptide–modified MWCNT

Carbon nanotubes (CNTs) consist of rolled graphene sheets with diameters in the nanometre range and lengths in the micrometre range, and are useful materials with unique properties. Matsui and co–workers showed that nanotubular structures coated with a histidine–rich peptide can serve as templates to generate mineralized gold nanoparticles on the nanotube surface (Djalali et al, 2003). The possibility of using CNTs as building blocks for nanoelectronic components or devices requires uniform and monodisperse metal coatings of the CNTs for conductivity purposes. With this in mind, the chemically–coupled–peptide–promoted method of mineralization was shown to be a general method for any suitably modified surface. The CoPt peptide could easily be coupled to an amine surface–functionalised MWCNT by the standard carbodiimide protocol to give peptide–modified MWCNT ($^{\text{Peptide–CoPt}}$MWCNT). Incubation of $^{\text{Peptide–CoPt}}$MWCNT with cobalt chloride, hexachloroplatinic acid and sodium borohydride reductant, followed by purification after 24 hours shows, by TEM, the initiation of mineralization (Figure 3.21–B) at, presumably, the sites of peptide coupling. This process is analogous to that which occurs on mineralization of $^{\text{Peptide–CoPt}}$CPMV conjugates as described above. Repeating the mineralization process sequentially over seven days produced a thick, *ca.* 20 nm, fairly uniform coating, of CoPt on the surface of the MWCNT as confirmed by TEM (Figure 3.21–C) and EDXS (Figure 3.22).

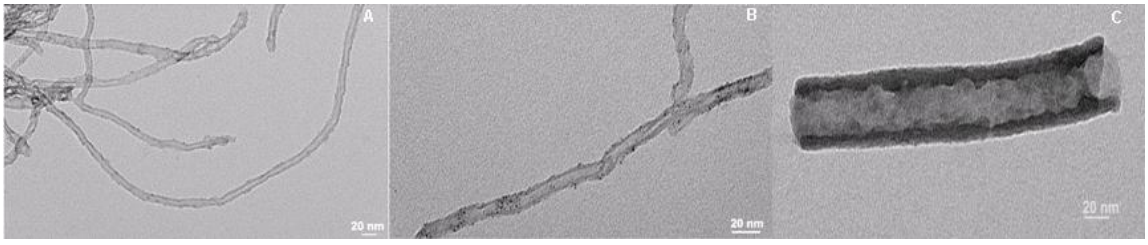

Figure 3.21– Unstained TEM images of peptide–promoted mineralization of amine–functionalised MWCNT. (A) amine–functionalised MWCNT; (B) $^{\text{Peptide–CoPt}}$MWCNT after 24 hours mineralization showing initial nucleation sites of CoPt; (C) CoPt–mineralized MWCNT after 7 days.

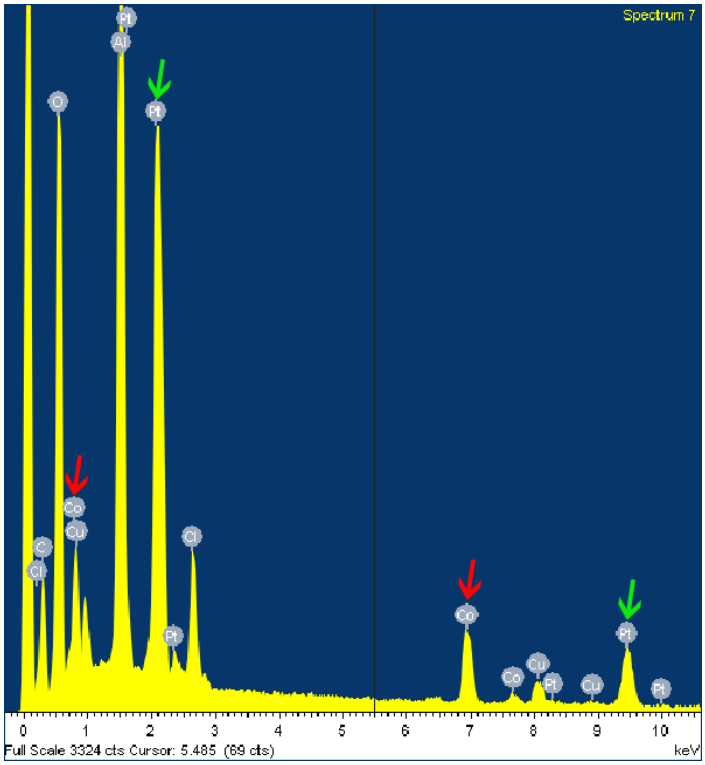

Figure 3.22– EDX spectrum of CoPt–mineralized MWCNT. Major peaks for each metal indicated with arrows.

3.4 Conclusions

In conclusion, the successful attachment of peptide that promote certain types of mineralization to the external surface of CPMVwt and MWCNT is only the beginning and may lead to the synthesis of metallic nanoshells with interesting magnetic and other properties. This approach is proven to be general to any surface that could be suitably functionalised.

3.5 REFERENCES

Ahmad, G., Dickerson, M. B, Church, B. C., Cai, Y., Jones, S. E., Naik, R. R., King, J. S., Summers, C. J., Kröger, N., Sandhage, K. H. (2006). Rapid, Room–Temperature Formation of Crystalline Calcium Molybdate Phosphor Microparticles via Peptide–Induced Precipitation. Advanced Materials **18**, 1759–1763.

Aljabali, A.A.A., Sainsbury, F., Lomonossoff, G.P., and Evans, D.J. (2010b). Cowpea Mosaic Virus Unmodified Empty Viruslike Particles Loaded with Metal and Metal Oxide. Small ***6***, 818–821.

Baeuerlein, E. (2004). Biomineralization: progress in biology, molecular biology and application, 2nd completely rev. and extended edn (Weinheim, Wiley–VCH).

Brown, S. (1992). Engineered Iron Oxide–Adhesion Mutants of the Escherichia–Coli Phage–Lambda Receptor. P Natl Acad Sci USA ***89***, 8651–8655.

Brown, S., Sarikaya, M., and Johnson, E. (2000). A genetic analysis of crystal growth. Journal of Molecular Biology **299**, 725–735.

Chen, R., and Lockwood, D.J. (2002). ChemInform Abstract: Developments in Luminescence and Display Materials over the Last 100 Years as Reflected in Electrochemical Society Publications. ChemInform **149***:* 569–578.

Chun–Long, C., and Nathaniel, L.R. (2010). Peptide–Based Methods for the Preparation of Nanostructured Inorganic Materials. Angewandte Chemie International Edition 49, 1924–1942.

Descalzo, A.B., Martinez–Manez, R., Sancenon, R., Hoffmann, K., and Rurack, K. (2006). The supramolecular chemistry of organic–inorganic hybrid materials. Angew Chem–Int Edit **45**, 5924–5948.

Dessens, J.T., and Lomonossoff, G.P. (1993). Cauliflower mosaic virus 35S promoter–controlled DNA copies of cowpea mosaic virus RNAs are infectious on plants. J Gen Virol **74** *(Pt 5)*, 889–892.

Djalali, R., Chen, Y., and Matsui, H. (2003). Au Nanocrystal Growth on Nanotubes Controlled by Conformations and Charges of Sequenced Peptide Templates. Journal of the American Chemical Society *125*, 5873–5879.

Evans, D.J. (2008). The bionanoscience of plant viruses: templates and synthons for new materials. Journal of Materials Chemistry ***18***, 3746–3754.

Flynn, C.E., Lee, S., Peelle, B.R., and Belcher, A.M. (2003a). Viruses as vehicles for growth, organization and assembly of materials. Acta Materialia ***51***, 5867–5880.

Flynn, C.E., Mao, C., Hayhurst, A., Williams, J.L., Georgiou, G., Iverson, B., and Belcher, A.M. (2003b). Synthesis and organization of nanoscale II–VI semiconductor materials using evolved peptide specificity and viral capsid assembly. Journal of Materials Chemistry ***13***, 2414–2421.

Gao, X.D., Li, X.M., and Yu, W.D. (2004). Morphology and optical properties of amorphous ZnS films deposited by ultrasonic–assisted successive ionic layer adsorption and reaction method. Thin Solid Films ***468***, 43–47.

Hyeon, T. (2003). Chemical synthesis of magnetic nanoparticles. Chem Commun, 927–934.

Kind, H., Bittner, A. M., Cavalleri, O., Kern, K., Greber, T. (1998). Electroless Deposition of Metal Nanoislands on Aminothiolate–Functionalized Au(111) Electrodes. The Journal of Physical Chemistry B ***102***, 7582–7589.

Li, C., Botsaris, G.D., and Kaplan, D.L. (2002). Selective in Vitro Effect of Peptides on Calcium Carbonate Crystallization. Crystal Growth & Design ***2***, 387–393.

Liang, H.P., Zhang, H. M., Hu, J. S., Guo, Y. G., Wan, L. J., Bai, C. L., (2004). Pt hollow nanospheres: Facile synthesis and enhanced electrocatalysts. Angew Chem–Int Edit ***43***, 1540–1543.

Lin, T., and Johnson, J.E. (2003). Structures of picorna–like plant viruses: implications and applications. Adv Virus Res ***62***, 167–239.

Lin, T., Porta, C., Lomonossoff, G., and Johnson, J.E. (1996). Structure–based design of peptide presentation on a viral surface: the crystal structure of a plant/animal virus chimera at 2.8 A resolution. Fold Des ***1***, 179–187.

Lomonossoff, G.P., and Johnson, J.E. (1991). The synthesis and structure of comovirus capsids. Prog Biophys Mol Biol ***55***, 107–137.

Lomonossoff, G.P., Johnson, J. E. (1996). Use of macromolecular assemblies as expression systems for peptides and synthetic vaccines. Curr Opin Struct Biol ***6***, 176–182.

Mao, C., Solis, D.J., Reiss, B.D., Kottmann, S.T., Sweeney, R.Y., Hayhurst, A., Georgiou, G., Iverson, B., and Belcher, A.M. (2004). Virus–based toolkit for the directed synthesis of magnetic and semiconducting nanowires. Science ***303***, 213–217.

Merzlyak, A., and Lee, W. (2006). Phage as templates for hybrid materials and mediators for nanomaterial synthesis. Current Opinion in Chemical Biology *10*, 246–252.

Naik, R.R., Brott, L.L., Clarson, S.J., and Stone, M.O. (2002a). Silica–precipitating peptides isolated from a combinatorial phage display peptide library. J Nanosci Nanotechno ***2***, 95–100.

Naik, R.R., Stringer, S.J., Agarwal, G., Jones, S.E., and Stone, M.O. (2002b). Biomimetic synthesis and patterning of silver nanoparticles. Nature Materials ***1***, 169–172.

Nam, K.T., Kim, D.W., Yoo, P.J., Chiang, C.Y., Meethong, N., Hammond, P.T., Chiang, Y.M., and Belcher, A.M. (2006). Virus–enabled synthesis and assembly of nanowires for lithium ion battery electrodes. Science ***312***, 885–888.

Nanda, J., Sapra, S., Sarma, D. D., Chandrasekharan, N., Hodes, G., (2000). Size–Selected Zinc Sulfide Nanocrystallites: Synthesis, Structure, and Optical Studies. Chemistry of Materials ***12***, 1018–1024.

Porta, C., Spall, V.E., Lin, T.W., Johnson, J.E., Lomonossoff, G.P., Findlay, K.C., Gergerich, R.C., Farrance, C.E., and Lomonossoff, G.P. (2003). Cowpea mosaic virus–based chimaeras. Effects of inserted peptides on the phenotype, host range, and transmissibility of the modified viruses. Virology ***310***, 50–63.

Porta, C., Spall, V.E., Loveland, J., Johnson, J.E., Barker, P.J., and Lomonossoff, G.P. (1994). Development of Cowpea Mosaic Virus as a High–Yielding System for the Presentation of Foreign Peptides. Virology ***202***, 949–955.

Reiss, B.D., Mao, C., Solis, D.J., Ryan, K.S., Thomson, T., and Belcher, A.M. (2004). Biological Routes to Metal Alloy Ferromagnetic Nanostructures. Nano Letters ***4***, 1127–1132.

Royston, E., Lee, S.Y., Culver, J.N., and Harris, M.T. (2006). Characterization of silica–coated tobacco mosaic virus. J Colloid Interface Sci ***298***, 706–712.

Royston, E.S., Brown, A.D., Harris, M.T., and Culver, J.N. (2009). Preparation of silica stabilized Tobacco mosaic virus templates for the production of metal and layered nanoparticles. J Colloid Interface Sci ***332***, 402–407.

Scott, J.K., and Smith, G.P. (1990). Searching for peptide ligands with an epitope library. Science ***249***, 386–390.

Shah, S.N., Steinmetz, N.F., Aljabali, A.A., Lomonossoff, G.P., and Evans, D.J. (2009). Environmentally benign synthesis of virus–templated, monodisperse, iron–platinum nanoparticles. Dalton Transactions **9:** 8479–8480.

Shenton, W., Mann, S., Colfen, H., Bacher, A., Fischer, M. (2001). Synthesis of Nanophase Iron Oxide in Lumazine Synthase Angew Chem Int Ed Engl ***40***, 442–445.

Slocik, J.M., and Naik, R.R. (2006). Biologically Programmed Synthesis of Bimetallic Nanostructures. Advanced Materials ***18***, 1988–1992.

Smith, G.P., and Scott, J.K. (1993). Libraries of Peptides and Proteins Displayed on Filamentous Phage. Method Enzymol ***217***, 228–257.

Steinmetz, N.F., and Evans, D.J. (2007). Utilisation of plant viruses in bionanotechnology. Org Biomol Chem ***5***, 2891–2902.

Steinmetz, N.F., Lomonossoff, G.P., and Evans, D.J. (2006). Decoration of Cowpea mosaic virus with multiple, redox–active, organometallic complexes. Small ***2***, 530–533.

Steinmetz, N.F., Shah, N.S., J. E. Barclay, Rallapalli, G., Lomonossoff, G.P., and Evans, D.J. (2009). Virus–Templated Silica Nanoparticles. Small ***5***, 813–816.

Sun, S. (2006). Recent Advances in Chemical Synthesis, Self–Assembly, and Applications of FePt Nanoparticles. Advanced Materials ***18***, 393–403.

Sun, S., Murray, C. B., Weller, D., Folks, L., Moser, A., (2000). Monodisperse FePt Nanoparticles and Ferromagnetic FePt Nanocrystal Superlattices. Science ***287***, 1989–1992.

Tamerler, C., Khatayevich, D., Gungormus, M., Kacar, T., Oren, E.E., Hnilova, M., and Sarikaya, M. (2010). Molecular biomimetics: GEPI–based biological routes to technology. Peptide Science ***94***, 78–94.

Tamerler, C., and Sarikaya, M. (2009). Molecular biomimetics: nanotechnology and bionanotechnology using genetically engineered peptides. Philos T R Soc A ***367***, 1705–1726.

Tan, Y.N., Lee, J.Y., and Wang, D.I.C. (2010). Uncovering the Design Rules for Peptide Synthesis of Metal Nanoparticles. Journal of the American Chemical Society ***132***, 5677–5686.

Whaley, S.R., English, D.S., Hu, E.L., Barbara, P.F., and Belcher, A.M. (2000). Selection of peptides with semiconductor binding specificity for directed nanocrystal assembly. Nature *405*, 665–668.

4 Charge promoted mineralization

4.1 Introduction

It was apparent, from using peptides coupled to the CPMV exterior capsid to promote specific mineralization, that the specificity of the peptide is something imbedded within the peptide sequence (Aljabali et al, 2011; Mann, 2001; Willett et al, 2005) although it is not fully understood. The composition of the peptides identified by the phage–display peptide library and their ability to selectively initiate the nucleation is linked to the biochemical features of the peptides; this property depends on the peptide composition and structure and not the peptide sequence. Proteins enriched with acidic amino acids (aspartic and glutamic acid) have been suggested as nucleation sites for binding Ca^{2+} during the controlled formation of calcite (Addadi & Weiner, 1985; Wierzbicki et al, 1994) and calcite deposition on a carboxylate–terminated self-assembled monolayer (SAM) (Han & Aizenberg, 2003). However, the presence of charged amino acids (such as glutamic and aspartic acid) led me to believe that the charge within the peptide is involved in initiation of nucleation that can ultimately lead to mineralization of CPMV particles.

Although the precise reason for selectivity of peptides toward inorganic materials is not known, the sequence of the peptides used in the previous chapter suggested to me that the overall charge within the peptide is responsible for the initiation of nucleation, although it is not clear if it is responsible for selectivity as well. This hypothesis has been used to generate mineralized CPMV particles by changing the surface charge of CPMV particles.

This chapter will describe that there is no requirement for the use of mineral/metal specific peptides or the electroless deposition process for the CPMV–templated formation of monodisperse mineralized nanoparticles; it is sufficient to simply increase the virus surface negative charge by a chemical covalent modification process. The charge–modified CPMV, as proof–of–principle, was coated with cobalt or iron oxide to give monodisperse nanoparticles of about 32 nm diameter. Further, the iron oxide–CPMV nanoparticle surface can be functionalised

with, for example, a thiolated oligosaccharide, showing the potential for a range of modifications as depicted in Figure 4.1.

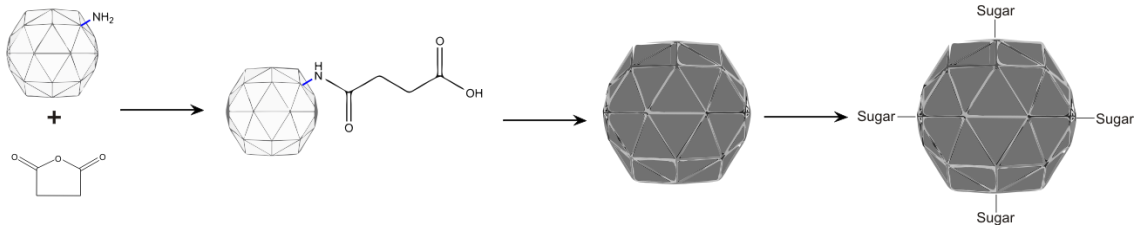

Figure 4.1– Schematic representation of the covalent modification of surface–exposed amines on the CPMVwt with succinamate (approx. 240 per virion) followed by mineralization and functionalisation with a thiolated oligosaccharide.

In addition, polyelectrolyte surface–modified CPMVwt can be used for the templated synthesis of gold coated CPMV particles (Au–CPMV). A cationic polyelectrolyte, poly(allylamine) hydrochloride (PAH), was electrostatically adsorbed to the external surface of the virus capsid, which promotes the adsorption of anionic gold complexes, which were then easily reduced, under mild conditions, to form a metallic gold layer. As expected, the gold surface can be further modified with thiol reagents. In contrast, reaction of polyelectrolyte–modified CPMV (^{PA}CPMV) with pre–formed gold nanoparticles resulted in the self–assembly of large, hexagonally packed, tessellated–spheres.

4.2 Experimental

4.2.1 Materials

Dimethyl sulfoxide ≥ 99.9% (DMSO), iron(III) chloride hexahydrate, iron(II) chloride tetrahydrate, hexachloroplatinic acid, anhydrous cobalt(II) chloride, poly(allylamine hydrochloride) (PAH, MW~ 15,000), poly(fluorescein isothiocyanate allylamine hydrochloride) (FITC–PAH, MW~ 9291), gold(III) chloride trihydrate 99.9+%, tetrachloroauric acid and sodium borohydride were purchased from Sigma–Aldrich; succinic anhydride from Alfa Aesar; potassium carbonate from BDH; hydroxylamine hydrochloride, 99%, from Lancaster Synthesis; DyLight–594 NHS Ester from Thermo Scientific. All reagents were used without further

purification. Solutions were prepared using Milli–Q water with a resistivity of 18.2 MΩ cm (Millipore).

4.2.2 ^{Succinamate}CPMV

CPMV particles (10 mg ml^{-1}, 1 ml) suspended in 10 mM sodium phosphate buffer pH 7.0 were reacted with a 2000 molar excess of succinic anhydride dissolved in DMSO and the final DMSO concentration was adjusted to 20% (v/v). The reaction pH was monitored and maintained if needed at pH 7.0 by the addition of a few drops of 1 mM NaOH. The reaction was left overnight at 4 °C, then the modified particles were purified on PD–10 desalting columns, followed by overnight dialysis using 100 kDa molecular weight cut–off membranes against 10 mM sodium phosphate buffer pH 7.0. The yield of ^{Succinamate}CPMV conjugate (superscript proceeding the virus acronym refers to external modification), determined by UV–vis absorption at 260 nm, was between 80–90% based on the initial virus concentration. The particle integrity was established by native agarose gel electrophoresis, TEM, DLS and zeta potential measurements.

4.2.3 ^{Succinamate}CPMV quantification

The number of succinic anhydride moieties per particle was determined for ^{Succinamate}CPMV conjugate as follows. ^{Succinamate}CPMV suspended in 10 mM sodium phosphate buffer pH 7.0 was reacted with a 2000 molar excess of NHS ester–activated amine specific dye, DyLight594, in DMSO. The DMSO level was adjusted to 20% (v/v) and the reaction left to proceed at 4 °C overnight while gently stirring. The doubly functionalised particles were purified on a PD–10 column equilibrated with 10 mM sodium phosphate buffer pH 7.0, and eluted samples were concentrated on 100 kDa cut–off columns before being layered onto 5 ml 10%–50% sucrose gradients as described in section (2.17.1). The fractions containing the virus particles were collected and dialysed against 10 mM sodium phosphate buffer pH 7.0 for 2 days with changing buffer every 12 hours. After further concentration on 100 kDa cut–off columns,

fluorescence was examined by either UV–vis or on agarose electrophoresis gels, a lack of fluorescence indicating the complete modification of the virus by succinic anhydride.

4.2.4 Co–CPMV

^{Succinamate}CPMV pre–activated particles (3 mg ml^{-1}, 1 ml) suspended in 10 mM sodium phosphate buffer pH 7.4 were incubated with 20 mM cobalt(II) chloride at ambient temperature, while gently shaking at 50 rpm for 1–2 hours. Freshly prepared sodium borohydride (2mM) in Milli–Q water was added and the mixture incubated for another 10–30 minutes at ambient temperature. Particles were recovered by centrifugation at 14000 rpm (bench top, Eppendorf) for 20 minutes. The supernatant containing the Co–CPMV nanoparticles was further purified on PD–10 desalting columns. The eluted fractions were layered on sucrose gradients (as described in section 2.17.1) and the fractions containing mineralized particles were collected and dialysed against 10 mM sodium phosphate buffer pH 7.0 for 15 hours.

4.2.5 Iron oxide–CPMV

^{Succinamate}CPMV pre–activated particles (1–1.2 mg ml^{-1}, 2 ml) suspended in 10 mM sodium phosphate buffer pH 7.4 were incubated with 2 mM iron(II) chloride tetrahydrate and 4 mM iron(III) chloride hexahydrate at ambient temperature, while gently shaking at 50 rpm for 1–2 hours. The pH was raised slowly to 10.2 by dropwise addition of 1 mM sodium hydroxide and incubated for another hour at ambient temperature. As a control experiment, CPMVwt particles were incubated with the same concentration of iron salts for 1 hour prior to raising the pH to 10.2 for another hour and purified as described above for Co–CPMV. Sucrose gradient centrifugation was essential to remove all the impurities from the sample.

4.2.6 Mössbauer spectroscopy analysis

Samples were analysed by Professor Dave Evans and Mrs Elaine Barclay. Detailed experimental procedures are explained in section 2.13.

4.2.7 Vibrating sample magnetometry (VSM) of iron oxide–CPMV

The magnetic measurements were conducted as a collaborative project with Drs. Oscar Céspedes and Sarah Staniland, School of Physics and Astronomy, University of Leeds, United Kingdom. Detailed experimental procedures are presented in section 2.14.

4.2.8 Metal–CPMV functionalisation with thiolated oligosaccharide

Freshly prepared iron oxide–CPMV or Au–CPMV particles (1 mg ml^{-1}, 3 ml) suspended in 10 mM sodium phosphate buffer pH 7.0, were incubated with 0.5 mg of 1–thio–β–D–maltoheptaose. The reaction mixture was purified on a PD–10 column, dialysed against 10 mM sodium phosphate buffer pH 7.0 for 2 days and concentrated using 100 kDa molecular weight cut–off membranes. ^{Oligosaccharide}metal–CPMV particles were analysed by mass spectrometry.

4.2.9 Au–CPMV functionalisation with cysteamine

To Au–CPMV (1 mg ml^{-1}) suspended in 10 mM sodium phosphate buffer pH 7.4 was added an aqueous solution of cysteamine hydrochloride (1 mg). The reaction was left to proceed for ca. 12 hours at ambient temperature. ^{Cysteamine}CPMV particles were dialysed for 24 hours against 100 mM sodium phosphate, 0.15 M NaCl, buffer pH 7.4 using 100 kDa dialysis membranes. ^{Cysteamine}CPMV particles were incubated with amine–specific DyLight–594 NHS ester (65 µg) for 2 hours at ambient temperature while gently stirring. $^{DyLight–594–cysteamine}$Au–CPMV particles were purified on sucrose gradient as described above, and then dialysed for 24 hours against 10 mM sodium phosphate buffer pH 7.4.

4.2.10 MALDI–TOF mass spectrometry (MS)

MS analysis was performed on iron oxide–CPMV and Au–CPMV both addressed with thiolated oligosaccharide (1–thio–β–D–maltoheptaose). Particles were mixed in a 1:1 ratio with the matrix (2,4,6–trihydroxyacetophenone, 10 mg ml^{-1} in 70% aqueous acetonitrile) and 1 µl spotted onto a ground steel MALDI target plate (Bruker Daltonics, Bremen, Germany). After

drying, the sample was analysed on a Bruker Ultraflex TOF/TOF. The instrument was calibrated using Bruker standards (ca. 200 laser shots). Samples were analysed using a laser power of approx. 25% and spectra were summed from ca. 30 x 15 laser shots. Data were processed in FlexAnalysis (Bruker). MS analysis was conducted in collaboration with Dr. Abdul Rashid, John Innes Centre, UK.

4.2.11 CPMV–Poly(allylamine) hydrochloride (^{PA}CPMV)

Freshly prepared CPMV particles (1 mg ml^{-1}, 1 ml) were suspended in Milli–Q water and added dropwise over 5 minutes, with continuous stirring, to a freshly prepared PAH (1 mg ml^{-1}) solution in aqueous 0.25 M NaCl. The cationic polyelectrolyte was allowed to adsorb onto the virus capsid for 30 minutes while gently shaking at 4 °C. The polycation–coated CPMV particles (^{PA}CPMV) were washed 3–4 times with Milli–Q water (15 ml) on 100 kDa cut–off membranes, followed by dialysis against 10 mM sodium phosphate buffer pH 7.0 for 3 hours. ^{PA}CPMV was obtained in approximately 50% yield.

$^{FITC–PA}$CPMV was prepared by a similar method except that the incubation was for 15 minutes.

4.2.12 Gold hydroxide solution

Gold(III) chloride trihydrate (17.4 ml of 25 mM solution) was diluted with Milli–Q water (982.6 ml), and then potassium carbonate (249 mg, 1.8 mM) was added. The solution was aged for 1–2 days in the dark (foil wrapped) at 4 °C, during which it changed colour from yellow to colourless due to the formation of gold hydroxide (Graf & van Blaaderen, 2002; Kuo et al, 2008).

4.2.13 Gold coated CPMV nanoparticles (Au–CPMV)

Freshly prepared ^{PA}CPMV particles (1–1.5 mg ml^{-1}, 1ml) were incubated with gold hydroxide solution (1 ml) as prepared above. The reaction solution was left stirring at room temperature for 2 hours before adding a freshly prepared aqueous solution of hydroxylamine hydrochloride to a final concentration of 20 mM. The reaction was left to proceed for a further

20 minutes at ambient temperature. Au–CPMV particles were spun at 14000 rpm (bench top centrifuge) for 20 minutes to remove any large aggregates before being layered onto 5 ml 10%–50% sucrose gradients (as described in section 2.17.1). Sucrose fractions containing Au–CPMV particles (bluish colour) were collected and dialysed against 10 mM sodium phosphate buffer pH 7.0 for 15 hours using 100 kDa molecular weight cut–off membranes. The Au–CPMV particles were concentrated and the yield determined, by UV–vis absorption at 260 nm, to be approximately 50–60% based on starting concentration of ^{PA}CPMV.

4.2.14 Gold nanoparticle (AuNP) preparation

A modification of a published protocol was used (Hone et al, 2003). In brief, tetrachloroauric acid trihydrate ($HAuCl_4.3H_2O$) (12.5 mg, 0.032 mM) was dissolved in water (100 ml) and the solution heated to 60 °C. A second solution of trisodium citrate dihydrate (50 mg, 0.170 mM) in water (50 ml) was also heated to 60 °C. Both solutions were rapidly mixed and heated with stirring at 85 °C for 150 minutes. After cooling, the red wine–coloured solution was filtered through a syringe filter (0.22 μm) and stored at 4 °C. TEM and DLS confirmed a AuNP size of 10 – 18 nm.

4.2.15 ^{PA}CPMV and pre–formed AuNP (tessellated–spheres)

^{PA}CPMV particles (1 mg ml^{-1}, 400 μl) and a suspension of citrate–capped gold nanoparticles (400 μl, AuNP as prepared in 4.2.14) were reacted together with gentle stirring at ambient temperature for 10–15 minutes. The solution colour changed from red to light purple. UV–vis spectroscopy was used to monitor the formation of tessellated–spheres as confirmed by TEM.

For the characterisation methods used in this chapter (immunological detection, TEM, SEM, NTA, agarose gels, EDXS, and ZP) refer to chapter 2.

4.3 Results and Discussion

4.3.1 Charge promoted mineralization

The previous studies on CPMV mineralization as described in chapter 3, and those of others (Addadi & Weiner, 1985; Wierzbicki et al, 1994), suggested that the initiation of mineralization is related to the presence of negatively charged amino acids. CPMV can be considered as an anionic macromolecule at neutral pH with an isoelectric point (p*I*) of 4.3 ± 0.1 (Kewalramani et al, 2011). In order to create suitable conditions for templated surface mineralization, CPMV particles were covalently modified with succinic anhydride to increase the virus capsid surface negative charge. Succinic anhydride has a cyclic structure that is highly reactive toward nucleophiles (amines). Attack of a nucleophile at one of the carbonyl groups opens the anhydride ring, forming a covalent bond to the lysine amine–nitrogen and a free carboxylate group at the other end of the ring–opened molecule (Hermanson, 2008); Figure. 4.1. Coverage of at least 240 surface addressable lysines with succinamate was achieved. No amine–specific dye could be coupled to the virus capsid post–modification, as shown by the lack of dye absorbance in the UV–vis spectrum following rigorous purification (as described in section 2.17), confirming that no addressable lysine groups remain.

$^{\text{Succinamate}}$CPMV particle integrity was established by uranyl acetate–stained TEM images as shown in Figure 4.2–A. As expected, there was no significant difference in size or structure compared with CPMVwt. $^{\text{Succinamate}}$CPMV was found to be stable for at least two months in 10 mM sodium phosphate buffer pH 7.0. In addition, TEM shows no aggregation of $^{\text{Succinamate}}$CPMV particles on any of the samples prepared during this study.

$^{\text{Succinamate}}$CPMV particles in buffer were incubated with the appropriate reagents for mineralization. $^{\text{Succinamate}}$CPMV when incubated with cobalt chloride followed by reduction with sodium borohydride gave cobalt coated CPMV nanoparticles (Co–CPMV). Treatment under alkaline hydrolysis conditions that favour the formation of magnetite (Wu et al, 2009), Fe_3O_4, by incubation with a 2:1 mixture of iron(II) and iron(III) salts followed by raising the pH to approximately 10.2 for 1 hour, gave iron oxide coated CPMV particles (iron oxide–CPMV).

The unstained TEM images of the mineralized particles reveal monodisperse nanoparticles of *ca.* 32 nm. The appearance of the mineralized CPMV particles is similar to that which has been previously observed for templated mineralized–CPMV as discussed in chapter 3. For particles obtained by alternative methods see chapters 3, 4, and 5 (Aljabali et al, 2010b; Aljabali et al, 2011; Shah et al, 2009a; Steinmetz et al, 2009b).

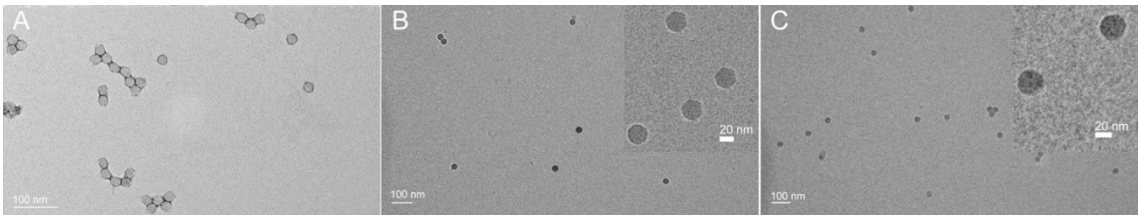

Figure 4.2– TEM images for (A) uranyl acetate stained ^{Succinamate}CPMV, (B) unstained Co–CPMV and (C) unstained iron oxide–CPMV particles from sucrose gradient. Inset shows higher magnification particles.

The presence of succinamate, and hence the extra surface negative charge, was essential for templated–mineralization. CPMVwt when incubated under identical conditions, with the same concentration of reagents, resulted in visible bulk precipitation and only non–specific mineralization; particles with a wide size distribution were obtained as shown by TEM in Figure 4.3.

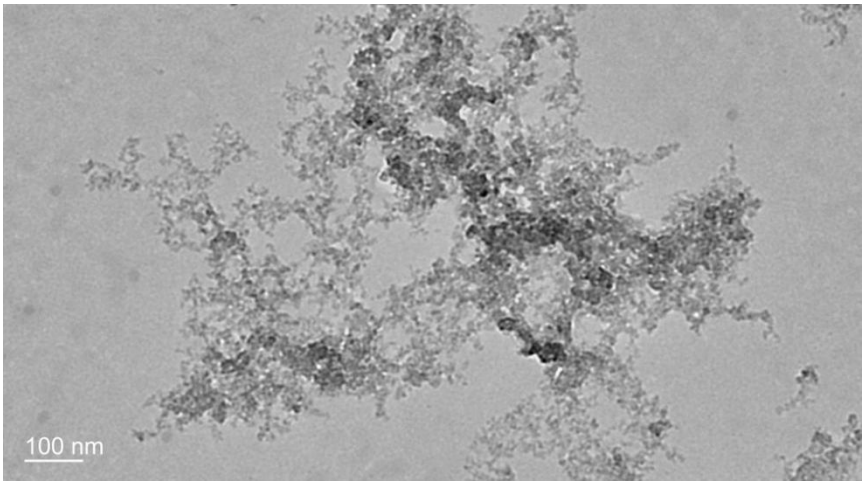

Figure 4.3– Unstained TEM of positive control of CPMVwt under identical mineralization conditions as those to form templated iron oxide–CPMV, only non–specific mineral formation of variable particle size was observed.

^{Succinamate}CPMV particles have a zeta potential almost two–and–a–half fold more negative than CPMVwt, consistent with successful surface modification and the consequent increase in surface negative charge; the data is summarised in Table 4.1. The ZP values for suspensions of mineralized Co–CPMV and iron oxide–CPMV are considerably more negative than that for CPMVwt, of *ca.* –12 mV, and for ^{Succinamate}CPMV of ca. –28 mV, indicating that the colloids have good stability and show no propensity to aggregate.

	Diameter (nm)	Polydispersity (%)	Zeta potential (mV)
CPMVwt	28.2 ± 0.4	13.0	–12.3 ± 1.40
^{Succinamate}CPMV	28.9 ± 0.3	16.5	–28.2 ± 2.34
Co–CPMV	31.2 ± 0.5	18.4	–41.2 ± 1.15
Iron oxide–CPMV	32.4 ± 0.5	20.9	–39.0 ± 2.4

Table 4.1– Dynamic light scattering and zeta potential measurements.

Native agarose gel electrophoresis as shown in Figure 4.4, visualised by ethidium bromide staining of encapsidated RNA or Coomassie blue staining of protein, also reflected the increased surface negative charge of ^{Succinamate}CPMV, as the particles migrate further in the gel than CPMVwt particles. Agarose gel electrophoresis of iron oxide–CPMV (Figure 4.4–A), stained with ethidium bromide, shows some weak fluorescent intensity associated with bands of different mobility to CPMVwt and ^{Succinamate}CPMV, suggesting limited porosity of the iron oxide surface to ethidium bromide, which intercalates with encapsidated RNA. However, Coomassie blue stained gels detect no colouration for the mineralized particles, consistent with the mineralized virus surface being inaccessible to this stain (Figure 4.4–B). Co–CPMV when run on an agarose gel (Figure 4.4) cannot be visualised by either ethidium bromide or Coomassie staining, implying that the cobalt forms an impervious shell on the virus surface.

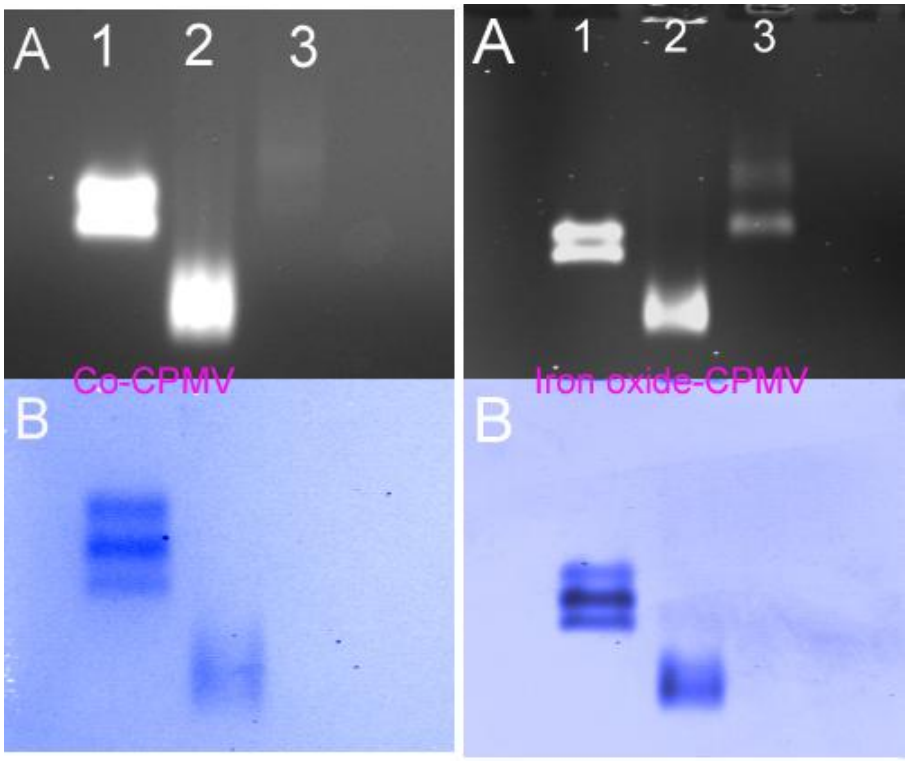

Figure 4.4– Agarose gel electrophoresis (1.2%) of intact CPMV particles visualised by (A) ethidium bromide staining, (B) coomassie staining. Lane 1, CPMVwt; 2, $^{\text{Succinamate}}$CPMV; 3, mineralized–CPMV.

Energy dispersive X–ray spectroscopy (EDXS, Figure 4.5) of Co–CPMV and iron oxide–CPMV confirmed the presence of cobalt, and iron and oxygen, respectively. There was no significant amount of oxygen in the EDXS of Co–CPMV, so there is no evidence of cobalt surface oxidation.

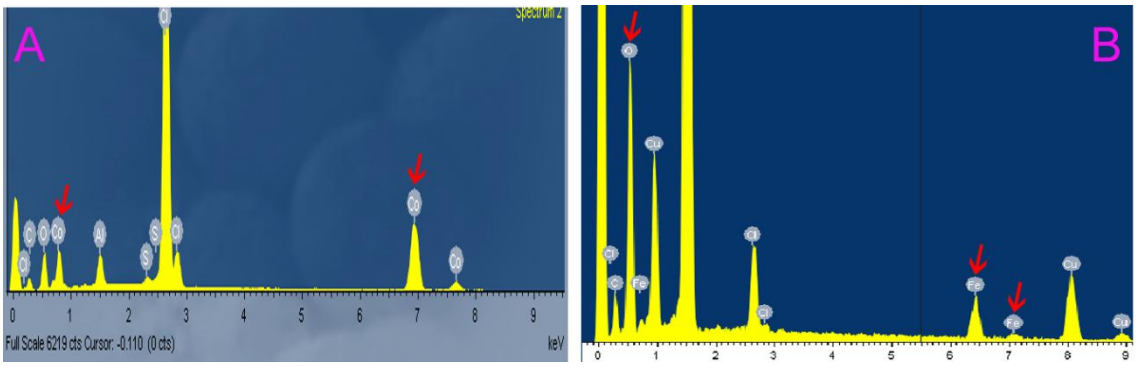

Figure 4.5– EDX spectrum of mineralized–CPMV particles. (A) Co–CPMV, cobalt peak indicated by red arrow, and (B) Iron oxide–CPMV, iron and oxygen peaks indicated by red arrows.

Immunological detection (dot blots) of the surface of both CPMVwt and ^{Succinamate}CPMV can be detected immunologically (Figure 4.6). However, both iron oxide–CPMV and cobalt–CPMV, when probed immunologically, could not be observed (Figure 4.6), consistent with the mineral surface–coating preventing access of the antibody. Co–CPMV particles were detected when stained with a cobalt specific dye, 1–nitroso–2–naphthol, whereas CPMVwt and ^{Succinamate}CPMV were not stained (Figure 4.6–B). Similarly, iron oxide–CPMV particles stained with Prussian blue (Figure 4.6–B) confirming the presence of iron (Aljabali et al, 2010c).

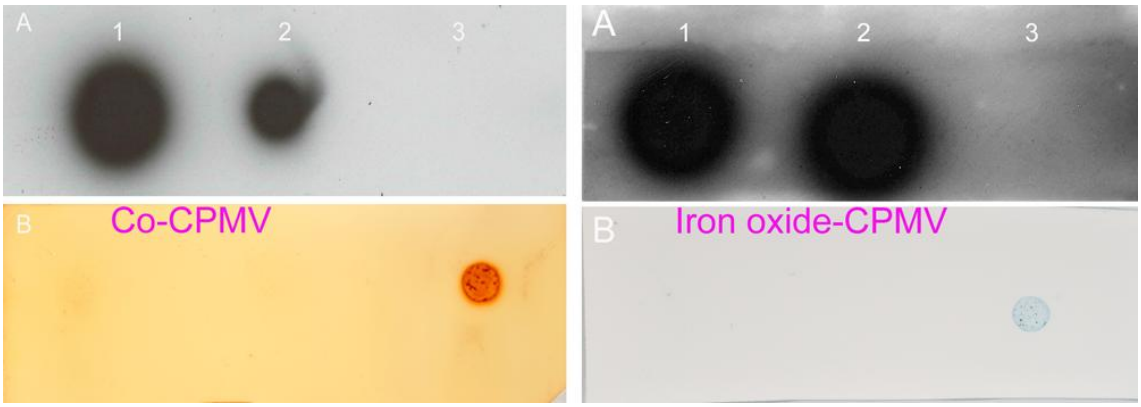

Figure 4.6– Intact particles spotted on a nitrocellulose membrane probed with (A) polyclonal antibodies raised against CPMV particles–dark spots show CPMV coat protein; (B) specific staining, 1–nitroso–2–naphthol to stain for cobalt and Prussian blue stain for iron. Column 1, CPMVwt; 2, ^{Succinamate}CPMV; 3, mineralized–CPMV.

Dynamic light scattering (DLS) and zeta potential measurements are collected in Table 4.1, Figure 4.7 and Figure 4.8. The average hydrodynamic diameter, from DLS, of the mineralized particles indicates a mineral coating of approximately 2 nm in each case, and the polydispersity shows that the particles are monodisperse. The particle size from DLS is in agreement with the observed TEM images.

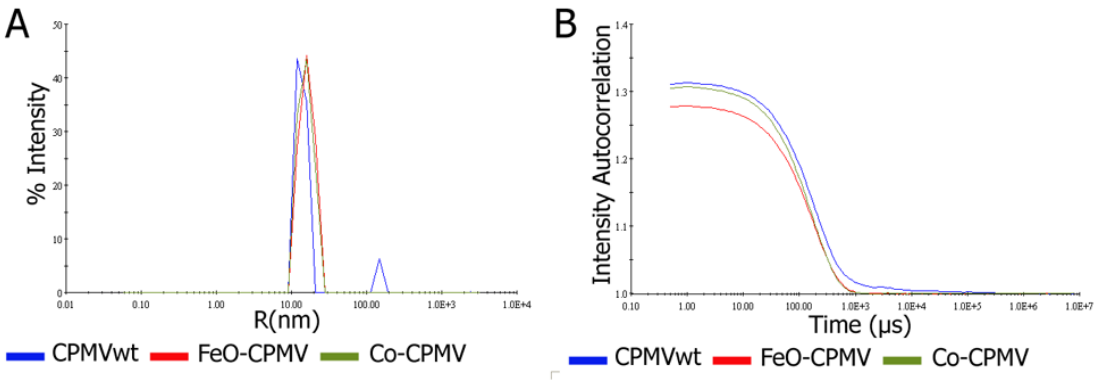

Figure 4.7– DLS and correlation plot for CPMVwt, Co–CPMV and iron oxide–CPMV particles.

The zeta potential for the mineralized particles suspended in buffer is considerably more negative than CPMVwt; by this criterion, the mineralized particles have good colloidal stability. ZP was a useful tool in monitoring the changes in the surface charge as a consequence of virus surface modification.

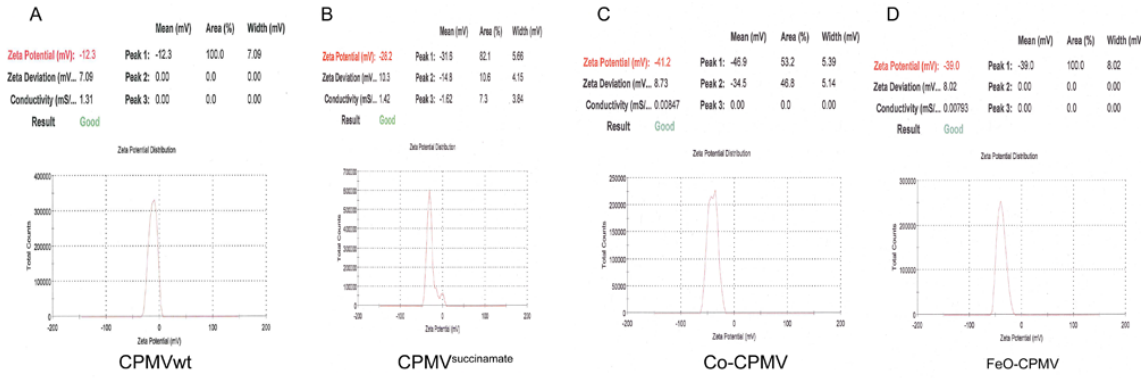

Figure 4.8– Zeta potential measurements of CPMVwt, $^{\text{Succinamate}}$CPMV, Co–CPMV and iron oxide–CPMV suspended in buffer at pH 7.2.

Although the conditions used for the formation of the iron oxide coating were chosen to favour mineralization with magnetite (Qu et al, 1999; Wu et al, 2009) as shown in equation 1, the presence of hematite (α–Fe_2O_3) or maghemite (γ–Fe_2O_3) cannot be discounted.

$$2FeCl_3 + FeCl_2 + 8NaOH \rightarrow Fe_3O_4 + 8NaCl + 4H_2O \ldots\ldots\ldots\ldots\ldots\ldots\ldots\ldots (1)$$

In an attempt to establish the form of iron oxide coating the surface of CPMV, Mössbauer spectra were recorded of samples of ^{57}Fe–enriched iron oxide–CPMV (Experiments were conducted by Prof. Dave Evans and Mrs Elaine Barclay). At 80 K, in frozen solution, a single quadrupole split doublet was observed with isomer shift (i.s.) of 0.49 mms^{-1} and quadrupole splitting (q.s.) of 0.64 mms^{-1}, Figure 4.9. These values are very similar to those recorded in the solid state (Figure 4.10) at 80 K, 0.48 and 0.61 mms^{-1}, respectively. At 298 K in the solid state, the i.s. was 0.37 mms^{-1}, as expected when changing the temperature by this amount, and the q.s., 0.61 mms^{-1}, was found to be invariant with temperature. The values of i.s.

and q.s. are fully consistent with the iron oxide being present on the surface of the virus as superparamagnetic magnetite nanoparticles; at room temperature i.s. values have been reported to range from 0.30 – 0.36 mms^{-1} and q.s. values from 0.60 – 0.65 mms^{-1} (Ambashta et al, 2005; Marques et al, 2008; Wang & Jiang, 2009). However, Mössbauer spectroscopy does not easily differentiate between magnetite and hematite nanoparticles, as the latter, when the particles are less than 10 nm in size, gave parameters in the range of i.s. 0.40 – 0.49 mms^{-1} and q.s. of 0.45 – 0.60 mms^{-1} (Camargo et al, 2004; Greenwood & Gibb, 1971).

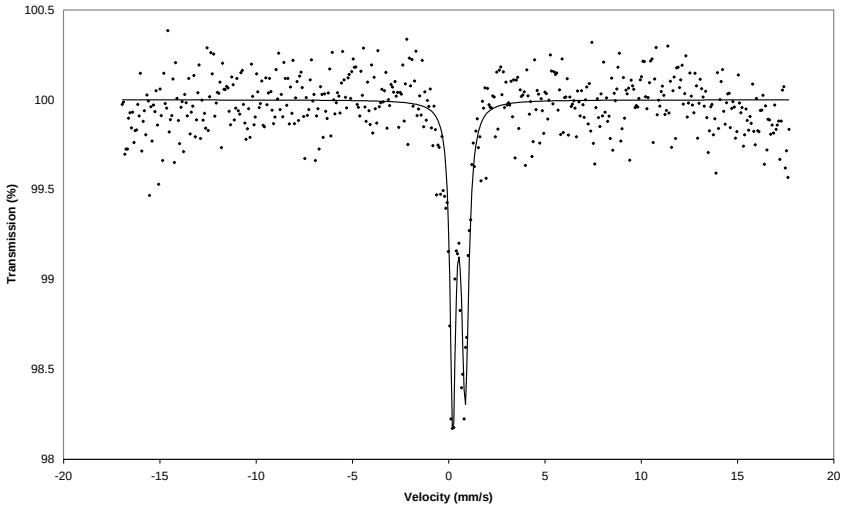

Figure 4.9– Frozen solution Mössbauer spectrum at 80 K of iron oxide–CPMV.

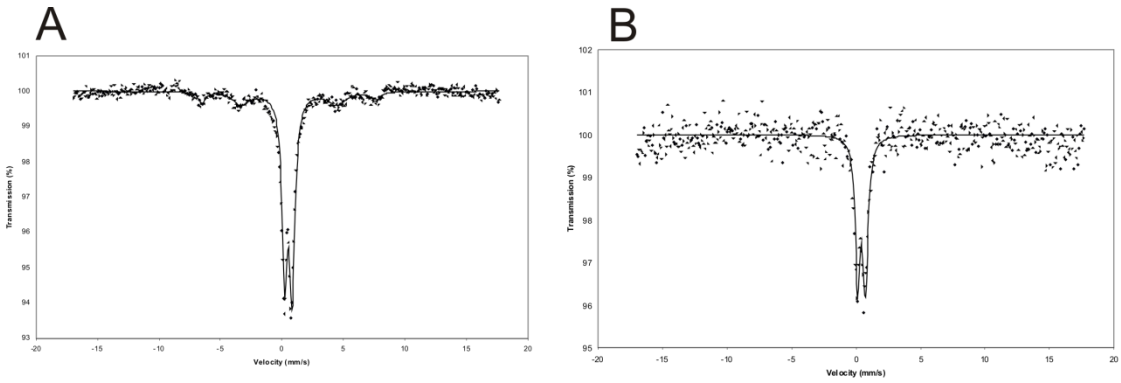

Figure 4.10– Mössbauer spectrum of iron oxide–CPMV in the solid state (A) At 80 K, there is a very small contribution from an underlying six–line spectrum. (B) At 298 K.

The single quadrupole split doublet for the superparamagnetic nanoparticles should be contrasted with the two, partially resolved, overlapping, hyperfine split, six–line spectra

observed for bulk magnetite Figure 4.11 and the single six–line spectrum observed for bulk hematite (Greenwood & Gibb, 1971).

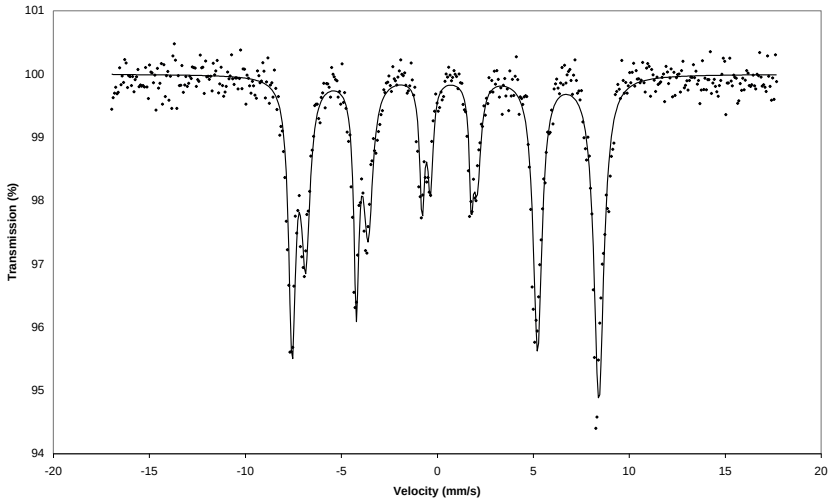

Figure 4.11– Mössbauer spectrum of bulk magnetite in the solid state at 80 K.

If the reaction time for the alkaline hydrolysis was too short a Mössbauer spectrum was obtained that showed two overlapping quadrupole split doublets (Figure 4.12). The minor doublet had parameters similar to those observed above for superparamagnetic magnetite nanoparticles and the major doublet had parameters (i.s. = 1.32 and q.s. = 3.09 mms^{-1}) that correspond to $Fe(OH)_2$ (Greenwood & Gibb, 1971); the alkaline hydrolysis and consequent formation of iron oxide was not complete.

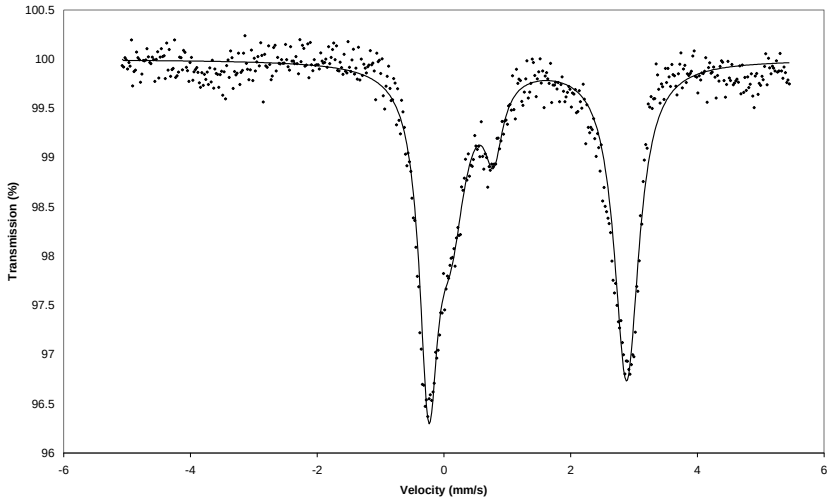

Figure 4.12– Frozen solution Mössbauer spectrum at 80 K of reaction intermediate. Major doublet corresponds to $Fe(OH)_2$ and minor doublet to nanoparticulate superparamagnetic iron oxide.

Vibrating sample magnetometry data, conducted by Dr Sarah Staniland and Dr Oscar Céspedes, of iron oxide–CPMV is also fully consistent with the particles exhibiting superparamagnetic behaviour with a blocking temperature (T_B) of around 60 K. The zero field cooled (ZFC) and field cooled (FC) magnetization curves (Figure 4.13) are typical magnetization curves for magnetic nanoparticles. Under FC conditions, there is no sharp change in the magnetization value from 380 K to 10 K. The ZFC curve shows a broad maximum at the temperature corresponding to T_B, below which there is a sharp decrease in magnetization. The Verway transition was not visible but this is normal for this size of particles. Variations of the magnetization of the sample as a function of applied field, hysteresis loops (Figure 4.13), are clearly superparamagnetic at temperatures above T_B and ferromagnetic below.

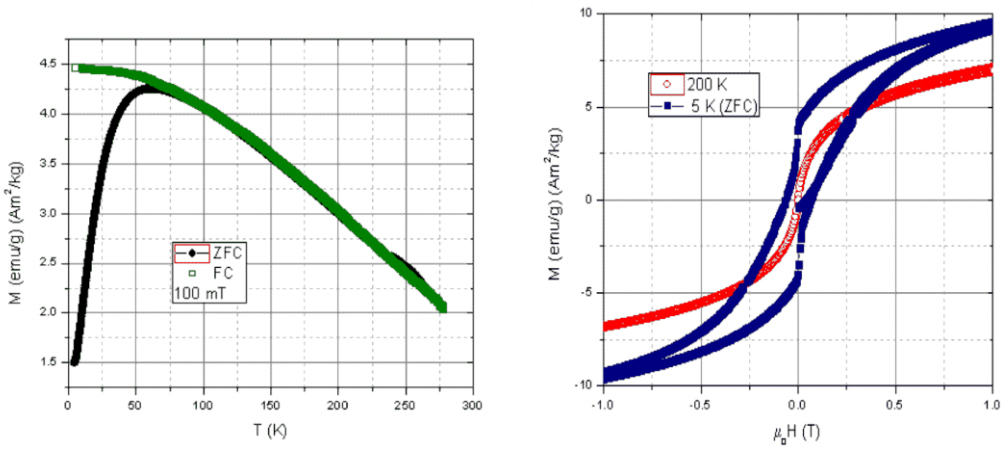

Figure 4.13– Zero field cooled (ZFC) and field cooled (FC) magnetization curves (left) and hysteresis loops (right) above (200 K) and below (5 K) the blocking temperature (60 K).

4.3.2 Iron oxide–CPMV functionalisation

Iron oxide–CPMV particles were functionalised with a thiolated oligosaccharide (1–thio–β–D–maltoheptaose), as proof–of–principle that the surface can be further modified, and characterized by mass spectrometry. After rigorous purification (as described in section 2.17) of the ^{Oligosaccharide}iron oxide–CPMV particles (as described in section 2.17), MALDI–TOF mass spectrometry (Figure 4.14) shows the presence of peaks with m/z of 1191.571 $[M+Na]^+$,

1207.551 $[M+K]^+$ and 2373.843 $[M_2+K]^+$, consistent with functionalisation of the iron oxide surface with the thiolated oligosaccharide. Although the thiolated oligosaccharide may bind directly to the iron within the iron oxide coating, it is also likely that the thiol group interacts with hydroxyl–groups generated on the surface by partial hydrolysis in aqueous media (Boyer et al, 2009a; Boyer et al, 2009b). The ease by which the surface iron oxide can be addressed with thiolated molecules demonstrates the potential for the modification of the nanoparticle surface with a range of chemical moieties.

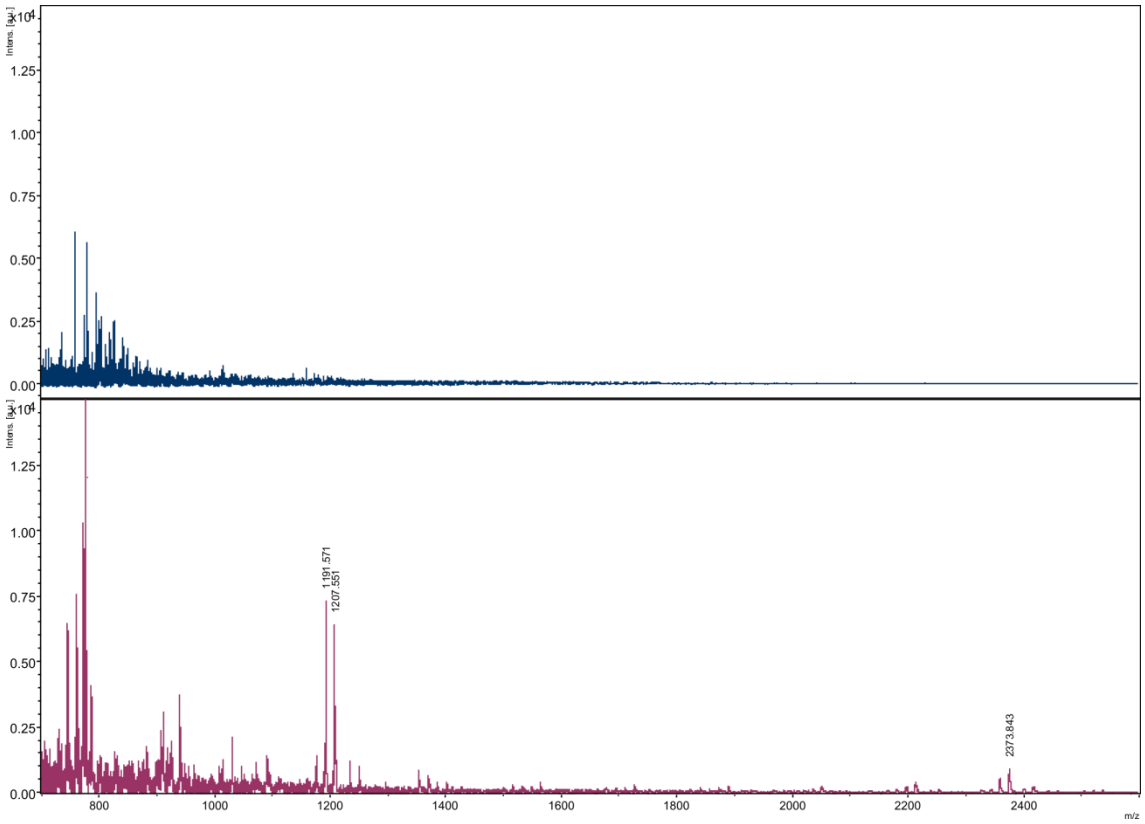

Figure 4.14– Mass spectrum of ^{Oligosaccharide}iron oxide–CPMV showing the corresponding peaks, $[M+Na]^+$= 1191.571, $[M+K]^+$ = 1207.551 and $[M_2+K]^+$= 2373.843. The upper panel is for iron oxide–CPMV and the lower panel is for ^{Oligosaccharide} iron oxide–CPMV.

4.4 CPMV–polyelectrolyte–templated gold nanoparticles

Gold nanoparticles have attracted significant interest because of their great potential in photothermal therapy, drug delivery and diagnostics (Ghosh et al, 2008), and for applications as plasmonic nanostructures for the optical sensing of biological and chemical analytes (Evans, 2008; Evans, 2009; Evans, 2010; Steinmetz & Evans, 2007). Access to a wide range of

derivatives and functional moieties adds to the versatility of gold nanoparticles for innumerable applications in the fields of biomedicine and nanotechnology.

The value of gold nanoparticles arises from a variety of desirable structural attributes. Additionally, the interaction of biological systems with gold nanoparticles has attracted considerable attention. For example, a living fungus can 'actively' assemble gold nanoparticles over its hyphae to give conducting microstructures (Sugunan et al, 2007). The bacterium *Escherichia coli* has been converted into a biocompatible bacteria–gold nanocomposite for photothermal anti–cancer therapy (Kuo et al, 2008) and Chilo iridescent virus (CIV) has been shown to be a useful core substrate for the fabrication of metallodielectric plasmonic nanostructures (Radloff et al, 2005a).

Genetically modified CPMV, with cysteine residues introduced onto its external surface, has been shown to bind to preformed nanogold (Blum et al, 2004; Wang et al, 2002a; Wang et al, 2002d). On the contrary, the approach presented in here is template synthesis of gold–coated CPMV particles.

Herein, a cationic polyelectrolyte, poly(allylamine) hydrochloride (PAH), was electrostatically adsorbed onto the external surface of the virus capsid. The polyelectrolyte (polymer whose repeating units bear an electrolyte group. These groups will dissociate in aqueous solutions, making the polymers charged) promotes the adsorption of anionic gold complexes, which were then easily reduced, under mild conditions, to form a metallic gold layer. The approach is depicted in Figure 4.15. The process is simple and environmentally friendly, as only aqueous solvent and ambient temperature and pressure are required. In addition, this route offers a way to produce Au–CPMV with a narrow size distribution. As expected, the gold surface can be further modified with thiol reagents. In contrast, reaction of polyelectrolyte–modified CPMV (^{PA}CPMV) with pre–formed gold nanoparticles resulted in the self–assembly of large, hexagonally packed, tessellated–spheres.

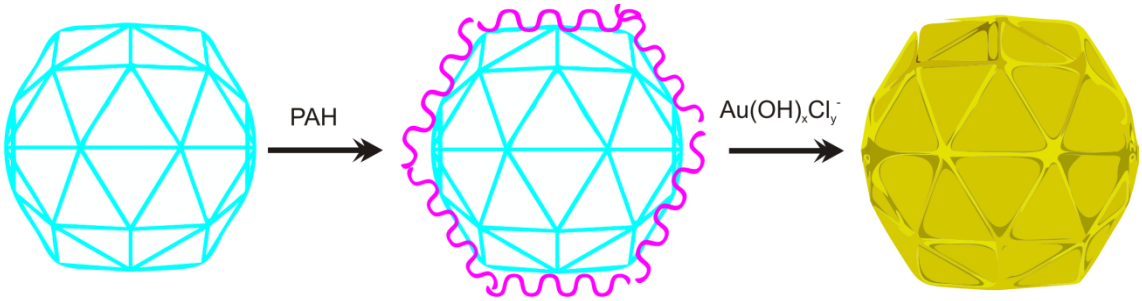

Figure 4.15– Schematic representation of the polyelectrolyte adsorption onto the CPMV capsid followed by the subsequent incubation with the gold solution to generate Au–CPMV.

4.4.1 Polyelectrolyte adsorption onto CPMV surface

As stated in section 4.3.1, CPMV can be considered as an anionic macromolecule at neutral pH with an isoelectric point (p*I*) of 4.3± 0.1 (Kewalramani et al, 2011). At physiological pH (pH 7.4), aspartic and glutamic acid residues situated on the virus capsid surface are deprotonated, so the surface presents an overall negative charge. Incubation of CPMV with PAH led to electrostatic adsorption of a thin layer of cationic polyelectrolyte onto the capsid surface as confirmed by zeta potential measurements. The negatively charged CPMVwt particles, in 10 mM sodium phosphate buffer pH 7.4, have a zeta potential of ca. –12.3 ± 1.76 mV (Aljabali et al, 2010b; Aljabali et al, 2011). After deposition of the polyelectrolyte, ^{PA}CPMV exhibits a zeta potential of +67.8 ± 2.35 mV; the sign of the potential is reversed, consistent with the surface charge changing from negative to positive.

Further confirmation of polyelectrolyte adsorption onto the surface of CPMV was obtained by the use of fluorescently labelled polyelectrolyte; fluorescein isothiocyanate–labelled poly(allylamine hydrochloride) (FITC–PAH). The UV–vis spectrum of $^{FITC–PA}$CPMV showed the presence of a new peak at 500 nm arising from the fluorescent label and confirming successful surface modification with $^{FITC–PAH}$CPMV (Figure 4.16).

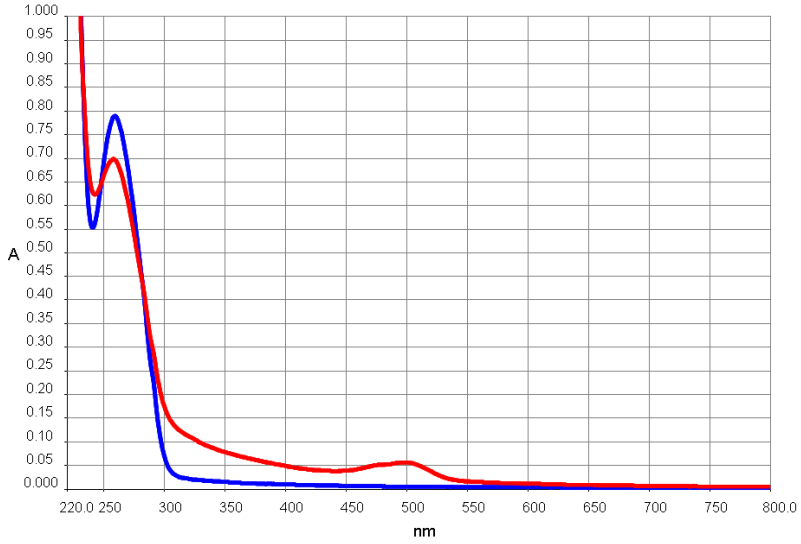

Figure 4.16– UV–vis absorption spectrum of CPMVwt (blue line) and $^{FITC–PA}$CPMV (red line).

Comparison of native agarose gel electrophoresis of CPMVwt, ^{PA}CPMV and $^{FITC–PA}$CPMV showed that: (a) both CPMVwt and ^{PA}CPMV were not visible without staining; (b) both ^{PA}CPMV and $^{FITC–PA}$CPMV resided in the sample well and did not migrate under the electric field conditions employed (Figure 4.17). The lack of migration from the well is probably a consequence of the presence of electrostatically bound polyelectrolyte on the virus surface and not of particle aggregation. DLS of ^{PA}CPMV (Figure 4.18) gave a hydrodynamic diameter of 32 nm for the polyelectrolyte–coated particles and a polydispersity value of 9.3% that confirmed narrow distribution and no aggregation.

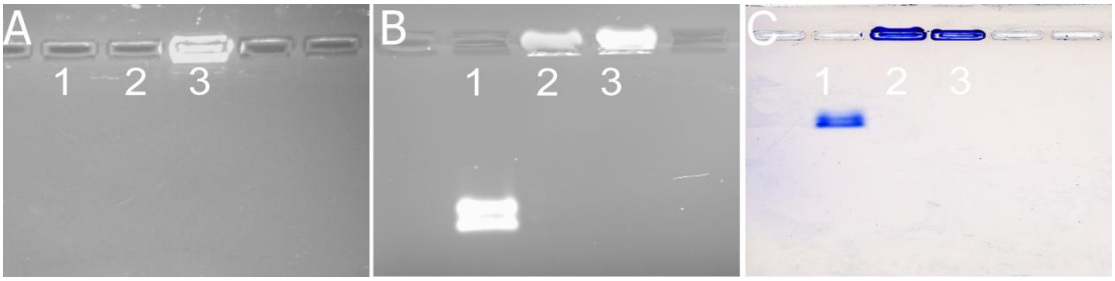

Figure 4.17– Agarose gel electrophoresis (1.2%). (A) unstained, (B) ethidium bromide stained and (C) coomassie blue stained. Lane 1, CPMVwt, Lane 2, ^{PA}CPMV and Lane 3, $^{FITC–PA}$CPMV.

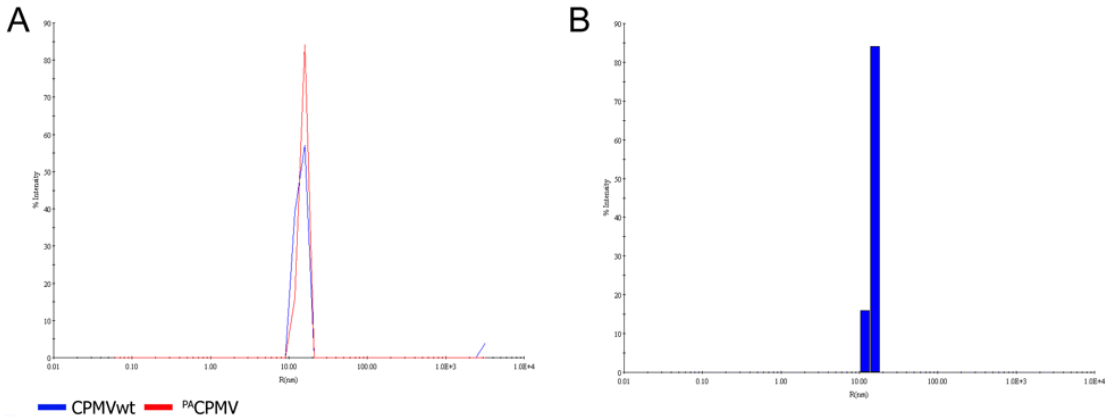

Figure 4.18– DLS of PACPMV showing narrow size range (hydrodynamic diameter 32 nm) and no aggregation (narrow size distribution in B).

PACPMV particle integrity was confirmed by negative staining TEM (Figure 4.19–A), the particles show a similar morphology to CPMVwt. No aggregation was observed in any of the TEM samples.

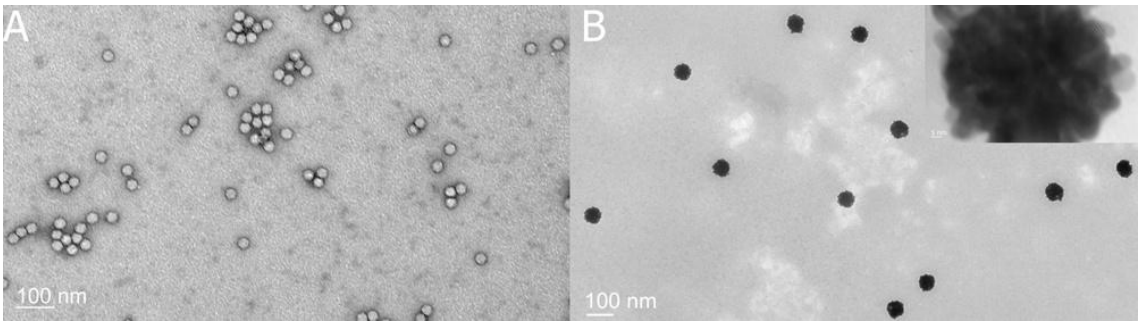

Figure 4.19– TEM images of (A) uranyl acetate stained PACPMV, (B) unstained Au–CPMV, inset is high magnification TEM image of unstained Au–CPMV.

4.4.1.1 Gold coated CPMV particles

An aqueous gold hydroxide solution was prepared by a published procedure (Graf & van Blaaderen, 2002; Kuo et al, 2008) from gold(III) chloride and potassium carbonate (Equation 2). Treatment of PACPMV with this solution for two hours, followed by hydroxylamine hydrochloride reduction for 20 minutes, and then rigorous purification (as described in section 2.17), produced gold coated CPMV nanoparticles as shown in Figure 4.19–B.

$$K_2CO_3 + 2H_2O \rightarrow H_2CO_3 + 2KOH$$

$$HCO_3^- + HAuCl_4 \rightarrow [AuCl_4]^- + H_2CO_3$$

$$[AuCl_4]^- + xOH^- \rightarrow Au(OH)_xCl_y^- \ (x + y = 4) + (4–y)Cl^- \ldots\ldots\ldots\ldots\ldots\ldots(2)$$

Initially, anionic gold(III) hydroxyl complex was electrostatically adsorbed onto the cationic surface of ^{PA}CPMV particles, and then this was reduced under mild conditions to give metallic gold at the surface. The reaction was accompanied by a colour change from colourless to light purple as seen in Figure 4.20–C and the UV–vis spectrum exhibited a surface plasmon resonance band at ca. 630 nm as seen in Figure 4.21. Additionally, both experiment controls (vial A and B in Figure 4.20) were investigated by TEM, unstained images shown in Figure 4.22 revealed a different morphology to that observed for the Au–CPMV particles (Figure 4.19-B).

Figure 4.20– Photographic images of gold coating reaction. (A) in the absence of ^{PA}CPMV, (B) in the presence of CPMVwt and (C) with ^{PA}CPMV forming Au–CPMV. Image was taken by Andrew Davis, Bio–imaging facilities at JIC.

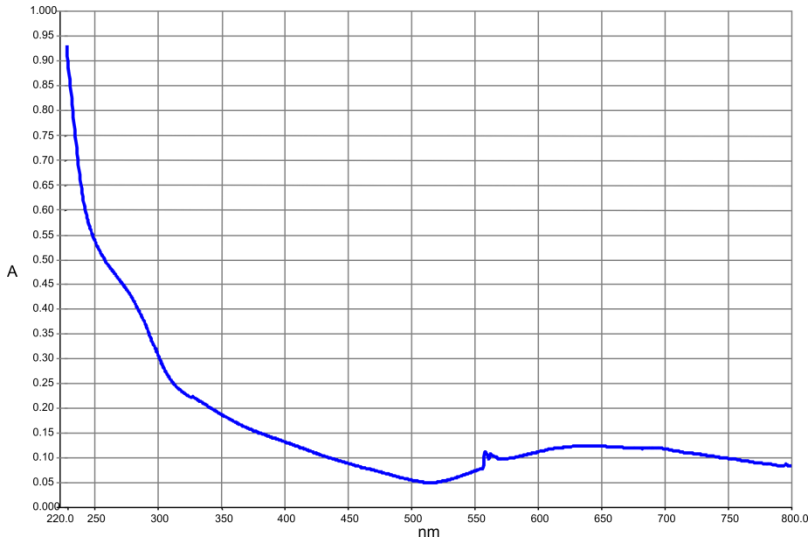

Figure 4.21– UV–vis absorption spectrum of Au–CPMV showing plasmon resonance peak at ca. 630 nm for 67 nm diameter Au–CPMV.

Unstained TEM images of Au–CPMV particles (Figure 4.19–B) confirmed that gold had been deposited on the surface and agreed with the DLS measurements. Unstained ^{PA}CPMV was not visible by TEM. The gold coating on the virus capsid was rough with an irregular surface (Figure 4.19–inset) and the mineralization of the surface probably occurred by an Ostwald ripening process (McNaught & Wilkinson, 1997). The structural appearance of the Au–CPMV particles is reminiscent of the morphological forms obtained when gold is electrolessly deposited onto the surface of gold nanoparticle seeded Chilo iridescent virus (Radloff et al, 2005a). Control experiments, keeping all other reaction conditions the same, where either ^{PA}CPMV was omitted (no virus) or CPMVwt was used, resulted in the immediate formation of a black precipitate of gold aggregates with a wide size distribution and irregular shapes as shown by TEM in (Figure 4.22).

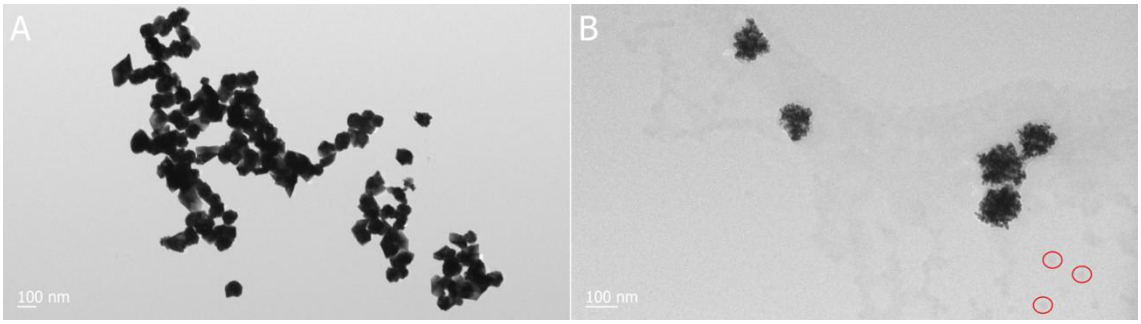

Figure 4.22– Unstained TEM images of products from (A) all reagents for Au–CPMV synthesis except ^{PA}CPMV (i.e. no virus) and (B) all reagents for Au–CPMV synthesis except that ^{PA}CPMV was substituted by CPMVwt. In both cases, large aggregates and irregular shaped particles were observed. In (B) a different morphology to templated Au–CPMV was observed, as the aggregates are comprised of multiple small gold nanoparticles; examples of unmineralized CPMV are shown in the red circles.

Au–CPMV particles suspended in buffer have a zeta potential of –46.9 ± 1.39 mV, of opposite sign to cationic ^{PA}CPMV and significantly more negative than CPMVwt. The higher negative values for the mineralized particles may be a consequence of the presence of phosphate in the buffer passivating the metal surface and generating a greater apparent negative charge under the conditions of measurement. Zeta potential is also an indication that the colloids have good stability and no propensity to aggregate in buffer solution.

The Au–CPMV particle size in buffer, as measured by DLS (Figure 4.23), shows an average hydrodynamic diameter of *ca.* 67 nm suggesting that the gold coating has a thickness of approximately 20 nm. The DLS polydispersity indicates that the particles are narrowly dispersed, in agreement with the observed TEM images, and that the coated CPMV particles are mineralized on their outer surfaces. The thickness of the gold coating can be controlled. Treatment of ^{PA}CPMV under the standard conditions as described in the experimental section (4.2.12) gave a particle size of *ca.* 67±5 nm. Keeping all other conditions the same but reducing the volume of the gold solution aliquot by half gave particles of *ca.* 40 nm diameter, whereas doubling the gold solution aliquot gave much larger particles of *ca.* 300 nm diameter.

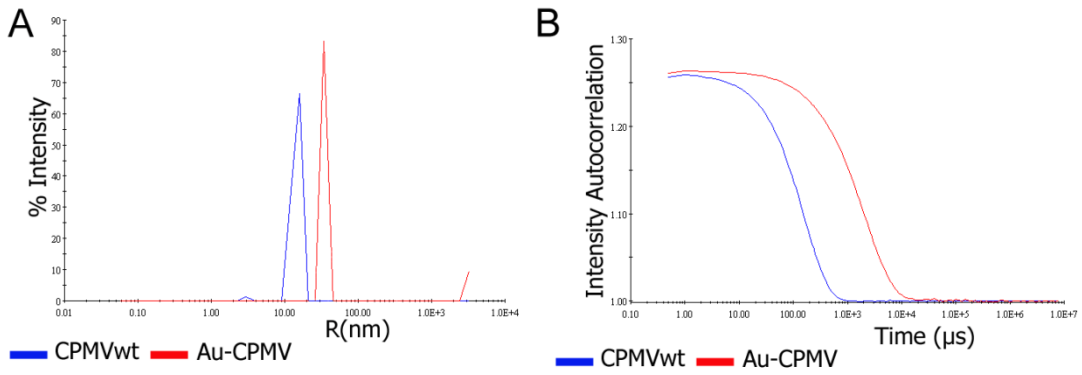

Figure 4.23– Dynamic light scattering (DLS) comparing CPMVwt and Au–CPMV. (A) hydrodynamic radius and (B) correlation plot.

Energy dispersive X–ray spectroscopy (EDXS) and DLS confirmed the presence of gold on the external surface of Au–CPMV as shown in Figure 4.24. In addition, nanoparticle–tracking analysis, based on laser light scattering microscopy, was also consistent with gold deposition (Figure 4.25). There was a significant increase in the relative refractive index of Au–CPMV compared to CPMVwt and ^{PA}CPMV. This analysis is also consistent with the mineralized particles being monodisperse as indicated by the particle size distribution; although there was a little non–specific aggregation under the measurement conditions employed.

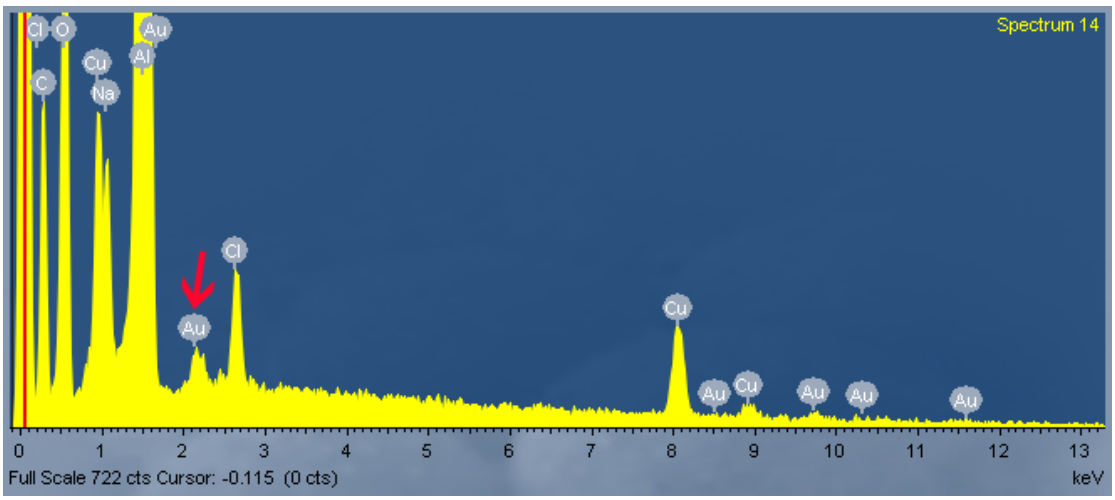

Figure 4.24– Energy dispersive X–ray spectroscopy of Au–CPMV particles. The arrow indicates the major gold peak.

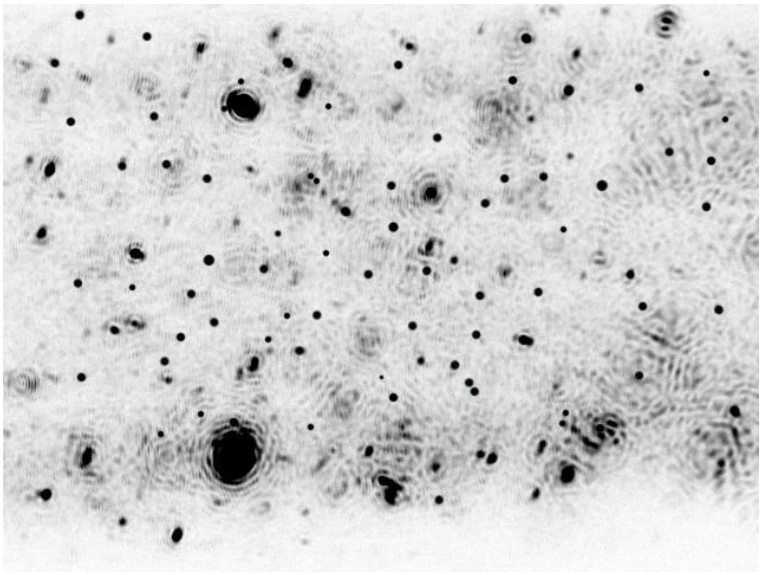

Figure 4.25– Negative image of a freeze–frame from nanoparticle tracking analysis of Au–CPMV nanoparticles. The particles appear individually as point scatterers under Brownian motion with a high refractive index.

Further, the CPMV coat protein of Au–CPMV was not detected immunologically (Figure 4.26). CPMVwt, ^{PA}CPMV and Au–CPMV were spotted onto a nitrocellulose membrane, which, after blocking, was probed with polyclonal antibodies raised in rabbits against CPMV particles. In the case of CPMVwt and ^{PA}CPMV a signal was obtained, confirming the presence of CPMV coat protein; for the Au–CPMV particles the coat protein was not accessible to the antibody presumably due to the metal coating.

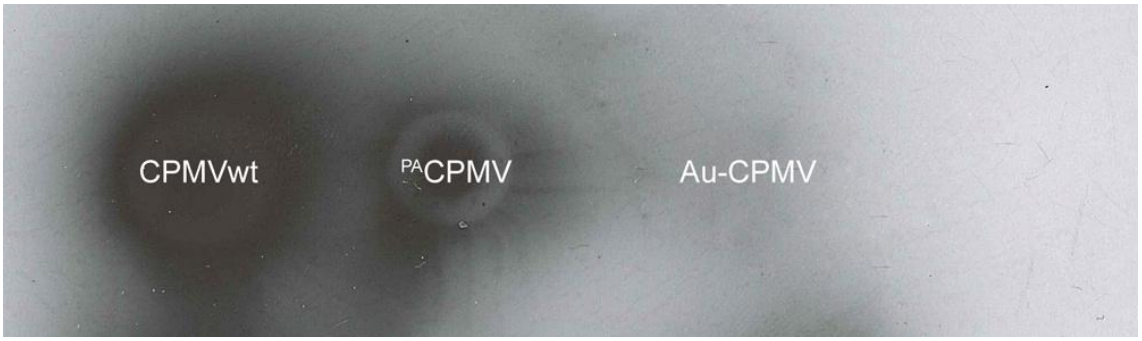

Figure 4.26– Immunological detection of coat protein for CPMVwt, ^{PA}CPMV and Au–CPMV intact particles. In the latter case, coat protein is inaccessible due to the gold coating.

4.4.1.2 Au–CPMV functionalisation

Au–CPMV particles were functionalised with a thiolated–oligosaccharide (1–thio–β–D–maltoheptaose), as proof–of–principle that the surface can be further modified and characterised by mass spectrometry. After rigorous purification of the ^{Oligosaccharide}Au–CPMV particles, MALDI–TOF mass spectrometry (Figure 4.27) showed the presence of peaks with m/z of 1191.453 $[M+Na]^+$, 1207.430 $[M+K]^+$ and 2373.803 $[M_2+K]^+$, consistent with functionalisation of the gold surface with the thiolated–oligosaccharide. In addition, Au–CPMV particles can be functionalised with cysteamine. The thiol group of the cysteamine binds to the gold surface; the amine group of the conjugated–cysteamine can then be reacted with an amine–specific fluorescent dye confirming that the gold surface has been modified (Figure 4.28). The ease by which the surface gold can be addressed with thiolated molecules demonstrates the potential for the modification of the nanoparticle surface with a range of chemical moieties. Such modified particles have the potential for development in applications such as photothermal therapeutics and in biosensory devices.

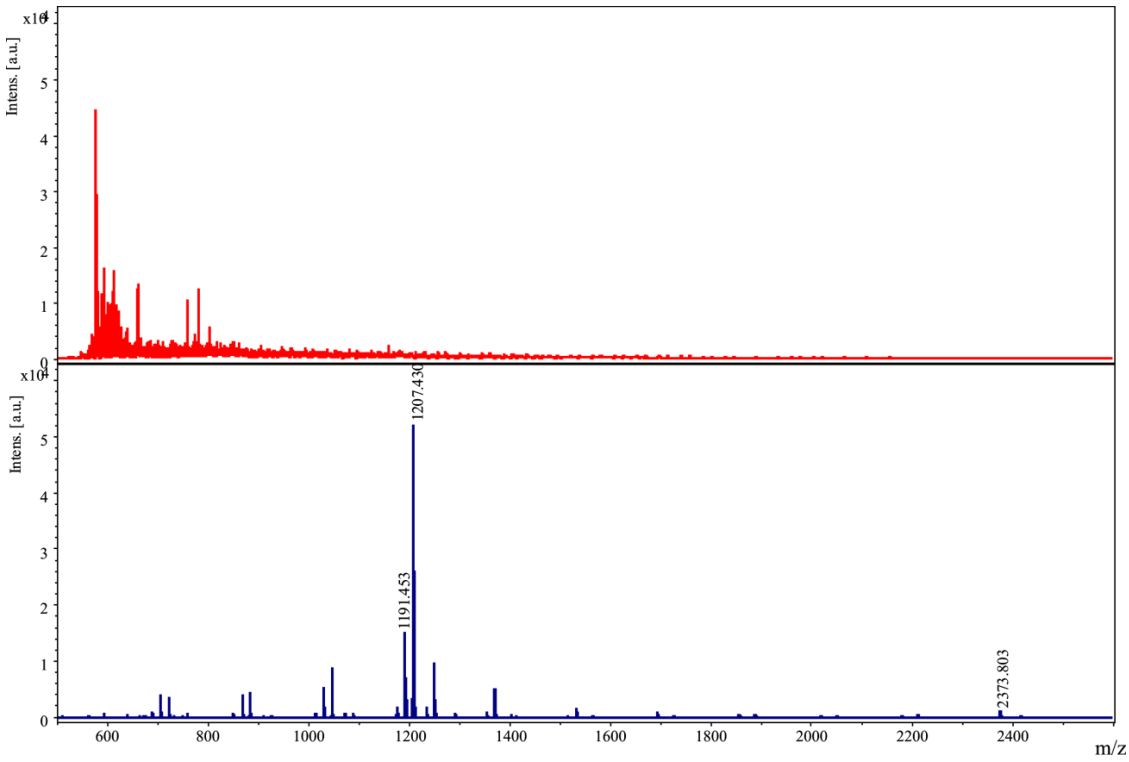

Figure 4.27– Mass spectrum of (top) negative control, i.e. Au–CPMV, and (bottom) ^{Oligosaccharide}Au–CPMV showing peaks 1191.453 $[M+Na]^+$, 1207.430 $[M+K]^+$ and 2373.803$[M_2+K]^+$.

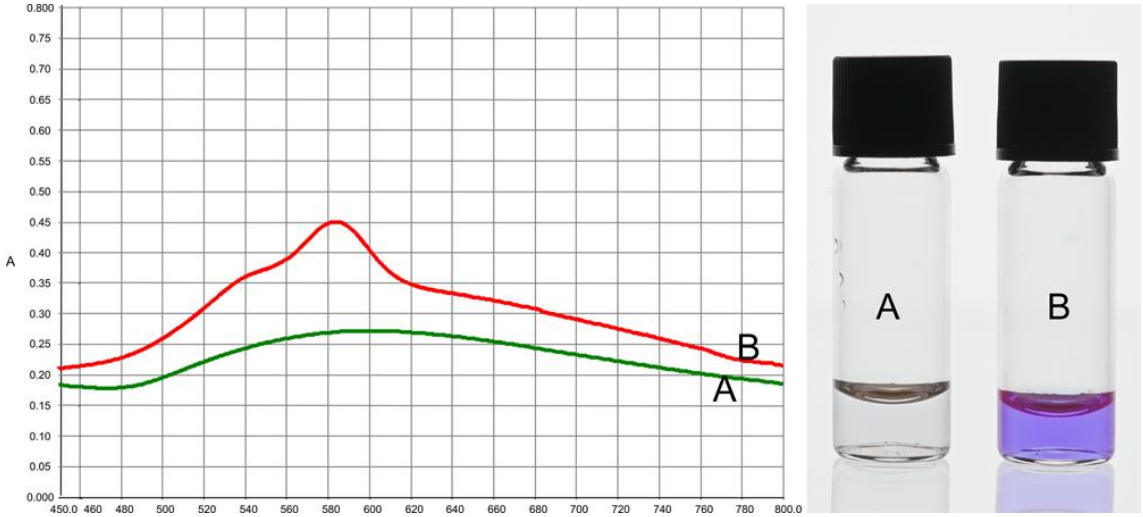

Figure 4.28– UV–vis absorption spectrum of Au–CPMV (A) and ^{Cysteamine}CPMV after reaction with amine–specific dye, $^{DyLight-594-Cysteamine}$Au–CPMV, (B). Right panel shows the corresponding photographic image confirming functionalisation of the gold surface with DyLight–594.

4.4.1.3 ^{PA}CPMV and pre–formed AuNP

In order to establish whether pre–formed gold nanoparticles could interact with ^{PA}CPMV, the polyelectrolyte–modified virus was incubated with citrate–capped gold nanoparticles (AuNP). The UV–vis spectrum presented in Figure 4.29 indicates that the interparticle distances in the tessellated–sphere are obviously less than the average particle diameter. This was further confirmed by the stained TEM images showed that large, hexagonally packed, tessellated–spheres had assembled that incorporated both virus and gold nanoparticles (Figure 4.30–B & C). These remarkable, spherical structures had diameters of up to several hundred nanometres. On mixing ^{PA}CPMV with AuNP there was an immediate colour change from red to pale purple as shown in Figure 4.30–A. The colour of the solution of such aggregates depends on the nanoparticle spacing and on the size of gold nanoparticles. Nanoparticle aggregates of gold with interparticle distances substantially greater than the average particle diameter appear red with λ_{max} ~ 520 nm, but as the interparticle distance in the aggregates decrease to less than approximately the average particle diameter, the colour becomes blue (Hainfeld & Powell, 2000; Nam et al, 2002). The 3–dimensional spherical shape was confirmed by scanning electron microscopy of sputter–coated particles (Figure 4.31).

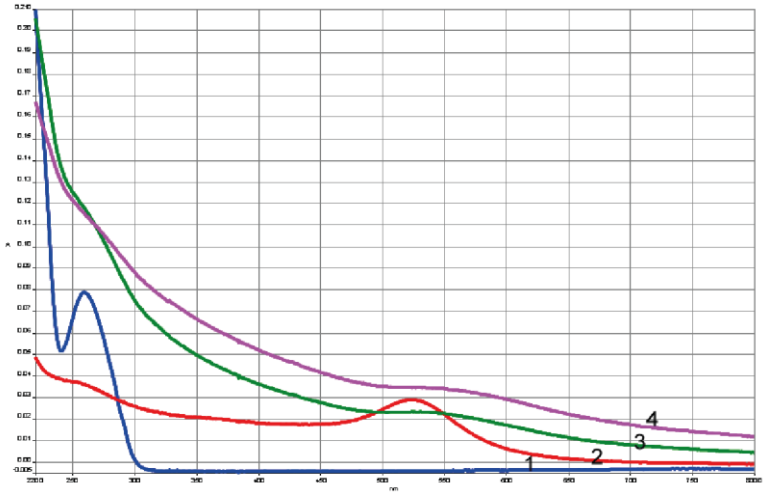

Figure 4.29– UV–visible spectrum of the tessellated–spheres. Spectrum (1) CPMVwt (2) gold nanoparticles with absorbance max at 520 nm, (3) the incubation of ^{PA}CPMV with AuNP after 2 minutes and (4) after 24 hours incubation.

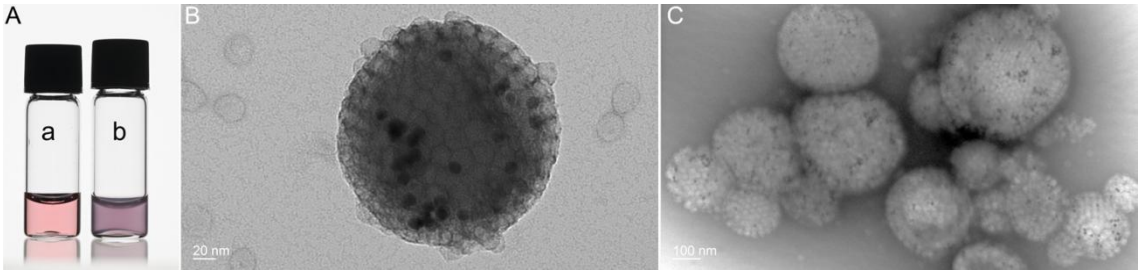

Figure 4.30– Tessellated–spheres formation. (A) photographic image of (a) AuNP and (b) ^{PA}CPMV mixed with AuNP. The colour change was immediate and corresponds to the self–assembly of tessellated–spheres. (B) Stained TEM image of a single tessellated–sphere showing the CPMV particles as hexagonally–packed mosaic pieces in a spherical arrangement together with gold nanoparticles and (C) tessellated–spheres of a range of sizes. The black spheres within the tessellated–sphere are gold nanoparticles.

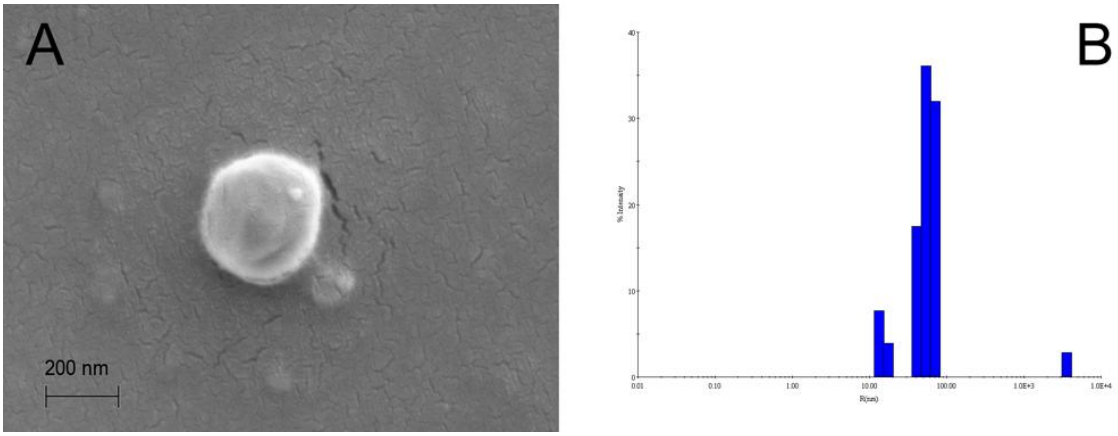

Figure 4.31– Scanning electron microscope and DLS analysis of the tessellated–spheres. (A) single sputter–coated tessellated–sphere on a mica surface and (B) DLS analysis of tessellated–spheres showing 5% of the sample is the size of CPMVwt and the tessellated–spheres have an hydrodynamic radius of 115–120 nm.

The colour of the tessellated–spheres–containing solution in this case indicates that the interparticle distances in the tessellated–sphere are obviously less than the average particle diameter, which is also evident from the TEM studies. However, control experiments (Figure 4.32) showed that it was essential for both pre–formed ^{PA}CPMV and AuNP to be present for self–assembly. Reaction of either: (a) citrate with ^{PA}CPMV; (b) CPMVwt with both citrate and AuNP; or (c) PAH, citrate, CPMVwt and AuNP, resulted in no colour change and only gave, in each case, normal looking, non–self–assembled, virus particles as shown by TEM. Others have shown that CPMV (Li et al, 2008) and turnip yellow mosaic virus (Li et al, 2009) can be used to synthesise bio–colloidal composites based upon non–covalent interactions of the icosahedral plant viruses with poly(4–vinylpyridine). However, in these systems, in contrast to that reported here, the virus particles assemble on the surface of poly(4–vinylpyridine) polymer balls with hexagon–like packing to form "raspberry–like" structures. Recently, the electrostatic self–assembly of virus–polymer complexes of Cowpea chlorotic mottle virus and cationic amine functionalised linear polymers, dendrons and dendrimers has been described, and the effect of polymer size and ionic strength has been reported (Kostiainen et al, 2011). Hexagonal packing was observed within the virus–polymer structures but the structures were less symmetrical than those we observed. The mechanism of formation also must be different, as for ^{PA}CPMV to form self–assembled structures; it was a requirement that AuNP were present.

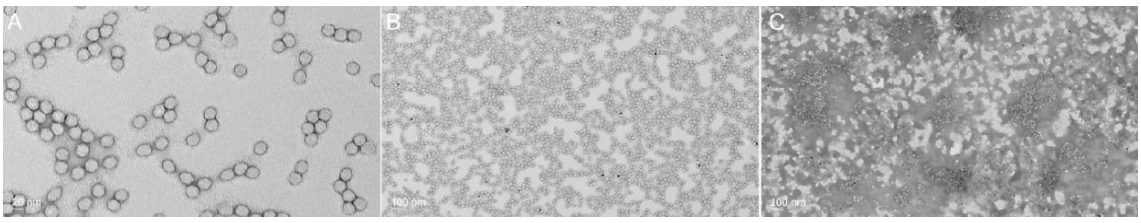

Figure 4.32– Uranyl acetate stained TEM images for ^{PA}CPMV/AuNP control experiments. (A) citrate with ^{PA}CPMV (no AuNP), (B) CPMVwt with both citrate and AuNP, (C) PAH, citrate, CPMVwt and AuNP.

4.4.2 Conclusion

It has been shown that by increasing the surface negative charge of CPMV by chemical modification of lysines with succinamate was sufficient to promote surface mineralization under mild conditions. The CPMV–templated cobalt and iron oxide nanoparticles that were produced are monodisperse with a diameter of ca. 32 nm. Further, the iron oxide–CPMV surface can be readily modified by reaction with thiol–containing molecules. The magnetic properties for iron oxide–CPMV particles were established.

A new approach has been described for the CPMV–templated synthesis of monodisperse gold nanoparticles. Cationic polyelectrolyte, poly(allylamine) hydrochloride, was electrostatically bound to the external surface of the virus capsid. The CPMV–polyelectrolyte conjugate, ^{PA}CPMV, has an increased surface positive charge compared to wild–type and readily attracts anionic gold complexes to the surface. Gold(III) ions were then easily reduced, under mild conditions, to form a metallic gold layer on the external surface of the virus capsid. By varying reaction conditions there was some control over the thickness of the gold coating. Au–CPMV particles might be developed in the future for possible photothermal cancer treatment. The gold surface can be further modified with thiol reagents; here a thiolated–oligosaccharide or cysteamine was used. In contrast, reaction of ^{PA}CPMV with pre–formed gold nanoparticles of 10–18 nm diameter resulted in the self–assembly of beautiful, large, hexagonally packed, tessellated–spheres. The tessellated–spheres are yet to be explored for possible future applications.

4.5 References

Addadi L, Weiner S (1985a) Interactions between Acidic Proteins and Crystals– Stereochemical Requirements in Biomineralization. *P Natl Acad Sci USA* **82:** 4110–4114

Aljabali AAA, Barclay JE, Butt JN, Lomonossoff GP, Evans DJ (2010a) Redox–active ferrocene–modified Cowpea mosaic virus nanoparticles. *Dalton Transactions* **39:** 7569–7574

Aljabali AAA, Barclay JE, Lomonossoff GP, Evans DJ (2010b) Virus templated metallic nanoparticles. *Nanoscale*, **2**, 2596-2600

Aljabali AAA, Sainsbury F, Lomonossoff GP, Evans DJ (2010c) Cowpea Mosaic Virus Unmodified Empty Viruslike Particles Loaded with Metal and Metal Oxide. *Small* **6:** 818–821

Aljabali AAA, Shah SN, Evans–Gowing R, Lomonossoff GP, Evans DJ (2011) Chemically–coupled–peptide–promoted virus nanoparticle templated mineralization. *Integrative Biology* **3:** 119–125

Ambashta RD, Mohammad YS, Mukadam MD, Singh S, Kishan Wattal P, Bahadur D (2005) Physical and chemical properties of nanoscale magnetite–based solvent extractant. *J Magn Magn Mater* **293:** 8–14

Blum AS, Soto CM, Wilson CD, Cole JD, Kim M, Gnade B, Chatterji A, Ochoa WF, Lin TW, Johnson JE, Ratna BR (2004) Cowpea mosaic virus as a scaffold for 3–D patterning of gold nanoparticles. *Nano Letters* **4:** 867–870

Camargo PHC, Nunes GG, Evans DJ, Leigh GJ, Tremiliosi–Filho G, Sá EL, Zarbin AJG, Soares JF (2004) Single–source precursor and homometal approaches to the sol–gel synthesis of iron and titanium oxides. In *Surface and Colloid Science*, Galembeck F (ed), Vol. 128, pp 221–226. Springer Berlin / Heidelberg

Evans DJ (2009) Exploitation of plant and archaeal viruses in bionanotechnology. *Biochem Soc Trans* **37:** 665–670

Flynn CE, Lee S, Peelle BR, Belcher AM (2003) Viruses as vehicles for growth, organization and assembly of materials. *Acta Materialia* **51:** 5867–5880

Ghosh P, Han G, De M, Kim CK, Rotello VM (2008) Gold nanoparticles in delivery applications. *Advanced Drug Delivery Reviews* **60:** 1307–1315

Graf C, van Blaaderen A (2002) Metallodielectric colloidal core–shell particles for photonic applications. *Langmuir* **18:** 524–534

Greenwood NN, Gibb TC. (1971) Mössbauer Spectroscopy Chapman and Hall Ltd, London.

Hainfeld JF, Powell RD (2000) New frontiers in gold labeling. *J Histochem Cytochem* **48:** 471–480

Han YJ, Aizenberg J (2003) Effect of Magnesium Ions on Oriented Growth of Calcite on Carboxylic Acid Functionalized Self–Assembled Monolayer. *Journal of the American Chemical Society* **125:** 4032–4033

Hermanson TG (2008) *Bioconjugate Techniques*, second edn. London: Academic Press.

Hone DC, Haines AH, Russell DA (2003) Rapid, quantitative colorimetric detection of a lectin using mannose–stabilized gold nanoparticles. *Langmuir* **19:** 7141–7144

Kewalramani S, Wang S, Lin Y, Nguyen HG, Wang Q, Fukuto M, Yang L (2011) Systematic approach to electrostatically induced 2D crystallization of nanoparticles at liquid interfaces. *Soft Matter* **7:** 939–945

Kostiainen MA, Hiekkataipale P, de la Torre JA, Nolte RJM, Cornelissen JJLM (2011) Electrostatic self–assembly of virus–polymer complexes. *Journal of Materials Chemistry* **21:** 2112–2117

Kuo WS, Wu CM, Yang ZS, Chen SY, Chen CY, Huang CC, Li WM, Sun CK, Yeh CS (2008) Biocompatible bacteria@Au composites for application in the photothermal destruction of cancer cells. *Chem Commun (Camb)***:** 4430–4432

Li T, Niu Z, Emrick T, Russell TP, Wang Q (2008) Core/Shell Biocomposites from the Hierarchical Assembly of Bionanoparticles and Polymer. *Small* **4:** 1624–1629

Li T, Ye B, Niu Z, Thompson P, Seifert S, Lee B, Wang Q (2009) Closed–Packed Colloidal Assemblies from Icosahedral Plant Virus and Polymer. *Chemistry of Materials* **21:** 1046–1050

Lomonossoff GP, Hamilton WDO (1999) Cowpea mosaic virus–based vaccines. *Curr Top Microbiol* **240:** 177–189

Manchester M, Steinmetz NF. (2009) Viruses and nanotechnology. *Current Topics in Microbiology and Immunology,*. Springer Berlin Heidelberg, Berlin, Heidelberg.

Mann S (2001) Biomineralization: Principals and Concepts in Bioinorganic Materials Chemistry, Vol. 3: Oxford University Press.

Marques RFC, Garcia C, Lecante P, Ribeiro SJL, Noé L, Silva NJO, Amaral VS, Millán A, Verelst M (2008) Electro–precipitation of Fe3O4 nanoparticles in ethanol. *J Magn Magn Mater* **320:** 2311–2315

McNaught AD, Wilkinson A. (1997) IUPAC. Compendium of Chemical Terminology. *(the "Gold Book")*. Blackwell Scientific Publications, Oxford, Vol. 2nd ed.

Naik RR, Stringer SJ, Agarwal G, Jones SE, Stone MO (2002) Biomimetic synthesis and patterning of silver nanoparticles. *Nature Materials* **1:** 169–172

Nam J, Park S, Mirkin CA (2002) Bio–Barcodes Based on Oligonucleotide–Modified Nanoparticles. *Journal of the American Chemical Society* **124:** 3820–3821

Qu SC, Yang HB, Ren DW, Kan SH, Zou GT, Li DM, Li MH (1999) Magnetite nanoparticles prepared by precipitation from partially reduced ferric chloride aqueous solutions. *Journal of Colloid and Interface Science* **215:** 190–192

Radloff C, Vaia RA, Brunton J, Bouwer GT, Ward VK (2005) Metal Nanoshell Assembly on a Virus Bioscaffold. *Nano Letters* **5:** 1187–1191

Shah SN, Steinmetz NF, Aljabali AA, Lomonossoff GP, Evans DJ (2009) Environmentally benign synthesis of virus–templated, monodisperse, iron–platinum nanoparticles. *Dalton Transactions***:** 8479–8480

Singh P, Gonzalez MJ, Manchester M (2006) Viruses and their uses in nanotechnology. *Drug Develop Res* **67:** 23–41

Steinmetz NF, Evans DJ (2007) Utilisation of plant viruses in bionanotechnology. *Org Biomol Chem* **5:** 2891–2902

Steinmetz NF, Lomonossoff GP, Evans DJ (2006) Decoration of Cowpea mosaic virus with multiple, redox–active, organometallic complexes. *Small* **2:** 530–533

Steinmetz NF, Shah NS, J. E. Barclay, Rallapalli G, Lomonossoff GP, Evans DJ (2009) Virus–Templated Silica Nanoparticles. *Small* **5:** 813–816

Sugunan A, Melin P, Schnurer J, Hilborn JG, Dutta J (2007) Nutrition–driven assembly of colloidal nanoparticles: Growing fungi assemble gold nanoparticles as microwires. *Advanced Materials* **19:** 77–79

Uchida M, Klem MT, Allen M, Suci P, Flenniken M, Gillitzer E, Varpness Z, Liepold LO, Young M, Douglas T (2007) Biological containers: Protein cages as multifunctional nanoplatforms. *Advanced Materials* **19:** 1025–1042

Wang L, Jiang J (2009) Preparation of Fe₃O₄ Spherical Nanoporous Particles Facilitated by Polyethylene Glycol 4000. *Nanoscale Research Letters* **4:** 1439–1446

Wang Q, Kaltgrad E, Lin TW, Johnson JE, Finn MG (2002a) Natural supramolecular building blocks: Wild–type cowpea mosaic virus. *Chemistry & Biology* **9:** 805–811

Wang Q, Lin T, Tang T, Johnson J, Finn mG (2002b) Icosahedral Virus Particles as Addressable Nanoscale Building Blocks13. *Angewandte Chemie International Edition* **41:** 459–462

Whaley SR, English, D. S., Hu, E. L., Barbara, P. F., Belcher, A. M., (2000) Selection of peptides with semiconductor binding specificity for directed nanocrystal assembly. *Nature* **405:** 665–668

Wierzbicki A, Sikes CS, Madura JD, Drake B (1994) Atomic force microscopy and molecular modeling of protein and peptide binding to calcite. *Calcif Tissue Int* **54:** 133–141

Willett RL, Baldwin KW, West KW, Pfeiffer LN (2005) Differential adhesion of amino acids to inorganic surfaces. *Proc Natl Acad Sci USA* **102:** 7817–7822

Wu W, He Q, Jiang C (2009) ChemInform Abstract: Magnetic Iron Oxide Nanoparticles: Synthesis and Surface Functionalization Strategies. *ChemInform* **40:** 397–415

5 Electroless metal deposition on CPMV

5.1 Introduction

Metallic nanoparticles have attracted much interest because of their size–dependent magnetic, optical and electrical properties that give them significant potential for applications such as data storage, catalysts and nanomagnets (Feldheim & Foss, 2002). Further, hollow metallic nanoparticles may offer enhanced properties, which may be useful in catalysis and as drug delivery vehicles (Kim et al, 2002; Liang et al, 2004; Lu et al, 2009). Such nanoparticles consume less material in their preparation and may be cheaper to produce than solid nanoparticles.

Examples of the use of biological entities in the synthesis of nanomaterials by deposition of metals from solution by direct reduction of the metal onto the biological template include: modification of the surface of Tobacco mosaic virus (Dujardin et al, 2003b; Knez et al, 2006; Knez et al, 2003b; Schlick et al, 2005b); gold templated onto Chilo iridescent virus (Radloff et al, 2005b); templated synthesis of metallic coatings on genetically modified bacteriophage M13 (Flynn et al, 2003b).

This chapter will describe the extension of the use of CPMV as a template for fabricating metallic nanoparticles without any prior genetic or chemical modification to the virus capsid and, importantly, without the need of peptides to act as nucleation sites as been previously discussed in chapter 3. Electroless deposition (ELD) is an autocatalytic redox process in which metal ions are chemically reduced to metal in the absence of an external current. ELD has become a commonly used process and allows the production of thin layers of metals and alloys with uniform thickness and composition (Mallory & Hajdu, 1996). The metallization of CPMV by pre–activation of the capsid surface with palladium(II) followed by ELD of cobalt, nickel, iron, platinum, cobalt–platinum and nickel–iron at room temperature, resulted in monodisperse metallic nanoparticles by a method that is environmentally friendly, simple and quick.

5.2 Experimental

5.2.1 Materials

Sodium tetrachloropalladate, cobalt(II)chloride, nickel(II)chloride hexahydrate, chloroplatinic acid hexahydrate, dimethylaminoborane, sodium hypophosphite, maleic acid and boric acid were purchased form Sigma–Aldrich; ammonium chloride and iron(II) sulfate from BDH; nickel sulfate from Fisher Scientific; and trisodium citrate dihydrate from Riedel–de Häen. All were used as supplied without further purification.

5.2.2 Pre–activation of CPMV with palladium

CPMV particles (4 mg ml^{-1}, 400 µl) suspended in 10 mM sodium phosphate buffer pH 7.0, were incubated with 400 µl of 3 mM sodium tetrachloropalladate freshly prepared in Milli–Q water. To prevent hydrolysis of palladate, the reaction pH was adjusted to 3.8, by dropwise addition of 1mM HCl, and 400 µl of aqueous 1 M NaCl was added. The reaction solution was incubated at ambient temperature with gentle stirring for 30 minutes. The $^{Pd2+}$CPMV particles produced were purified on PD–10 columns (GE Healthcare) equilibrated with saline solution (500 mM NaCl in Milli–Q water, pH 5.0), the eluted sample was dialysed on 100 kDa molecular weight cut–off membranes (Spectrum Labs) against saline solution for 4 hours. The $^{Pd2+}$CPMV particle integrity was established by TEM after uranyl acetate staining. Before the electroless deposition of the desired metals, $^{Pd2+}$CPMV had first to be reduced with 5 mM of either dimethylaminoborane (DMAB) or sodium hypophosphite, NaH_2PO_2. The reaction was allowed to proceed at ambient temperature for 30 minutes to generate Pd^0 clusters at the surface, which in turn act as nucleation sites for metal deposition. Pd^0–CPMV was washed 3–5 times on 100 kDa cut–off columns (Millipore). The Pd^0–CPMV particle integrity was ascertained by TEM, EDXS, agarose gel electrophoresis and zeta potential measurements.

5.2.3 ELD of metal coating

Equal volumes of pre–activated Pd^0–CPMV (2–5 mg ml^{-1}) in saline solution (500 mM), aqueous sodium chloride solution (1M) and plating solution (containing metal salt, reducing

agent, ammonium chloride and trisodium citrate) were stirred for 2–3 minutes at ambient temperature. CPMV concentrations and reaction conditions are summarised in Table 5.1. All plating solutions were used within four days of their preparation. Metallized–CPMV particles were purified as described below.

Metal	Pd^0–CPMV (mg ml^{-1})	Metal Salt (100 mM)	Reductant (500 mM)	NH_4Cl	$Na_3Citrate$	pH
Co	3.2	$CoCl_2$	DMAB	900 mM	170 mM	8.0
Fe	4.5	$FeSO_4$	NaH_2PO_2	900 mM	180 mM	8.1
Ni	4.0	$NiCl_2$	DMAB	900 mM	170 mM	8.0
Pt	2.3	H_2PtCl_4	NaH_2PO_2	900 mM	170 mM	6.0

Table 5.1– Pd^0–CPMV concentration and plating solution composition.

5.2.4 ELD of mixed metal coating

5.2.4.1 CoPt–CPMV

Pre–activated Pd^0–CPMV (400 µl of 4.5 mg ml^{-1}, 1 ml), suspended in 500 mM saline solution pH 5.0, was stirred at ambient temperature with 400 µl of aqueous sodium chloride solution (1M) and a mixture of 200 µl each of cobalt and platinum plating solutions at pH 8.0 for 2–4 minutes.

5.2.4.2 NiFe–CPMV

A 1:1:1 (v/v/v) mixture of pre–activated Pd^0–CPMV (3.5 mg ml^{-1}, 1 ml), suspended in 500 mM saline solution pH 5.0, aqueous sodium chloride solution (1M) and a NiFe plating solution, prepared by adaptation of a published procedure (Yi et al, 2010), [comprising nickel sulfate (100 mM), ferrous sulfate (100 mM), sodium hypophosphite (100 mM), trisodium citrate (200 mM), maleic acid (50 mM) and boric acid (200 mM)] at pH 6 was gently stirred, at ambient temperature, for 2–4 minutes.

5.2.5 Purification of metallized particles

After reaction, solutions were spun at 14000 rpm (bench top, Eppendorf) for 20 minutes to remove any large aggregates, the supernatant was collected and purified on PD–10 columns, and eluted samples were concentrated on 100 kDa cut–off columns before being layered onto 5 ml 10%–50% sucrose gradients as described in section 2.17.1. After further concentration on 100 kDa cut–off columns, the concentration of metallized–CPMV was determined photometrically at 260 nm. Recovery of metallized–CPMV was approximately 50–70% based on the initial virus concentration.

5.3 Results and Discussion

5.3.1 $^{Pd2+}$CPMV activation

It has been previously reported that amine–functionalised surfaces pre–activated with Pd^0 clusters promote the ELD of metals (Dressick et al, 1994; Falkner et al, 2005; Kind et al, 1998). Incubation of CPMV particles with a sodium tetrachloropalladate solution, followed by chemical reduction with DMAB or NaH_2PO_2, at pH 3.8, is expected to produce islands of palladium clusters on the virus capsid surface. These then act as nucleation sites for the subsequent ELD of metal. Only metallic Pd^0 can act as the catalyst for the metallization but not Pd^{2+}.

$$Pd^{2+} + 2e^- \rightarrow Pd^0$$

$$3M^{2+} + Me_2NHBH_3 + 3H_2O \rightarrow 3M + B(OH)_3 + Me_2NH_2^+ + 5H^+$$

The virus particles were very stable under the reaction conditions employed; neither reducing agents nor ELD solutions disrupted the virus capsid structure. The integrity of the initially isolated $^{Pd2+}$CPMV particles was confirmed by uranyl acetate negatively stained TEM (Figure 5.1–A). The zeta potential of –10.6 ± 1.5 mV was similar to that of wild–type (~ –12 mV).

On reduction of $^{Pd2+}$CPMV, islands of Pd^0 clusters distributed over the capsid surface were formed but these did not fully coat the virus. The unstained TEM image for Pd^0–CPMV revealed dark clusters scattered on the virion surface (Figure 5.1–B). Note that only on reduction are the particles visible in the unstained image. On reduction of $^{Pd2+}$CPMV to Pd^0–CPMV there was no significant change in the particle size (Figure 5.2). Furthermore, EDXS confirmed that palladium is present on the external surfaces of the particles (Figure 5.3–B). The zeta potential for Pd^0–CPMV particles were considerably more negative than those for wild–type and $^{Pd2+}$CPMV particles (Figure 5.4) and the scan consists of two peaks, this might be because two different surfaces are present on the particles (protein & Pd^0); the suspension of Pd^0–CPMV particles in buffer is a stable colloid. Further, agarose gel electrophoresis of Pd^0–CPMV stained with ethidium bromide showed some fluorescent intensity from a band of different mobility to wild–type, suggesting that the Pd^0–CPMV surface has some porosity sufficient to allow intercalation of ethidium bromide with the encapsidated RNA (Figure 5.5). This is consistent with incomplete coverage of the capsid surface with palladium clusters. When the gel was stained with Coomassie blue, colouration was observed for each of the Pd^0–CPMV and the wild–type particles, again consistent with the virus protein surface not being fully coated with palladium.

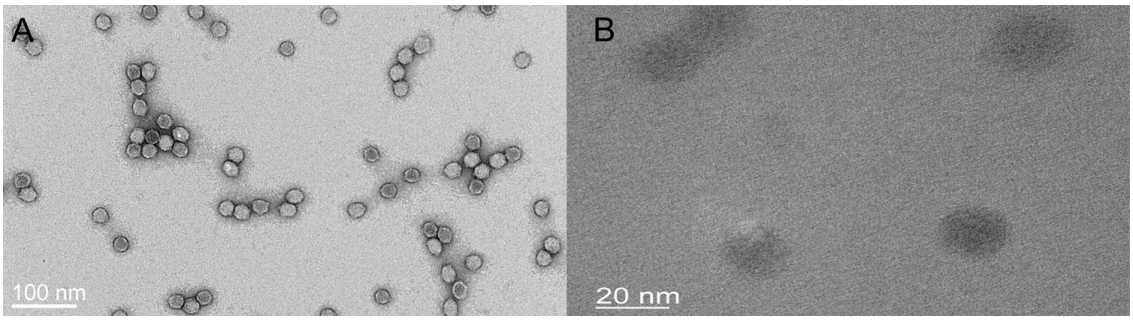

Figure 5.1– TEM image of (A) $^{Pd2+}$CPMV stained with 2 % uranyl acetate solution; (B) unstained Pd^0–CPMV particles.

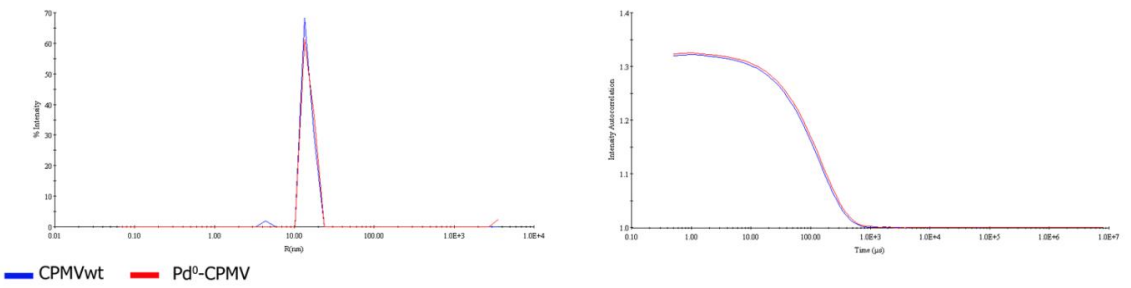

Figure 5.2– DLS comparing wild–type CPMV and Pd⁰–CPMV particles.

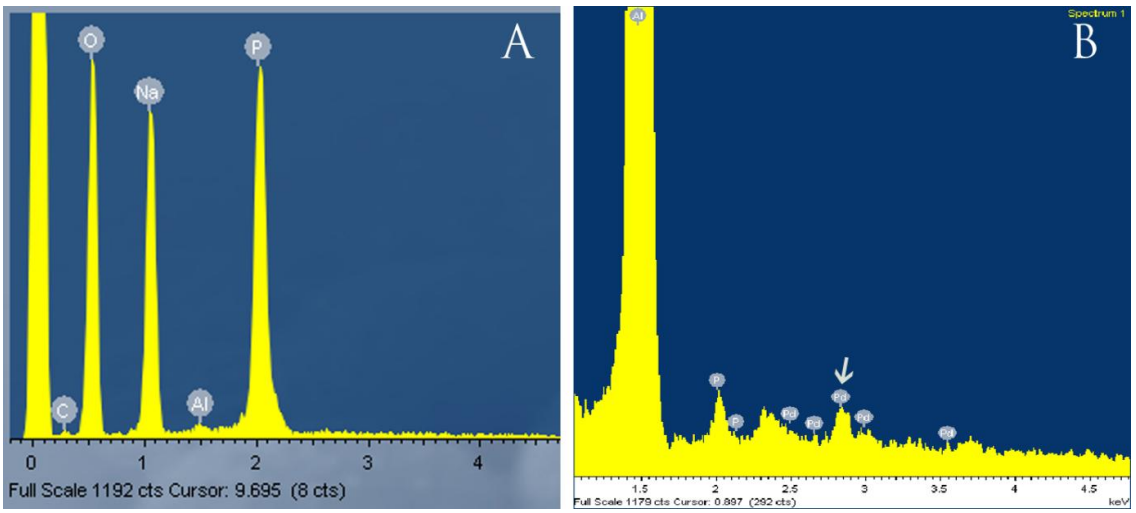

Figure 5.3– EDX spectrum of Pd⁰–CPMV metallized particles. (A) CPMVwt and (B) Pd⁰–CPMV. Major palladium peak indicated by arrow.

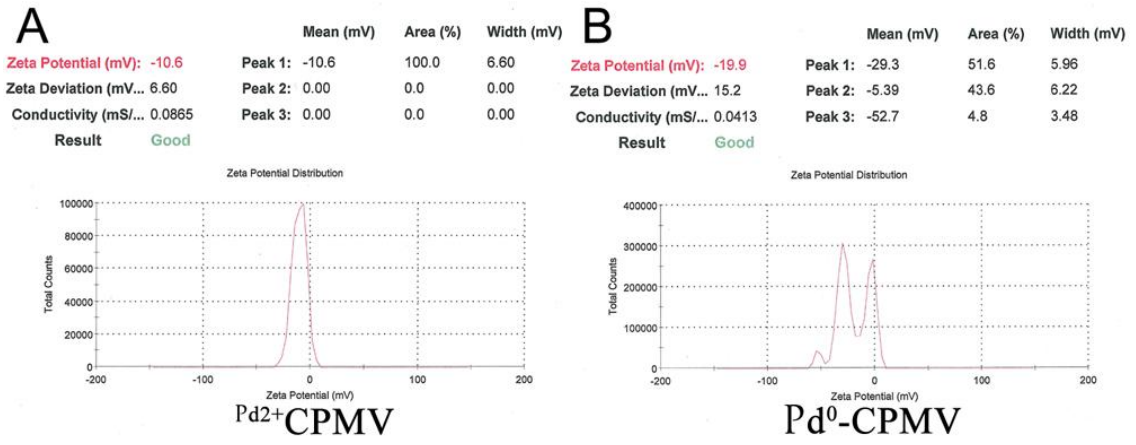

Figure 5.4– Zeta potential measurement of (A) $^{Pd2+}$CPMV particles , (B) Pd⁰–CPMV particles suspended in buffer at pH 7.0.

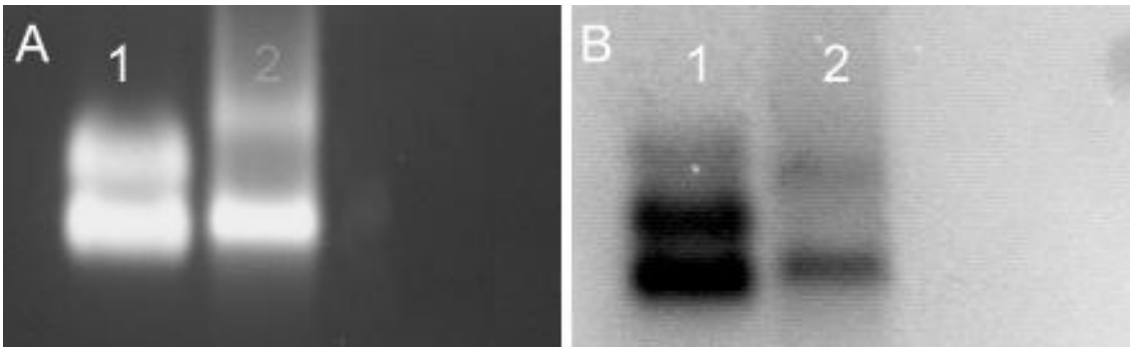

Figure 5.5– Agarose gel (1.2%) of CPMV particles visualised by (A) ethidium bromide staining, (B) Coomassie staining. Lane 1, CPMVwt; 2, Pd^0–CPMV.

5.3.2 Metallization of CPMV

For the metallization process, the pre–activated Pd^0–CPMV particles were dispersed in ELD solutions (Table 5.1). The reaction time was generally restricted to two minutes and deposition was stopped by washing the particles thoroughly with Milli–Q water. The metallization of CPMV particles was confirmed by TEM (Figure 5.6); unstained images reveal dense, monodisperse, metallized nanoparticles of *ca.* 31–34 nm. CPMVwt cannot be visualised in an unstained TEM image. Control experiments performed under identical conditions, with wild–type CPMV, without CPMV, and without Pd^0–CPMV particles, all gave non–specific, visible bulk precipitation of metal with a wide size distribution as observed by TEM (data not shown). Thus, pre–activation of CPMV is essential for the controlled nanoshell formation. EDXS confirmed that cobalt, iron, nickel, and platinum coated the external surfaces of the respective Co–, Fe–, Ni–, Pt–, CoPt and NiFe–CPMV nanoparticles (Figure 5.7). The DLS of the particles in buffer confirmed the change in the particle size implying that the coating on each particle is approximately 2–3 nm (Table 5.2). The DLS polydispersity shows that the particles are monodisperse and that the particles are uniformly metallized on their outer surfaces, in agreement with the observed TEM images.

	$CPMV_{wt}$ diameter (nm)	Polydispersity (%)	Metallized particles (nm)	Polydispersity (%)	Zeta potential (mV)
Ni–CPMV	27.4 ± 0.4	14.1	32.4 ± 0.4	20.9	–44.0 ± 2.0
Co–CPMV	26.8 ± 0.5	14.3	32.0 ± 0.5	13.3	–41.2 ± 2.5
Pt–CPMV	27.2 ± 0.5	14.0	32.6 ± 0.5	16.3	–33.2 ± 2.5
Fe–CPMV	27.6 ± 0.3	9.0	31.0 ± 0.3	14.0	–39.7 ± 1.8
NiFe–CPMV	27.9 ± 0.5	10.0	31.4 ± 0.5	24.6	–66.3 ± 2.4
CoPt–CPMV	28.6 ± 0.3	12.2	34.4 ± 0.3	13.6	–61.7 ± 2.2
Pd^0–CPMV	29.6 ± 0.3	13.5	30.2 ± 0.1	14.7	–19.0 ± 0.5

Table 5.2– Diameter and polydispersity measured by dynamic light scattering of wild–type CPMV and metallized–CPMV, and zeta potential of metallized–CPMV nanoparticles.

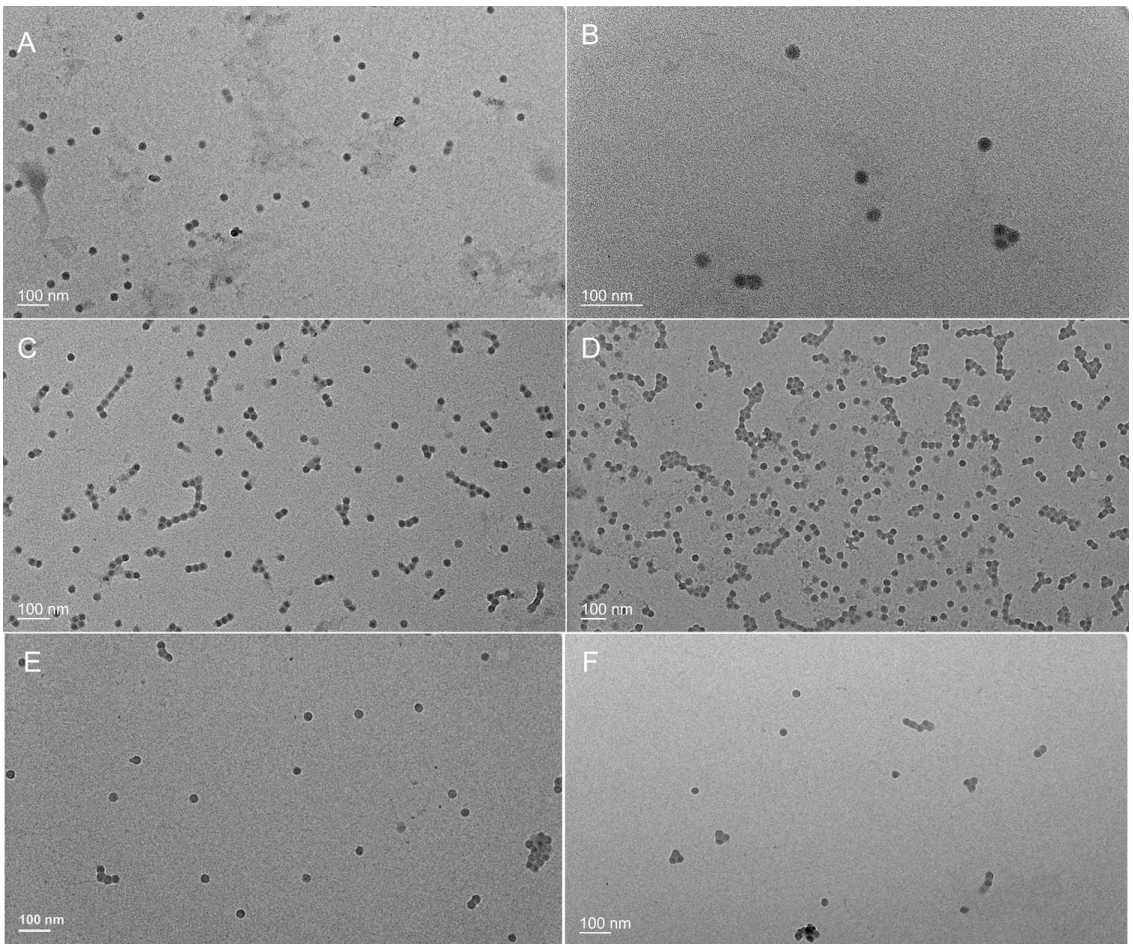

Figure 5.6– Unstained TEM images of metallized CPMV particles (A) Co–CPMV, (B) Fe–CPMV, (C) Ni–CPMV, (D) Pt–CPMV, (E) CoPt–CPMV, and (F) NiFe–CPMV.

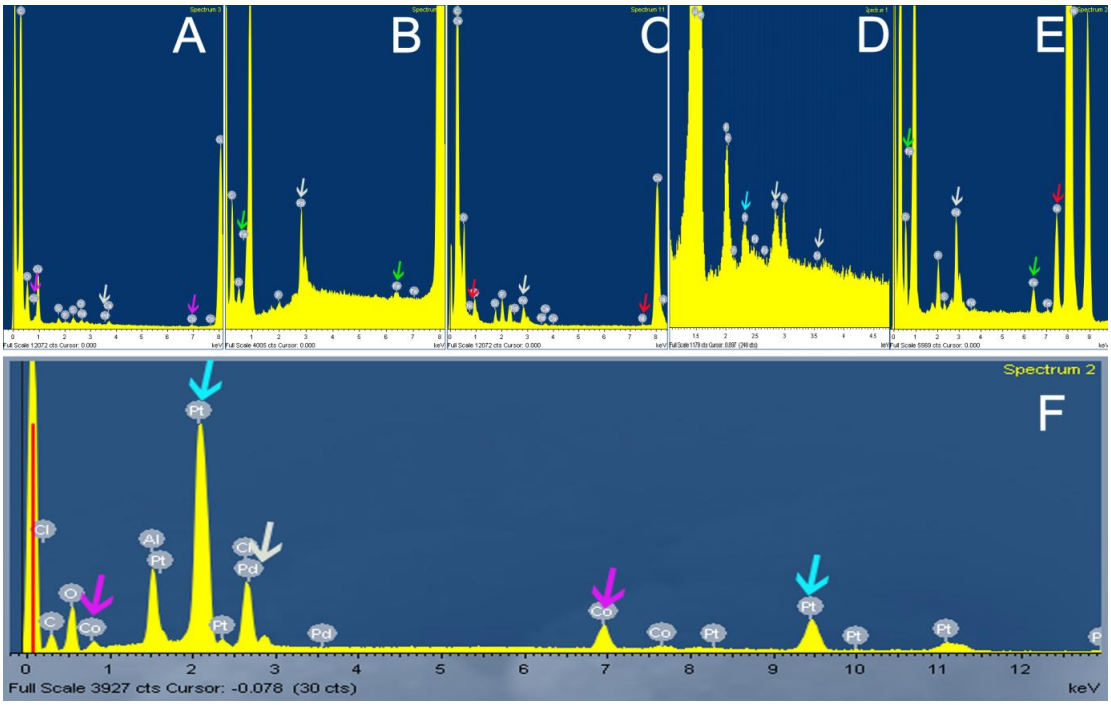

Figure 5.7– EDX spectrum of metallized CPMV particles (A) Co–CPMV, (B) Fe–CPMV, (C) Ni–CPMV, (D) Pt–CPMV, (E) NiFe–CPMV and (F) CoPt–CPMV metallized particles. Major metal peaks indicated by arrows.

The zeta potential for suspensions of the metallized particles in buffer are considerably more negative than that for CPMVwt, and show that the colloids have good stability (Table 5.3). In addition, the CPMV coat protein of Co–CPMV, Fe–CPMV, Ni–CPMV, Pt–CPMV, CoPt–CPMV and NiFe–CPMV was not detected immunologically implying that the coat protein was not accessible to the antibody as it is coated with metal (Figure 5.8). In addition, when each of the metallized particles was observed by agarose gel electrophoresis with coomassie blue staining, no protein bands were observed, this is consistent with the virus protein surface not being accessible to the stain as it is coated with metal (Figure 5.9). However, when the electrophoretic gel was stained with ethidium bromide, slight fluorescent intensity was observed, in some cases, suggesting that the metal shell may have limited porosity sufficient to allow intercalation of ethidium bromide with the encapsidated RNA.

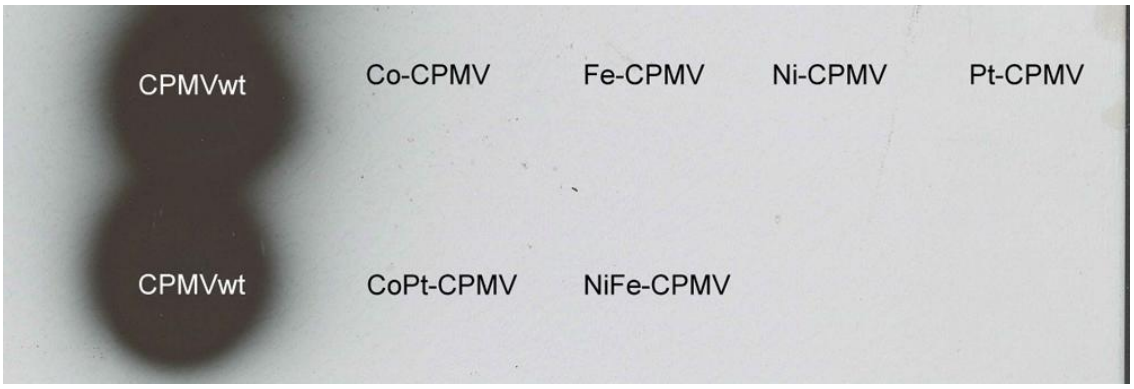

Figure 5.8– Immunological detection of CPMV coat protein of metallized particles spotted on a nitrocellulose membrane probed with polyclonal antibodies raised against CPMV. Only CPMVwt was detected.

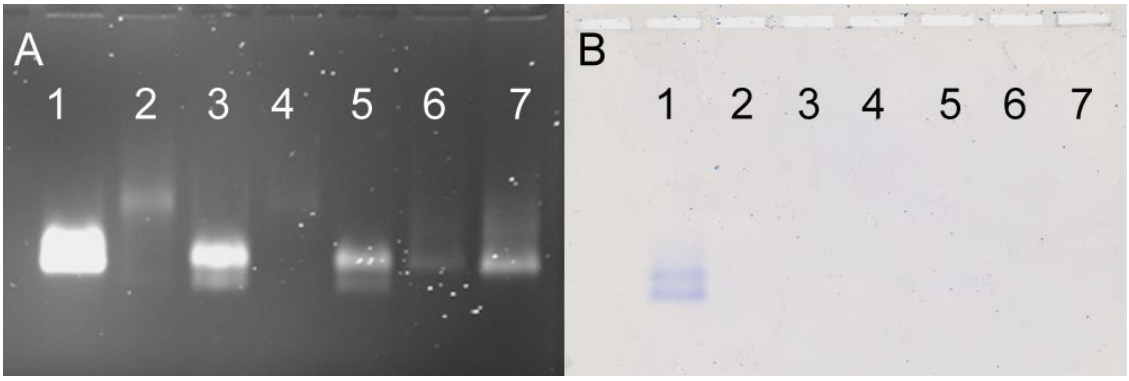

Figure 5.9– Agarose gel (1.2%) of CPMV particles visualised by ethidium bromide staining (A) and Coomassie blue staining (B). Lane 1, wild–type CPMV; 2, Co–CPMV; 3, Fe–CPMV; 4, Ni–CPMV; 5, Pt–CPMV; 6, CoPt–CPMV; and 7, NiFe–CPMV.

Nanoparticle tracking analysis (NTA) was also consistent with metallization of the virus (Figure 5.10). There was a significant increase in the relative refractive index compared to wild–type particles. The analysis is also consistent with the metallized particles being monodisperse as indicated by the particle size distribution. For Ni–CPMV particles, atomic force microscopy (AFM) images confirmed the uniformity of the metallized particles (Figure 5.11).

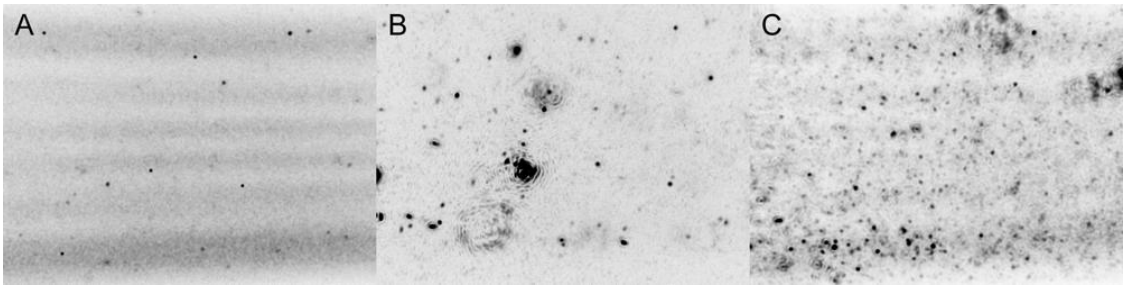

Figure 5.10– Negative image of a freeze–frame from nanoparticle tracking analysis for metallized–CPMV nanoparticles showing that the particles appear individually as point scatterers under Brownian motion with a high refractive index. (A) Co–CPMV; (B) Ni–CPMV; (C) CoPt–CPMV.

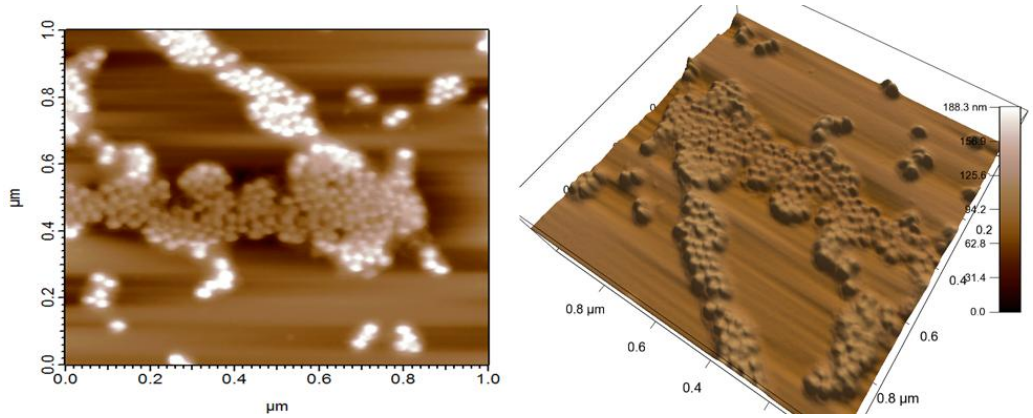

Figure 5.11– AFM image for Ni–CPMV dried on a glass slide and its corresponding 3D image.

It has been reported that the use of different reductants, DMAB or hypophosphite, can result in different sized palladium clusters forming on a surface (Knez et al, 2003a). However, it was observed that there was no significant change in the size of the Pd^0–CPMV particles on varying the reductant. However, in the case of metallization with cobalt, for example, the thickness of the metallic coating was dependent on the incubation time with ELD solution, growing from about 2 nm after two minutes incubation to 9 nm after 10 minutes (Table 5.3); hence providing some control over the nanoparticle shell thickness.

Particle	Diameter (nm)	Polydispersity (%)
$CPMV_{wt}$	27.6 ± 0.2	9.0
Pd^0–CPMV	30.2 ± .02	13.9
Co–CPMV (2 minutes)	32.0 ± 0.5	13.3
Co–CPMV (3 minutes)	37.6 ± 0.2	25.1
Co–CPMV (5 minutes)	39.2 ± 0.3	18.5
Co–CPMV (10 minutes)	46.4 ± 0.5	13.3

Table 5.3– Diameter and polydispersity measured by dynamic light scattering of wild–type CPMV and Co–CPMV nanoparticles on variation of incubation time with the ELD solution.

5.4 Conclusions

The work described in this chapter has extended the utilisation of the CPMV capsid for templated nanoparticle fabrication. ELD of Co, Ni, Fe, Pt, CoPt and NiFe on Pd^0–pre–activated CPMV resulted in the formation of monodisperse, metallic–shells fully coating the virus capsid external surface. The metallization process is simple, quick and efficient and can be performed under conditions that are environmentally friendly. The particles may have some applications as catalysts, for example, Pt–CPMV particles might be useful as catalyst of H_2 production. The particles syntheses require less material than their synthetic particles and they have larger surface area.

5.5 References

Aljabali AAA, Barclay JE, Lomonossoff GP, Evans DJ (2010) Virus templated metallic nanoparticles. *Nanoscale* **2:** 2596–2600

Aljabali AAA, Shah SN, Evans–Gowing R, Lomonossoff GP, Evans DJ (2011) Chemically–coupled–peptide–promoted virus nanoparticle templated mineralization. *Integrative Biology* **3:** 119–125

Dickerson MB, Sandhage KH, Naik RR (2008) Protein– and Peptide–Directed Syntheses of Inorganic Materials. *Chemical Reviews* **108:** 4935–4978

Dressick WJ, Dulcey CS, Georger JH, Calabrese GS, Calvert JM (1994) Covalent Binding of Pd Catalysts to Ligating Self–Assembled Monolayer Films for Selective Electroless Metal–Deposition. *J Electrochem Soc* **141:** 210–220

Dujardin E, Peet C, Stubbs G, Culver JN, Mann S (2003) Organization of Metallic Nanoparticles Using Tobacco Mosaic Virus Templates. *Nano Letters* **3:** 413–417

Evans DJ (2008) The bionanoscience of plant viruses: templates and synthons for new materials. *Journal of Materials Chemistry* **18:** 3746–3754

Falkner JC, Turner ME, Bosworth JK, Trentler TJ, Johnson JE, Lin T, Colvin VL (2005) Virus Crystals as Nanocomposite Scaffolds. *Journal of the American Chemical Society* **127:** 5274–5275

Feldheim DL, Foss CA (2002) Metal nanoparticles: synthesis, characterization, and applications, New York: Marcel Dekker.

Flynn CE, Lee SW, Peelle BR, Belcher AM (2003) Viruses as vehicles for growth, organization and assembly of materials. *Acta Mater* **51:** 5867–5880

Kim SW, Kim M, Lee WY, Hyeon T (2002) Fabrication of hollow palladium spheres and their successful application to the recyclable heterogeneous catalyst for Suzuki coupling reactions. *Journal of the American Chemical Society* **124:** 7642–7643

Kind H, Bittner AM, Cavalleri O, Kern K, Greber T (1998) Electroless deposition of metal nanoislands on aminothiolate–functionalized Au(111) electrodes. *J Phys Chem B* **102:** 7582–7589

Knez M, Bittner AM, Boes F, Wege C, Jeske H, Maiss E, Kern K (2003a) Biotemplate synthesis of 3–nm nickel and cobalt nanowires. *Nano Letters* **3:** 1079–1082

Knez M, Kadri A, Wege C, Gosele U, Jeske H, Nielsch K (2006) Atomic layer deposition on biological macromolecules: Metal oxide coating of tobacco mosaic virus and ferritin. *Nano Letters* **6:** 1172–1177

Knez M, Sumser MP, Bittner AM, Wege C, Jeske H, Hoffmann DMP, Kuhnke K, Kern K (2003b) Binding the Tobacco Mosaic Virus to Inorganic Surfaces. *Langmuir* **20:** 441–447

Liang HP, Zhang HM, Hu JS, Guo YG, Wan LJ, Bai CL (2004) Pt hollow nanospheres: Facile synthesis and enhanced electrocatalysts. *Angew Chem–Int Edit* **43:** 1540–1543

Lu W, Xiong C, Zhang G, Huang Q, Zhang R, Zhang JZ, Li C (2009) Targeted photothermal ablation of murine melanomas with melanocyte–stimulating hormone analog–conjugated hollow gold nanospheres. *Clin Cancer Res* **15:** 876–886

Mallory GO, Hajdu JB (eds) (1996) *Electroless Plating: Fundamentals and Applications*. Norwich, New York: Noyes Publications/ William Andrew Publishing, LLC

Radloff C, Vaia RA, Brunton J, Bouwer GT, Ward VK (2005) Metal nanoshell assembly on a virus bioscaffold. *Nano Letters* **5:** 1187–1191

Rosi NL, Chen CL (2010) Peptide–Based Methods for the Preparation of Nanostructured Inorganic Materials. *Angew Chem–Int Edit* **49:** 1924–1942

Schlick TL, Ding ZB, Kovacs EW, Francis MB (2005) Dual–surface modification of the tobacco mosaic virus. *Journal of the American Chemical Society* **127:** 3718–3723

Shah SN, Steinmetz NF, Aljabali AA, Lomonossoff GP, Evans DJ (2009) Environmentally benign synthesis of virus–templated, monodisperse, iron–platinum nanoparticles. *Dalton Transactions***:** 8479–8480

Yi J, Lee S, Kim J, Lee S (2010) Fabrication of ultrafine hollow Ni and Ni/Fe fibers and their dispersion characteristics in the epoxy matrix. *Surface and Coatings Technology* **204:** 1419–1425

6 Empty Virus–like particles (eVLPs)

6.1 Introduction

Virus–like particles (VLPs) are a subclass of virus nanoparticles; their external structures are identical to native viruses, but they are devoid of genetic material and thus cannot replicate. VLPs are often spontaneously formed when virus structural proteins are produced in heterologous expression systems (*E. coli*, yeast, baculoviruses and plant based expression system) (Mason et al, 2006). VLPs hold great potential in vaccine development, drug encapsulation and drug delivery (Ren et al, 2006a). For example, Tomato bushy stunt virus (TBSV) has been genetically engineered to display antigenic peptide sequences from Human immunodeficiency virus–1 (HIV–1) and induces an immune response (Joelson et al, 1997; Ludwig & Wagner, 2007; Plummer & Manchester, 2010). Such molecules will retain the desirable features of native virus but without their infectivity.

The encapsulation of small molecules within host particles is of great potential in the field of nanotechnology. The formed nanoparticles are highly monodisperse as they are constrained by the host size and shape. There are many kinds of potential hosts including protein cages, viral capsids, lipid coats, polymers, and synthesized organic capsid–like structures (discussed in more detail in the Introduction). The internal environment of protein cages is separated from the outside by a porous protein shell that restricts the types of encapsulated molecules that can enter. Self–assembled empty virus–like particles (eVLPs) can be used as constrained environments for the preparation of nanomaterials and encapsulation of foreign materials (cargo) and have potential applications in drug delivery (Conn & Rebek, 1997).

The possibility to synthesize nanoparticles within the empty capsids of eVLPs is advantageous as the capsid constrains the size of the cargo within; eVLPs have been used to encapsulate foreign molecules *in vitro* (Douglas & Young, 1999). However, there is to date no *in vitro* study on material loading of CPMV eVLPs. This chapter will focus on the synthesis and

characterisation of cobalt and iron oxide nanoparticles produced within highly monodisperse size–constraining CPMV eVLPs. In addition, the internal chemistry of eVLPs and drug loading within the cavity will be explored. The coat protein of CPMV eVLPs has an inner diameter of ~25–27 nm and act as size–limiting vessels for metallic core nanoparticle formation. The monodispersity of the particles, along with their nano–sized dimensions, are attractive features for material synthesis and drug delivery applications, which will be explored in this chapter.

6.1.1 CPMV eVLPs

The recent development of a method for the production of large quantities of CPMV eVLPs in plants (Saunders et al, 2009) was the motivation behind the research described in this chapter. The mature large (L) and small (S) proteins are produced by the cleavage of the precursor (VP60) by the action of a virus–encoded proteinase (24K proteinase). CPMV eVLP production takes advantage of the highly efficient plant transient expression system, pEAQ–HT (Sainsbury & Lomonossoff, 2008; Sainsbury et al, 2009). The pEAQ–HT system is used to simultaneously express the VP60 coat protein precursor and the 24K proteinase in plants via agro–infiltration. Efficient processing of VP60 to the L and S proteins occurs, leading to the formation of eVLPs (Montague et al, 2011; Saunders et al, 2009). The simplified process is depicted in Figure 6.1. CPMV eVLPs possess the same structure as CPMVwt but they lack the genetic material within the capsid as shown in Figure 6.2.

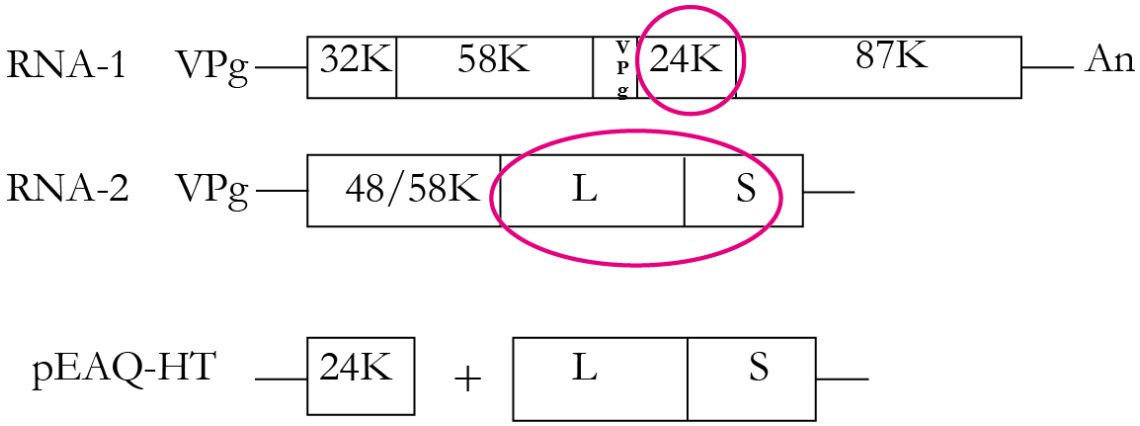

Figure 6.1– Schematic representation of the production of eVLP using pEAQ–HT system. Adapted from (Saunders et al, 2009).

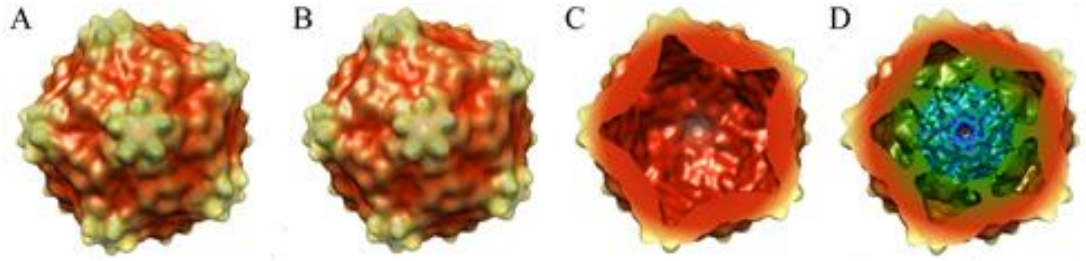

Figure 6.2– Cryo–EM reconstruction of CPMV particles. Purified particles were flash–frozen in vitreous ice, and then subjected to cryo–electron microscopy. (A) reconstruction of CPMVwt exterior, (B) reconstruction of CPMV eVLPs, (C) internal view of CPMV eVLPs showing empty capsid and (D) average reconstruction of CPMVwt. Kyle Dent and Neil Ranson, University of Leeds performed cryo–EM and computational analysis.

6.2 Experimental

Throughout this chapter, superscript following the virus name denotes molecules attached to the external surface and subscript denotes molecules within or attached to the interior of the capsid

6.2.1 CPMV eVLP production

CPMV eVLPs were produced using the pEAQ–HT system to simultaneously express the VP60 coat protein precursor and the 24K proteinase in plants via agro–infiltration. CPMV eVLPs were isolated from plants and purified by methods similar to those used for wild–type CPMV (J. Wellink, 1998) but omitting the chloroform step. The agroinoculation and eVLPs extraction was done in collaboration with Miss Pooja Saxena and Mrs Elaine Barclay, Biological Chemistry, John Innes Centre, UK).

Particle integrity was confirmed by TEM, gel electrophoresis and DLS. The eVLPs were stored in 10 mM sodium phosphate buffer pH 7.0 at 4 ºC. The concentration of the eVLPs can be calculated from their UV–vis absorbance at 280 nm (Figure 6.3) using an extinction coefficient ε of CPMV eVLPs at λ_{280} = 1.28 ml $mg^{-1}cm^{-1}$. The eVLPs were purified further after the final ultracentrifuge step using a combination of dialysis and gel filtration. The concentration was determined using UV–Vis (see section 2.9).

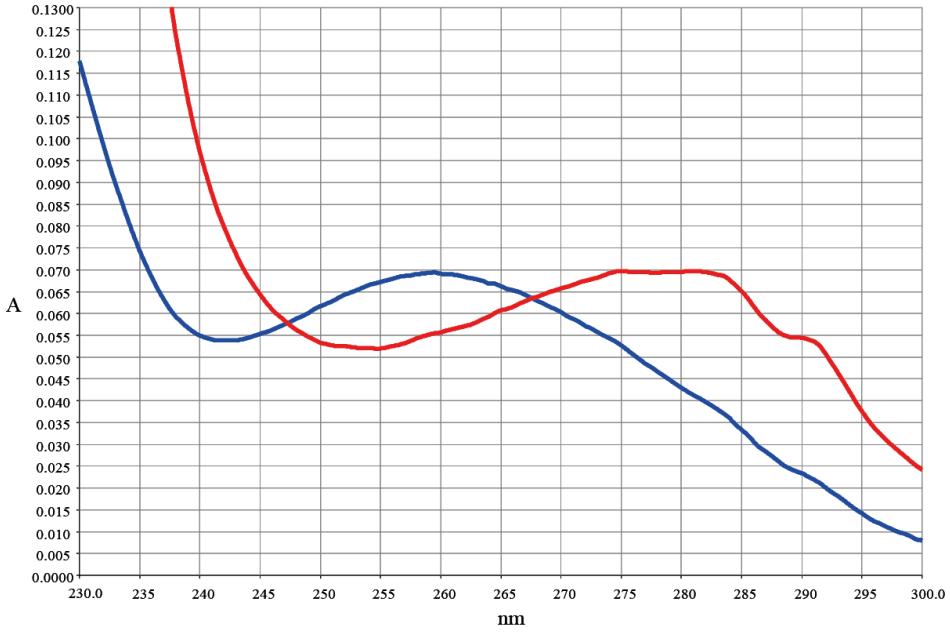

Figure 6.3– UV–vis spectrum of CPMV eVLPs (red), with a maximum at 280 nm from protein and wild–type CPMV (blue) with a maximum at 260 nm arising from internal RNA.

6.2.2 Encapsulation of cobalt within CPMV eVLPs ($VLPs_{cobalt}$)

CPMV eVLPs (1 mg, 0.5 ml) suspended in 10 mM sodium phosphate buffer pH 7.0 were incubated with a final concentration of aqueous cobalt chloride solution of 10 mM at ambient temperature while gently stirring. After 30–40 minutes, the sample was purified on PD–10 desalting columns (GE Healthcare). The eluted sample was washed twice with MilliQ water (3 ml each) and concentrated in 10 mM sodium phosphate buffer by centrifugal ultrafiltration. The sample was then incubated with a freshly prepared aqueous solution of sodium borohydride to a final concentration of 5 mM for a further 30 minutes at ambient temperature. The cobalt–loaded particles ($VLPs_{cobalt}$) were dialyzed overnight using 100 kDa molecular–weight cutoff membranes (Float–A–LyzerG2, Spectrum Laboratories) against 10 mM sodium phosphate buffer pH 7.0 or layered onto sucrose gradient (section 2.17.1). The $VLPs_{cobalt}$ were concentrated by centrifugal ultrafiltration using 100 kDa molecular–weight cutoff columns (Millipore). The yield of $VLPs_{cobalt}$ was 70% relative to the initial eVLP concentration as determined by UV–vis spectrophotometry. A control experiment, under identical conditions but using RNA–1 containing particles (Bottom component), gave visible bulk precipitation with a wide size distribution of particles as confirmed by DLS and TEM.

6.2.3 Encapsulation of iron oxide within CPMV eVLPs ($VLP_{iron\ oxide}$)

CPMV eVLPs (1 mg, 3 ml) suspended in 10 mM sodium phosphate buffer pH 7.0 were treated with a solution of ferric and ferrous sulfate in a molar ratio of 2:1 (10 mM: 5 mM), which favours the formation of Fe_3O_4; the pH after the addition was 3.5–3.8. The mixture was incubated overnight (~15 hours) while gently stirring at 4 °C. The particles were then washed twice with MilliQ water on 100 kDa cutoff columns (Millipore). The pH was raised to 10.1 by the gradual addition of 1 mM sodium hydroxide, and the particles were kept at this pH for 60–70 minutes. A combination of dialysis (100 kDa membrane) and sucrose gradient was used to purify the particles (see section 2.17.1). 175 µl fractions containing mineralized particles were collected and dialysed against 10 mM sodium phosphate buffer using 100 kDa (molecular–weight cut–off membranes) (Float–A–Lyzer G2, Spectrum Laboratories). The yield of $VLP_{iron\ oxide}$ was 30–40% relative to the initial eVLP concentration as determined by UV–vis spectrophotometry. A control experiment, with the same concentration of ferric/ferrous ions at the same pH but without the eVLPs (no virus particles), was performed under the same reaction conditions. An orange colour was observed and DLS indicated aggregation of iron oxide particles with a wide range of particle size distribution.

6.2.4 Mössbauer analysis of $VLP_{iron\ oxide}$

Prof. Dave Evans and Mrs Elaine Barclay conducted Mössbauer experiments. The particles were analysed as described in section 2.13.

6.2.5 Vibrating sample magnetometer (VSM) measurements of $VLP_{iron\ oxide}$

The particles were analysed as described in section 2.14. (The magnetic measurements were conducted as a collaborative project with Drs. Oscar Céspedes and Sarah Staniland, School of Physics and Astronomy, University of Leeds, United Kingdom).

6.2.6 Staining for cobalt and iron within eVLPs

VLP_{cobalt} and $VLP_{iron\ oxide}$ particles were probed for cobalt and iron using the appropriate stain as described in section 2.17, for immunological detection of the coat protein see section 2.13.3.

6.2.7 Biotinylation of eVLPs (^{Biotin}VLPs)

CPMV eVLPs and VLP_{cobalt} particles were biotinylated using an adaptation of a standard procedure (Steinmetz et al, 2006a). In brief, particles suspended in 10 mM sodium phosphate buffer pH 7.0 were reacted with a 2000 molar excess of biotin–N–hydroxysuccinimide ester (Aldrich) dissolved in dimethylformamide (DMF); the final concentration of DMF: water was adjusted to 10% (v/v). The reaction was left overnight at 4 °C, and then the ^{Biotin}VLPs and $^{Biotin}VLPs_{cobalt}$ were dialyzed using 100 kDa molecular–weight cut–off membranes (Float–A–Lyzer G2, Spectrum Laboratories) against 10 mM sodium phosphate buffer for 2 days. The sample was concentrated and the concentration of eVLPs determined from absorption at 280 nm. The binding of each $^{Biotin}VLPs_{cobalt}$ or ^{Biotin}VLPs to a streptavidin–modified chip was monitored by surface plasmon resonance (SPR).

6.2.8 Surface plasmon resonance (SPR)

^{Biotin}VLPs samples were spotted onto a series S Sensor Chip SA (Biacore); the chip has a carboxymethylated dextran matrix pre–immobilized with streptavidin. Binding was measured in response units (RU). The instrument is a four–flow cell system (each flow cell volume is 0.06 ml) equipped with a temperature control unit and an optical system to measure the molecular interaction occurring on the sensor chip in real–time. The instrument was used in manual run mode with a flow rate of 10 µl/min, at ambient temperature, with PBS pH 7.4 as running buffer. Flow cell 1 was a negative control with biotin–N–hydroxysuccinimide ester, flow cell 2 a positive control with multi–injection steps using ^{Biotin}VLPs with a contact time of 1 minute until each run reached saturation (the overall time for chip saturation was 360 seconds). Flow cell 3 and 4 showed the sensogram presented in Figure 6.9 during association and dissociation

measurements of ^{Biotin}VLPs and $^{Biotin}VLP_{cobalt}$ on a streptavidin–modified chip. The association is measured at approximately the same concentration as determined by UV–vis spectrophotometry.

6.2.9 Infusion of rhodamine or doxorubicin into CPMV eVLPs

1–2 mg ml^{-1} CPMV eVLPs were incubated with a 2000:1 molar ratio of rhodamine hydrochloride or doxorubicin hydrochloride dissolved in DMSO. The DMSO level was adjusted to 10–20 % (v/v), and the reaction was left to proceed at 4 ºC overnight (12–16 hours). The samples ($VLPs_{rhodamine}$ or $VLPs_{dox}$) were then purified on PD–10 gel filtration columns pre–equilibrated with 10 mM sodium phosphate buffer pH 7.0. The eluted fractions were collected and dialysed for 2 days at ambient temperature against 10 mM sodium phosphate buffer pH 7.0. The rhodamine or doxorubicin was quantified by fluorescence measurement. $VLPs_{rhodamine}$ were measured at an excitation wavelength of λ_{500} nm and extinction coefficient of 80000 M^{-1} cm^{-1}. For $VLPs_{dox}$ the extinction coefficient ε_{484} is 13500 M^{-1} cm^{-1}.

As a control experiment, the bottom component (which contains RNA–1) was treated as described above.

6.2.10 Gemcitabine and cisplatin loading

CPMV eVLPs (1 mg ml^{-1}) suspended in Milli–Q water just prior to the experiment were incubated with an aqueous solution of 0.5 mg of gemcitabine or cisplatin in 0.2 ml Milli–Q water and kept in a shaker at 4 °C. After overnight incubation, the $VLPs_{drug}$ were washed once with Milli–Q water using 100–kDa cutoff membranes, the recovered particles were then used for the LBL experiment as described below. As wild–type CPMV particles contain ~10% eVLPs, bottom component particles (containing RNA–1) were used as a negative control.

6.2.11 LBL formation onto $eVLPs_{drug}$

Layer–by–layer (LBL) assembly was used to prepare polyelectrolyte multilayer–coated CPMV eVLPs. A solution of the cationic polyelectrolyte (PAH) (1 mg) dissolved in 1 ml of aqueous 0.25 M NaCl was prepared and added to 2 mg ml^{-1} CPMV $eVLPs_{gemcitabine}$ suspended in

Milli–Q water just prior to the reaction. The cationic polyelectrolyte was allowed to adsorb onto the virus capsid for 15–20 minutes while stirring at 2000 rpm at ambient temperature. The $^{PAH}VLPs_{gemcitabine}$ were washed 4 times with Milli–Q water using 300 kDa cut–off membranes (Sartorius Stedim Biotech). $^{PAH}VLPs_{gemcitabine}$ were re–dispersed in Milli–Q water by vortexing. Before the next polyelectrolyte coating step, the washing process was repeated twice to remove any non–adsorbed cationic polyelectrolyte. Deposition of anionic polyelectrolyte (PSS; 1mg ml^{-1} solution containing 0.25 M NaCl) was carried out using the same approach as for the first layer. The layer deposition was repeated as in the first cycle on the recovered $^{(PAH/PSS)1}VLPs_{gemcitabine}$ to generate thicker multi–polyelectrolyte coatings denoted $^{(PAH/PSS)2}VLPs_{gemcitabine}$. Particle integrity was investigated and recorded (see result section).

6.2.12 *In vitro* gemcitabine release and quantification

The $^{(PAH/PSS)1\ or\ 2}VLPs_{gemcitabine}$ was investigated under simulated physiological conditions at pH 7.4 and in an acidic environment (sodium acetate buffer, pH 5.3 as prepared in section 2.5) at 37 °C to assess the feasibility of drug release from CPMV eVLPs.

As gemcitabine is easily tracked due to its fluorescence, it was selected to demonstrate proof–of–principle *in vitro* gemcitabine release. The $^{(PAH/PSS)2}VLPs_{gemcitabine}$ were re–suspended in 5 ml of 0.15 M sodium phosphate buffer pH 7.4 and transferred into a dialysis cassette (MW cut–off 100 kDa). The cassette was placed in 50 ml of 0.150 M sodium phosphate buffer pH 7.4 or in sodium acetate buffer at pH 5.3. The release study was performed at 37 °C in a Thermo Micromixer (FINEPCR) incubator shaker. 10 µl of $^{(PAH/PSS)2}eVLPs_{gemcitabine}$ (inside the dialysis membrane) was removed at set time points and analysed by agarose gel electrophoresis to monitor the electrolyte break down. After 24 hours incubation, the native intact form of eVLPs was observed by agarose gel electrophoresis (see results section). The gemcitabine was quantified from the accumulated dialysis solution using a molar extinction coefficient of ε_{299}= 5710 M^{-1} cm^{-1} (Lammers et al, 2009).

6.2.13 Internal chemistry (modifying internal cysteines)

CPMV eVLPs (1–1.5 mg, 1 ml) suspended in 0.1M sodium phosphate buffer pH 7.0 were incubated with a 2000 molar excess of DyLight–488 maleimide (Thermo Scientific) in DMSO. The final concentration of DMSO was adjusted to 10% (v/v). The reaction was left to proceed for 8 hours or overnight (~15 hours) while gently stirring at 4 °C. A combination of dialysis (100 kDa membrane), PD–10 gel filtration columns and sucrose gradient was used (2.1 ml 10%–50% sucrose gradients centrifuged at 137000 g for 1.5 hours at 4 ºC; 175 µl fractions containing $VLP_{DyLight–488}$ were collected and dialysed against 10 mM sodium phosphate buffer for 48 hours using 100 kDa molecular–weight cut–off membranes (Float–A–Lyzer G2, Spectrum Laboratories)). The yield of $VLP_{DyLight–488}$ was 60% relative to the initial eVLP concentration as determined by UV–vis spectrophotometry.

Reducing conditions: the crystal structure of CPMVwt revealed Cys–187 and Cys–355 formed disulfide bonds. Therefore, the same approach described above was repeated with the addition of a final concentration of 10 mM tris(2–carboxyethyl)phosphine (TCEP) to cleave the disulfide bond and make more cysteine thiol groups available for chemical modification.

6.2.14 ^{A20FMDV2}VLPs

Two approaches have been adopted to either couple the peptide (A20FMDV2) to the eVLPs surface, using SPDP as described in section 2.16 or alternatively for simplicity, as described here, a one–step reaction to form a thioester bond, section 2.14. Carboxylate groups on the external surface of CPMV particles were derivatised through the formation of an active ester intermediate using EDC (Hermanson, 2008). EDC and A20FMDV2 peptide in 10 mM sodium phosphate buffer pH 7.0, both in 2000 molar excess, were added to CPMV eVLPs. The reaction was stirred overnight at 4 °C and the ^{A20FMDV2}eVLPs particles were purified and concentrated as described in the general methods section. The yield of the conjugated particle was between 80–90% based on the initial virus concentration. Modified particles were characterised by agarose gel electrophoresis and their integrity was confirmed by TEM.

6.2.15 ^{A20FMDV2}VLPs peptide quantification

The number of peptides per particle was determined for ^{A20FMDV2}VLPs as follows. ^{A20FMDV2}VLPs in 10 mM sodium phosphate buffer pH 7.0 was reacted with a 1000:4000 molar ratio of EDC and Sulfo–NHS in aqueous solution, as described in section 2.15. A 2000 molar excess of freshly prepared cascade blue ethylenediamine dye (Invitrogen), dissolved in 10 mM sodium phosphate buffer, was added. The reaction scheme is depicted in Figure 6.4. The reaction was left to proceed at 4 °C overnight while gently stirring. The doubly–functionalised particles ^{A20FMDV2}VLPs$^{cascade\ blue\ dye}$ were purified on a PD–10 column equilibrated with 10 mM sodium phosphate buffer pH 7.0, and eluted fractions were concentrated on 100 kDa cut–off columns before being layered onto 5 ml 10%–50% sucrose gradients. The gradients were centrifuged at 137000g for 1 to 1.5 hours at 4 °C; 300 µL fractions were collected and dialysed against 10 mM sodium phosphate buffer pH 7.0 for 2 days, changing the buffer every 12 hours. After further concentration on 100 kDa cut–off columns, the number of remaining reactive carboxylates was calculated, from the absorbance of the dye at λ_{399} and $\varepsilon = 27000\ M^{-1}\ cm^{-1}$, to be ~100–110 ± 8 per virion. This equates to approximately 45–50 peptides being bound to each eVLP. Moreover, a control experiment was conducted with unmodified eVLPs and the cascade blue dye and the number of dyes was found to be ~145–150 dye per virus, this is almost full coverage of all surface accessible carboxylates.

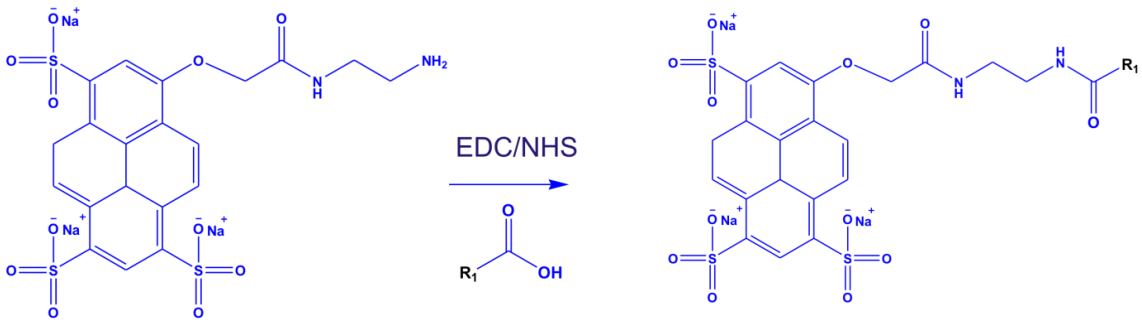

Figure 6.4– The side–chain primary amine group of cascade blue ethylenediamine was coupled to the remaining carboxylate groups on the virus capsid using the carbodiimide reaction, R_1 represents the virus.

6.3 Results and discussion

6.3.1 Internal mineralization of CPMV eVLPs

Internal mineralization of CPMV eVLPs with cobalt and iron oxide have been achieved for the first time. Incubation of CPMV eVLPs, suspended in 10 mM sodium phosphate buffer pH 7.0, with cobalt chloride solution, followed by washing, then subsequent reduction with sodium borohydride gave cobalt–loaded VLPs ($VLPs_{cobalt}$) in which cobalt is encapsulated within the capsid core while preserving the external capsid surface for further modifications. The general method is depicted in Figure 6.5. Recovery of $VLPs_{cobalt}$ was approximately 70% based on initial CPMV eVLP concentration.

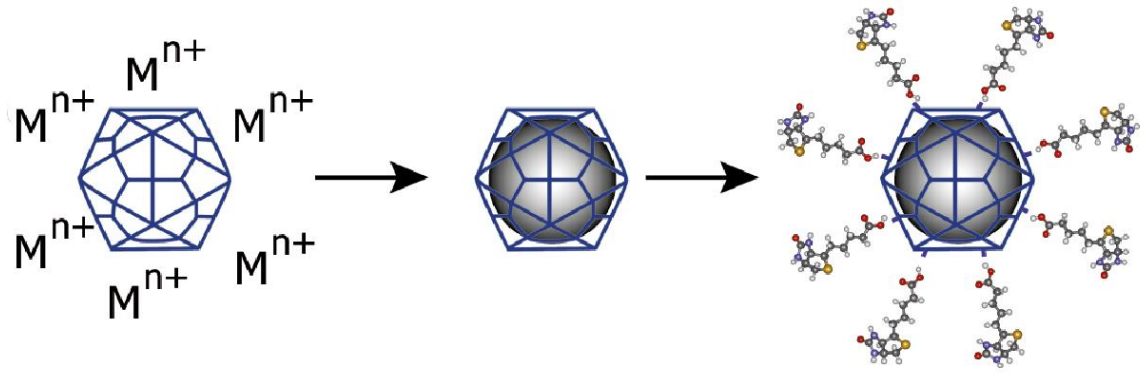

Figure 6.5– Schematic representation of loading eVLPs with metal ions. The subsequent reduction of the metal ions (M^{n+}) resulted in the formation of metallic cores within the eVLPs. In addition, the capsid was preserved and can be biotinylated. Reproduced from Aljabali et al 2010.

A similar approach can be employed to generate internalized iron oxide. A suspension of CPMV eVLPs was treated with a mixture of ferric and ferrous sulfate solutions in a molar ratio of 2:1, under alkaline hydrolysis conditions that favour the formation of Fe_3O_4, magnetite, as depicted in the equation below. However, the presence of hematite (α–Fe_2O_3) or maghemite (γ–Fe_2O_3) cannot be discounted.

$$2FeCl_3 + FeCl_2 + 8NaOH \rightarrow Fe_3O_4 + 8NaCl + 4H_2O$$

After mixing overnight at pH 3.7–4.2, the particles were washed on 100 kDa cut–off columns before the pH was raised to 10.1. The resultant iron oxide–VLPs ($VLPs_{iron\ oxide}$) were purified and obtained in 40–45% yield based on initial CPMV eVLP concentration.

An unstained TEM image clearly shows electron–dense material, cobalt or iron oxide, was formed within eVLPs, and that sucrose density centrifugation eliminates almost all of the reaction impurities, Figure 6.6. CPMV eVLPs, prior to the reaction, were not visible by TEM without staining. Based on the results from TEM, the average size of internally mineralized eVLPs was 31.5 ± 2 nm, which agrees with the unmodified particle size. Further, the metallic core within VLPs of ~ 25 nm is in agreement with the internal diameter of eVLPs.

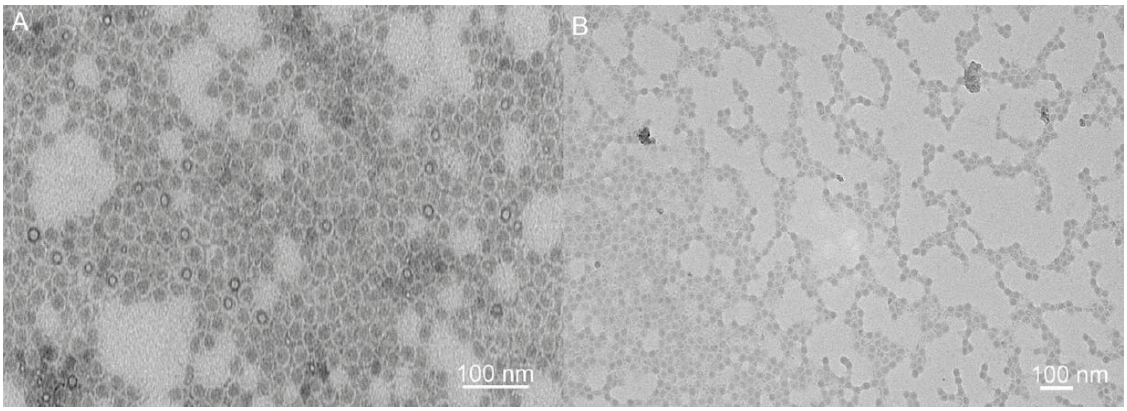

Figure 6.6– Unstained TEM images of internally mineralized CPMV eVLPs. A) $VLPs_{cobalt}$ and B) $VLPs_{iron\ oxide}$.

A negative stain of the modified particles with either 2% UA or 1% phosphotungstic acid (PTA) showed the presence of the complete protein shell encapsulating ~25 nm metallic cores, Figure 6.7. Two morphologies were observed with UA staining as is also seen for eVLPs (unmodified particles) this might be because of partial loading or it is a stain property Figure 6.7. When staining with 1% PTA only one morphology was observed. The bright ring around the solid core in Figure 6.7 panel C represents the intact coat protein surrounding the metallic core.

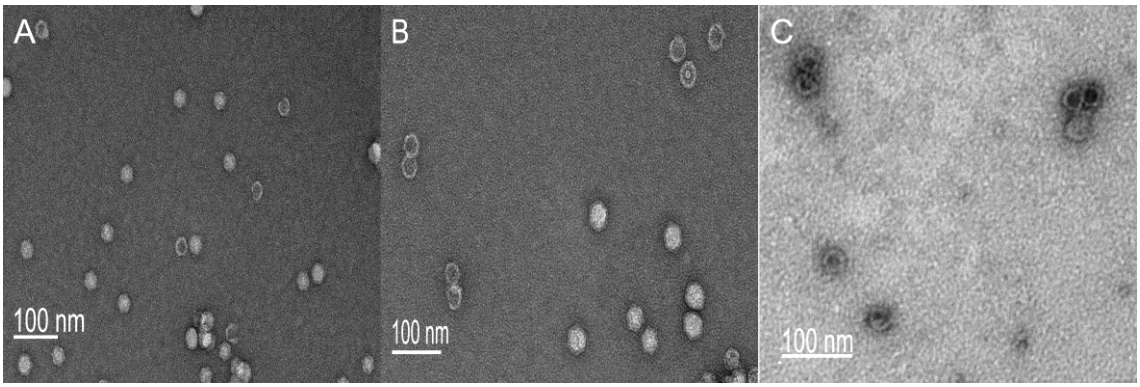

Figure 6.7– Negatively stained internally mineralized CPMV eVLPs. Panel (A) $VLPs_{cobalt}$, (B) $VLPs_{iron\ oxide}$ both stained with 2% uranyl acetate, and (C) $VLPs_{iron\ oxide}$ stained with 1% PTA. The white ring is the coat protein surrounding solid metallic cores.

Furthermore, the metallic cores could be extracted by disruption of the coat protein of the modified particles. Particles were heated for 10 minutes at 80–90 °C with 20 % (w/v) SDS. Unstained TEM reveals 10% of the metallic cores were approximately 25–28 (± 2) nm in diameter (Figure 6.8–A), the rest of the sample forming large aggregates. Staining the cobalt metallic cores with UA or PTA did not result in the same morphologies and the white ring of the coat protein was absent. In addition, DLS analysis confirmed the presence of a peak corresponding to the internal cavity size of ~ 25 nm with most of the sample being aggregated (Figure 6.8–B). This is direct confirmation that the capsid is important in preventing aggregation. The high percentage aggregation is possibly due to the metallic cores not being produced from single domain crystals and therefore upon capsid dissociation, the metallic multi–domains fall apart and aggregates formed.

The DLS data of the mineralized particles in 10 mM sodium phosphate buffer pH 7.0 (Figure 6.9), confirms that the external diameter of the VLPs of 31.9 (± 2.0) nm compared to 32.0 (± 2.0) nm for CPMV eVLP does not change significantly on internalization of cobalt or iron oxide and that the particles remain monodisperse. The data is in full agreement with the observed TEM images.

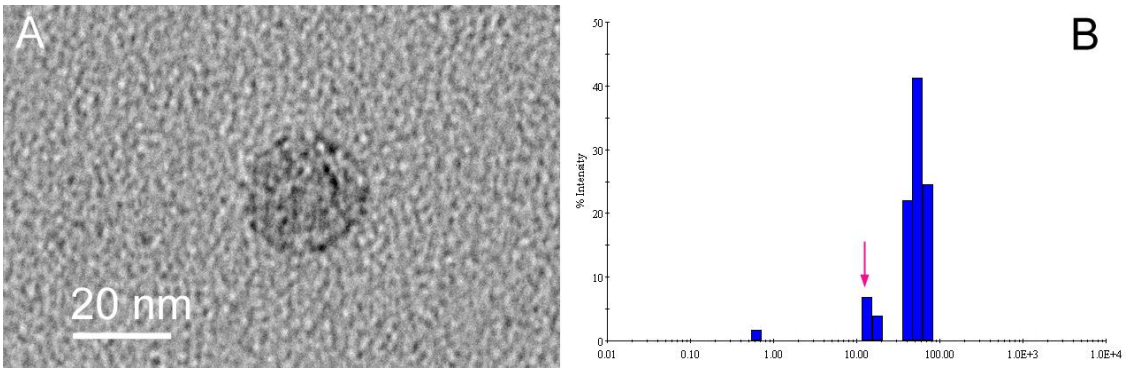

Figure 6.8– Metallic core analysis post protein capsid disruption. (A) Unstained TEM image of one of the cobalt cores resulting from disruption of the capsids. The cobalt particle size of ca. 26 nm is as expected if the interior cavity of the VLP is fully filled and (B) corresponding DLS measurement, the arrow indicates the particles size within the VLPs.

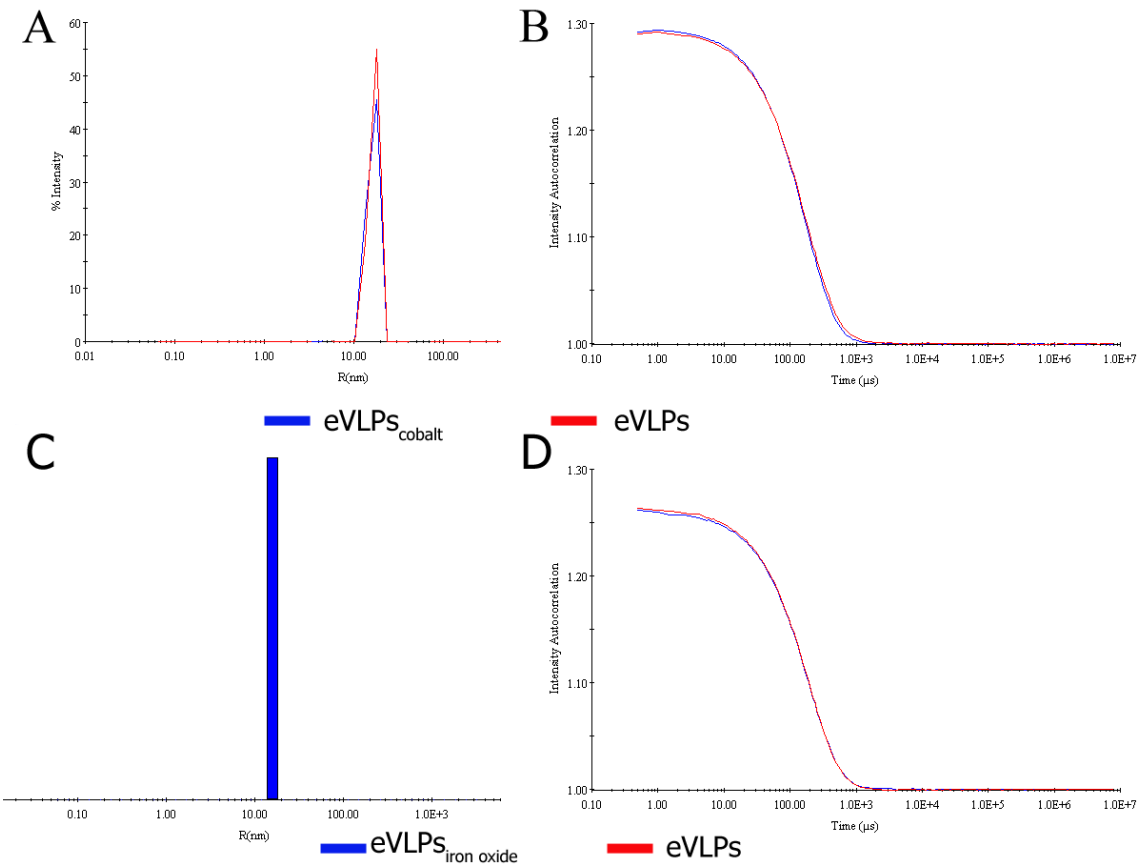

Figure 6.9– DLS data of $VLPs_{cobalt}$, and $VLPs_{iron\ oxide}$: (A) comparison between hydrodynamic radius of $VLPs_{cobalt}$, and $VLPs_{iron\ oxide}$; (B) correlation plot for $VLPs_{cobalt}$, and eVLPs; (C) regularization graph of DLS of purified $VLPs_{iron\ oxide}$; (D) correlation plot for $VLPs_{iron\ oxide}$. All readings were recorded at 21°C in triplicate.

Energy dispersive X–ray spectroscopy (EDXS) confirms the presence of cobalt, and iron and oxygen, data is represented in Figure 6.10. In addition, there was an insignificant amount of oxygen in $VLPs_{cobalt}$ and thus no evidence for cobalt oxide formation. The zeta potentials, as shown in Figure 6.11, for suspensions of eVLPs (–32.0 ± 2.3 mV), $VLPs_{cobalt}$ (–32.9 ± 1.8 mV) and $VLPs_{iron\ oxide}$ (–32.1 ± 2.4 mV) indicate that the colloids have good stability and show little propensity to aggregate, as was confirmed by TEM, Figure 6.6. In each case, control experiments were performed under identical conditions except for the absence of eVLPs or by using "B component" in which both gave non–specific bulk precipitation with a wide size distribution of nanoparticles as observed by TEM and DLS; thus, the eVLPs are essential for controlled nanoparticle growth.

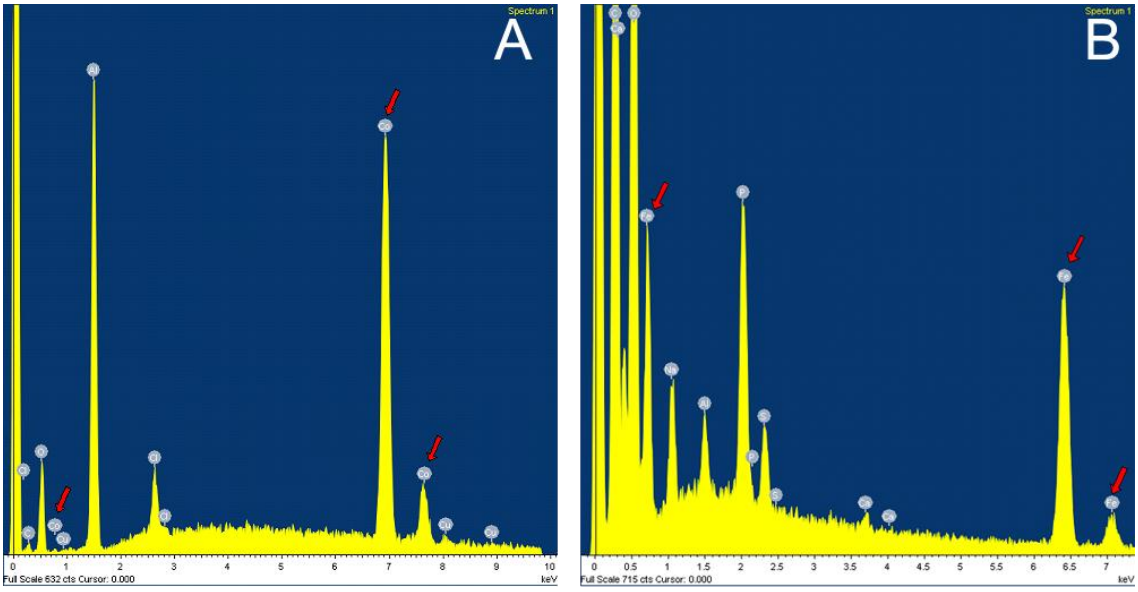

Figure 6.10– Elemental energy–dispersive X–ray spectroscopy analysis. (A) $VLPs_{cobalt}$ showing the presence of cobalt, indicated by red arrows, and (B) of $VLPs_{iron\ oxide}$ showing the presence of iron, indicated by red arrows. Aluminium signal is from the sample holder.

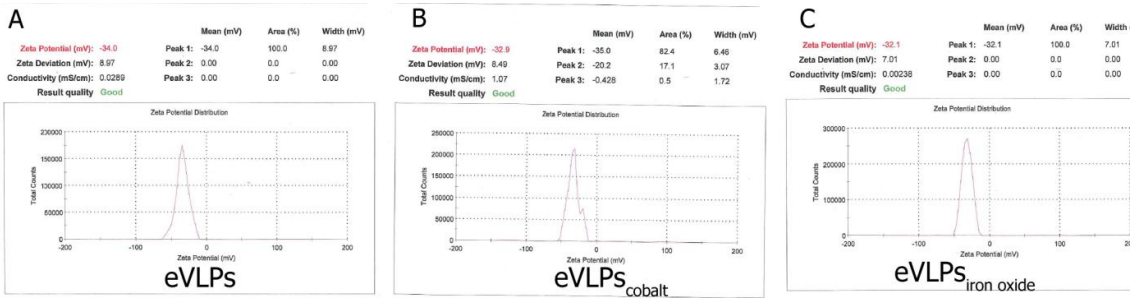

Figure 6.11– Examples of zeta potential results for (A) CPMV eVLPs, (B) $VLPs_{cobalt}$ and (C) $VLPs_{iron\ oxide}$. Data show no significant change of the particle outer–surface confirming the mineralization is internal.

Previously, it has been found that externally mineralized CPMV particles are robust and the coat proteins cannot be released even by denaturation under harsh conditions (e.g. denaturing with sodium dodecyl sulfate at 100 ºC for 30 min) as demonstrated in chapter 3 (Aljabali et al, 2011; Steinmetz et al, 2009b). Here, however, sodium dodecyl sulfate polyacrylamide gel electrophoresis (SDS–PAGE) of the denatured proteins from "top component" and wild–type CPMV isolated from infected plants, which consist of naturally occurring empty particles from a wild–type infection, CPMV eVLPs, $VLPs_{cobalt}$ and $VLPs_{iron\ oxide}$ (Figure 6.12–A) all gave a similar pattern of bands after Coomassie Blue staining consisting of the L and S capsid proteins. The difference in the size of the S proteins isolated from wild–type virus and the eVLP samples is due to the differing degrees of C–terminal processing. These results indicate that the coat proteins are accessible, indicating that the mineralization is, indeed, internal. Further confirmation that the capsid structure is preserved, and that the eVLPs were not externally mineralized, was provided by analysis of the intact particles by agarose gel electrophoresis (Figure 6.12–B). Coomassie Blue staining revealed that all the VLPs, which were devoid of RNA, whether containing internalized metal/metal oxide or not, had the same mobility. By contrast, the RNA–containing particles from natural populations of particles gave a typical complex pattern.

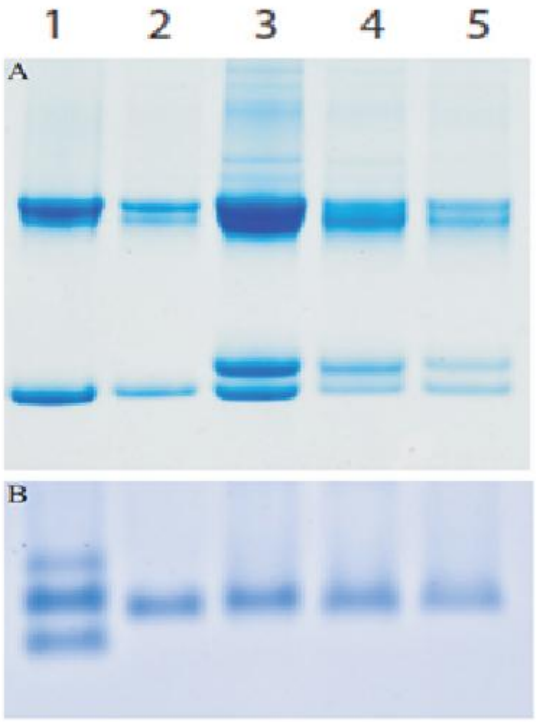

Figure 6.12– Gel electrophoresis analysis for internally mineralized CPMV eVLPs. A) SDS–PAGE and B) native 1% agarose gel stained with coomassie blue. Lane 1: CPMVwt; lane 2: CPMVwt "top component" (devoid of RNA); lane 3: CPMV eVLPs; lane 4: $VLPs_{cobalt}$; lane 5: and $VLPs_{iron\ oxide}$.

Further analysis confirmed that the mineralized VLPs contained both the coat proteins and either cobalt or iron, respectively. Samples of each unmineralized eVLP, $VLPs_{cobalt}$ and $VLPs_{iron\ oxide}$ were spotted onto a nitrocellulose membrane, which, after blocking, was probed with polyclonal antibodies raised in rabbits against CPMV particles. The binding of the antibodies was detected using a goat anti–rabbit IgG coupled to horseradish peroxidise and the signals were visualised by chemiluminescence. In each case, a dark signal was obtained confirming the presence of CPMV coat protein in all the VLP samples (Figure 6.13–A). This is in contrast to external mineralization of CPMV where the coat protein is not immunologically detected. Similarly, each of eVLP, $VLPs_{cobalt}$ and $VLPs_{iron\ oxide}$ were spotted onto a nitrocellulose membrane and probed with either a cobalt–specific stain (1–nitroso–2–naphthol) or Prussian blue staining to identify iron. Only the $VLPs_{cobalt}$ stained orange (Figure 6.13–B), showing the presence of cobalt, and only the $VLPs_{iron\ oxide}$ stained blue, showing the presence of iron, within the VLPs (Figure 6.13–C).

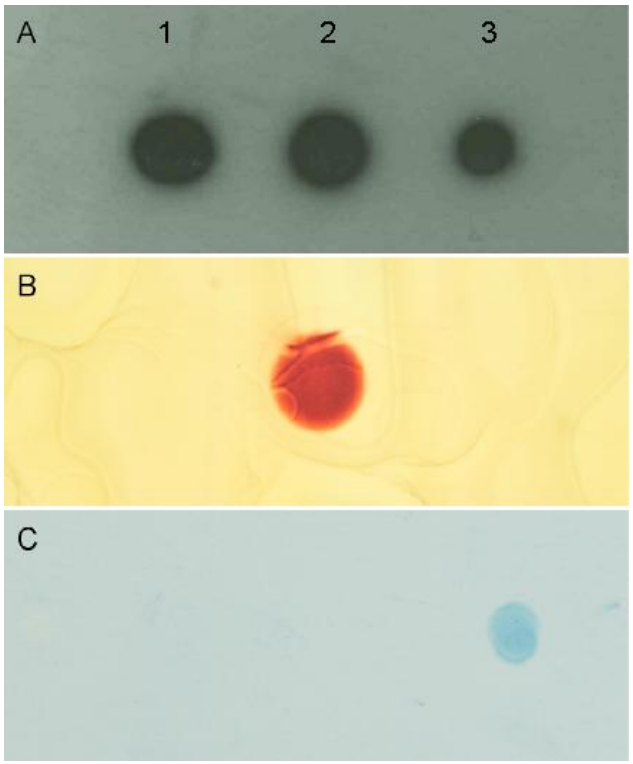

Figure 6.13– Images of VLPs spotted on a nitrocellulose membrane probed with: (A) polyclonal antibodies raised against CPMV particles – dark spots show intact CPMV coat protein; (B) 1–nitroso–2–naphthol to stain for cobalt; (C) Prussian blue stain for iron. Column 1, eVLPs; column 2, $VLPs_{cobalt}$; column 3, $VLPs_{iron\ oxide}$.

To demonstrate that the external coat of the metal containing VLPs is still amenable to chemical modification, $VLPs_{cobalt}$ were functionalised at solvent–exposed lysines with succinimide ester activated biotin by an adaptation of a previously published standard procedure (Steinmetz et al, 2006a). The binding of both $^{Biotin}VLPs_{cobalt}$ and $^{Biotin}VLPs$ to streptavidin–modified chips was monitored by surface plasmon resonance (SPR). In each case a response was observed, Figure 6.14, confirming that chemical modification of the VLP capsid exterior had successfully occurred, irrespective of the internal mineralization. This provides the first evidence that the external surface of eVLPs and internally mineralized VLPs can be chemically modified using the same approach taken for wild–type CPMV. Comparison of normalized sensograms recorded at the same VLP concentration (based on protein content as estimated by UV–visible spectroscopy) showed a two and a half fold increase in resonance units consistent with the increase in mass associated with the loading of cobalt within the VLP. To confirm the

covalent attachment of $^{Biotin}VLPs_{cobalt}$ to the modified chip, the chip was examined using AFM as shown in Figure 6.15.

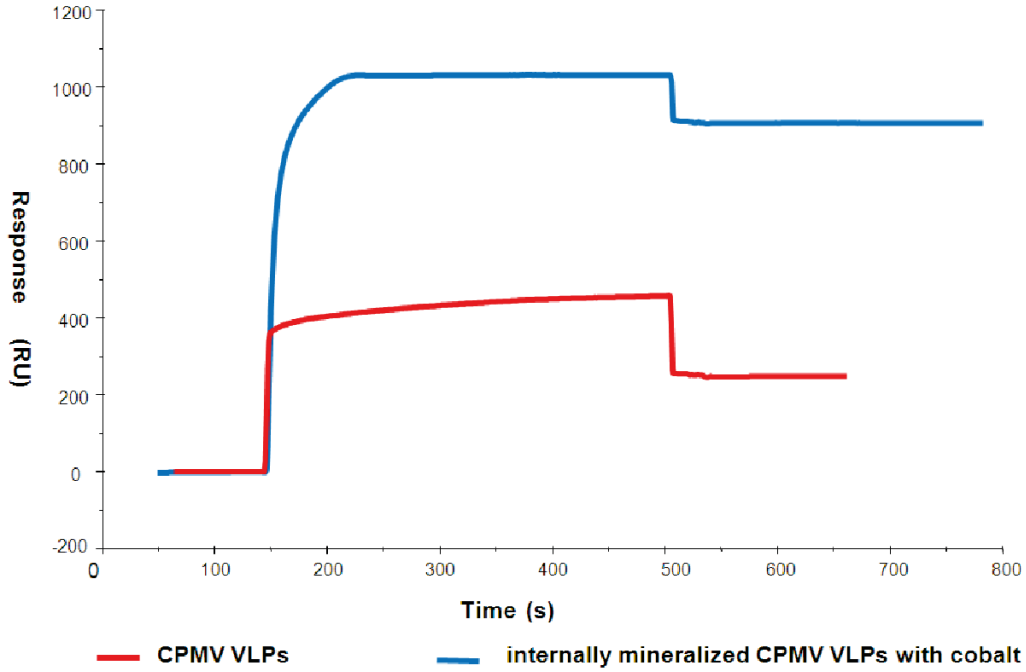

Figure 6.14– Sensogram showing the evolution of resonance units (RU) versus time during association and dissociation measurements of $^{Biotin}VLPs$ (red) and $^{Biotin}VLPs_{cobalt}$ (blue) on a streptavidin–modified chip. The association is measured at approximately the same concentration (as determined by UV–vis spectroscopy) of $^{Biotin}VLPs$ A delay of 100 seconds is applied and the association is allowed to occur during 360 seconds before the flow is switched to buffer for the dissociation step.

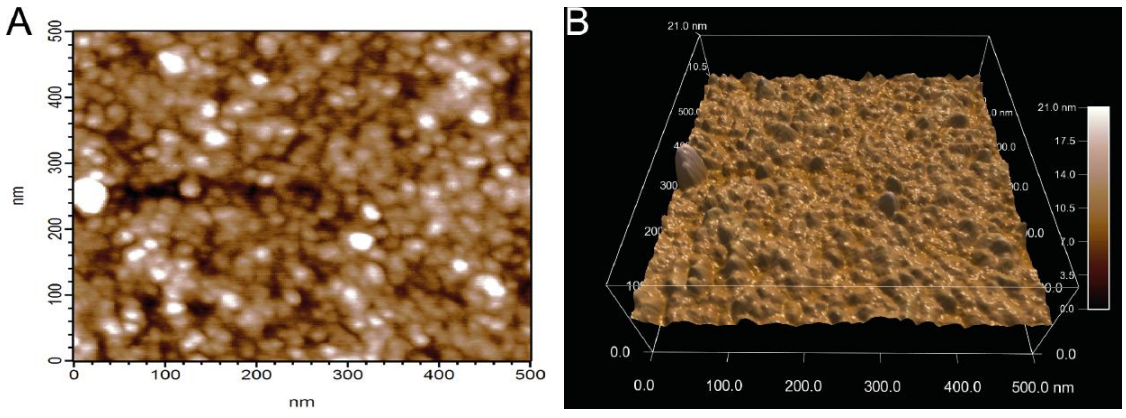

Figure 6.15– AFM image for $^{Biotin}VLPs_{cobalt}$ on a SA–functionalised chip. (A) Chip surface with $^{Biotin}VLPs_{cobalt}$, (B) 3–D image of the same surface.

In an attempt to establish the nature of the iron oxide formed within the eVLPs, Mössbauer spectroscopy analysis for the particles in frozen solution was obtained as shown in Figure 6.16. At 80 K, in frozen solution, a single quadrupole split doublet was observed with isomer shift (i.s.) of 0.45 mms^{-1} and quadrupole splitting (q.s.) of 0.81 mms^{-1}. The values of i.s. and q.s. are consistent with the iron oxide being present within the virus capsid $VLPs_{iron\ oxide}$ as superparamagnetic magnetite nanoparticles; at room temperature i.s. values have been reported to range from 0.30 – 0.36 mms^{-1} and q.s. values from 0.60 – 0.65 mms^{-1} (Wang & Jiang, 2009).

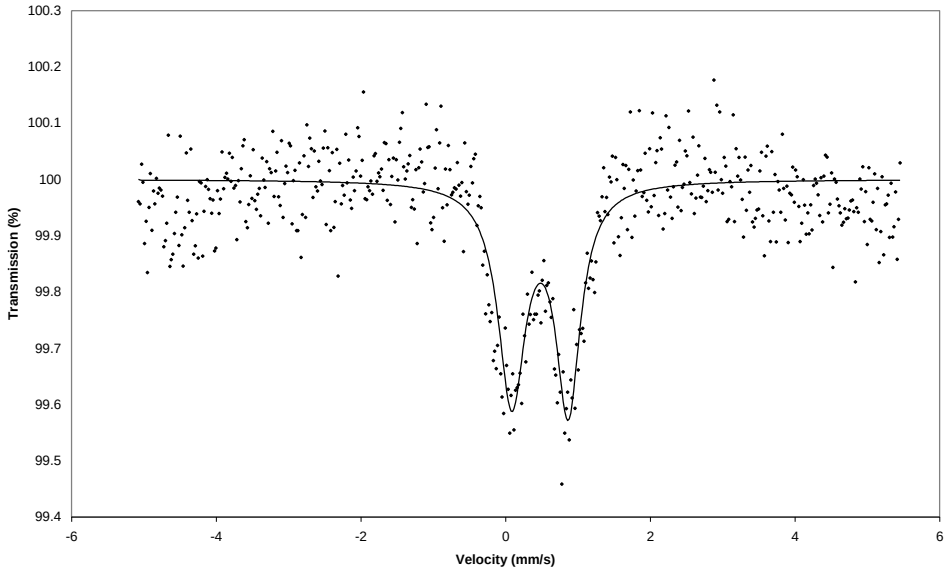

Figure 6.16– Frozen solution Mössbauer spectrum at 80 K of $VLPs_{iron\ oxide}$.

Vibrating sample magnetometry of $VLPs_{iron\ oxide}$ is also fully consistent with the particles exhibiting superparamagnetic behaviour with a blocking temperature (T_B) of around 60 K and ferromagnetic behaviour below the blocking temperature. The zero field cooled (ZFC) and field cooled (FC) magnetization curves (Figure 6.17) are typical magnetization curves for magnetic nanoparticles. Under FC conditions, there is no sharp change in the magnetization value from 300 K to 10 K. The ZFC curve shows a broad maximum at the temperature corresponding to TB, below which there is a decrease in magnetization.

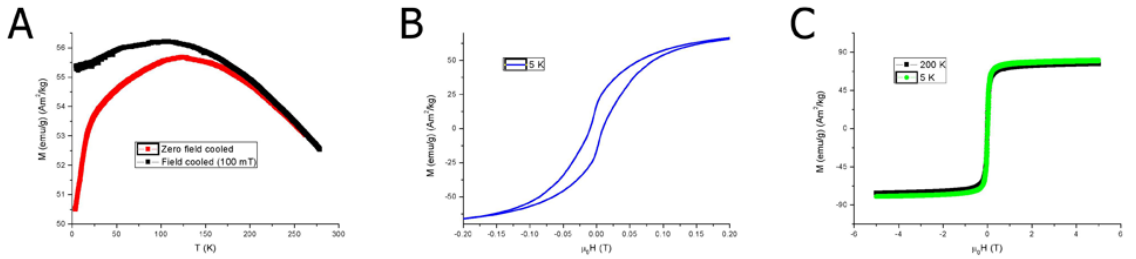

Figure 6.17– Zero field cooled (ZFC) and field cooled (FC) of $VLPs_{iron\ oxide}$ particles. (A) magnetization curves (B) hysteresis loops at (5 K) and (C) hysteresis loops above (200 K) and below (5 K) the blocking temperature (60 K).

The now readily available CPMV eVLPs were used, without further genetic or chemical modification, to easily encapsulate cobalt or iron oxide within the capsid interior. Previously, it has been shown that CPMVwt particles are permeable to caesium ions and that penetration probably occurs via channels at the five–fold axes of the virus particles, where the S subunits cluster. These channels are funnel–shaped, with the narrow end at the outer surface of the virus particle and the wider end in the interior (Lin & Johnson, 2003). The opening at the narrow end is about 7.5 Å in diameter. Further down the five–fold axis, a second constriction can be found which occurs as a result of the three N–terminal residues of the S subunits forming a pentameric annulus structure. In this structure, the amino group of the N–terminus forms a hydrogen bond with the main chain carbonyl oxygen of the neighbouring third residue, the opening at this point is ca. 8.5 Å as shown in Figure 6.18. It is proposed that it is through these channels that the cobalt and iron ions enter the inside of the eVLP. The fact that the pentameric annulus controls access to the interior of the eVLP is supported by the observation that the addition of a methionine residue to the N–terminus of the S protein prevents penetration by cobalt ions, presumably by occluding the channel with a bulky side chain. In addition, it was confirmed that the presence of the 24 amino acids extension on the C–terminus, which are responsible for the slow–migrating form (S) upon particle separation by electrophoresis, prevented loading with cobalt and iron oxide (Sainsbury F. et al, 2011). Normally, these 24 a.a are trimmed (not cleaved) with plant proteinase. Alternatively, the 24-a.a extension can be trimmed with chymotrypsin to convert the slow–migrating to the fast–migrating form *in vitro* (Niblett & Semancik, 1969a).

The charge on the internal surface of the capsid is negative, arising from glutamic acid and aspartic acid residues. The electrostatic interactions between the internal surface and the incorporated metal ions entrap them within the capsid. Even six hours dialysis against buffer does not remove the electrostatically entrapped metal ions. On further treatment, either reduction for cobalt or alkaline hydrolysis for the iron oxide, the metal ions act as nucleation sites for metal particle formation or further autocatalytic hydrolysis (Wade et al, 1991) to produce iron oxide, respectively. The encapsulation processes occur at ambient temperature, in aqueous media, producing little waste, so are environmentally friendly. In addition, amino acid residues on the exterior surface of the internally mineralized particles remain amenable for chemical modification. The ability to both encapsulate materials (e.g. nanoparticles or drugs) within the eVLP and to chemically modify the external surface opens up routes for the further development of CPMV–based systems for the targeted delivery of therapeutic agents and for other uses in biomedicine.

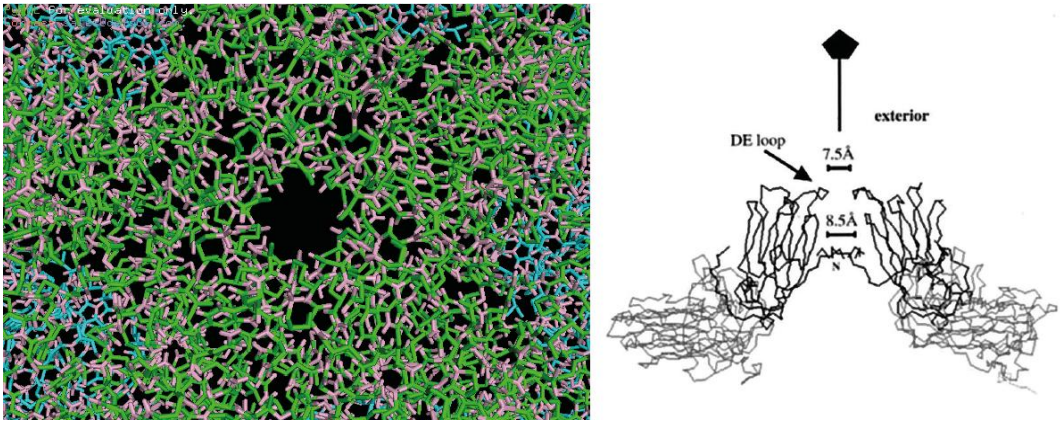

Figure 6.18– Illustration of one of 12 pentamers of CPMV at the five–fold axis. Showing the pore with an average opening of 7.5 Å. Images generated with PyMOL–1–2b8eval version. The accessible surface profile of CPMV half capsid file is available at http://viperdb.scripps.edu with PDB–ID (1NY7). Right panel is reproduced from (Lin & Johnson, 2003).

6.3.2 $VLPs_{iron\ oxide}$ as possible targeted hyperthermia therapeutics

In recent decades, the major challenge for oncologists has been the understanding of biological mechanisms underlying tumour formation, as well as the development of therapies

that can reduce or even eliminate these tumours (Ito et al, 2005). One method is hyperthermia treatment, which is a therapeutic procedure that promotes the increase of temperature in the targeted tissues. Hyperthermia activity is based on the fact that a temperature increase to between 41–45 °C can induce tumour death (Gamarra et al, 2010; Harima et al, 2001; Harima & Sawada, 2009). Investigating the application of magnetic materials to promote hyperthermia began in 1957, in which Gilchrist treated various tissue samples with 20–100 nm particles of γ–Fe_2O_3 exposed to a 1.2 MHz magnetic field (Gilchrist et al, 1957). Iron oxide nanoparticles exposure to external magnetic field can generate heat through oscillation of their magnetic moment therefore generating regional heating. In this temperature range, tumour cells are generally found to be more heat–sensitive compared to normal cells because tumour cells are poorly oxygenated (Berry & Curtis, 2003), It has been demonstrated that the ideal iron oxide nanoparticles are within the size range of 20–25 nm (personal communication, Prof Quentin Pankhurst, The Royal Institution of Great Britain). Therefore, CPMV eVLPs offer an ideal nanocontainer of internal diameter ~ 25–26 nm to generate highly monodisperse iron oxide nanoparticles. The $VLPs_{\text{iron oxide}}$, as has been demonstrated, can be easily functionalised with biocompatible reagents or targeting moieties. The proposed mechanism is depicted in Figure 6.19.

CPMV eVLPs have been loaded with iron oxide and externally functionalised with A20FMDV2 peptide, which binds specifically to the surface integrin present on many tumours (for further discussion see chapter 9). The peptide was designed with a biotin group at one end to help detection with streptavidin functionalised gold nanoparticles as shown in Figure 6.20. $^{\text{A20FMDV2}}$VLPs particles were reacted with cascade blue dye as described in section 6.2.15 to quantify the number of peptides bound to the capsid. The doubly–functionalised particles $^{\text{A20FMDV2}}\text{VLPs}^{\text{Cascade blue dye}}$ were purified rigorously by sucrose gradient followed by dialysis against 10 mM sodium phosphate buffer pH 7.0. The number of remaining reactive carboxylates was calculated, from the absorbance of the dye at λ_{399} and $\varepsilon = 27000\ M^{-1}\ cm^{-1}$, to be ~100–110 ± 8 per virion. This equates to approximately 45–50 peptides being bound to each eVLP. Moreover, a control experiment was conducted with unmodified eVLPs and the cascade blue

dye and the number of dyes was found to be ~145–150 dye per virus, this is almost full coverage of all surface accessible carboxylates. The next step will be to test these particles for thermal properties in collaboration with Prof. Quentin Pankhurst, The Royal Institution of Great Britain.

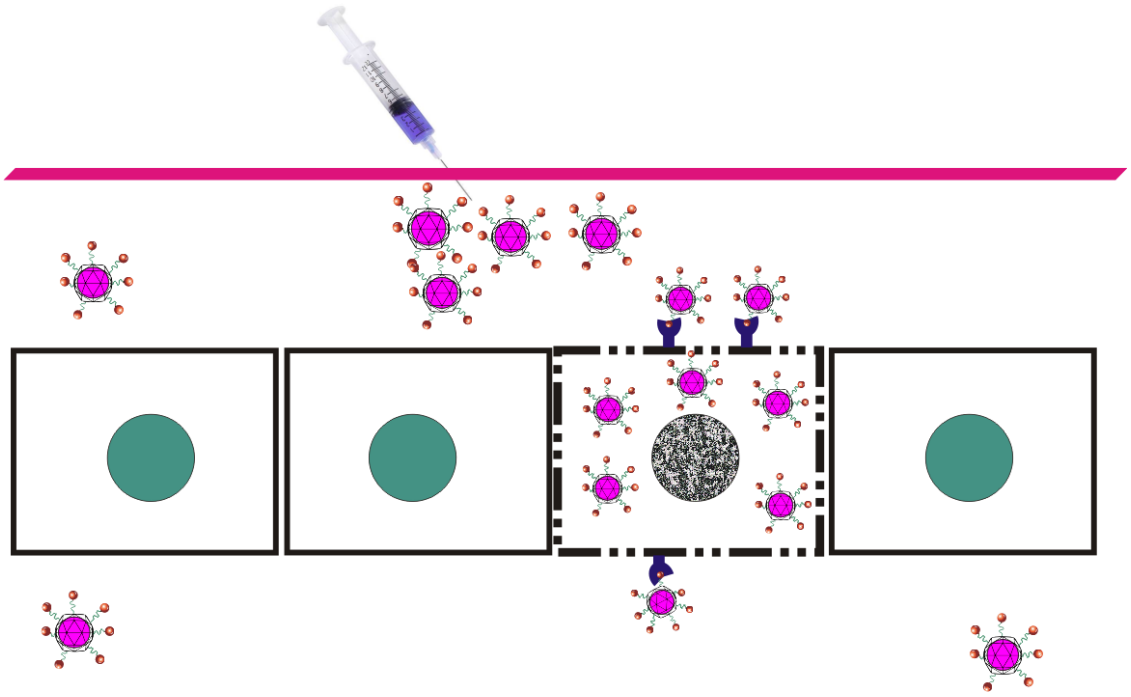

Figure 6.19– Schematic illustration of the mechanism of hyperthermia treatment using iron oxide loaded CPMV eVLPs. Iron oxide loaded particles are specifically designed to selectively attach to the cancer cells without affecting the healthy cells. The localized particle in an external magnetic field generates heat destroying the targeted cells.

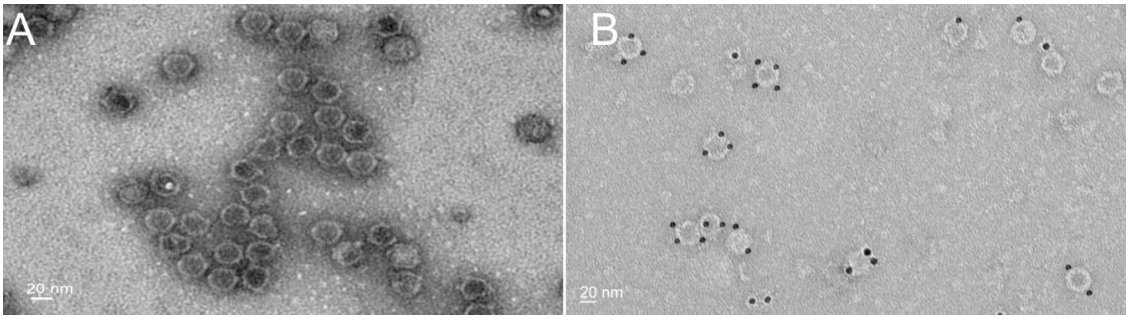

Figure 6.20– TEM images for (A) stained $VLPs_{iron\ oxide}$ and (B) $^{A20FMDV2}VLPs_{iron\ oxide}$ detected by streptavidin functionalised gold nanoparticles. It has been found that there are 40–50 peptides per virus using a carboxylate–specific fluorescent dye.

6.4 Internal functionalisation of CPMV eVLPs

Further to the internal mineralization of CPMV eVLPs, studies on the chemical modification of the interior of the capsid will be presented in this section. These studies focussed on internal cysteines, which have been identified previously (Wang et al, 2002d; Wang et al, 2003b). As there are no accessible cysteines on the exterior of CPMV particles, the internal cysteines provide a unique functional amino acid within the virus particles.

CPMV eVLPs can be viewed as molecular "nano–vessels". Thus, therapeutic molecules can be housed within their interior, anticancer drugs and positively charged molecules can be diffused and trapped within the interior of eVLPs. Housing drug molecules within eVLPs may restrict their functionality until their release is triggered by host cell acid hydrolase enzymes that are contained within the lysosomes. In addition, some protein cages, including CCMV, have structural features that allow for the controlled encapsulation and release of material (Douglas & Young, 1998a; Speir et al, 1995). Herein, the uses of CPMV eVLPs as a potential drug carrier are explored.

6.4.1 Results and discussion

6.4.1.1 Diffusion of molecules into CPMV eVLPs

The results in Sections 6.3.1 and 6.3.2 demonstrated the ability of CPMV eVLPs to encapsulate metals and metal oxides within the capsid. The next step was to expand further the versatility of CPMV eVLPs to package other smaller molecules. As previously described, the pores are essential for material diffusion and for allowing the inner cavity to be accessible. Once inside the interior cavity, the diffused materials either can interact with the negatively charged interior or can be covalently attached to specific amino acids depending upon the chemistry used. Covalent interior modification has been reported in the literature for CPMV, MS2 and TMV (Hooker et al, 2007b; Hooker et al, 2004; Schlick et al, 2005b(Rhee et al, 2011)).

The ability to modify the external surface with moieties for diseased cell targeting, along with the packaging capacity, enables CPMV eVLPs to perform as multifunctional

nanocontainers. Moreover, the results presented here indicate that the diffusion mechanism is charge–related. Therefore, positively charged molecules such as rhodamine, gemcitabine and doxorubicin (Figure 6.21) were selected together with cisplatin drug to test the loading capabilities of eVLPs.

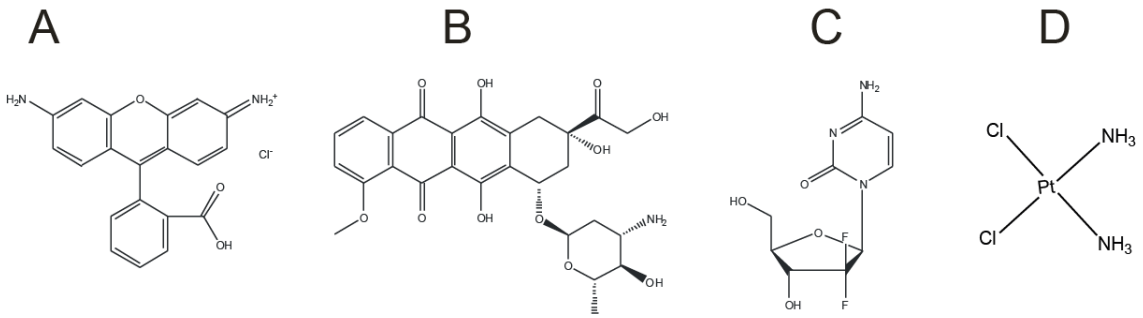

Figure 6.21– Chemical structures for (A) rhodamine hydrochloride, (B) doxorubicin, (C) gemcitabine and (D) cisplatin.

6.4.1.2 VLPs$_{rhodamine}$

Most of the reported work in the literature using eVLPs as drug carriers requires further modifications to the virus particles. For example, MS2 requires genetic engineering to the capsid in order to package molecules (Brown et al, 2002). On the contrary, the approach described here offers a direct route to packaging molecules without the need for further modification of CPMV eVLPs but by using the natural properties of the native particles. The loading capacity of rhodamine was determined photometrically to be ~20–30 molecules per virus (Figure 6.22). TEM analysis confirmed the integrity of the modified particles and did not result in a detectable change in the capsid diameter or morphology, Figure 6.23. The ability to diffuse positively charged rhodamine is presumably due to the electrostatic interaction with the overall internal anionic surface of the virus capsid and not because of covalent attachment. The VLPs$_{rhodamine}$ were monitored by spectrophotometry over 4 days without the loss of the fluorescent signal or its intensity, suggesting strong electrostatic interaction within the interior of the capsid, which is sufficient to trap the positively charged rhodamine. It is still not clear why there are a low number of rhodamine molecules per virus. A control experiment was

performed where rhodamine was incubated with bottom component particles (containing RNA–1), at the same molar ratio, followed by identical protocols for purification and characterisation. There was no fluorescent signal detected on unstained agarose gel electrophoresis, Figure 6.24 lane 2. This is direct evidence that the particles must be empty in order to incorporate rhodamine.

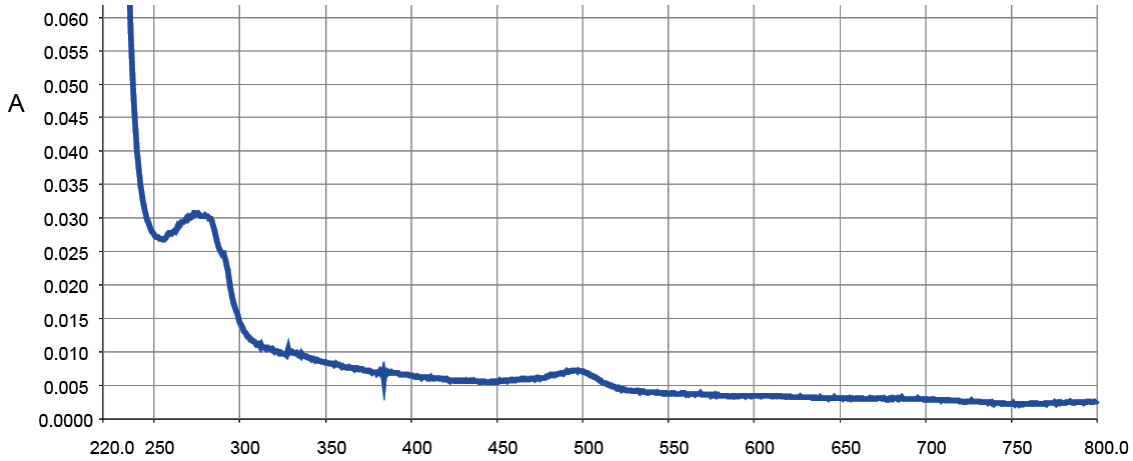

Figure 6.22– UV–vis for $VLPs_{rhodamine}$. Rhodamine was measured with an excitation wavelength at 500 nm and extinction coefficient of 80000 M^{-1} cm^{-1}.

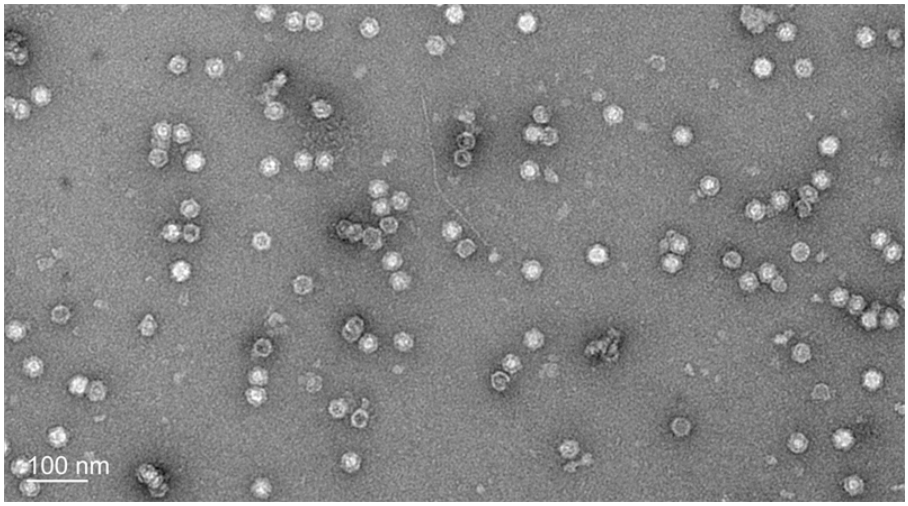

Figure 6.23– TEM image of $VLPs_{rhodamine}$ stained with 2% UA.

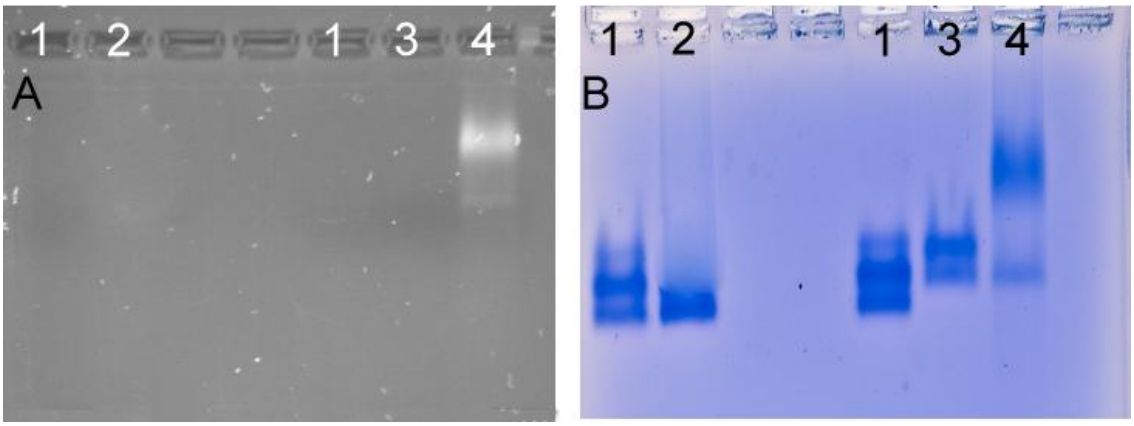

Figure 6.24– Wild–type and $VLPs_{rhodamine}$ on a 1.2% agarose gel. (A) Unstained, (B) Coomassie stained gels. Lane 1, wild–type CPMV; 2, CPMV "bottom component" (positive control); 3, eVLPs; 4, $VLPs_{rhodamine}$. Only $VLPs_{rhodamine}$ were visible in the unstained gel because of rhodamine entrapment within eVLPs.

6.4.1.3 $VLPs_{doxorubicin}$

Doxorubicin is commonly used in cancer therapy but has undesirable cytotoxicity and side effects. It is also a very popular research tool due to its fluorescence properties (Mohan & Rapoport, 2010). To minimize these side effects, an attempt has been made here to encapsulate doxorubicin in biodegradable naturally occurring nanoparticles, CPMV eVLPs. Doxorubicin is a positively charged chemotherapeutic agent so it might interact with the negatively charged interior of the capsid.

eVLPs were incubated with doxorubicin followed by rigours purification (as described in section 2.17) and native gel electrophoresis was employed to verify that doxorubicin was present within the eVLPs. Unstained native agarose gel electrophoresis for the rigorously purified particles(as describe in section 2.17) revealed a fluorescent band as shown in Figure 6.25–A, this corresponds to $VLPs_{dox}$, whereas the free doxorubicin moved in the opposite direction. In addition, $VLPs_{dox}$ were visible in solution with a light raspberry colour. This suggests that the doxorubicin is present within the eVLPs and it is being kept inside the particles by an electrostatic interaction within the interior of the capsid. After staining by Coomassie blue, $VLPs_{dox}$ and eVLPs were visible on the same gel (Figure 6.25–C).

The spectrophotometric analysis of $VLPs_{dox}$ gave ~8–10 (± 3) molecules per virus capsid. The doxorubicin showed no leakage or diffusion through the opened pores over the four days that the particles were monitored. A fundamental issue in drug delivery is the ability of the drug to reach its target within the nucleus (Topoisomerase–2). In the case of doxorubicin, this approach appears very promising, as the drug might slowly diffuse from the particles without relying on degradation of the particles. This approach is still under investigation.

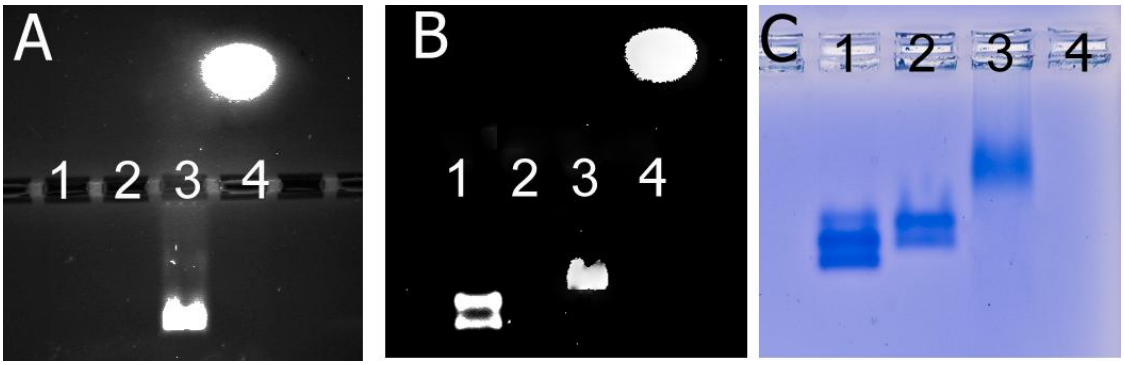

Figure 6.25– eVLPs and $VLPs_{dox}$ on a 1.2% agarose gel. (A) unstained, (B) ethidium bromide stained and (C) Coomassie stained gels. Lane 1, wild–type CPMV; 2, eVLPs; 3, $VLPs_{dox}$; 4, free doxorubicin. Only $VLPs_{dox}$ were visible in the unstained gel because of doxorubicin entrapment within eVLPs.

6.4.1.4 Internal chemistry of CPMV eVLPs

The cysteine side chain is a reactive nucleophile that can react with a large variety of molecules (Hermanson, 2008). However, as wild–type CPMV particles contain no cysteines on the exterior of the capsid (Wang et al, 2002a) this makes cysteine–labelling specific to within the eVLPs. It has been shown that small thiol–selective dyes such as ethylmercury phosphate (EMP), fluorescein and thiol–selective stilbene derivatives (Wang et al, 2002e) can be coupled to the interior of wild–type CPMV. EMP was found to be coupled to an internal cysteine residue on the L subunit, at amino acid position 295, whereas the 5–maleimidofluorescein was attached to cysteines on both the S and L subunit, though the exact positions have not been identified yet. Internal labelling with nanogold, with a diameter of 1.4 nm, could not be achieved, as the pore size is approximately 7.5 Å (Wang et al, 2002d; Wang et al, 2003b).

Chemical modification of the interior cysteines within CPMV eVLPs with sulfhydryl–reactive fluorescent dye (DyLight–488 maleimide) was explored. Incubating DyLight–488 maleimide with eVLPs, followed by rigorous purification, resulted in an average of 60–70 (± 2) dyes per virus covalently attached, presumably to the interior surface, Figure 6.26. Repeating this experiment five times resulted in consistent labelling with almost the same numbers of dyes per virus. The data suggests one dye per asymmetric unit. Applying the same approach, as a control experiment, with the CPMV "bottom component" resulted in no fluorescence detected on agarose gel or by UV–vis.

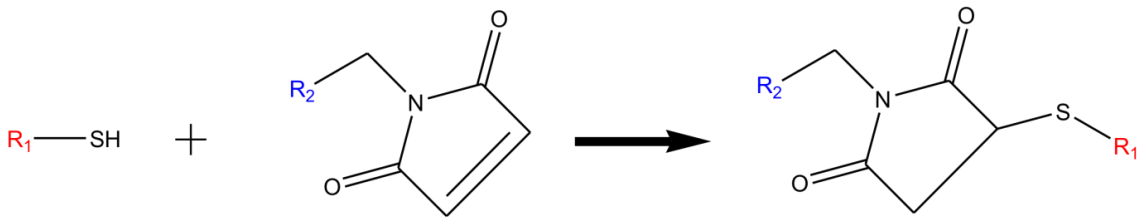

Figure 6.26– The double bond of maleimide reacts specifically with sulfhydryl groups to form a stable thioether bond. R_1 represents the virus and R_2 represents the maleimide containing dye.

Examination of the crystal structure of wild–type CPMV, which is similar to CPMV eVLPs, from the VIPERDB database suggested that the dye is possibly bound to cysteine 295 of the large protein as shown in Figure 6.27. Furthermore, the crystal structure revealed a possible disulfide bridge formed between Cys–187 and Cys–355. The distance between Cys–187 and Cys–355 is 2.82 Å as shown in Figure 6.27, a distance consistent with the published data for disulfide bond formation (Sevier & Kaiser, 2002).

Based on this knowledge, the second approach involved the addition of 10 mM TCEP as a reducing agent together with the DyLight–488 maleimide and CPMV eVLPs. Interestingly, the spectroscopic analysis resulted in approximately 120 (± 10) dyes per virus; presumably, the reducing agent disrupts the disulfide bond between Cys–187 and Cys–355, making another thiol group available. The number of dyes per virus was consistent upon repeating the experiments five times. The size of the dye might be blocking the third cysteine side chain thiol. Incubating

TCEP with the virus particles followed by purification and then conducting the same reaction, resulted in no significant changes in the number of dyes covalently bound to the interior of the virus capsid.

The characterisation of the modified particles with or without the reducing agents revealed no morphological changes and the particles remained intact as confirmed by agarose gel electrophoresis, Figure 6.28. The intensity of the $VLPs_{DyLight-488}$ differs between the two conditions (with or without reducing agent), this presumably arises from differential modification of the L and S coat proteins, and the corresponding UV–vis spectrum is shown in Figure 6.29. The difference in the intensity of the modified particles is clear in the presence of TCEP and confirmed by the quantitative analysis (Figure 6.29–B). Particle integrity was confirmed by TEM. The addition of the reducing agent has no effect on particle stability or morphology as shown in Figure 6.30.

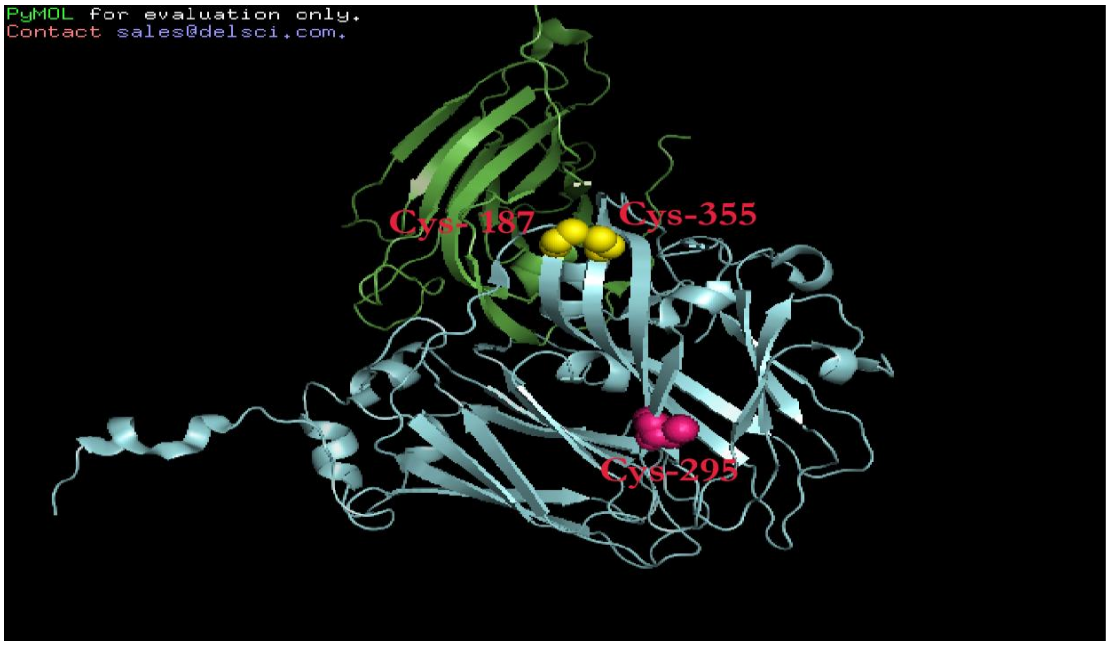

Figure 6.27– The CPMV asymmetric unit. (Small subunit in green; large subunit in blue) with positions of the possibly accessible cysteines. Cys–295 is the most likely to be accessible while Cys–187 and Cys–355 form disulfide bonds. Inside view image generated by PyMol free evaluation software.

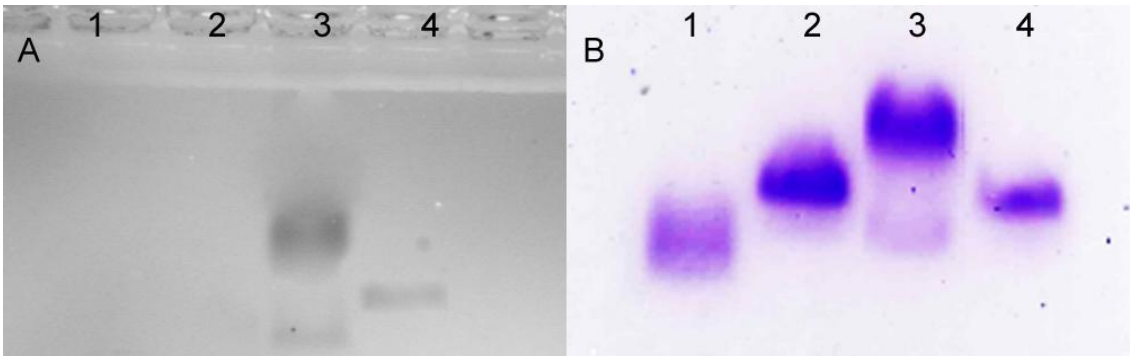

Figure 6.28– Wild–type and $VLPs_{DyLight–488}$ migration on a 1.2% agarose gel. (A) unstained, (B) Coomassie stained gels. Lane 1, wild–type CPMV; 2, eVLPs (positive control); 3, $VLPs_{DyLight–488}$ (double the amount in order to see the weak band); 4, $VLPs_{DyLight–488}$ reduced.

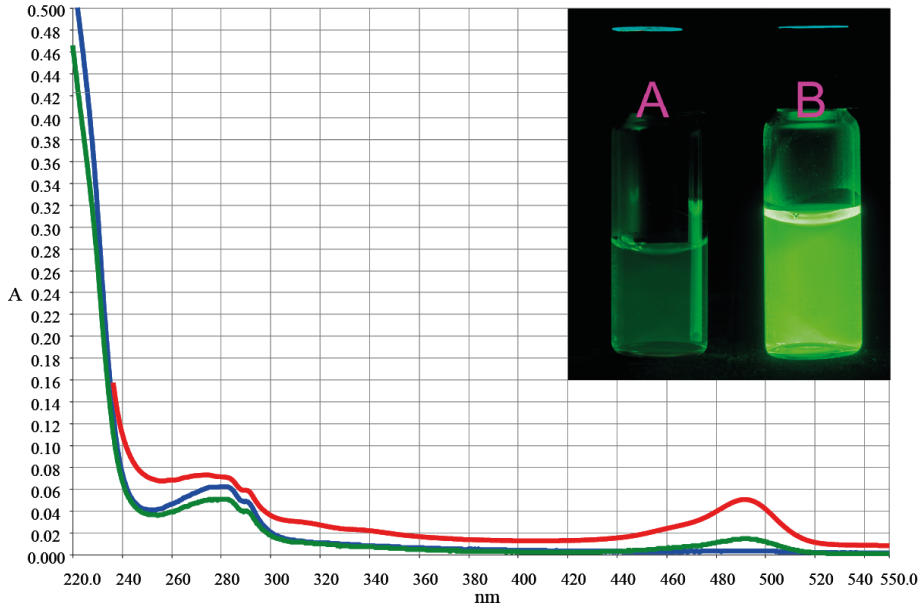

Figure 6.29– UV–visible spectrum for $VLPs_{DyLight–488}$. Blue line is unmodified eVLPs; green line, $VLPs_{DyLight–488}$ unreduced; red line, $VLPs_{DyLight–488}$ reduced. The inset is a digital image of A, $VLPs_{DyLight–488}$ unreduced and B, $VLPs_{DyLight–488}$ reduced.

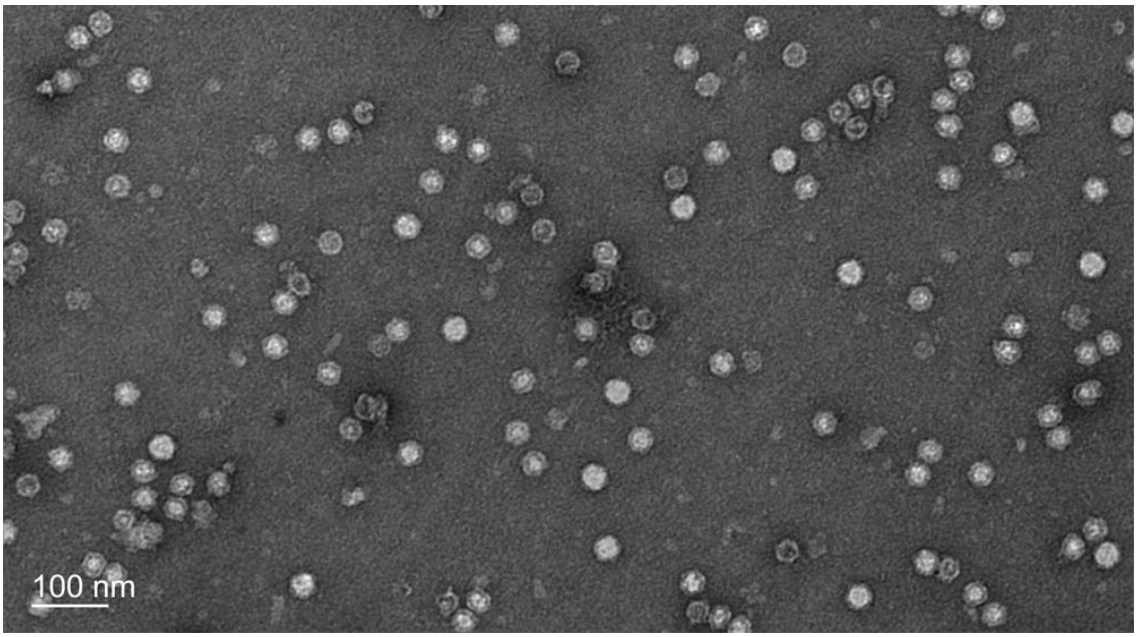

Figure 6.30– TEM image of $VLPs_{DyLight-488}$ in the presence of TCEP. The particles were purified on sucrose gradient and stained with 2% UA.

6.4.1.5 Encapsulation of anti-cancer drugs within eVLPs via LBL approach

The layer–by–layer (LBL) technique is a versatile tool for the controlled fabrication of multimaterial surface coatings (Leguen et al, 2007). The degradable–layered structure would be advantageous for drug delivery and has the potential to carry targeting agents. The aim of this work was to investigate if CPMV eVLPs coated with polyelectrolyte could be used to carry anticancer drugs.

CPMV eVLPs do not appear to have a built–in mechanism for controlled drug encapsulation and release as for CCMV (Speir et al, 1995), RCNMV (Loo et al, 2007) and MS2 (Wu et al, 1995). As an initial attempt to infuse molecules within eVLPs, rhodamine and doxorubicin were studied. However, relying on the electrostatic interaction of the positively charged molecules within the virus capsid is not sufficient to deliver a high payload of drugs to the targeted diseased cells.

CPMV can be considered as an anionic macromolecule with an isoelectric point (p*I*) of 4.3 ± 0.1 at physiological pH (pH 7.4) (Kewalramani et al, 2011). This property is valuable for

the electrostatic LBL self–assembly technique. Previously, it was shown to be possible to sequentially deposit a thin layer of cationic polyelectrolyte such as poly(allylamine hydrochloride) (PAH) onto the wild–type CPMV capsid by electrostatic adsorption of positively charged polyelectrolyte, PAH, onto the CPMV capsid. Subsequent treatment with gold containing solution followed by reduction, resulted in gold coating the CPMV particles, denoted Au–CPMV (see chapter 4). Here, a LBL approach was adopted to trap drug molecules within the eVLPs by the sequential deposition of oppositely charged polyelectrolytes on the external surface, Figure 6.31.

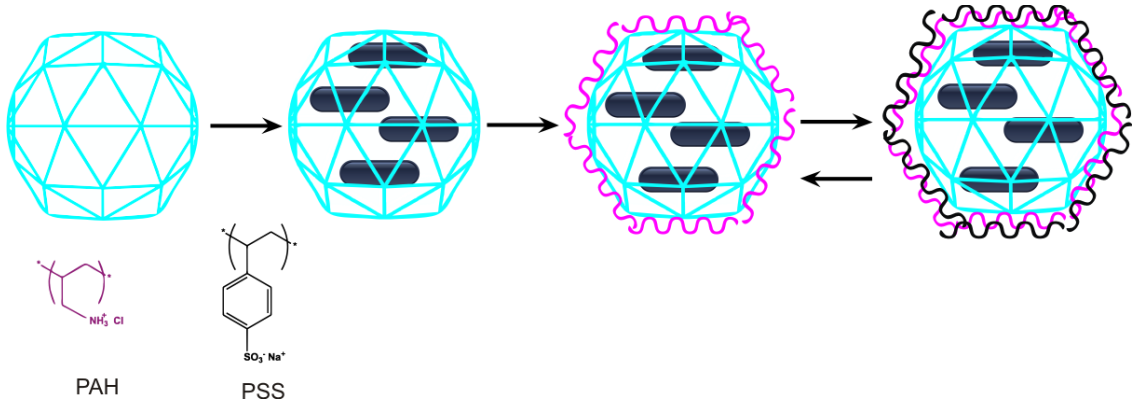

Figure 6.31– Schematic representation of the deposition of polycation/polyanion onto eVLPs. Particles were incubated with gemcitabine or cisplatin followed by deposition of PAH and PSS electrolytes. Polyanion/polycation coated particles were washed thoroughly between each step of the electrolyte deposition with Milli–Q water. TPolyanion/polycation process was repeated for either one or two cycles.

Gemcitabine or cisplatin were incubated with eVLPs. The subsequent deposition of alternating polyelectrolytes was monitored by zeta potential (ZP) measurements. The complete reversal of surface charge is a crucial factor for the stepwise growth of the multilayer electrolytes. The negatively charged CPMV eVLPs particles (uncoated) have a ZP value of ca. –31.9 (± 2.5) mV. The presence of PAH on the virus capsid caused a reversal in the ZP to approximately +67.8 (± 2.0) mV for $^{PAH}VLPs_{drug}$ whereas $^{(PAH/PSS)1}VLPs_{drug}$ have a ZP value of –55.3 (± 1.7) mV, Figure 6.32. Alternating ZP measurements with the subsequent deposition of cationic/anionic electrolytes, confirmed the stepwise formation of the PAH/PSS/PAH layers on

the eVLPs capsid. Furthermore, alternating polycation/polyanion to generate thicker electrolyte shells enabled the preparation of $^{(PAH/PSS)2}VLPs_{drug}$.

PAH and poly(styrenesulfonate) (PSS) were selected because they are a well–studied combination and the process conditions, including salt concentration, pH and incubation times, are well established (Goldenberg et al, 2002; Shenoy et al, 2003; Zahr et al, 2004). The PAH/PSS combination was therefore used to form a degradable polyelectrolyte shell on the eVLPs capsid. Both PAH and PSS were selected as they are salt and pH responsive, this property might be vital in acting as a release mechanism for the encapsulated drug molecules. The release time was dependent on the thickness of the assembled polyelectrolyte layers. Thicker shells led to longer release times; this was measured by the time it took polyelectrolyte–coating on the particles to dissolve and the return of the native form of particles as shown by agarose gel electrophoresis Figure 6.34.

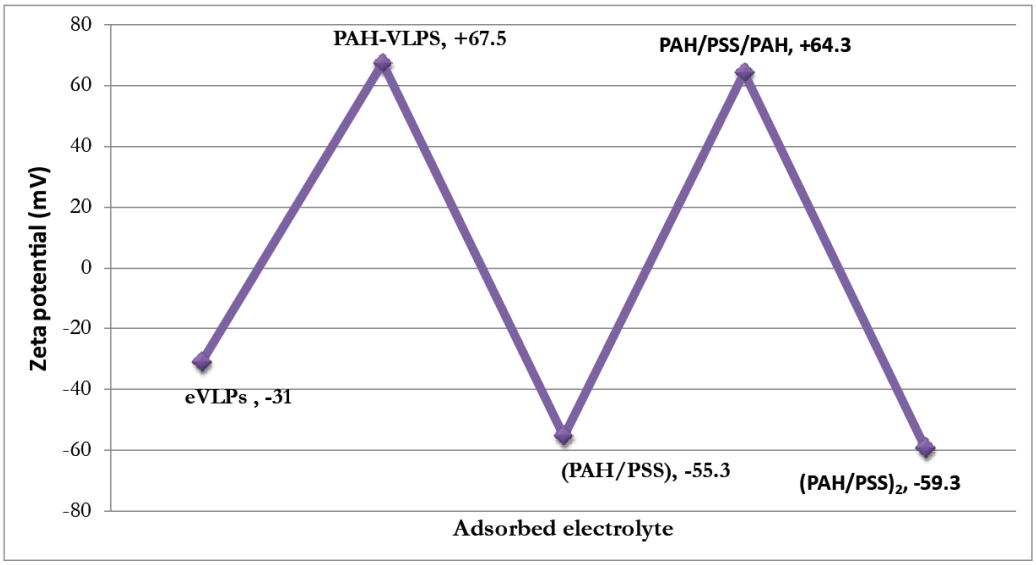

Figure 6.32– Charge reversal on alternate adsorption of polyelectrolyte on $^{(PAH/PSS)1–2}VLPs_{gemcitabine}$.

To visually determine whether LBL assembly successfully encapsulated the drug particles, TEM was used to examine the surface characteristics, integrity, and size of the polyelectrolyte coated eVLPs. Figure 6.33 shows no morphological change of $^{(PAH/PSS)2}VLPs_{drug}$ and that the particles remain intact and monodisperse. The diameter of the virus is approximately 30–31 nm indicating an increase of ~2–3 nm in diameter as measured from TEM

images. This was in agreement with the measured DLS data, which showed an increase in 2 nm per layer.

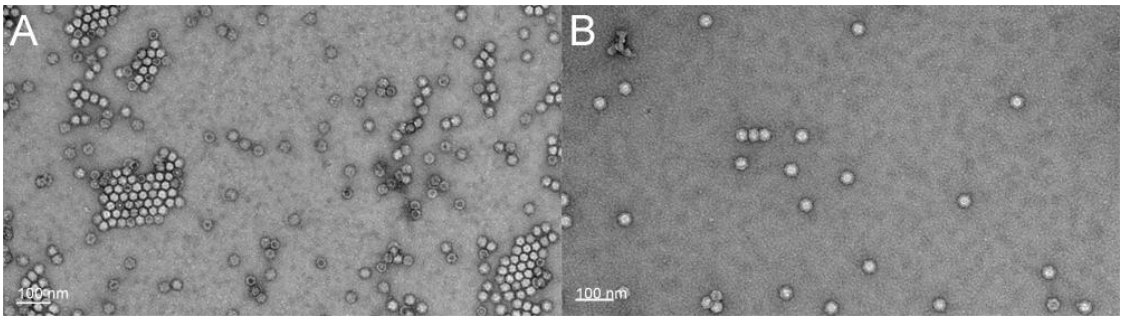

Figure 6.33– Stained TEM images of polyelectrolyte coated $VLPs_{drug}$. (A) $^{(PAH/PSS)2}VLPs_{gemcitabine}$; (B) $^{(PAH/PSS)2}VLPs_{cisplatin}$. The particles are intact and narrowly distributed without any significant morphological changes. The particle diameter increased by 2–3 nm and no aggregation was recorded on any of the samples prepared.

In addition, due to the fluorescence property of gemcitabine, the integrity of the $^{(PAH/PSS)2}VLPs_{gemcitabine}$ particles was confirmed by agarose gel electrophoresis. Figure 6.34–A shows an unstained agarose gel of wild–type CPMV, a positive control of $VLPs_{gemcitabine}$ and the polyelectrolyte coated $^{(PAH/PSS)2}VLPs_{gemcitabine}$. According to their migration in an electric field towards the anode, intact virions of CPMVwt can be separated into a higher– and lower–mobility form. The $^{(PAH/PSS)2}VLPs_{gemcitabine}$ particles show no mobility on agarose gel Figure 6.34–lane 3. This is not a consequence of the massive increase in the particles size or because of particle aggregation but probably due to the presence of the charged electrolytes on the particle surface. This was supported by no aggregation being observed in any of the prepared samples using TEM as shown in Figure 6.33. Moreover, removing the polyelectrolytes resulted in the polyelectrolyte coated particles returning to their native form for either wild–type CPMV or eVLPs as confirmed by agarose gel electrophoresis. The fluorescence band on the unstained agarose gel resulted from the pyrimidine group on the gemcitabine, indicating successful drug encapsulation (Figure 6.34–A). Coomassie stained agarose (Figure 6.34–B) confirms the presence of the coat protein and that the particles were intact.

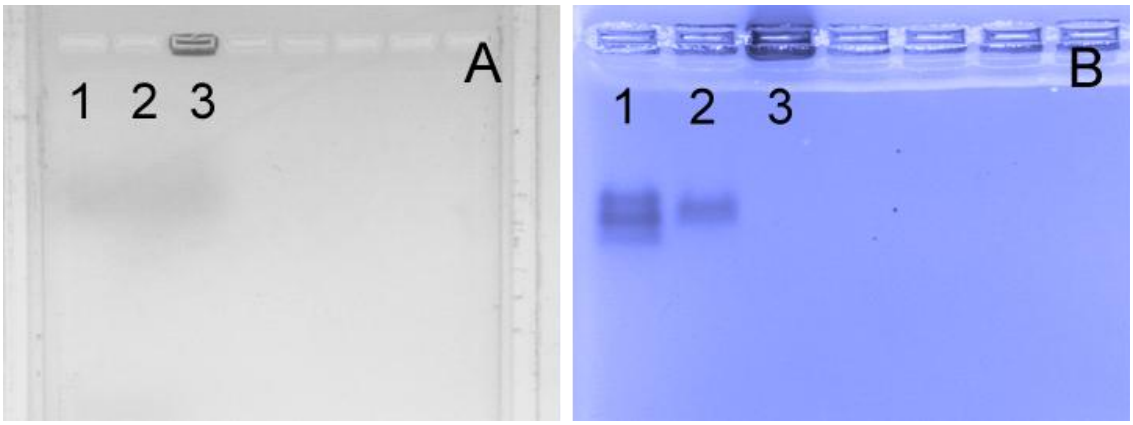

Figure 6.34– Agarose gel electrophoresis of gemcitabine loaded VLPs. (A) unstained; (B) Coomassie stained. Lane 1; CPMV wild–type, 2; $eVLPs_{gemcitabine}$, 3; $^{(PAH/PSS)2}VLPs_{gemcitabine}$. The bands on the unstained gel correspond to the successful encapsulation of gemcitabine within the $^{(PAH/PSS)2}VLPs_{gemcitabine}$.

In a control experiment, and to demonstrate that the electrolyte is essential for drug encapsulation within CPMV eVLPs, gemcitabine was incubated with eVLPs Figure 6.35 lane 2 following the same procedure described earlier. The agarose gel shows no changes in the bands mobility and no fluorescent signal was detected suggesting that the gemcitabine is not encapsulated within the eVLPs upon staining with Coomassie blue (Figure 6.35–B). Moreover, $VLPs_{gemcitabine}$ did not show any fluorescence bands in unstained gels. This is in agreement with the need for the electrolytes to entrap the drug molecules within the VLPs; only wild–type particles were visible with ethidium bromide staining (Figure 6.35–A). However, the rhodamine and doxorubicin encapsulation within the capsid without the need for the polyelectrolyte was based on the electrostatic interaction. This might have to do with the size and the strength of the electrostatic interaction within the capsid interior.

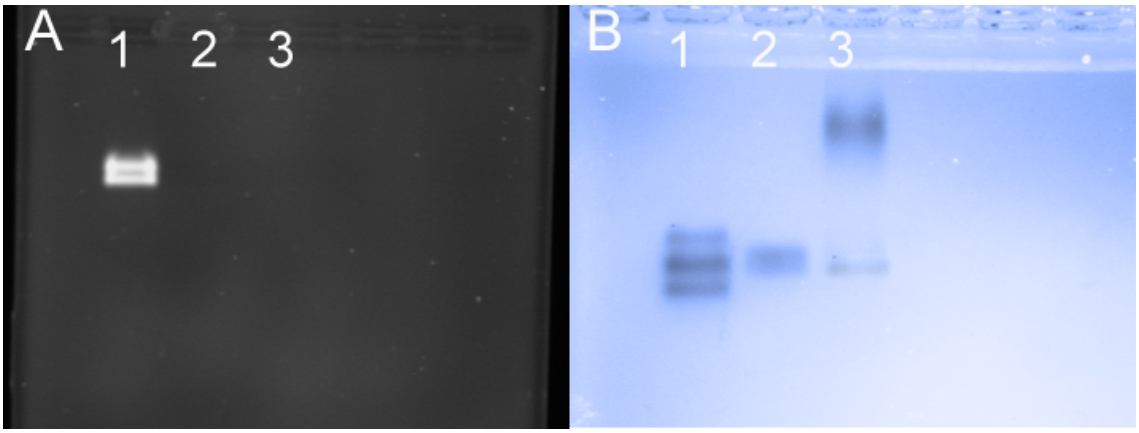

Figure 6.35– Coomassie stained gel electrophoresis for $VLPs_{gemcitabine}$ (without electrolyte coatings). (A) ethidium bromide and (B) Coomassie stained agarose gel electrophoresis. Lane 1: wild–type CPMV; 2: eVLPs; 3: $VLPs_{gemcitabine}$.

EDXS elemental analysis for $^{(PAH/PSS)2}VLPs_{gemcitabine}$ and $^{(PAH/PSS)2}VLPs_{cisplatin}$ confirmed the presence of fluorine (gemcitabine) and platinum (cisplatin), respectively, Figure 6.36. As a negative control $^{(PAH/PSS)2}$VLPs did not reveal any corresponding elements. This confirms that both gemcitabine and cisplatin were encapsulated within the VLPs.

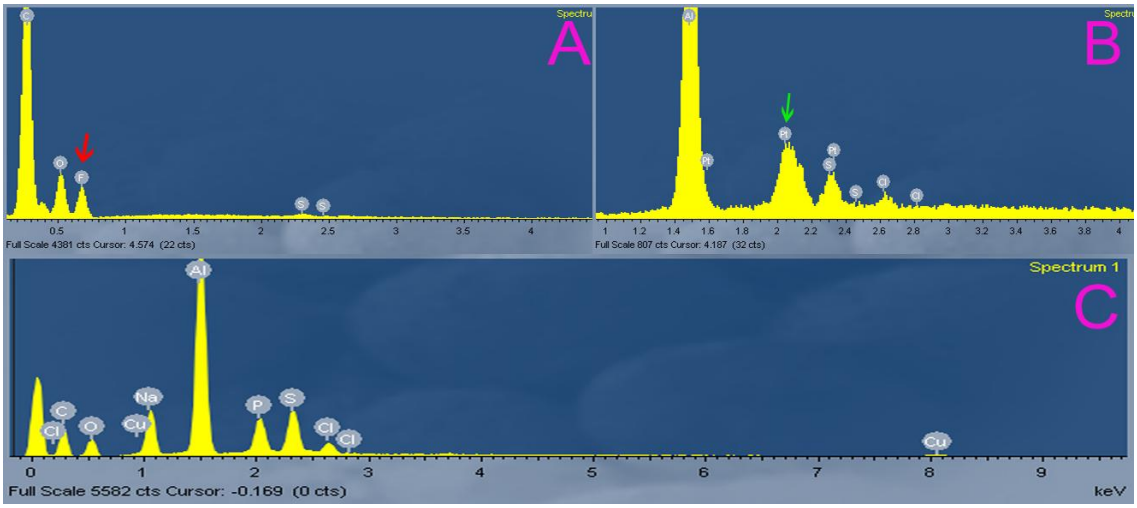

Figure 6.36– Elemental energy–dispersive X–ray spectroscopy analysis of (A) $^{(PAH/PSS)2}VLPs_{gemcitabine}$ (B) $^{(PAH/PSS)2}VLPs_{cisplatin}$ (C) negative control $^{(PAH/PSS)2}$VLPs. The arrows indicate major peaks.

6.4.1.6 Release studies

Evidence that gemcitabine was encapsulated within the polymer coated CPMV eVLPs was obtained by deliberately rupturing the polyelectrolyte layers by incubating $^{(PAH/PSS)2}VLPs_{gemcitabine}$ with 0.15 M buffer pH 7.4 at 37 °C. Several different conditions were tried before establishing this as the best conditions within the physiological range. Faster release was accomplished in the same buffer at pH 9–10 or acetate buffer pH 5.3. Agarose gel electrophoresis was a very useful tool in tracking the changes in the polyelectrolyte disintegration. Figure 6.37 confirmed the removal of the polyelectrolytes and release of the encapsulated drug molecules from within eVLPs. The modified $^{(PAH/PSS)2}VLPs_{gemcitabine}$ particles were dialysed against 0.150 M sodium phosphate buffer at pH 7.4 and 37 °C, the first 2 hours revealed no visible bands on the gel and there was no free gemcitabine detected in the dialysis buffer. However, after 20–24 hours incubation, native intact form of eVLPs was observed in lane 3, Figure 6.37–D, and the gemcitabine was detected in the dialysate. However, the lower mobility band highlighted in lane 3 indicated the presence of the 24 aa C–terminus extension of the particles, which, in recent experiments has been shown to block the pores (see 6.4.1.7). Therefore, the same experiment was repeated with "top component particles" (TOP) extracted on caesium chloride gradient from wild–type that lack the 24 aa extension.

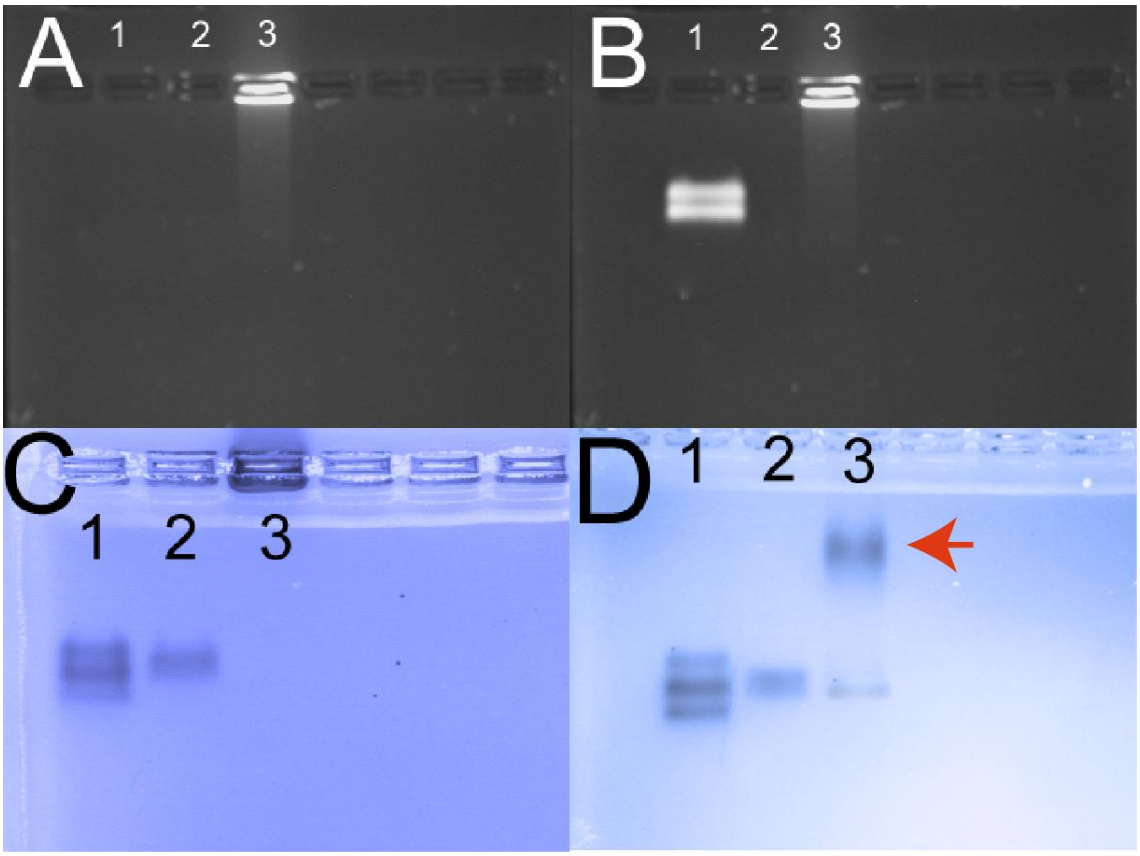

Figure 6.37– Release studies using gel electrophoresis for $^{(PAH/PSS)2}VLPs_{gemcitabine}$. (A) unstained (B) ethidium bromide stained (C) Coomassie stained before the dialysis against 0.15 M sodium phosphate buffer pH 7.4, and (D) Coomassie stained after the dialysis. Lane 1: wild–type CPMV; lane 2: CPMV eVLPs (positive control); lane 3: $^{(PAH/PSS)2}VLPs_{gemcitabine}$. The observed band is in agreement with the removal of the polyelectrolyte and release of the drug molecules while the eVLPs remain intact. The red arrow indicates the higher mobility band of eVLPs with the 24 aa un–cleaved.

Agarose gel electrophoresis for native particles was used to monitor the electrolyte breakdown at set time points. A lag (delay) in the release of $^{(PAH/PSS)2}TOP_{gemcitabine}$ was observed, the first two hours resulted in no gemcitabine molecules being detected in the aqueous solution and agarose gel electrophoresis confirmed no changes to the particles pattern. The release profile gel is shown in Figure 6.38; the result suggests slow degradation of the electrolyte shell in the first six hours as a result of the polyelectrolyte being partially ruptured. As a result, free gemcitabine molecules were expelled from the interior of the eVLPs as confirmed spectrophotometrically and quantified as described in section 6.2.12. Once the electrolyte capsule starts to rupture, the electrostatic interactions between the charged moieties of the polymer are probably weakened and this will lead to the degradation of the polyelectrolyte shell.

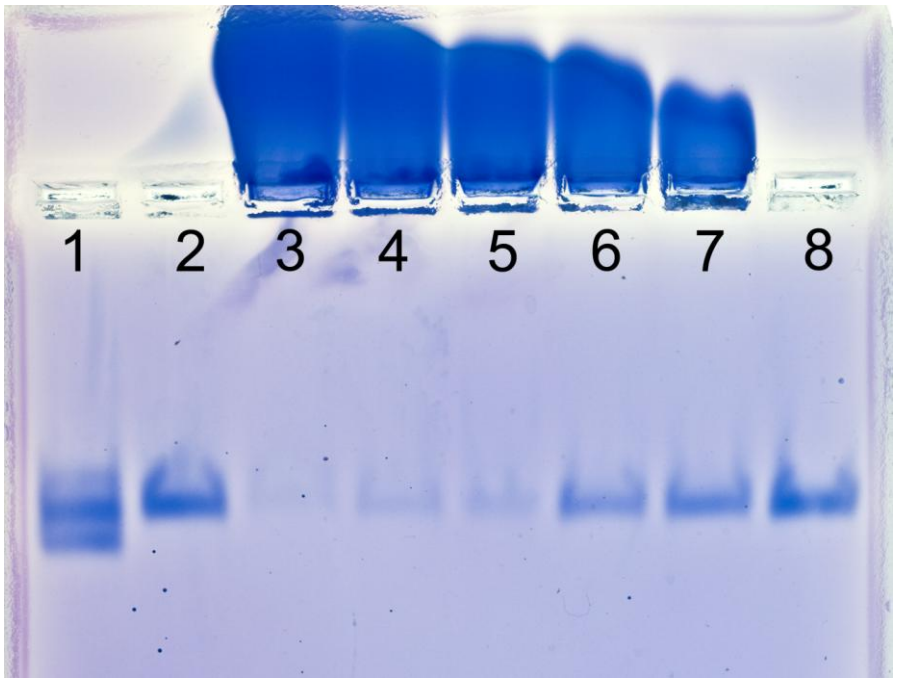

Figure 6.38– $^{(PAH/PSS)2}TOP_{gemcitabine}$ drug release using 0.150 M sodium phosphate buffer at pH 7.4 and 37 °C. Lane 1, wild–type CPMV; 2, "TOP component"; 3–8, $^{(PAH/PSS)2}TOP_{gemcitabine}$ after 2, 4, 6, 8, 12 and 24 hours.

6.4.1.7 The effect of the 24 amino acids C–terminus extension on loading

It has been demonstrated that the pores at the five–fold axis are essential for the loading of eVLPs with metals and metal oxides (Aljabali et al, 2010c). These pores were a key factor governing the success of material diffusion. Although the size and charge of the encapsulated molecules are important and limited by the pore size. However, it was also observed that sometimes it was impossible to diffuse material into eVLPs. Further investigation has been carried out by the Evans and Lomonossoff groups on this phenomenon and its role in internal mineralisation. The external twenty four amino acid residues originating from the carboxyl terminus of the S coat protein prevents internal mineralisation of the particle (Sainsbury, F. et al, just accepted manuscript in ChemBioChem). Therefore, the removal of the 24 aa extension is essential for material diffusion into the eVLPs. This could be achieved by chymotrypsin treatment of the particles prior to any loading experiment.

6.5 Conclusions

The synthesis of metal and metal oxides within readily available CPMV eVLPs is both size and shape–constrained by the inner cavity of the virus. Evidently, small molecules have access to the interior of the virus through pores at the 5–fold axis, this was supported by the observation that the addition of a methionine residue to the N–terminus of the S protein prevents penetration by cobalt ions, presumably by occluding the channel with a bulky side chain (Aljabali et al, 2010c). The charge on the internal surface of the capsid is negative, arising from glutamic acid and aspartic acid residues. The electrostatic interactions between the internal surface and the incorporated metal ions entrap them within the capsid, as are positively charged molecules such as rhodamine and doxorubicin. In addition, the LBL self–assembly of polyelectrolytes was demonstrated to be successful in encapsulating gemcitabine and cisplatin within eVLPs. The stepwise assembly of alternating charged electrolytes, PAH and PSS, was confirmed by zeta potential experiments. TEM images confirmed the integrity of the particles and EDXS confirmed the presence of the drug molecules within eVLPs. The surface of the polyelectrolyte–coated eVLPs may be further functionalised with PEG molecules, to reduce the immune response, or with A20FMDV2 peptide for targeting. This approach offers a very promising method to generate multifunctional nanoparticles for targeting, imaging and specificity.

6.6 References:

Aljabali AAA, Sainsbury F, Lomonossoff GP, Evans DJ (2010) Cowpea Mosaic Virus Unmodified Empty Viruslike Particles Loaded with Metal and Metal Oxide. *Small* **6:** 818–821

Aljabali AAA, Shah SN, Evans–Gowing R, Lomonossoff GP, Evans DJ (2011) Chemically–coupled–peptide–promoted virus nanoparticle templated mineralization. *Integrative Biology* **3:** 119–125

Brown WL, Mastico RA, Wu M, Heal KG, Adams CJ, Murray JB, Simpson JC, Lord JM, Taylor–Robinson AW, Stockley PG (2002) RNA bacteriophage capsid–mediated drug delivery and epitope presentation. *Intervirology* **45:** 371 – 380

Conn MM, Rebek J (1997) Self–assembling capsules. *Chemical Reviews* **97:** 1647–1668

Douglas T, Young M (1998) Host–guest encapsulation of materials by assembled virus protein cages. *Nature* **393:** 152–155

Douglas T, Young M (1999) Virus particles as templates for materials synthesis. *Advanced Materials* **11:** 679–681

Gamarra LF, daCosta AJ, Mamani JB, Ruiz RD, Pavon LF, Sibov TT, Vieira ED, Silva AC, Pontuschka WM, Amaro E (2010) Ferromagnetic resonance for the quantification of superparamagnetic iron oxide nanoparticles in biological materials. *Int J Nanomed* **5:** 203–211

Gilchrist RK, Medal R, Shorey WD, Hanselman RC, Parrott JC, Taylor CB (1957) Selective Inductive Heating of Lymph Nodes. *Ann Surg* **146:** 596–606

Goldenberg LM, Jung B, Wagner J, Stumpe J, Paulke BR, Görnitz E (2002) Preparation of Ordered Arrays of Layer–by–Layer Modified Latex Particles. *Langmuir* **19:** 205–207

Harima Y, Nagata K, Harima K, Ostapenko VV, Tanaka Y, Sawada S (2001) A randomized clinical trial of radiation therapy versus thermoradiotherapy in stage IIIB cervical carcinoma. *Int J Hyperther* **17:** 97–105

Harima Y, Sawada S (2009) Hyperthermia classic commentary: 'A randomized clinical trial of radiation therapy versus thermoradiotherapy in stage IIIB cervical carcinoma' by Yoko Harima, International Journal of Hyperthermia 2001;17:97–105. *Int J Hyperther* **25:** 344–346

Hermanson TG (2008) *Bioconjugate Techniques*, second edn. London: Academic Press.

Hooker JM, Datta A, Botta M, Raymond KN, Francis MB (2007) Magnetic resonance contrast agents from viral capsid shells: A comparison of exterior and interior cargo strategies. *Nano Letters* **7:** 2207–2210

Hooker JM, Kovacs EW, Francis MB (2004) Interior surface modification of bacteriophage MS2. *J Am Chem Soc* **126:** 3718 – 3719

Ito A, Shinkai M, Honda H, Kobayashi T (2005) Medical application of functionalized magnetic nanoparticles. *Journal of Bioscience and Bioengineering* **100:** 1–11

J. Wellink (1998) Plant Virology Protocols: From Virus Isolation to Transgenic Resistance Vol. 81, Totowa, New Jersey: Humana Press

Joelson T, Akerblom L, Oxelfelt P, Strandberg B, Tomenius K, Morris TJ (1997) Presentation of a foreign peptide on the surface of tomato bushy stunt virus. *Journal of General Virology* **78:** 1213–1217

Kewalramani S, Wang S, Lin Y, Nguyen HG, Wang Q, Fukuto M, Yang L (2011) Systematic approach to electrostatically induced 2D crystallization of nanoparticles at liquid interfaces. *Soft Matter* **7:** 939–945

Lammers T, Subr V, Ulbrich K, Peschke P, Huber PE, Hennink WE, Storm G (2009) Simultaneous delivery of doxorubicin and gemcitabine to tumors in vivo using prototypic polymeric drug carriers. *Biomaterials* **30:** 3466–3475

Leguen E, Chassepot A, Decher G, Schaaf P, Voegel J, Jessel N (2007) Bioactive coatings based on polyelectrolyte multilayer architectures functionalized by embedded proteins, peptides or drugs. *Biomolecular Engineering* **24:** 33–41

Lin T, Johnson JE (2003) Structures of picorna–like plant viruses: implications and applications. *Adv Virus Res* **62:** 167–239

Lomonossoff GP, Hamilton WDO (1999) Cowpea mosaic virus–based vaccines. *Curr Top Microbiol* **240:** 177–189

Lomonossoff GP, Johnson JE (1996) Use of macromolecular assemblies as expression systems for peptides and synthetic vaccines. *Curr Opin Struc Biol* **6:** 176–182

Loo L, Guenther RH, Lommel SA, Franzen S (2007) Encapsidation of nanoparticles by red clover necrotic mosaic virus. *Journal of the American Chemical Society* **129:** 11111–11117

Ludwig C, Wagner R (2007) Virus–like particles–universal molecular toolboxes. *Curr Opin Biotechnol* **18:** 537–545

Mason H, Santi L, Huang Z (2006) Virus–like particles production in green plants. *Methods* **40:** 66–76

Mohan P, Rapoport N (2010) Doxorubicin as a Molecular Nanotheranostic Agent: Effect of Doxorubicin Encapsulation in Micelles or Nanoemulsions on the Ultrasound–Mediated Intracellular Delivery and Nuclear Trafficking. *Molecular Pharmaceutics* **7:** 1959–1973

Niblett CL, Semancik JS (1969) Conversion of Electrophoretic Forms of Cowpea Mosaic Virus in Vivo and in Vitro. *Virology* **38:** 685–693

Plummer EM, Manchester M (2010) Viral nanoparticles and virus–like particles: platforms for contemporary vaccine design. *Wiley Interdiscip Rev Nanomed Nanobiotechnol*

Ren Y, Wong S, Lim L (2006) In vitro–reassembled plant virus–like particles for loading of polyacids. *J Gen Virol* **87:** 2749–2754

Sainsbury F, Lomonossoff GP (2008) Extremely High–Level and Rapid Transient Protein Production in Plants without the Use of Viral Replication. *Plant Physiol* **148:** 1212–1218

Sainsbury F, Thuenemann EC, Lomonossoff GP (2009) pEAQ: versatile expression vectors for easy and quick transient expression of heterologous proteins in plants. *Plant Biotechnol J* **7:** 682–693

Saunders K, Sainsbury F, Lomonossoff GP (2009) Efficient generation of cowpea mosaic virus empty virus–like particles by the proteolytic processing of precursors in insect cells and plants. *Virology* **393:** 329–337

Schlick TL, Ding ZB, Kovacs EW, Francis MB (2005) Dual–surface modification of the tobacco mosaic virus. *Journal of the American Chemical Society* **127:** 3718–3723

Sevier CS, Kaiser CA (2002) Formation and transfer of disulphide bonds in living cells. *Nat Rev Mol Cell Bio* **3:** 836–847

Shenoy DB, Antipov AA, Sukhorukov GB, Möhwald H (2003) Layer–by–Layer Engineering of Biocompatible, Decomposable Core−Shell Structures. *Biomacromolecules* **4:** 265–272

Speir JA, Munshi S, Wang G, Baker TS, Johnson JE (1995) Structures of the native and swollen forms of cowpea chlorotic mottle virus determined by X–ray crystallography and cryo–electron microscopy. *Structure* **3:** 63–78

Steinmetz NF, Calder G, Lomonossoff GP, Evans DJ (2006) Plant Viral Capsids as Nanobuilding Blocks: Construction of Arrays on Solid Supports. *Langmuir* **22:** 10032–10037

Steinmetz NF, Shah NS, J. E. Barclay, Rallapalli G, Lomonossoff GP, Evans DJ (2009) Virus–Templated Silica Nanoparticles. *Small* **5:** 813–816

Wade VJ, Levi S, Arosio P, Treffry A, Harrison PM, Mann S (1991) Influence of Site–Directed Modifications on the Formation of Iron Cores in Ferritin. *Journal of Molecular Biology* **221:** 1443–1452

Wang L, Jiang J (2009) Preparation of Fept; Spherical Nanoporous Particles Facilitated by Polyethylene Glycol 4000. *Nanoscale Research Letters* **4:** 1439–1446

Wang Q, Kaltgrad E, Lin TW, Johnson JE, Finn MG (2002a) Natural supramolecular building blocks: Wild–type cowpea mosaic virus. *Chemistry & Biology* **9:** 805–811

Wang Q, Lin T, Tang T, Johnson J, Finn mG (2002b) Icosahedral Virus Particles as Addressable Nanoscale Building Blocks13. *Angewandte Chemie International Edition* **41:** 459–462

Wang Q, Lin TW, Johnson JE, Finn MG (2002c) Natural supramolecular building blocks: Cysteine–added mutants of cowpea mosaic virus. *Chem Biol* **9:** 813–819

Wang Q, Raja KS, Janda KD, Lin TW, Finn MG (2003) Blue fluorescent antibodies as reporters of steric accessibility in virus conjugates. *Bioconjugate Chemistry* **14:** 38–43

Zahr AS, de Villiers M, Pishko MV (2004) Encapsulation of Drug Nanoparticles in Self–Assembled Macromolecular Nanoshells. *Langmuir* **21:** 403–410

Kammen VA (1967) Purification and properties of the components of cowpea mosaic virus. *Virology* **31:** 633-642

Mastico RA, Talbot SJ, Stockley PG (1993) Multiple presentation of foreign peptides on the surface of an RNA-free spherical bacteriophage capsid. *J Gen Virol* **74 (Pt 4):** 541-548

Royston E, Ghosh A, Kofinas P, Harris MT, Culver JN (2007) Self-Assembly of Virus-Structured High Surface Area Nanomaterials and Their Application as Battery Electrodes. *Langmuir* **24:** 906-912

Wang Q, Kaltgrad E, Lin T, Johnson JE, Finn MG (2002) Natural supramolecular building blocks. Wild-type cowpea mosaic virus. *Chem Biol* **9:** 805-811

Wu M, Brown WL, Stockley PG (1995) Cell-Specific Delivery of Bacteriophage-Encapsidated Ricin A Chain. *Bioconjugate Chemistry* **6:** 587-595

Rhee J, Hovlid M, Fiedler JD, Brown SD, Manzenrieder F, Kitagishi H, Nycholat C, Paulson JC, Finn MG (2011) Colorful Virus-like Particles: Fluorescent Protein Packaging by the Qβ Capsid. *Biomacromolecules* **12:** 3977-3981

7 Electroactive CPMV nanoparticles

7.1 Introduction

Miniaturisation of electronically active moieties may play a major role in the nanoelectronics field to develop future electronic devices. However, the miniaturisation (top–down) approach presents a major challenge due to the physical size limitation of materials. Alternatively, bottom–up nanofabrication of electronically active molecules holds great potential in developing large–scale devices that are organised at the molecular level and are stable. One of the key issues is the controlled immobilisation of molecules onto well–defined surfaces. This could be achieved by the synthesis of highly monodisperse synthetic nanostructures such as dendrimers. Ferrocene and ferrocene–modified dendrimers hold great potential for the development of molecular electrochemical batteries (Astruc et al, 2009). For practical purposes, the chemical modification with ferrocene must be site–directed and controlled. Ferrocenes, viologens, quinones, and transition metals (e.g. Ni and Cu) have reversible electrochemical properties. Therefore, these redox centres are frequently used as active electrochemical components (Nijhuis et al, 2007). Ferrocene–based applications have raised considerable interest in many fields of analytical chemistry and recently in nanoscience. This is because of the well–established chemistry of ferrocenes and that the redox–responsive molecules are compatible with existing semiconductor–based microelectronic technology (Lee, 2008).

Ferrocene is stable in aerobic aqueous media and allows rapid and easy access to many derivatives. Besides, the electrochemical properties of ferrocenes both at the surface and in solution are attractive with respect to their detection and quantification (Seiwert & Karst, 2008). Ferrocene derivatives are of much interest in various areas of research and application, for example non–linear optics (Togni & Rihs, 1993), molecular sensors and receptors (Lopez et al, 2004; Newkome et al, 1999), as ferromagnets (Yang et al, 2007) and for electrochemistry and catalysis (Balzani, 2001; Togni & Hayashi, 1995). Further, ferrocenes have been incorporated

into dendrimers (Astruc et al, 2009) and coupled to silica nanoparticles (Beasley & Murray, 2009) for a range of applications.

Ferrocene molecules are organometallic compounds with two stable oxidation states. The chemical structure consists of two cyclopentadienyl rings bound on opposite sides of an iron atom (Staveren & Metzler–Nolte, 2004). Ferrocenes exhibit a reversible one–electron oxidation/reduction at low potentials. The ferrocene molecule is a typical example of a charge–storage molecule (Oms et al, 2005). The iron atom in ferrocene is Fe^{2+} and the ferrocene molecule is neutral. On removing an electron to the adjacent electrode, the iron atom becomes Fe^{3+} and the ferrocene molecule has an overall +1 charge. This charging/discharging property is of great importance in designing nanoelectronics devices or components (Tamura et al, 2008).

7.1.1 Ferrocene functionalised CPMVwt particles (^{Fc}CPMV)

^{Ferrocene}CPMV and ^{Fc}CPMV will be used to refer to ferrocene conjugated to the capsid (superscript refers to molecules bound to the exterior of the capsid). The incorporation of ferrocene moieties to CPMV provided motivation for the synthesis of dendrimer–like structures with well–defined sizes and functionalities (Steinmetz et al, 2006d). CPMV capsids are highly monodisperse, bearing functional surface exposed groups at the periphery of the capsid. Moreover, viruses are highly monodisperse in comparison to their synthetic counterparts. Furthermore, the dendrimer–like ^{Ferrocene}CPMV combines the unique and valuable redox properties of ferrocene moieties with the high symmetrical three–dimensional (3–D) architecture of the virus capsid. This allows precise positioning of the ferrocene onto the virus capsid and makes CPMVwt an ideal scaffold for the synthesis of electro–active viral nanoparticles.

As part of the Evans group's continuing effort to develop CPMV–based sensors, this chapter describes how various coupling strategies can be employed to give a range of ^{Fc}CPMV derivatives (Figure 7.1) in which the separation distance between ferrocene and virus surface can be controlled (Aljabali et al, 2010a). This maybe important for the control of electron hopping to solid electrode surfaces and the development of nanoelectronic components. To

generate electroactive CPMVwt particles, solvent–exposed amines and carboxylates on the surface of CPMVwt particles were utilised as binding sites for ferrocene moieties. The electrochemical behaviour of the modified particles was assessed in solution to select the best candidates for immobilisation onto a solid electrode surface.

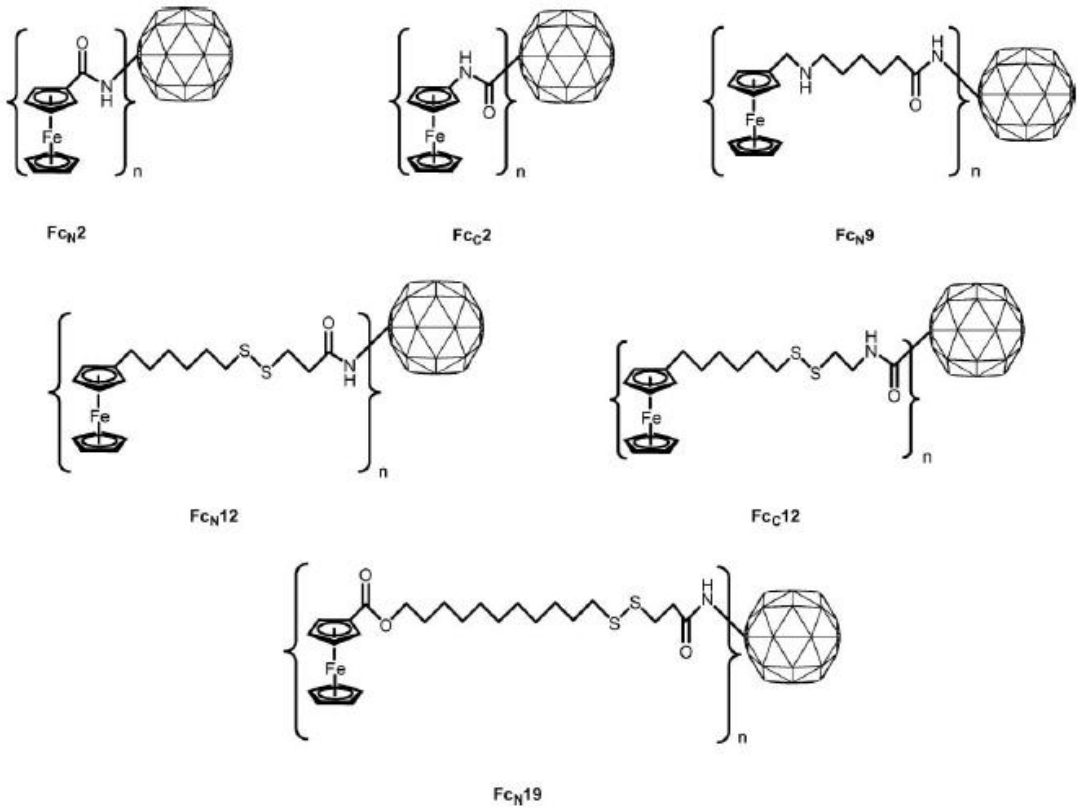

Figure 7.1– ^{Fc}CPMV derivative nomenclature.
Subscript N represents linkage to virus surface amine; C represents linkage to surface carboxylate; numeral gives number of atoms in link between ferrocene and virus surface, where virus surface is taken to be the ε C of the lysine side chain, the β C of aspartate and the γ C of glutamate. Reproduced from Aljabali et al, 2010.

7.2 Materials and Methods

7.2.1 Materials

All general reagents, 1–ethyl–3–(3–dimethlyaminopropyl)carbodiimide hydrochloride (EDC) was purchased from Novabiochem, *N*–hydroxysuccinimide (NHS) from Fluka, *N*–succinimidyl–3–(2–pyridyldithio)propionate (SPDP) from Pierce, 2–(2–pyridinyldithio)ethaneamine hydrochloride (PDEA) from GE Healthcare, sulfo–succinimidyl 4–

formylbenzoate sodium salt (sulfo–S–4FB) from Solulink and aminoferrocene from TCI Europe. *N*–(ferrocenylmethyl)–6–aminocaproic acid (Padeste et al, 2000) and 11–(ferrocenylcarbonyloxy)undecanethiol (Chidsey et al, 1990) were synthesised by published methods and their purity confirmed by ^{1}H–NMR and mass spectrometry by Mrs Elaine Barclay.

7.2.2 Methods: Coupling of ferrocene derivatives to CPMV

All ^{Ferrocene}CPMV modified particles were prepared freshly and used within a week. The samples were stored at 4 °C. Longer storage times resulted in a visible aggregation and precipitation.

7.2.2.1 EDC/NHS method

N–(ferrocenylmethyl)–6–aminocaproic acid, Fc6ac, and aminoferrocene, $FcNH_2$ were coupled to CPMV surface amine groups and CPMV surface carboxylate groups, respectively, by the standard EDC/NHS method (Steinmetz et al, 2006c; Steinmetz et al, 2006d). After stirring gently overnight at 4 ºC the ^{Fc}CPMV conjugates were purified either by gel filtration on a Sephacryl S–500 column (GE Healthcare) or by dialysis using 100 kDa molecular weight cut–off membranes (Float–A–Lyzer G2, Spectrum Laboratories) against 10 mM sodium phosphate buffer. The samples were concentrated on 100 kDa cut–off columns (Millipore) and the concentration of ^{Fc}virus conjugate was determined photometrically at 260 nm with 60–70 % recovery based on the starting materials. Agarose gel electrophoresis, TEM and DLS confirmed the integrity of the modified virus.

7.2.2.2 SPDP method

The ferrocene–thiols 6–(ferrocenyl)hexanethiol, Fc6SH, and 11–(ferrocenylcarbonyloxy)undecanethiol, Fc11SH, (Figure 7.2) were coupled to CPMV surface amine groups using *N*–succinimidyl–3–(2–pyridyldithio)–propionate (SPDP), the scheme is depicted in Figure 7.2. For detailed procedure, see section 2.14.

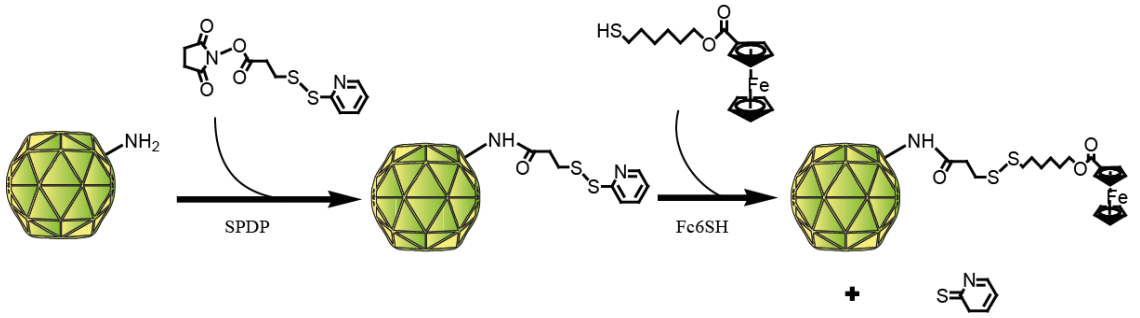

Figure 7.2– SPDP was used to modify the amine groups of CPMV to form amide bond linkages. The subsequent addition of thiolated ferrocene moieties resulted in disulfide bond formation.

7.2.2.3 PDEA method:

The method is adapted from (Frederix et al, 2004).The ferrocene–thiol Fc6SH was coupled to CPMV surface carboxylate groups with 2–(2–pyridinyldithio)ethaneamine hydrochloride (PDEA). To pre–activate the surface carboxylate groups, CPMV particles (10 mg ml^{-1}), suspended in 10 mM sodium phosphate buffer pH 7.0, were reacted with a freshly prepared solution of EDC (1000 molar excess) and NHS (4000 molar excess) for 2 hours at ambient temperature with gentle stirring. The pre–activated $^{2–(2–pyridinyldithio)ethaneamine}$CPMVparticles were purified on PD–10 Desalting Columns (GE Healthcare). The eluted sample was reacted with a solution of PDEA (1000 molar excess) in Milli–Q water overnight, purified on a 100 kDa cut–off column and washed thoroughly to remove any unreacted materials. PDEA derivatised CPMV particles were reacted overnight at 4 °C with Fc6SH (1000 molar excess) dissolved in DMSO, the final DMSO concentration being adjusted to 20 % (v/v), purified by gel filtration (Sephacryl S–500 column), and the eluted fractions collected and concentrated on 100 kDa cut–off columns. The ^{Fc}CPMV particle integrity was established by agarose gel electrophoresis, TEM and DLS.

7.2.3 Electrochemical measurements

^{Fc}CPMV in solution: Cyclic voltammetry was conducted with an AUTOLAB PGSAT 30 potentiostat in a conventional three–electrode cell with the sample in 10 mM sodium phosphate buffer, pH 7.0 at room temperature (ca. 25 ºC). The working electrode was a

pyrolytic graphite edge (PGE) disc with a diameter of 3 mm; Ag/AgCl (saturated KCl) was the reference electrode and platinum wire the counter electrode (all experiments were conducted with the same electrodes unless otherwise indicated). Analysis of the free ferrocene moieties was typically performed with a concentration of 5–10 mM (with 10% DMSO or DMF as necessary for solubility). Modified virions were typically studied at concentrations of 1 to 11 mg ml^{-1}. For each sample, cyclic voltammograms were recorded at scan rates from 5 to 200 mV s^{-1} in duplicate sets with the working electrode polished by abrasion with an aqueous slurry of 0.3 μm Al_2O_3 immediately prior to measuring each set. Consecutive voltammograms at each scan rate overlaid each other from the fourth scan onwards and these 'steady–state' voltammograms were analysed to determine peak potentials (E_p^a and E_p^c for the anodic and cathodic scans respectively) and peak current magnitudes (i_p^a and i_p^c for the anodic and cathodic scans respectively) at each scan rate. Analysis of 20 mV s^{-1} voltammetry performed at various times during the collection of each set of scan rates confirmed that the response was independent of time. Plots of peak current versus the square root of scan rate were found to be linear. The gradients were determined by linear regression and analysed by the Randles–Sevcik equation to determine the concentration of ferrocene in the sample and ultimately the number of ferrocene moieties per virus particle (Steinmetz et al, 2006d).

7.2.4 Methods: Coupling of ^{Fc}CPMV onto solid surfaces

7.2.4.1 Cleaning gold electrode

The gold surface (3 mm in diameter) was polished with 0.03 and 0.01 μm alumina slurry successively and then sonicated in a Milli–Q water bath for a minimum of two minutes. The electrode was cleaned in a freshly prepared piranha solution (70% H_2SO_4 : 30% H_2O_2), rinsed thoroughly with Milli–Q water, dried under a stream of argon and placed in a sealed vial containing 10 mM of the thiolated ligand in 50% ethanolic solution for 8–18 hours. Another cleaned surface was used as a control.

7.2.4.2 Cystamine and thioctic acid SAMs on gold surface

Gold electrode was immersed into 0.1M cystamine (in 50% ethanol: 50% Milli–Q water) or 0.1 M thioctic acid solutions prepared in 100 mM sodium phosphate buffer pH 7.0 and incubated overnight (12–15 hours) at 4 °C while gently stirring. The electrode was thoroughly washed with 50% (v/v) ethanol solution followed by sonication and washing again with 50% (v/v) ethanol solution to ensure removal of all the contaminants. SAMs formation was characterised by CV in 100 mM sodium phosphate buffer pH 7.0 at 0.1 V s^{-1} vs (Ag/AgCl) as a reference electrode. Optimised SAM formation conditions were repeated, assuming in the subsequent experiments that equivalent SAMs were formed under the same conditions.

7.2.4.3 ^{FcC2}CPMV immobilisation onto gold surface

A clean gold electrode was first soaked in 66.6 % ethanolic solution (v/v) thioctic acid for 8–15 hours at room temperature to form the SAM. After an ethanol rinse, to remove adsorbed thioctic acid, the doubly–functionalised $^{FcC2}CPMV^{NHS–ester}$, previously prepared and fully characterised in solution, was directly attached to the ester group of the thioctic acid. In brief, CPMV surface carboxylates were first activated with EDC/NHS and ferrocene bound to the lysines. The gold modified surface was immersed into 5–10 mg ml^{-1} of modified CPMV particles with stirring. The electrode was thoroughly washed before conducting any measurements. CV measurements were recorded at various time points from 2–15 hours.

7.2.4.4 Graphite electrode modification

Surface modification of freshly clean graphite surface was carried out at room temperature in a degassed solution (argon) of 0.1 M HCl (2 ml) containing 3 mM 4–azidobenzene diazonium tetrafluroborate, $[N_3C_6H_4N_2](BF_4)$. The amperometric reduction for the aryl diazonium salt was accomplished by scanning from 0 to –0.1V. The modified electrode surface was thoroughly washed with Milli–Q water followed by ethanol and sonicated in a water bath for 2–3 minutes. The electrode was kept in 10 mM sodium phosphate buffer prior to

the second step of the modification (incubation with the doubly functionalised virus). As a control experiment to establish if there is any signal in the absence of the virus, 0.5 mg of sulfo–NHS–phosphine (Thermo Scientific) dissolved in DMSO was prepared just before use and added to 3 ml 10 mM sodium phosphate buffer in a vial. The electrode was left on a shaker at 200 rpm at 4 °C overnight (16 hours) before being washed thoroughly with Milli–Q water and DMSO to remove any adsorbed excess. The electrode was then incubated with solution containing aminoferrocene (DMSO–buffer) for 14–16 hours the CV was then recorded after that.

7.2.4.5 CPMV modification for PGE electrode

7.2.4.5.1 PGE electrode modification

Surface functionalisation of the graphite electrode was carried out at ice–cold temperature in a deaerated solution (with argon); 3 ml of 0.1M HCl containing 2 mM of 4–azidobenzene diazonium or 4–ethyl–benzene diazonium (BF_4 salts). The reductive electrodeposition of the aryl diazonium salts was achieved amperometrically. The working electrode potential was set between minus 1 and 0 V. After the functionalisation, the electrode surface was thoroughly washed with Milli–Q water followed by ethanol to remove any adsorbed species.

7.2.4.5.2 Surface coupling of ^{Fc}CPMV by "click" chemistry

The modified electrode as described above was immersed in a 15 ml Milli–Q water solution containing 10 mM final concentration $CuSO_4$, L–ascorbic acid (10 mM), and the corresponding half of the "click" reaction (azide or alkyne). The "click" reaction was accomplished overnight before reacting ^{Fc}CPMV particles to the modified surface. The electrode was rinsed thoroughly with Milli–Q water and ethanol to ensure that any adsorbed species were washed off. Finally, the modified electrode was incubated in 0.1M sodium

phosphate buffer pH 7.0 with the doubly–functionalised particles $^{\text{Ferrocenecarboxylic acid}}\text{CPMV}^{\text{NHS–ester}}$. The electrode was rinsed rigorously with buffer before being scanned by CV.

Alternatively, virus azide particles $^{\text{Ferrocenecarboxylic acid}}\text{CPMV}^{\text{Azidorpropylamine}}$ were reacted with previously functionalised graphite surface as described in Figure 7.3. The protocol was provided by Prof. M. G. Finn, the Scripps research Institute (personal communication with Prof. Dave Evans). The final reaction conditions for the "click" chemistry with the modified virus in 0.1M sodium phosphate buffer pH 7.0 were: 0.25 mM $CuSO_4$ in Milli–Q water, 1.25 mM ligand tris[(1–benzyl–1H–1,2,3–triazol–4–yl)methyl] amine (TBTA–OH) in water, 5 mM sodium ascorbate freshly prepared, and 5 mM amino guanidine. The reaction was mixed well and was left to proceed for 1–2 hours followed by dialysis overnight ~16 hours.

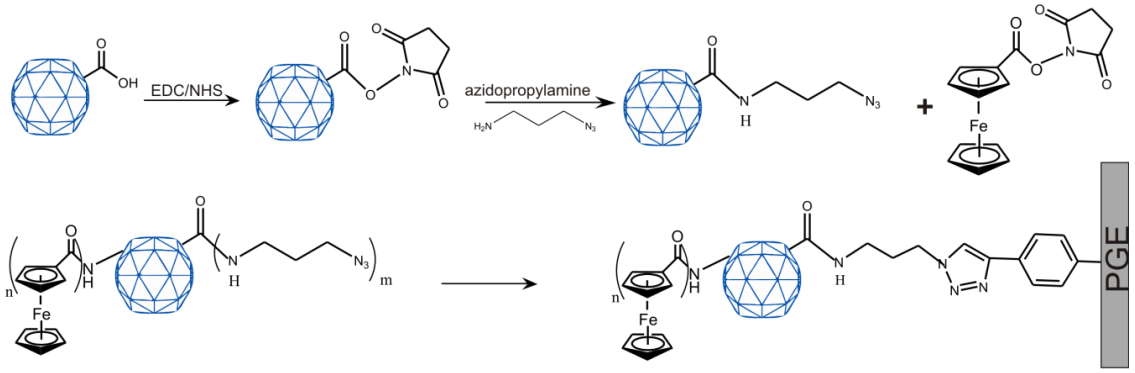

Figure 7.3– Doubly–functionalised $^{\text{Ferrocene carboxylic acid}}\text{CPMV}^{\text{Azidopropylamine}}$ particles. Where (m) refers to the number of azidopropylamine coupled to the virus and (n) refers to the number of ferrocenes bound to the virus.

7.3 Results and discussion

This chapter describes and evaluates several strategies for coupling of ferrocene onto CPMV capsid, to both amine and carboxylate groups of the surface exposed amino acids, using a range of conjugation strategies.

CPMV surface amine groups, arising from exposed lysines, can be readily coupled to ferrocene–carboxylate derivatives using EDC/NHS methods (Steinmetz et al, 2006d) and to ferrocene–thiols using SPDP reagent. The SPDP reagent in the current work was first coupled to

the amine groups of the virus by reaction with the succinimidyl group of the reagent. The $^{N-succinimidyl-3-(2-pyridyldithio)propionate}$CPMV derivative was isolated and purified. The pyridyl disulfide group of this derivative was then reacted with ferrocene–thiol; pyridine was liberated and a disulfide bond was formed between the ferrocene and the modified virus (Figure 7.1). Further, CPMV surface carboxylate groups, from exposed aspartic and glutamic acids, can be coupled to aminoferrocene, using EDC/NHS, or to ferrocene–thiol, Fc6SH, with PDEA (Figure 7.1). Prior to coupling of PDEA to the virus, the surface carboxylates were pre–activated with EDC/NHS; these react with the amine group on the PDEA reagent to form a stable amide bond. Ferrocene–thiol can then be coupled to the modified CPMV by thiol–disulfide exchange. In all cases, the ferrocene reagents were used in a large excess to ensure maximum coupling. Virus particles were recovered in approximately 70 – 80% yield based on initial wild–type concentration as determined spectrophotometrically. In each case, and as described below, ferrocenylation of the virus capsid occurs with retention of virus integrity, as was established by uranyl acetate negatively stained TEM which shows that the virus particles remain intact and that they are monodisperse with a diameter of approximately 28 nm (for example, Figure 7.4).

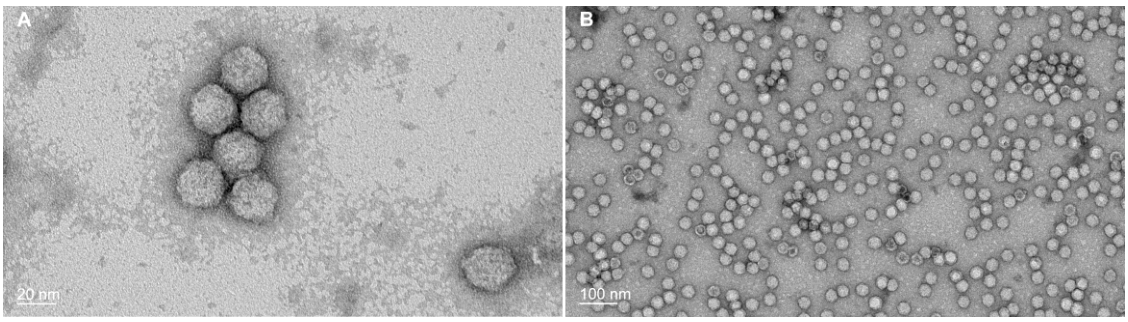

Figure 7.4– Transmission electron microscopy images of chemically modified particles after staining with 2% uranyl acetate. (A) CPMVwt; (B) ^{Aminoferrocene}CPMV, FcC12. Particles are monodisperse with ~28 nm diameter. Reproduced from (Aljabali et al, 2010).

DLS measurements gave the average diameter of the ^{Ferrocene}virus particles and confirmed monodispersity (Table 7.1). The DLS and the correlation data are presented in Figure 7.5.

^{Ferrocene}CPMV	Diameter (nm)	Polydispersity (%)
Fc_N2	29.8	24.5
Fc_N9	30.0	10.7
Fc_N12	32.0	20.6
Fc_N19	33.0	20.8
Fc_C2	29.4	11.8
Fc_C12	31.8	19.6

Table 7.1–Diameter and polydispersity of ^{Ferrocene}CPMV as determined by dynamic light scattering. Reproduced from Aljabali et al, 2010. Subscript N represents linkage to virus surface amine; C represents linkage to surface carboxylate

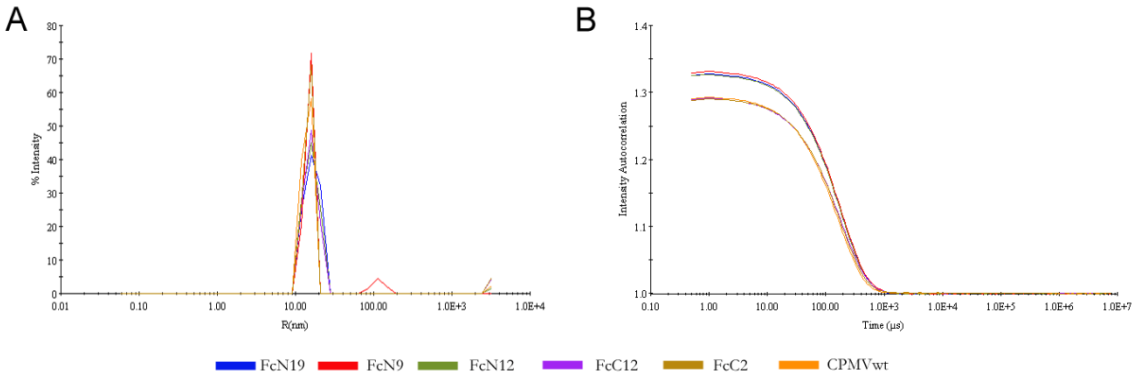

Figure 7.5–DLS of ^{Ferrocene}CPMV. Comparison of hydrodynamic radii (A) and correlation plots (B). ^{Ferrocene}CPMV particles at approximately 0.5 mg ml^{-1} in 10 mM sodium phosphate buffer pH 7.0 after filtration through 0.1 µm filters immediately prior to analysis. Measurements were taken every 10 seconds and 10 measurements were averaged from 3 runs at 21 °C. (Reproduced from (Aljabali et al, 2010a).

Intact virions of wild–type CPMV can be separated into a higher– and lower–mobility form by native gel electrophoresis according to their migration towards the anode. These forms are derived from the slow and fast form of the small subunit of the virus capsid and are a consequence of a carboxy–terminal cleavage of 24 amino acids of the small subunit (Sainsbury F. et al, 2011; Taylor et al, 1999). The higher–mobility band in the agarose gel represents virions with a cleaved small subunit. ^{Ferrocene}CPMV derivatives with shorter linker length, whether coupled through amine or carboxylate groups, Fc_C2 and Fc_N9, exhibit retarded mobility of the ferrocene–modified virus particles compared to wild–type CPMV (Figure 7.6), as has been previously observed for Fc_N2 (Steinmetz et al, 2006d), and is consistent with an increase in size and, therefore, decoration of the virions with ferrocene molecules. Surprisingly, ^{Ferrocene}CPMV particles with longer linker length and coupled via a disulfide linkage, Fc_N12,

Fc_C12 and Fc_N19, show enhanced mobility toward the anode as does a *N*–succinimidyl–3–(2–pyridyldithio)propionate CPMV derivative positive control (Figure 7.6–C). This unexpected behaviour is thought to arise because of a combination of size and charge effects perturbing mobility through the gel. However, they all migrate to a different extent than wild–type confirming that the particles have been modified.

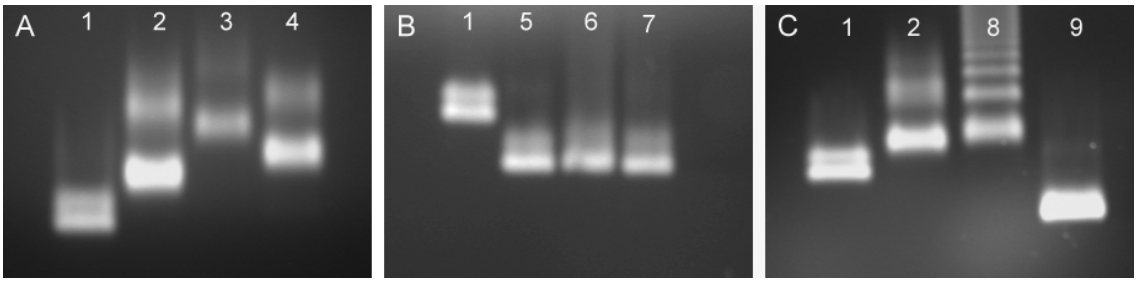

Figure 7.6– Wild–type and Ferrocene CPMV particles on a 1.2% agarose gel. (A) Lane 1, wild–type CPMV; 2, $CPMV^{NHS\ ester}$; 3, Fc_C2; 4, Fc_N9. (B) Lane 1, CPMVwt; *N*–succinimidyl–3–(2–pyridyldithio)propionate CPMV derivative; 6, Fc_N12; 7, Fc_N19. (C) Lane 1, CPMVwt; 2, NHS–ester CPMV; 8, 2–(2–pyridinyldithio)ethaneamide CPMV derivative; 9, Fc_C12.

Cyclic voltammetry established that the modified Ferrocene CPMV are redox–active nanoparticles, (e.g. Figure 7.7–A&B). The ratio of the peak currents, i_p^a/i_p^c, is close to unity showing the ferrocene/ferrocenium couple is electrochemically reversible. Ferrocene dendrimers showed similar properties due to fast rotation of the dendrimer compared to the electrochemical timescale, so that all the redox centres come close to the electrode within this timescale (Green et al, 1998). The peak currents were proportional to the square root of the scan rate, $\nu^{1/2}$, showing that oxidation and reduction were diffusion controlled (e.g. Figure 7.7). Plotting the measured peak currents *ip versus* the square root of the scan rate confirmed that the oxidation and reduction was diffusion controlled as seen in (Figure 7.7–A2 and B2).

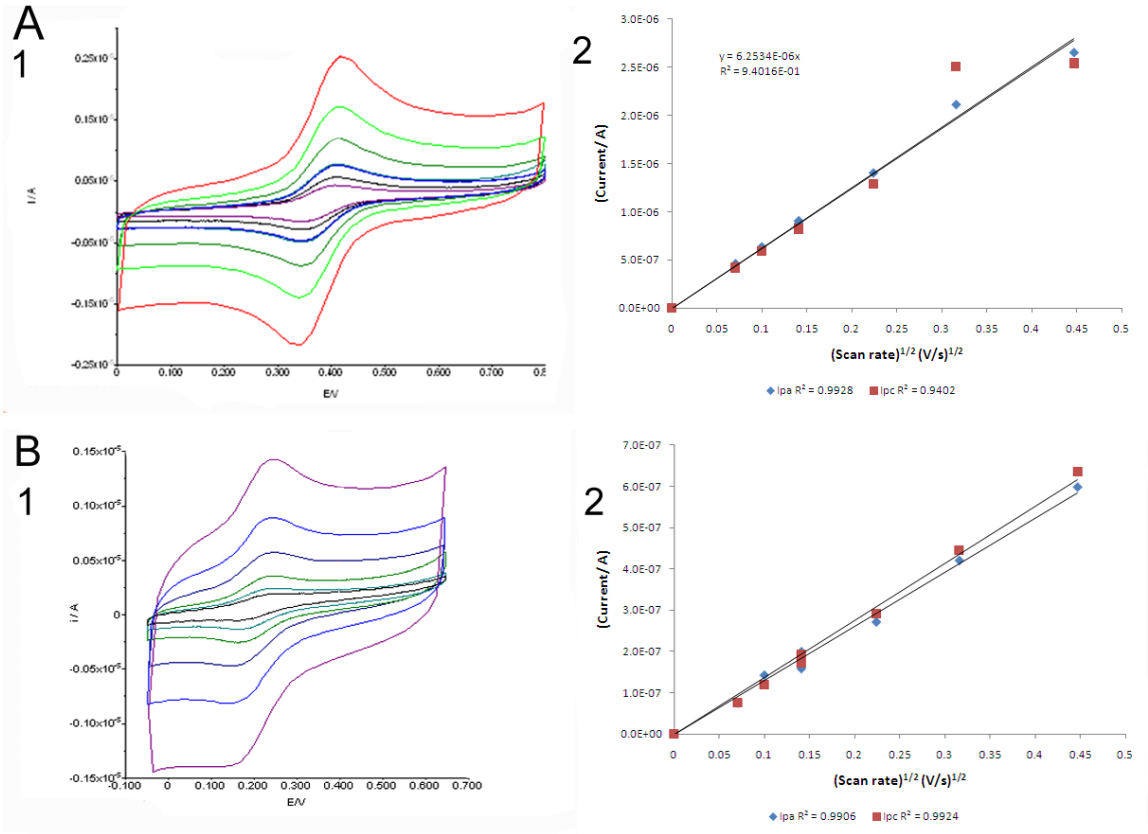

Figure 7.7– Cyclic voltammogram for some ^{Ferrocene}CPMV modified particles.
(A.1) Cyclic voltammograms of Fc_N9 at scan rates from 5 mV to 200 mV s^{-1}; (A.2) Variation of peak current with the square root of the scan rate. (B.1) Cyclic voltammogram of Fc_C2 at scan rates from 5 mV to 200 mV s^{-1}; (B.2) Variation of peak current with the square root of the scan rate. Reproduced from (Aljabali et al, 2010).

The concentration of ferrocene molecules in the ferrocene conjugated CPMV samples was determined using the Randles–Sevcik equation (Figure 7.8). The peak current, *ip*, is directly proportional to the analyte concentration (ferrocene) at 25 °C. The number of ferrocene molecules attached to CPMV was calculated from the slope equation depicted in Figure 7.8, using the CPMV diffusion coefficient from the reference (Steinmetz et al, 2006d); the results are summarised in Table 7.2. The minimum and maximum numbers for the attached ferrocene moieties per virion was based on an error of ± 5 % in the electrode area to give a more realistic estimation of the ferrocene moieties per virus. The complete set of data and the detailed calculation of all ^{Ferrocene}CPMV derivatives are attached as an appendix to this thesis.

$$i_p = k.n^{\frac{3}{2}}.A.\sqrt{D.V}\,.C_{Fc}$$

$$Slope = \left(\frac{i_p}{V}\right) = k.n^{\frac{3}{2}}.A\,.\sqrt{D}\,.C_{Fc}$$

Figure 7.8– Randles–Sevcik equation.

In this equation , i_p= current in amps, and is directly proportional to the analyte concentration, the temperature is assumed to be 25 °C , n=1; n is the number of electrons transferred per molecule, A is the surface area of the working electrode = 0.07 cm^2, D is the diffusion coefficient of CPMV particles in aqueous buffer solution = 0.16 x 10^{-6} cm^2 sec^{-1} (Steinmetz et al 2006); k is a constant of 2.69 x 10^5 C mol^{-1} $V^{-1/2}$ and v= scan rate over a range from v= 5 to 200 mV sec^{-1}; C_{FC} is ferrocene concentration.

Ferrocene reagent	$E^{1/2}$ (V)(± 0.015)	^{Ferrocene}CPMV	$E^{1/2}$ (V) (± 0.015)	Number of ferrocenes per virion (± 5%)
FcCOOH	0.322	Fc_N2	0.233	240
FcAC	0.425	Fc_N9	0.373	246
Fc6SH	0.455	Fc_N12	0.325	250
Fc11SH	0.450	Fc_N19	0.344	193
$FcNH_2$	0.380	Fc_C2	0.210	174
Fc6SH	0.455	Fc_C12	0.320	101

Table 7.2– Reduction potential ($E^{1/2}$) of ferrocene and ^{Ferrocene}CPMV *vs* Ag/AgCl (saturated KCl) and the average number of ferrocenes per CPMV virion as calculated from the linear plots of current versus the square–root of the scan rate and the Randles–Sevcik equation. In the case of FcCOOH the values are reproduced from Steinmetz et al, 2006c.

The asymmetric unit of CPMV can be maximally labelled, under standard conditions, at four of the five accessible lysines presented on the outer surface (Lys 38, 82 of S subunit and Lys 34, 99, 199 of L subunit). This provides a maximum of 240 addressable lysine sites on the CPMV virion surface (Evans, 2008; Manchester & Steinmetz, 2009; Steinmetz & Evans, 2007). Fc_N2, Fc_N9 and Fc_N12 show maximum coverage. However, when the linker length is increased further, as in Fc_N19, there is a decrease in the number of ferrocenes bound from about 240 to 193. Similarly, the maximum number of addressable carboxylates at the virion surface has been determined to be 180 of the 420 aspartate and glutamate residues on the outer surface (Asp 26, 44, 45, 85, and Glu 135 on the S subunit, and Asp 273 and Glu 319 of the L subunit) (Steinmetz et al, 2006a). The ^{Ferrocene}CPMV with a short linker, Fc_C2, shows maximum coverage, whereas that with a longer linker, Fc_C12, exhibits reduced coverage. The decrease in the number of

bound ferrocenes as a function of linker length is likely to be a consequence of the longer linker length molecules folding back onto the surface and blocking some of the other coordination sites. It is less likely to be a consequence of the different coupling strategies employed, as the conditions used should favour maximum coverage.

The distances between side chains of the surface–exposed lysines are depicted in Figure 7.9. Wang et al established lysine 38 (S) as the most reactive surface lysine (Wang et al, 2002a). ^{FcC12}CPMV particles showed a notably decreased number of ferrocene moieties per virus. Assuming Fc_C12 is coupled to lysine 38, the most reactive lysine, this could block the reactivity of adjacent lysine 99 (L). This is consistent with the quantitative data, which suggests the modification of three lysines per asymmetric unit. In addition, the Fc_C12 linker molecule as shown in Figure 7.10 with minimized energy revealed a molecule length of 22.16 Å. As the distance between the most reactive lysines is 18.1 Å, it is expected that Fc_C12 block the availability of the adjacent lysine. This effect equates to 60 ferrocene molecules per virus less than when shorter ferrocene derivatives are used.

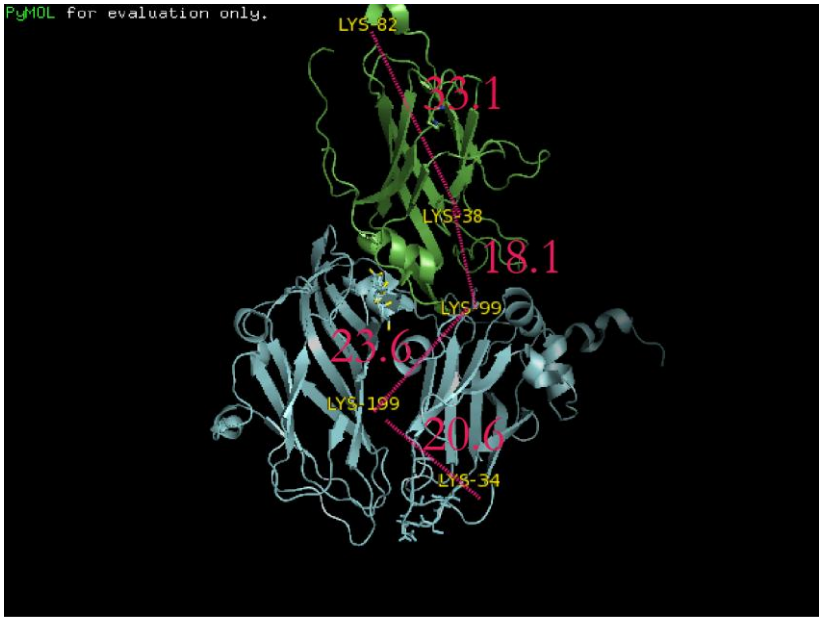

Figure 7.9– Addressable lysine residues on the exterior surface of the CPMV capsid with the separation distances. The asymmetric unit is composed of the small (S) subunit (green), and large (L) subunit. Depicted are addressable surface lysine residues with separation distance (Å); Lys 38 and Lys 82 on the S subunit, Lys 199 on the B domain of the L subunit, and Lys 34 and Lys 99 on the C domain of L. Images generated with PyMOL–1_2B8eval version. The accessible surface profile of CPMV capsid file is available at http://viperdb.scripps.edu with PDB–ID (1NY7).

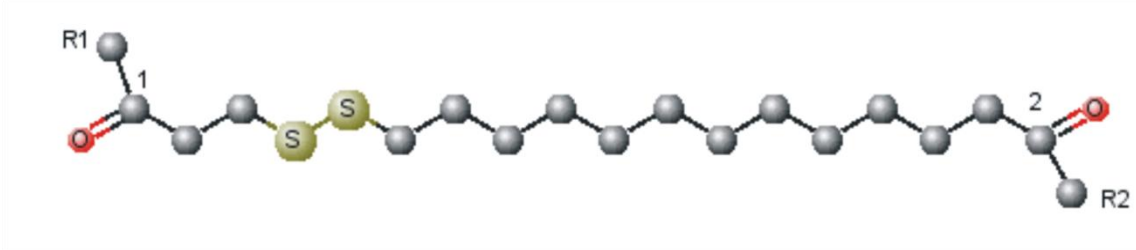

Figure 7.10– Schematic representation of FcC12 linker. The drawing was generated by MarvinSketch and MarvinSpace 5.3.2 software. The linear distance between the two peripheral carbons (1 and 2) is 22.18 Å, whereas the distance between the two most reactive lysines is 18.1 Å. R1 represents ^{SPDP}CPMV and R2 the ferrocene group.

Reduction potentials ($E_{½}$) determined for the free and conjugated ferrocene moieties from the average peak potentials are shown in Table 7.2. Conjugation to the virus results in destabilisation of the ferrocenium form as reflected in the lower $E_{½}$ for the conjugated form. In each case, and for all scan rates studied, the peak separation $|E_p^a – E_p^c|$ ranged from 55 to 70 (± 5) mV, which is close to the theoretical value expected for a one–electron process (59 mV at 25 °C). Thus, the voltammetry indicates that the ferrocenyl centres coupled to the CPMV surface behave as independent and electronically isolated units with apparently homogeneous redox properties. Electronic isolation is likely to reflect a spacing of the ferrocene units across the virion surface that prevents their close approach for electron transfer. Given that the ferrocene units are conjugated to multiple environments on the surface of the asymmetric unit, the homogeneity of the redox properties suggests the ferrocenes exhibit similar reduction potentials at all of these sites.

7.4 ^{Fc}CPMV immobilisation on electrode surface

Here are outlined results of preliminary studies on surface modification for future applications in the fabrication of functional nanodevices. The aim was to couple ^{Fc}CPMV to a solid electrode surface to obtain electron flow. According to the literature, the most commonly used method for chemical modification of surfaces is the deposition of self–assembled monolayers (SAMs) and Langmuir–Blodgett (LB) films, which generate ultrathin films (Tredgold, 1991). SAMs commonly achieve covalent modification of surfaces. Some examples are thiolated and disulfides on gold; silanes on oxide surfaces; carboxylic acids on metal oxides

(Ulman, 1996). Dendritic macromolecules have been used to modify gold or carbon electrodes (Lojou & Bianco, 2006).

Willner and colleagues demonstrated the ability to construct multi–layered nanoparticle electrodes that are porous (Lahav et al, 1999). The immobilisation or covalent attachment of molecules to a surface, at a precise location, to generate highly defined miniaturised nanodevices is of great interest in nanoelectronics and biofuel cells that utilise enzymes to convert chemical energy into electrical energy (Pizzariello et al, 2002).

Dendrimers modified with redox–active ferrocenyls were used for the construction of a multilayered assembly of enzymes via LBL deposition (Jang et al, 2009). ^{Ferrocene}CPMV immobilisation on a suitable solid surface provides unique features for the generation of ordered nanoparticle assembly, which is essential in nanoelectronic applications and development. Also important is efficient electron exchange between the immobilised ferrocene and the electrode.

A gold solid surface is one of the easiest materials to use as a solid support; thiols and disulfide adsorb easily to form SAMs. A SAM is essentially an organization of molecules at the solid–liquid interface induced by the affinity between the surface and the ligand, and can be easily prepared by immersing a freshly cleaned gold surface in a solution of appropriate thiol.

7.4.1 Coupling onto solid surfaces

One of the important advantages of SAM is that it can be prepared very easily and simply. The surface is dipped into a solution containing the appropriate ligand molecules followed by thorough washing with the same solvent as the ligand was prepared in. Modified virus immobilisations to SAM functionalised surfaces, presented here are based on monolayer formation of SAMs onto solid surfaces. Thiol–terminated ligands, such as cystamine and thioctic acid, react efficiently with gold surfaces leaving amine or ester groups to couple to the virus surface. Schematic representation of this approach is depicted in Figure 7.11.

Rigorous cleaning and pre–treatment of gold surfaces was necessary to facilitate formation of well–defined monolayers onto the surfaces. Piranha solution (70% H_2SO_4: 30%

H_2O_2) (Bain et al, 1989) and electrochemical treatment to remove oxide contamination by cycling the potential range from +0.5 to –1.4V in 0.5 M H_2SO_4 electrolyte were adopted here.

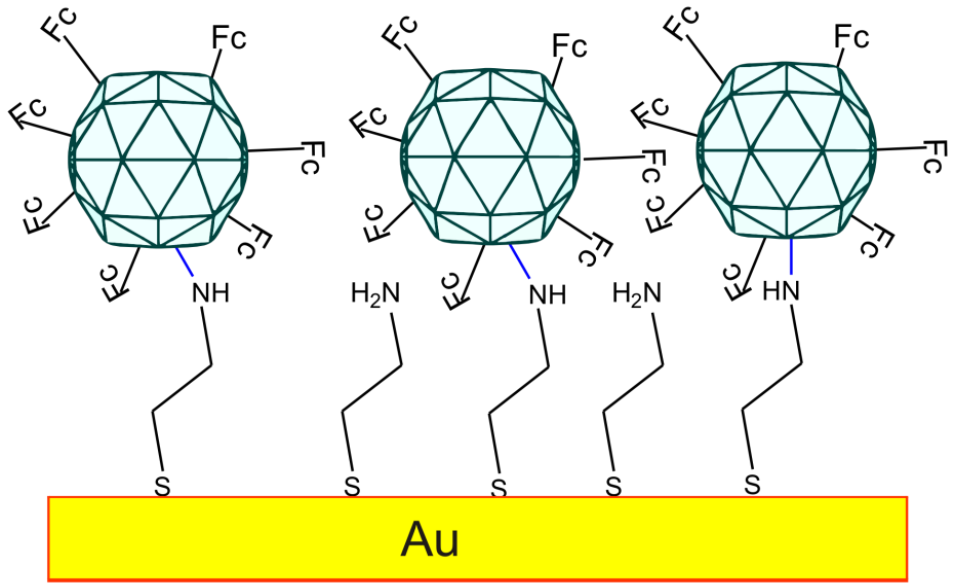

Figure 7.11– Schematic of ^{Ferrocene}CPMV particles immobilised onto gold surface through cystamine SAM formed on Au surface.

7.4.2 Results and discussion of ^{Fc}CPMV onto solid surfaces

Gold electrode cleanliness was monitored by cyclic voltammetry (CV) in 0.1 M H_2SO_4, the CV of clean gold surface shows an oxidation peak at +1.3 V (vs. Ag/AgCl in saturated KCl for all experiments presented here) and a reduction peak at +0.9 V (vs. Ag/AgCl) corresponding to metal oxide formation and reduction (Figure 7.12). Cyclic voltammetry was finished with the electrode at a negative potential to ensure an oxide–free gold surface. A typical cyclic voltammogram of clean gold surface free from any contaminants is shown in Figure 7.12.

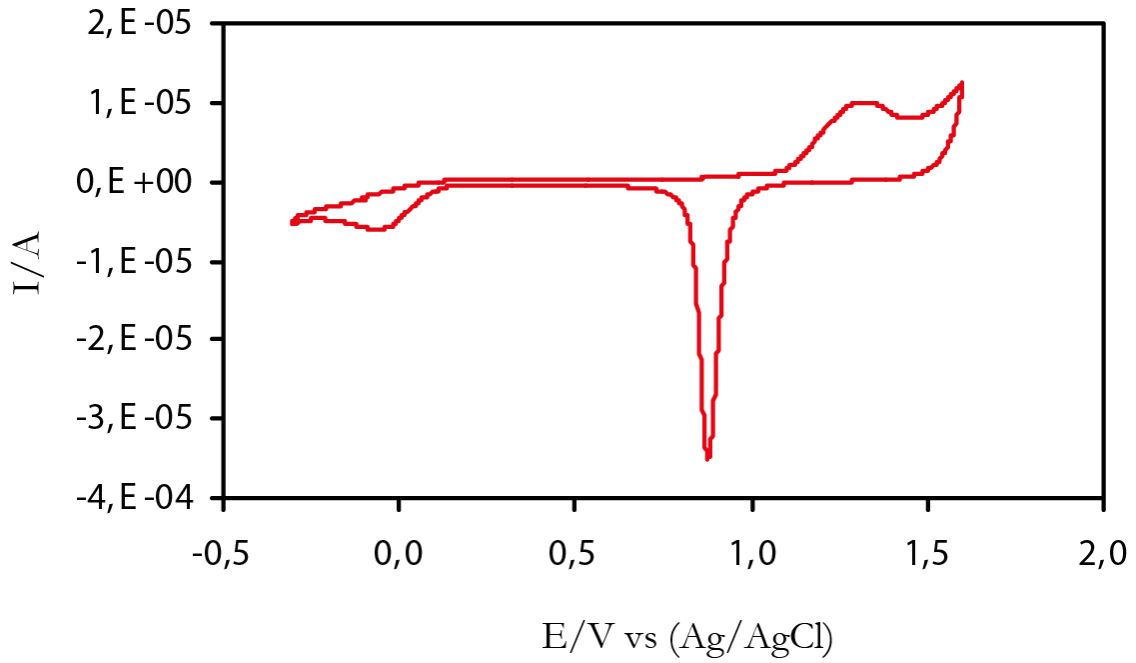

Figure 7.12– Typical CV of a clean gold electrode in 0.1M H_2SO_4 at 100 mV s^{-1}. This shows a characteristic anodic peak at +1.3 V and a cathodic peak at +0.9 V.

7.4.2.1 SAMs formation and characterisation on gold surface

The simplest way to confirm adsorption of thiol–based moieties on a gold surface is the disruptive reduction of the formed cystamine SAM in 0.1 M sodium phosphate buffer, 0.15 M NaCl, pH 7.0 at 100 mV s^{-1}. This is illustrated in Figure 7.13 where the CV showed a reduction peak at –0.7 V (*v*s. Ag/AgCl) indicating the presence of cystamine SAM. Subsequent scans showed no such peak, which is consistent with the disruption of the thiols bound to the gold and consequent loss of the assembled monolayer. The aforementioned property, although useful in quantifying and confirming the SAMs formation, demonstrates the limitation of the use of gold surfaces and does not allow further use of the electrodes. However, it was used to optimise the SAM formation assuming in the subsequent experiments that equivalent SAMs were formed under the same conditions.

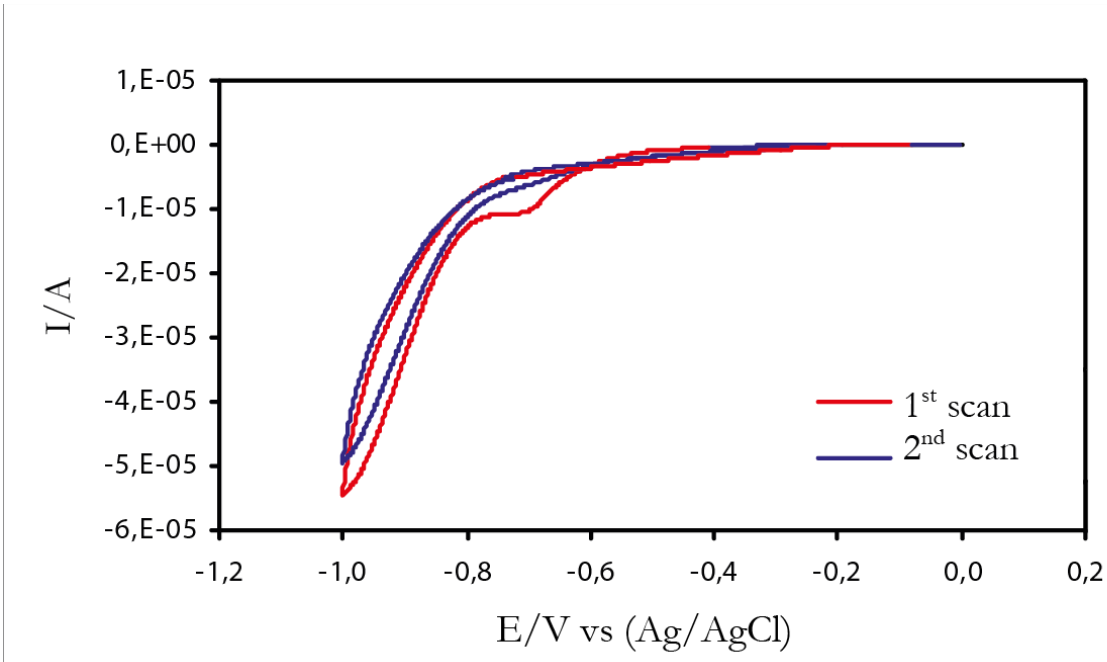

Figure 7.13– Cyclic voltamograms for the removal of cystamine SAM from the Au surface by the electroreduction. 1st and 2nd CVs showing the reduction of the Au–S bond in 0.1M sodium phosphate buffer pH 7.0 at 100 mV s^{-1}.

Initially, ferrocenecarboxylic acid was coupled onto the cystamine–functionalised Au surface to establish the feasibility of using ^{Ferrocene}CPMV particles for surface modification. A very weak electrochemical signal resulted (Figure 7.14). This was very difficult to reproduce as the voltammetric response of the Au electrode in the absence of ferrocene often showed features in the region where the ferrocene signal is expected, most likely due to impurities adsorbed onto the Au electrode surface.

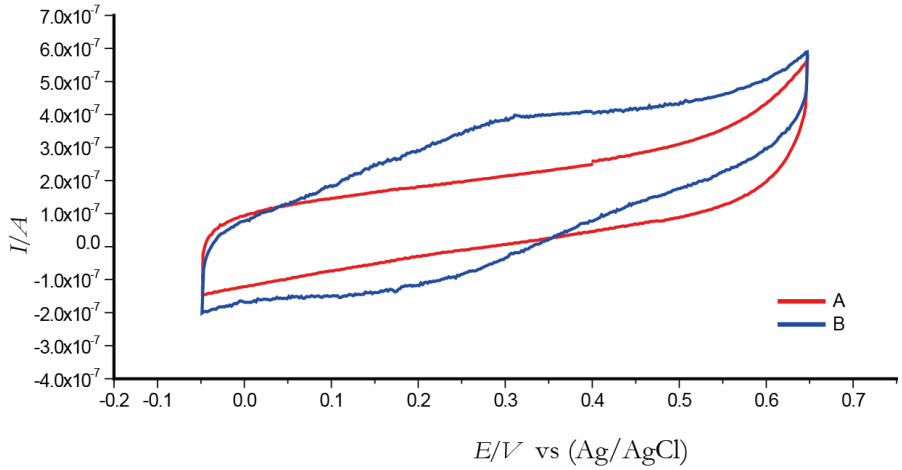

Figure 7.14– Ferrocenecarboxylic acid attached to cystamine functionalised Au surface.
A represents cystamine–functionalized Au surface (unmodified) and B represents ferrocene attached to Au surface at scan rate of 20 mV s^{-1}.

It was initially proposed to modify Au surfaces with different thiolated moieties (i.e. cystamine and thioctic acid) to which ^{Fc6ac}CPMV and ^{FcC2}CPMV particles could be coupled. The ferrocene moieties used for this work had different linker lengths (see section 7.1.1) in order to establish which ferrocene moieties on the virus capsid could transfer electrons to the Au surface. The coupling reaction of ^{Ferrocene}CPMV to the Au surface was conducted in 0.1 M sodium phosphate pH 7.0 overnight. The electrochemical results showed no communication between the presumably immobilised ^{Ferrocene}CPMV and the Au electrode.

To investigate whether the ^{Ferrocene}CPMV is actually coupled to the SAM functionalised Au surface, fluorescent labelling and IR spectroscopy was attempted. However, due to the nature of the electrode used for the experiments, IR spectroscopy could not be pursued further. Fluorescent labelling of CPMV particles followed by immobilisation on an NHS terminated Au surface (via thioctic acid) resulted in no significant signal being detected using fluorescence microscopy. In addition, in an attempt to confirm modification of the Au surface with ^{Fc6ac}CPMV particles, CV was performed in 0.1 M H_2SO_4, as shown in Figure 7.15, and a shift in the oxidation peak was observed. This suggests that the surface is modified maybe with the SAM but does not conclusively confirm CPMV attachment.

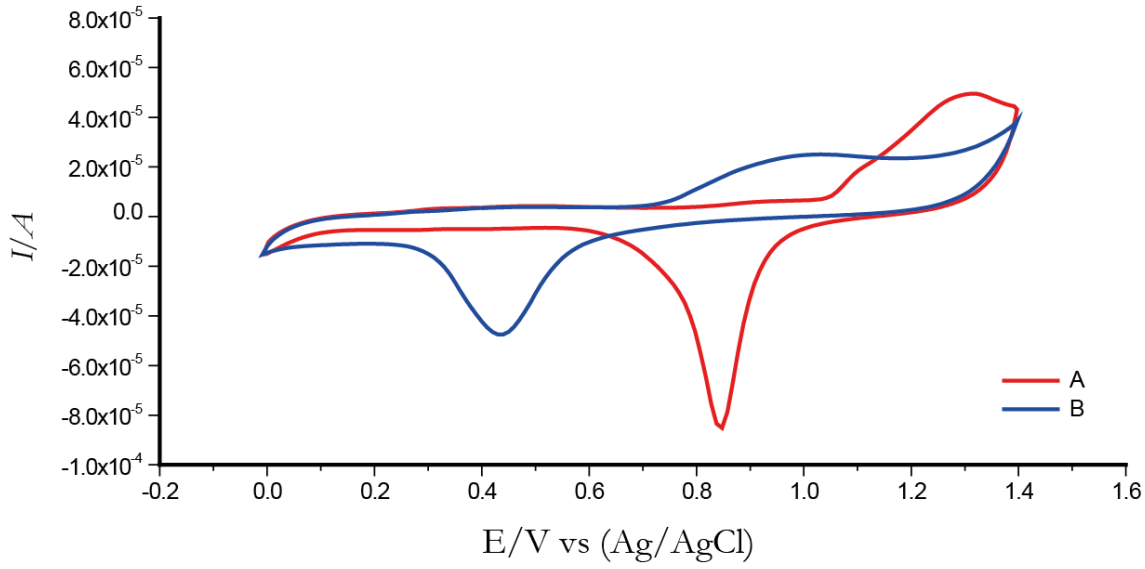

Figure 7.15– CV scans of Au surface before and after attachment of ^{Fc6ac}CPMV particles. A, CV scans before attaching ^{Ferrocene}CPMV and B, after the immobilisation of ^{Fc6ac}CPMV particles. Scan rate of 100 mV s^{-1} in 0.1M H_2SO_4.

The electrochemical analysis of ^{Ferrocene}CPMV in aqueous solution revealed a reversible one–electron signal as explained in detail at the beginning of this chapter. However, no electron transfer through ^{Fc6ac}CPMV and ^{FcC2}CPMV to the gold surface was observed; repetition of this approach did not result in any CV response. Due to the poor quality of the data obtained repeatedly, it is not clear whether the ferrocene centres are not close enough to the electrode or the modified virus particles are acting as insulators and preventing electron hopping. Another possibility is that the ^{Ferrocene}CPMV was not successfully attached to the electrode surface because of a very low reactivity of the NHS terminated monolayer.

7.4.2.2 SAMs formation and characterisation on graphite electrode

As evidence for electroactive ^{Fc6ac}CPMV and ^{FcC2}CPMV on gold could not be obtained, it was desirable to try a graphite surface. It has been reported in the literature that chemical treatment of a graphite surface resulted in a stronger and faster covalent attachment of an azide– or acetylene–terminated layer on the electrode surface (Evrard et al, 2008). Generating an aryl radical that couples with the graphite electrode to form a C–C bond is a well accepted mechanism (Allongue et al, 1997). The graphite surface activation procedure is depicted in Figure 7.16.

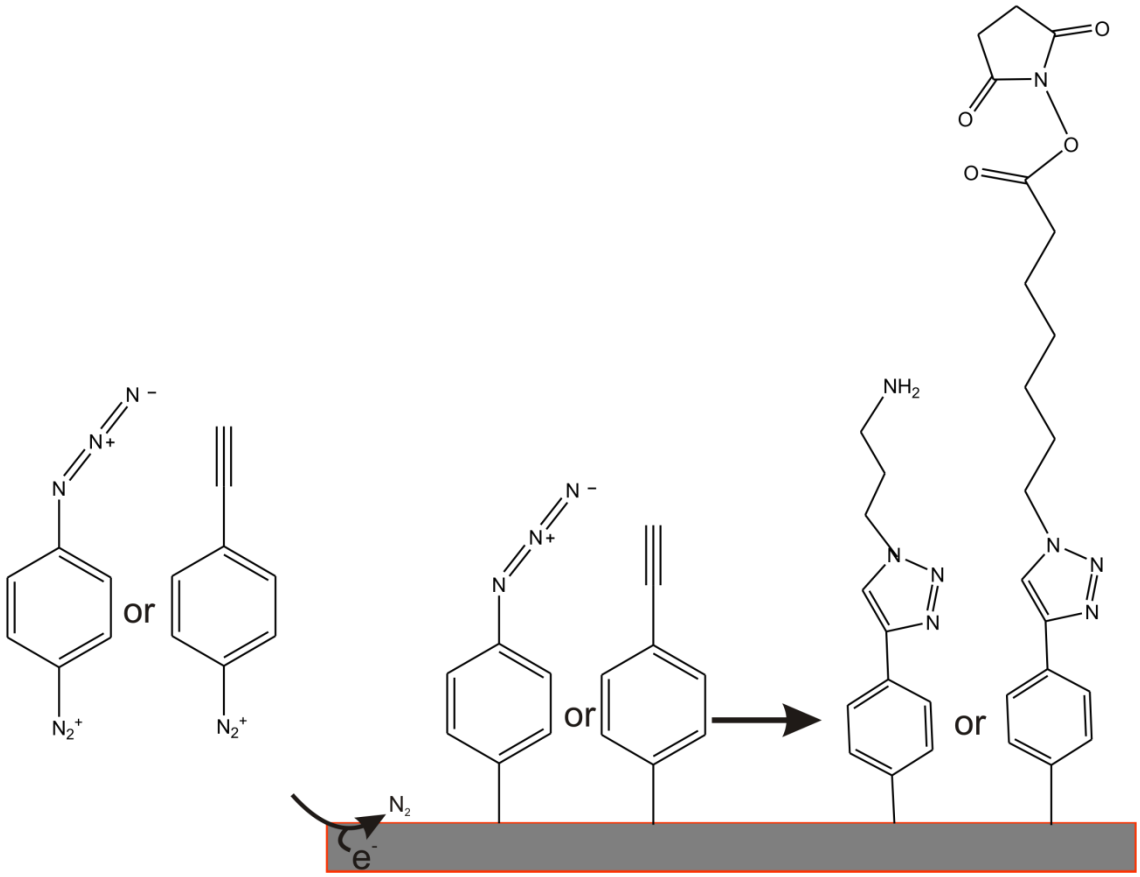

Figure 7.16– Schematic illustration of carbon electrode functionalisation. Electroreduction of phenylazide or phenylacetelyene for immobilisation on PGE electrode. 2 mM (fixed for all experiments) of diazonium salts in 0.1M HCl at scan rate of 0.1Vs^{-1} at ice–cold temperature. The electrodeposition time was ≥ 1minute.

This approach offers several advantages over thiolate SAMs: strong linkage of the linker to the electrode surface, fast surface modification (obtained in under a minute), and easy control over functionalisation coverage (Evrard et al, 2008). The SAM formation on the PGE surface was coupled with acetylene or azide–bearing molecules attached to the virus capsid by "click" chemistry (Allongue et al, 1997; Evrard et al, 2008).

CV monitored the SAMs deposition onto the graphite surface. The CV was recorded of 2 mM diazonium salt at PGE electrode in 0.1 M HCl solution at ice–cold temperature. The first CV scans exhibited a well–defined, reproducible, and irreversible reduction peak at ~ –550 mV. This characteristic corresponds to the typical electroreduction of diazonium salts, leading to the elimination of a nitrogen molecule and the production of an aryl radical, Figure 7.17 line D. This radical has been reported in the literature to attack the surface and to form a covalent bond

between the aryl group and the carbon surface of the electrode (Corgier et al, 2005; Vakurov et al, 2004). The second and third CV scans revealed very low currents, evidence of surface saturation and a result of a very fast deposition processes (<1 min) suggesting that a monolayer was achieved.

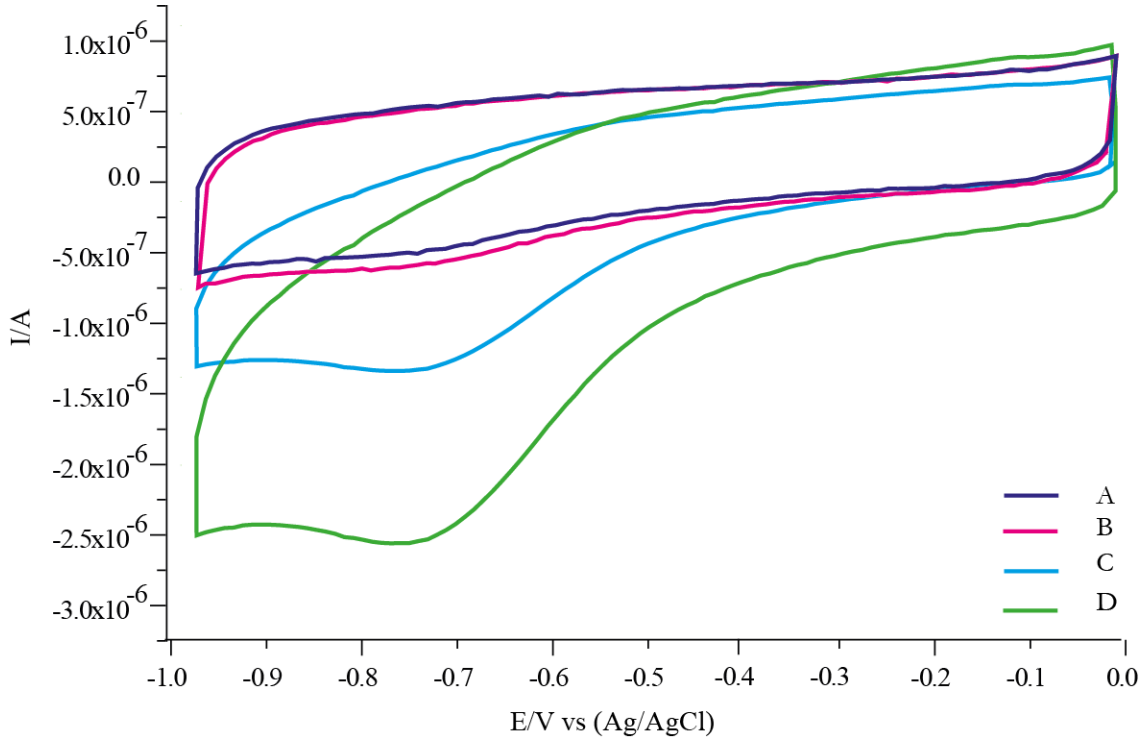

Figure 7.17– CV scans for the confirmation of successful modification of PGE electrode before and after the modification. (A) PGE clean electrode before the modification, (B) PGE after modification, (C) second scan and (D) first scan. 2 mM of either $N_3C_6H_4N_2^+$ or $HC{\equiv}C{-}C_6H_4{-}N_2^+$ in 0.1M HCl and scan rate of 0.1V s^{-1} on ice cold temperature.

To demonstrate the utility of "click" chemistry, the incorporation of aryl diazonium salts to the graphite surface was exploited. The subsequent azide–alkyne cycloaddition reaction was investigated using two approaches: Firstly, "click" reaction between the functionalised PGE surface and the doubly functionalised virus $^{\text{Fc6ac or FcC2}}$CPMV$^{\text{azide or alkyne}}$. Secondly, the "click" reaction was accomplished prior to coupling $^{\text{Fc6ac or FcC2}}$CPMV to the assembled SAM on PGE surface. However, performing "click" reaction in the presence of the virus was difficult as in most trials disassembly of the particles or aggregate formation resulted. Therefore, the "click"

chemistry was performed on the solid surface first, followed by the addition of the modified virus.

Although the graphite surface modification was relatively easy and quick, the subsequent "click" reaction proved to be difficult. As a control experiment, the aminoferrocene (no virus) was used to assess if it is possible for electron communication with the graphite surface. The PGE surface was functionalised with alkyne salt followed by the "click" reaction to esterified monopropargylamide derivative of glutaric acid (PRGL–ac); this in turn was reacted with aminoferrocene. The obtained CV scans are shown in Figure 7.18. The optimum condition that generates the ferrocene signal was subsequently used for all immobilisations of the modified CPMV particles onto the PGE surface.

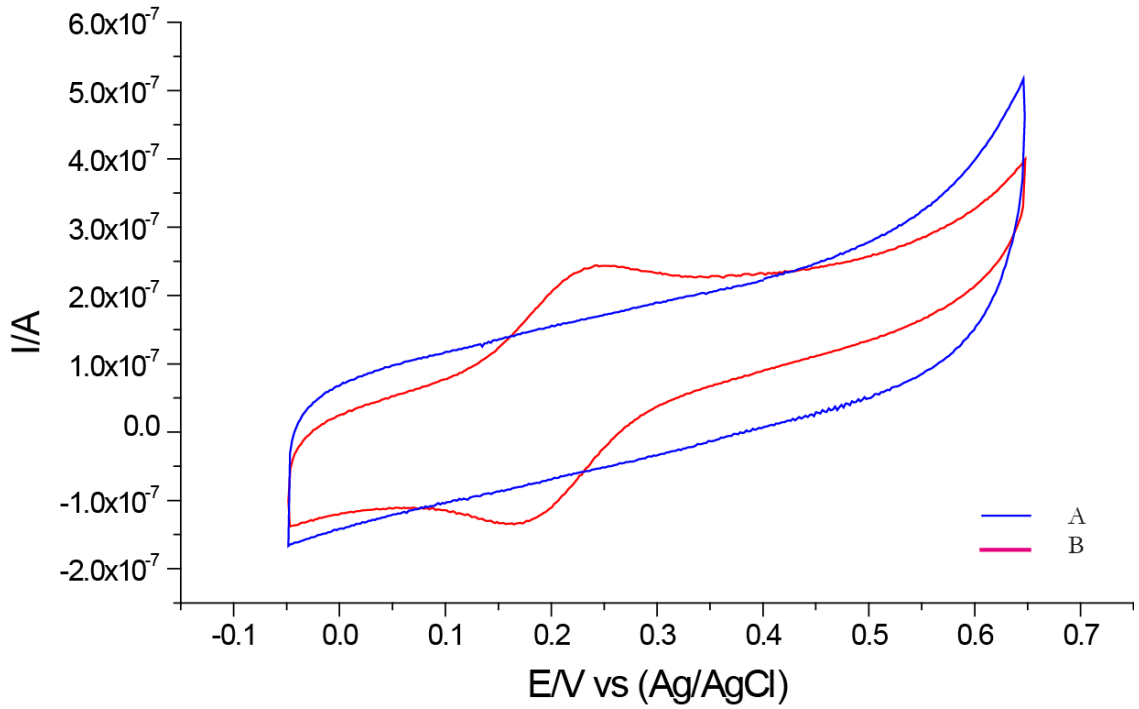

Figure 7.18– CV scans for aminoferrocene conjugated to SAM layer formed via "click" chemistry reaction. A is clean surface and B is the aminoferrocene functionalised PGE surface, scan rate of 0.020 V s^{-1}.

However, the best results obtained from ^{Aminoferrocene}CPMV are shown in Figure 7.19. The signal was so weak and there was a reproducibility issue. It is still not known whether the

entire PGE surface was covered with the modified virus or if there is insufficient electron hopping and exchanging with the surface. Further work is required to investigate whether the virus is acting as an electron insulator and preventing electron hopping.

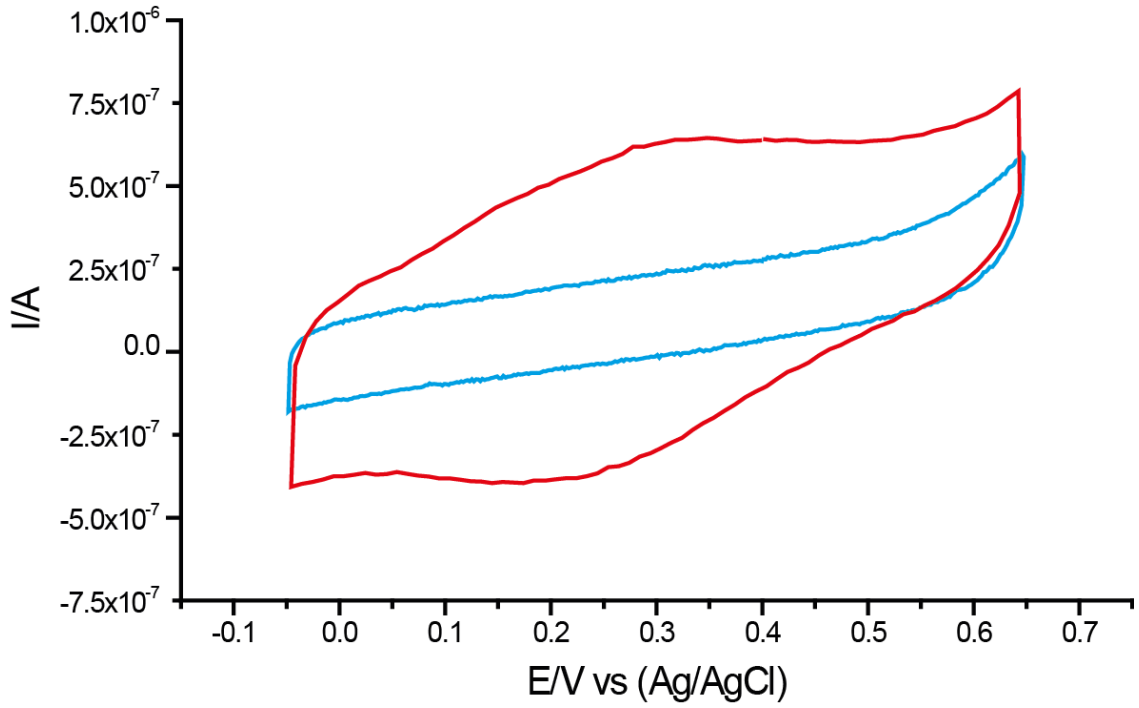

Figure 7.19– CV scans for ^{Aminoferrocene}CPMV conjugated to PGE surface. Blue line is clean surface and red line is the ^{Aminoferrocene}CPMV conjugated to the functionalised PGE surface. Scan rate of 0.1 V s^{-1} in 0.1M sodium phosphate buffer pH 7.0 at ambient temperature ~ 25 °C.

7.5 Conclusions

Viral nanoparticles offer a level of monodispersity almost far beyond the chemist's capabilities. The incorporation of relatively complex and fragile viral nanoparticles in nanoscale electronic devices or components is still far–fetched with major complications. In this chapter, the concept of chemical modification of viral nanoparticles was employed to position redox–active molecules via covalent modification.

It has been shown that both amine and carboxylate groups on the surface of CPMV can be decorated with ferrocene, with various linker lengths, utilising a range of conjugation strategies. The number of ferrocenes, determined electrochemically, per virus particle decreases with the length of the linker. Several ferrocene immobilisation strategies have been adopted to

generate ^{Ferrocene}CPMV hybrids. Cyclic voltammetry was used to both verify and quantify the active functionalities of immobilised ferrocene moieties onto the virus capsid. The multiple redox–active ferrocene moieties on the virus capsid are electrochemically independent, with a reduction potential window of 0.16 V that is dependent on the site of modification and the length of the ferrocene derivatives. The number of ferrocenes coupled to each virus ranged from about 100–240 dependent on the conjugation site and the linker length.

The ferrocene moieties on the outer surface of the virus are electrochemically independent and can act as multielectron reservoirs. The modified virus particles provide a selection of redox active nano–components. The goal was to explore how these can be assembled onto solid electrode surfaces and take advantage of the relay–mechanism from the ferrocene centre to the next moiety (hopping electron transfer); these hybrids may act as electron transfer mediators for the development of redox catalysts, biosensors and nanoelectronic devices.

From the obtained results, it was not clear whether the ferrocene centres are not close enough to the electrode surface or the modified virus particles are acting as insulators and preventing electron hopping. Another possibility is that the ^{Ferrocene}CPMV was not successfully attached to the electrode surface because of a very low reactivity of the NHS terminated monolayer. It might be useful to look for different PGE electrode that could be charachtirised by the available spectroscopy methods at the University of East Anglia facilities. It might be also worth trying ^{Fc}AuNp attached to PGE electrode prior to use ^{Ferrocene}CPMV particles.

7.6 References:

Aljabali AAA, Barclay JE, Butt JN, Lomonossoff GP, Evans DJ (2010) Redox–active ferrocene–modified Cowpea mosaic virus nanoparticles. *Dalton Transactions* **39:** 7569–7574

Allongue P, Delamar M, Desbat B, Fagebaume O, Hitmi R, Pinson J, Savéant J (1997) Covalent Modification of Carbon Surfaces by Aryl Radicals Generated from the Electrochemical Reduction of Diazonium Salts. *Journal of the American Chemical Society* **119:** 201–207

Astruc D, Ornelas C, Ruiz J (2009a) Dendritic molecular electrochromic batteries based on redox–robust metallocenes. *Chemistry* **15:** 8936–8944

Bain CD, Evall J, Whitesides GM (1989) Formation of Monolayers by the Coadsorption of Thiols on Gold – Variation in the Head Group, Tail Group, and Solvent. *Journal of the American Chemical Society* **111:** 7155–7164

Balzani V (2001) *Electron transfer in chemistry*, Weinheim ; New York: Wiley–VCH.

Beasley CA, Murray RW (2009) Voltammetry and redox charge storage capacity of ferrocene–functionalized silica nanoparticles. *Langmuir* **25:** 10370–10375

Chidsey CED, Bertozzi CR, Putvinski TM, Mujsce AM (1990) Coadsorption of ferrocene–terminated and unsubstituted alkanethiols on gold: electroactive self–assembled monolayers. *Journal of the American Chemical Society* **112:** 4301–4306

Corgier BP, Marquette CA, Blum LJ (2005) Diazonium–protein adducts for graphite electrode microarrays modification: Direct and addressed electrochemical immobilization. *Journal of the American Chemical Society* **127:** 18328–18332

Evans DJ (2008) The bionanoscience of plant viruses: templates and synthons for new materials. *Journal of Materials Chemistry* **18:** 3746–3754

Evrard D, Lambert F, Policar C, Balland V, Limoges B (2008) Electrochemical functionalization of carbon surfaces by aromatic azide or alkyne molecules: a versatile platform for click chemistry. *Chemistry* **14:** 9286–9291

Frederix F, Bonroy K, Reekmans G, Laureyn W, Campitelli A, Abramov MA, Dehaen W, Maes G (2004) Reduced nonspecific adsorption on covalently immobilized protein surfaces using poly(ethylene oxide) containing blocking agents. *Journal of Biochemical and Biophysical Methods* **58:** 67–74

Green SJ, Pietron JJ, Stokes JJ, Hostetler MJ, Vu H, Wuelfing WP, Murray RW (1998) Three–Dimensional Monolayers: Voltammetry of Alkanethiolate–Stabilized Gold Cluster Molecules. *Langmuir* **14:** 5612–5619

Jang W, Kamruzzaman S., Lee C, Kang I (2009) Bioinspired application of dendrimers: From bio–mimicry to biomedical applications. *Progress in Polymer Science* **34:** 1–23

Lahav M, N. S. A., Willner I (1999) Au–nanoparticle–bis–bipyridinium cyclophane superstructures: assembly, characterization and sensoric applications. *Journal of the Chemical Society, Perkin Transactions 2***:** 1925–1931

Lee TMH (2008) Over–the–counter biosensors: Past, present, and future. *Sensors–Basel* **8:** 5535–5559

Lojou E, Bianco P (2006) Assemblies of dendrimers and proteins on carbon and gold electrodes. *Bioelectrochemistry* **69:** 237–247

Lopez JL, Tarraga A, Espinosa A, Velasco MD, Molina P, Lloveras V, Vidal–Gancedo J, Rovira C, Veciana J, Evans DJ, Wurst K (2004) A new multifunctional ferrocenyl–substituted ferrocenophane derivative: optical and electronic properties and selective recognition of Mg2+ ions. *Chemistry* **10:** 1815–1826

Manchester M, Steinmetz NF. (2009) Viruses and nanotechnology. *Current Topics in Microbiology and Immunology,*. Springer Berlin Heidelberg, Berlin, Heidelberg.

Newkome GR, He E, Moorefield CN (1999) Suprasupermolecules with Novel Properties: Metallodendrimers. *Chem Rev* **99:** 1689–1746

Nijhuis CA, Ravoo BJ, Huskens J, Reinhoudt DN (2007) Electrochemically controlled supramolecular systems. *Coordination Chemistry Reviews* **251:** 1761–1780

Oms O, Le Bideau J, Vioux A, Leclercq D (2005) Ferrocenylphosphonic acid: from molecule to electro–active hybrid materials. *Comptes Rendus Chimie* **8:** 1237–1242

Padeste C, Grubelnik A, Tiefenauer L (2000) Ferrocene–avidin conjugates for bioelectrochemical applications. *Biosens Bioelectron* **15:** 431–438

Pizzariello A, Stred'ansky M, Miertus S (2002) A glucose/hydrogen peroxide biofuel cell that uses oxidase and peroxidase as catalysts by composite bulk–modified bioelectrodes based on a solid binding matrix. *Bioelectrochemistry* **56:** 99–105

Seiwert B, Karst U (2008) Ferrocene–based derivatization in analytical chemistry. *Anal Bioanal Chem* **390:** 181–200

Staveren DR, Metzler–Nolte N (2004) Bioorganometallic Chemistry of Ferrocene. *Chemical Reviews* **104:** 5931–5986

Steinmetz NF, Calder G, Lomonossoff GP, Evans DJ (2006a) Plant Viral Capsids as Nanobuilding Blocks: Construction of Arrays on Solid Supports. *Langmuir* **22:** 10032–10037

Steinmetz NF, Evans DJ (2007) Utilisation of plant viruses in bionanotechnology. *Org Biomol Chem* **5:** 2891–2902

Steinmetz NF, Lomonossoff GP, Evans DJ (2006b) Cowpea Mosaic Virus for Material Fabrication: Addressable Carboxylate Groups on a Programmable Nanoscaffold. *Langmuir* **22:** 3488–3490

Steinmetz NF, Lomonossoff GP, Evans DJ (2006c) Decoration of Cowpea mosaic virus with multiple, redox–active, organometallic complexes. *Small* **2:** 530–533

Tamura K, Akutagawa N, Satoh M, Wada J, Masuda T (2008) Charge/Discharge Properties of Organometallic Batteries Fabricated with Ferrocene–Containing Polymers. *Macromolecular Rapid Communications* **29:** 1944–1949

Taylor KM, Spall VE, Butler PJ, Lomonossoff GP (1999) The cleavable carboxyl–terminus of the small coat protein of cowpea mosaic virus is involved in RNA encapsidation. *Virology* **255:** 129–137

Togni A, Hayashi T (1995) Ferrocenes: homogeneous catalysis. organic synthesis. materials science, Weinheim ; New York: VCH.

Togni A, Rihs G (1993) Synthesis and structure of enantiomerically pure ferrocene derivatives for nonlinear optics. *Organometallics* **12:** 3368–3372

Tredgold RH (1991) An Introduction to Ultrathin Organic Films– from Langmuir–Blodgett to Self–Assembly – Ulman,A. *Nature* **354:** 120–120

Ulman A (1996) Formation and structure of self–assembled monolayers. *Chemical Reviews* **96:** 1533–1554

Vakurov A, Simpson CE, Daly CL, Gibson TD, Millner PA (2004) Acetylcholinesterase–based biosensor electrodes for organophosphate pesticide detection: I.Modification of carbon surface for immobilization of acetylcholinesterase. *Biosensors and Bioelectronics* **20:** 1118–1125

Wang Q, Kaltgrad E, Lin TW, Johnson JE, Finn MG (2002) Natural supramolecular building blocks: Wild–type cowpea mosaic virus. *Chemistry & Biology* **9:** 805–811

Yang H, Jiang W, Lu Y (2007) Ferromagnetic conductive polypyrrole doped with water–soluble ferrocene derivative. *Materials Letters* **61:** 1439–1442

8 ^{Enzyme}CPMV nanoparticles

8.1 Introduction

Enzyme–nanoparticle conjugates that take advantage of the catalytic ability of the bound enzyme have been reported in the literature for various applications (Katz & Willner, 2004; Niemeyer, 2001). For example, the enzymes horseradish peroxidase (HRP) and glucose oxidase (GOX) have been sequentially co–immobilized in polyelectrolyte multilayers on silica nanoparticles to facilitate the overall enzymatic reaction; the GOX layer generating hydrogen peroxide in the presence of β–D–glucose that diffuses toward the HRP layer to be reduced to water in the presence of *o*–dianisidine (HRP substrate) (Pescador et al, 2008). The objective described here was to examine the use of CPMV as a solid support to construct enzyme–based functional virus particles. Two well-studied enzymes were employed as model enzymes: HRP and GOX. The preparation of ^{Enzyme}CPMV conjugate was by covalent modification of wild–type CPMV.

HRP is a hemoprotein enzyme of molecular weight 40 kDa that can catalyze the reaction of hydrogen peroxide with certain organic, electron–donating substrates to yield highly coloured products. The presence of the heme group gives the enzyme its characteristic brown colour and maximum absorption at 403 nm. HRP is a glycoprotein that contains significant amount of carbohydrate. Thus mild oxidation of the enzyme sugar residues with sodium periodate generates reactive aldehyde groups that can be used for conjugation to amine containing molecules (Hermanson, 2008).

GOX is a flavoenzyme that catalyses the oxidation of ß–D–glucose to D–glucono–1,5–lactone and hydrogen peroxide, using molecular oxygen as the electron acceptor. The enzyme consists of two identical subunits (MW 80 kDa each) bound together by disulfide linkages (O'Malley & Weaver, 1972). GOX contains two tightly bound flavin adenine dinucleotide (FAD) cofactors, one per subunit. GOX contains 16 % carbohydrate by weight that could be

oxidised with sodium periodate to generate aldehyde groups. GOX is widely used in diagnostic assays for the determination of glucose concentration in physiological fluids (Hermanson, 2008).

Enzymes possess unique catalytic properties compared to chemical catalysts: biocompatibility, higher efficiency and specific selectivity toward substrates. These particular properties make enzymes suitable as biocatalysts for *in vitro* reactions. Enzymes have been successfully immobilized on many surfaces, e.g., gold nanoparticles (Yáñez–Sedeño & Pingarrón, 2005), magnetic nanoparticles (Caruso & Schüler, 2000) and carbon nanotubes (Lin et al, 2004).

Enzyme immobilization restricts the movement of the enzymes, which in turn provides a physical support through the covalent binding of the enzymes to the virus capsid and therefore prevents the aggregation of the enzyme particles. The immobilisation techniques represented here use covalent attachment of two frequently used enzymes, HRP and GOX, as a starting point to demonstrate the possibilities for virus–enzyme hybrids. Different immobilisation strategies were exploited to couple the enzymes to the virus capsid through covalent attachment with various length linkers, which could result in different performances for the immobilized enzyme.

The activation method (periodate method), which has been used here to generate functional groups on the surface of the glycosylated enzymes (HRP and GOX), takes advantage of the carbohydrates present on the enzyme to generate aldehyde groups. These groups could be used directly or subsequently modified to add longer spacers such as adipic acid dihydrazide (ADH) (Basu et al, 2003a; Hermanson, 2008). This method is still gentle enough not to lose the enzymatic activity. However, enzyme immobilisation often results in the undesirable alteration of the enzymes' 3D conformation (Grunes et al, 2003; Willner et al, 2007).

This chapter describes preliminary studies to evaluate several strategies for enzyme immobilisation on the virus capsid. Enzyme immobilisation is defined here as the restriction of the enzyme mobility in a fixed space by covalent attachment to the surface of CPMV.

8.2 Materials and Methods

8.2.1 Materials

All general reagents, HRP (type VI–A, Product code P6782), glucose oxidase (GOX from *Aspergillus niger*), D–glucose and 6–(ferrocenyl)hexanethiol were purchased from Sigma–Aldrich UK and used without further purification. 1–ethyl–3–(3–dimethlyaminopropyl)carbodiimide hydrochloride (EDC) was purchased from Novabiochem, *N*–hydroxysuccinimide (NHS) from Fluka.

8.2.2 Enzyme activation (periodate method)

HRP or GOX (10 mg) was dissolved in 10 mM sodium phosphate buffer pH 7.0 (1 ml) and a freshly prepared aqueous solution of sodium periodate was added to a final concentration of 10 mM. The reaction solution was left to react for 30 minutes with stirring, protected from light in a brown vial at 4 °C to prevent periodate breakdown. The reaction was accompanied by a colour change from brownish/gold to light green in the case of HRP. The activated enzyme was purified using a Sephadex G–25 matrix (PD–10 column) equilibrated with 10 mM sodium phosphate buffer pH 7.0. Eluted samples (200 µl) were collected and monitored for GOX at 280 nm and for HRP at 403 nm and were quantified by measuring the absorbance at 403 nm using an extinction coefficient of $\varepsilon = 102\ mM^{-1}\ cm^{-1}$ (Dunford, 1979). Activated enzyme was used immediately after activation or stored for no more than two weeks at –20° C. Fresh samples were prepared as and when required.

8.2.3 Enzyme–adipic acid dihydrazide (E–ADH)

The method was adapted from (Basu et al, 2003a) in which ADH (100 mg) was mixed with the freshly prepared periodate–oxidised enzyme (HRP or GOX) , followed by the addition of 10 µl of 5 M sodium cyanoborohydride in 1 M NaOH (Sigma) per millilitre of the reaction solution to stabilise the hydrazone bond. The reaction was left to proceed while gently stirring overnight at 4 °C. Excess and unbound reagents were purified as described above, followed by

dialysis against 10 mM sodium phosphate buffer pH 7.2 using 10 kDa cut–off membrane (Pierce).

8.2.4 ^{Enzyme}CPMV

Varieties of methods were employed to immobilise activated HRP or GOX onto the CPMV capsid.

8.2.4.1 $^{Allylamine\ linkage}$CPMV (Schiff Base)

A generated aldehyde group on the HRP enzyme can react with primary amines on the virus surface to form an allylamine linkage (Hermanson, 2008). The Schiff base has a relatively labile bond that is readily reversed by hydrolysis in aqueous solution. Therefore, the product is stabilised by sodium cyanoborohydride reduction (Hermanson, 2008), as depicted in Figure 8.1. A 2000 molar excess of freshly oxidised HRP was incubated with 1 mg ml^{-1}

CPMV particles suspended in 0.1M sodium phosphate buffer pH 8.5. 10 µl of 5 M sodium cyanoborohydride in 1 N NaOH was then added. The reaction was allowed to proceed for 2 hours at ambient temperature. The modified particles were purified on PD–10 columns followed by dialysis against 0.1 M sodium phosphate buffer pH 7.0 for 2 days. A quantity of 5 mg ml^{-1} esterified enzyme was incubated with CPMV particles (10 mg ml^{-1}, 1.5 ml) in 10 mM sodium phosphate buffer pH 7.0. The reaction was left overnight (16 hours) at 4 °C to react. ^{HRP}CPMV particles were purified on a Sephacryl S–500 gel filtration column followed by further washing and concentration on 100 kDa cut–off columns until no HRP activity was detected in the supernatant (by addition of H_2O_2 and TMB) in order to ensure the removal of all unbound enzymes.

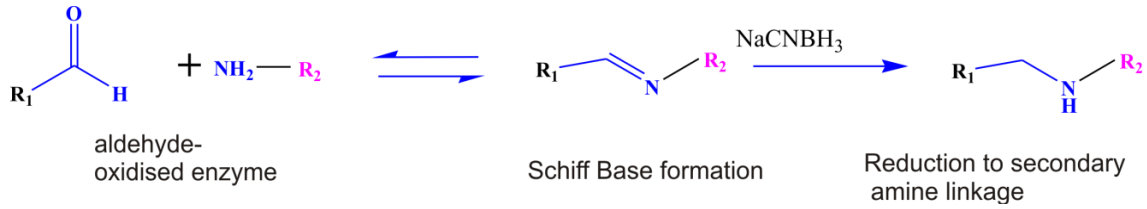

Figure 8.1– Aldehyde groups generated on the enzyme surface can react with amine nucleophiles to form reversible Schiff base intermediates. In the presence of suitable reductant, such as sodium cyanoborohydride, the Schiff base is stabilised to a secondary amine bond. The scheme is reproduced from (Hermanson, 2008). R_1 refer to enzyme and R_2 refers to CPMVwt.

8.2.4.2 $^{HRP–streptavidin–Biotin}$CPMV

^{Biotin}CPMV was made following our standard protocol (Steinmetz et al, 2006a) and see section 6.2.7. Commercially available streptavidin–HRP (Upstate) was mixed in a 200:1 molar ratio to ^{Biotin}CPMV particles; the reaction was left to proceed overnight at 4 °C while gently stirring. $^{HRP–streptavidin–Biotin}$CPMV hybrid was purified on a Sephacryl S–500 column; the eluent was monitored at 280 nm. Fractions were collected, concentrated and further analysed.

8.2.4.3 HRP–ADH + DyLight488–NHSester

Previously prepared HRP–ADH (1mg, 1ml) was incubated with DyLight488–NHS ester. HRP in a ratio of 1:10 with DyLight488–NHS ester to ensure partial modification. Dye–labelled enzyme was dialysed against 10 mM sodium phosphate buffer to remove all unbound dye for 36 hours with buffer change approximately every 12 hours. Dye–labelled enzyme was incubated in a 200 molar ratio to CPMVwt particles and the reaction left to proceed as described in section 7.2.8.4.

8.2.4.4 $^{Enzyme–ADH}$CPMV

This approach was employed for both HRP and GOX enzymes. The virus particles suspended in 10 mM sodium phosphate buffer pH 7.0 were activated via EDC/NHS as reported previously, followed by either purification on PD–10 or through column filtration on 300K MWCO membranes (Sartorius Stedim). The esterified virus was concentrated and further

incubated with enzyme–ADH in a 200 molar excess. The reaction mixture was left to proceed overnight at 4 °C while gently stirring. The ^{Enzyme}CPMV hybrid was purified on a gel–filtration column (Sephacryl S–500), fractions were collected, concentrated and further analysed.

8.2.4.5 $^{(Fc6ac)–GOX–ADH}$CPMV^{Fc6ca}

$^{GOX–ADH}$CPMV particles prepared as above were incubated with *N*–(ferrocenylmethyl)–6– aminocaproic acid (Fc6ac), a mediator for amperometric enzymatic analysis. This was found to be a better approach than modifying the CPMV particles with ferrocene carboxylic acid first, bearing in mind that the ferrocene could be bound to both the virus and the enzyme. Doubly–functionalised particles $^{(Fc6ac)–GOX–ADH}$CPMV^{Fc6ac} were purified as described earlier.

8.2.4.6 ^{Benzaldehyde}CPMV approach

The protocol is adapted from (Brunel et al, 2010). Sulfo–succinimidyl 4–formylbenzoate sodium salt (sulfo–S–4FB) (Solulink) in Milli–Q water was added in 2000 molar excess to CPMV (10 mg ml^{-1}, 1 ml) suspended in 10 mM sodium phosphate buffer pH 7.0 for 20 hours at ambient temperature (25 °C). CPMV was desalted as described (section 2.14.2). The eluted sample was concentrated on 100 kDa cut–off membranes before being layered onto 5 ml 10%–50% sucrose gradient (section 2.14.1). The ^{Benzaldehyde}CPMV conjugate was incubated with 200 molar excess of freshly oxidised HRP and incubated at ambient temperature (12–15 hours). Modified particles were then purified by gel filtration (section 2.14.2). The concentration was determined by UV–vis spectrophotometry with a recovery yield of 80–90% based on the initial virus concentration. Particle integrity was confirmed by agarose gel electrophoresis and TEM.

8.2.4.7 ^{SATP}CPMV approach

N–Succinimidyl–S–acetylthiopropionate (SATP) was prepared according to the manufacturer's instruction and as has been published previously (Steinmetz et al, 2007). After the deprotection on the chemically introduced thiol group, the particles were incubated with

HRP–maleimide (commercially obtained). $^{HRP–maleimide–SATP}$CPMV particles were purified as described earlier.

8.2.5 Electrochemical measurements

For $^{(Fc6ac)–GOX–ADH}$CPMV^{Fc6ac}: Particles suspended in 0.1M sodium phosphate buffer pH 7.0 were added to the three–electrode cell (described in section 7.2.3). The clean PGE electrode was immersed in 0.1 M sodium phosphate buffer, pH 7.0 and the electrochemical response was allowed to stabilise before adding the doubly–functionalised particles. The current response to the glucose concentration change was measured while gently stirring. 10 µl of glucose stock solution (0.5 M in 0.1 M phosphate buffer pH 7.0) was added typically at time intervals of 1 minute. The change in current is proportional to the apparent activity of enzyme immobilised on the virus particles. The amperometric studies were performed at ambient temperature (25° C).

8.2.6 HRP concentration using UV–vis analysis

The concentration of HRP stock solutions was determined using the characteristic absorbance of the heme group at 403 nm and an extinction coefficient of 102 mM^{-1} cm^{-1} (Dunford, 1979).

8.2.6.1 Catalytic activity of ^{Enzyme}CPMV and free enzymes

$^{HRP–ADH}$CPMV: The catalytic activity of $^{HRP–ADH}$CPMV and free HRP was tested using 3,3',5,5'–tetramethylbenzidine (TMB) substrate catalyzed by HRP in the presence of H_2O_2. Briefly, one tablet of TMB was dissolved in 10 ml of 10 mM sodium phosphate buffer pH 7.0 so the subsequent analysis of $^{HRP–ADH}$CPMV would be under the same buffer conditions. 2 µl of fresh 30% hydrogen peroxide was added just prior to use to the TMB substrate solution. The reaction was carried out in 96–well Elisa plates. 50 µl of 2 M H_2SO_4 per 100 µl reaction mixture was used to stop the reaction. A multi–well reader at 450 nm quantified the generated colour. Averaging the 12 replicates from each known HRP concentration was plotted using Excel 2007 software to generate a calibration curve. The absorbance of three independent plates was used to

generate the calibration curve. Data was plotted and the concentration of HRP from the sample was obtained.

$^{GOX–ADH}$**CPMV**: Amplex Red Glucose/Glucose Oxidase assay kit (Invitrogen, cat. No A22189). The kit was used according to the manufacturer's instruction. The reaction was protected from light at all times.

8.3 Results and discussion

8.3.1 Enzyme oxidation (activation) with periodate

Sodium metaperiodate is used to oxidize hydroxyl groups on adjacent carbon atoms of the polysaccharide residues in the glycoproteins, forming reactive aldehyde residues suitable for coupling with amines or hydrazide–containing molecules. For example, HRP contains 21% by mass carbohydrate according to the PDB data bank (1H58). The reaction cleaves the carbon–carbon bond between two adjacent (vicinal) secondary hydroxyls to create two terminal aldehyde groups (Hermanson, 2008). Herein, the approach was used to oxidize hydroxyl–containing carbohydrate within the HRP and GOX to create reactive aldehyde groups, which could be further modified with suitable linker such as ADH, this process is depicted in Figure 8.2.

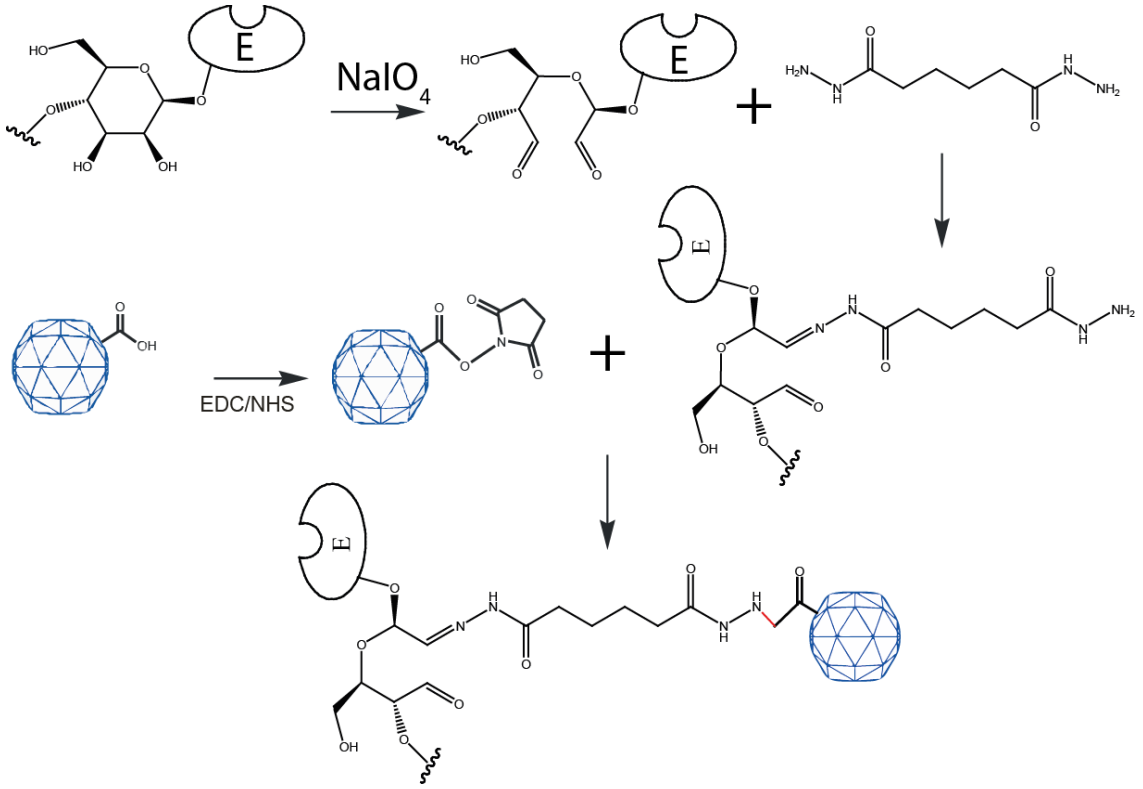

Figure 8.2– Enzymes that are glycoproteins, like HRP and GOX, may be oxidised with sodium metaperiodate to produce reactive aldehyde residues. The oxidation by metaperiodate of vicinal hydroxyl groups of the carbohydrate moieties generate aldehyde groups followed by hydrazone bond formation between enzyme and ADH; and subsequently the conjugation of ADH–enzyme onto $^{NHS-ester}$CPMV surface–exposed carboxylate forms an amide bond.

8.3.2 ^{Enzyme}CPMV

The reaction of the preactivated enzyme with CPMV particles resulted in the formation of $^{HRP\ or\ GOX}$CPMV. Intact virions of ^{Enzyme}CPMV were characterised by native gel electrophoresis according to their migration towards the anode. ^{Enzyme}CPMV derivatives joined by various length linkers, exhibited various mobility patterns as shown in Figure 8.3. This behaviour is thought to arise because of a combination of size and charge effects perturbing the mobility through the gel. However, all migrate to a different extent than wild–type (negative control) and positive controls ($^{NHS-ester}$CPMV) confirming that the particles have been modified and that the particles remain intact after bioconjugation.

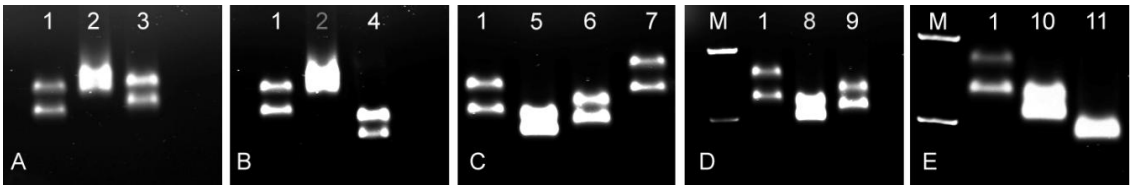

Figure 8.3– Wild–type and ^{Enzyme}CPMV particles separated on a 1.2% agarose gel using various coupling chemistries stained with ethidium bromide. (A) Schiff base approach to couple oxidised enzyme to the surface lysines, (B) HRP–ADH coupled to the surface carboxylate, (C) ^{SATP}CPMV and commercially activated maleimide HRP, (D) ^{SF4}CPMV and HRP–ADH, and (E) $^{NHS–LC–LC\ biotin}$CPMV and streptavidin–HRP. Lane 1, CPMVwt; 2, $^{NHS–ester}$CPMV; 3, ^{HRP}CPMV; 4, $^{HRP–ADH}$CPMV; 5, ^{SATP}CPMV protected; 6, ^{SATP}CPMV unprotected; 7, $^{Mal–HRP–SATP}$CPMV; 8, ^{SF4}CPMV; 9, $^{HRP–ADH–SF4}$CPMV; 10, $^{NHS–LC–LC–biotin}$CPMV; 11, $^{HRP–SA–Biotin}$CPMV, and M is marker 1.5 kb.

Further evidence to support the successful bioconjugation of the enzyme to the virus capsid was provided by comparison of the SDS–PAGE of denatured modified and unmodified CPMV particles. The clearest results were obtained with the HRP–ADH approach as shown in Figure 8.4. SDS–PAGE revealed two extra bands on the modified particles at approximately 62 and 80 kDa (, lane 3), corresponding to the size of one conjugated enzyme (~ 40 kDa) to the S and L proteins respectively. This suggests partial modification to the L or the S and there is no preference to which lysine the enzyme will be coupled to, in addition unmodified L and S are observed. However, the Schiff base approach resulted in only one extra band matching the 62 kDa (i.e successful modification of S). After much optimisation, only the HRP–ADH approach was pursued further. Tryptic digest and further analysis using Mass Spectrometry TOF–MS and OptiPrep on the extra bands highlighted in Figure 8.4 did not reveal any fragments of HRP sequence, the mass spectral peaks of $^{HRP–ADH}$CPMV were barely detectable. This was possibly to do with the trypsin used for digestion being unable to cleave in the presence of heme group; acid treatment prior to the tryptic digest may be needed to overcome this (Personal communication with Dr. Mike Naldrett, JIC) (Kvaratskhelia et al, 1999). The SDS–PAGE also revealed that unmodified S and L coat protein is also present in the modified particles, which means that not all of the protein subunits are coupled with enzymes. This could be because the dimensions of the enzyme are possibly blocking some binding sites. It is worth mentioning that none of the intermediate controls revealed any extra bands. This eliminates any suspicion of cross–linking between the subunits or that the particles are unmodified. Furthermore,

fluorescent labelling of HRP–ADH enzyme with DyLight 488–NHS Ester was carried out as described in section 7.2.8.3. After rigorous purification, the labelled enzyme was conjugated to the virus capsid. Doubly labelled particles $^{HRP–ADH}CPMV^{DyLight488}$ were rigorously purified and the particles were found to be fluorescent, suggesting the enzyme is coupled to the capsid. The number of dyes per HRP was determined spectrophotometrically as shown in Figure 8.5 and estimated to be 2.45 dye per enzyme and 14 ± 3 enzymes per virus. The extinction coefficients used are: ε_{HRP}, 102 mM^{-1} cm^{-1}, $\varepsilon_{DyLight488}$, 70000 M^{-1} cm^{-1} and ε_{CPMV}, 8.1 mg ml^{-1} cm^{-1}. The molecular mass for HRP is 40 kDa and for the CPMVwt is 56 kDa.

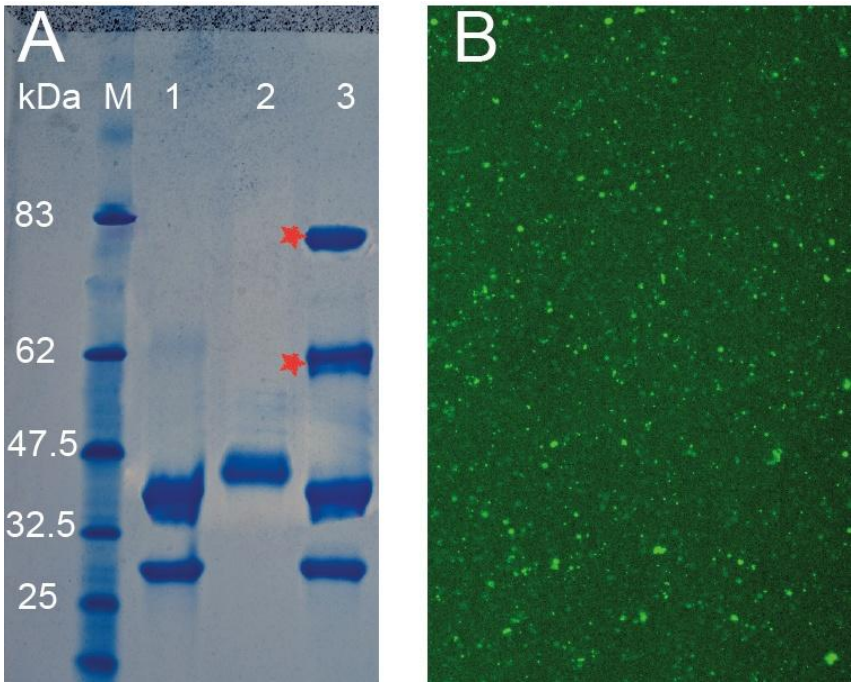

Figure 8.4–SDS–PAGE of $^{HRP–ADH}CPMV$ particles. Modified particles were purified on sucrose gradient followed by gel filtration on Sephacryl–S500 column. (A) Modified particles were pooled and were separated by 4–12% SDS–PAGE and Coomassie stained. Asterisk denotes bands that were submitted for mass spectrometry. Lane 1, CPMVwt; 2, HRP–ADH; and 3, $^{HRP–ADH}CPMV$; M is prestained protein marker. (B) $^{HRP–ADH}CPMV^{DyLight\ 488}$ image dried on coverslip and viewed by Leica SP2 inverted confocal microscope (image was taken by Mr. Grant Calder).

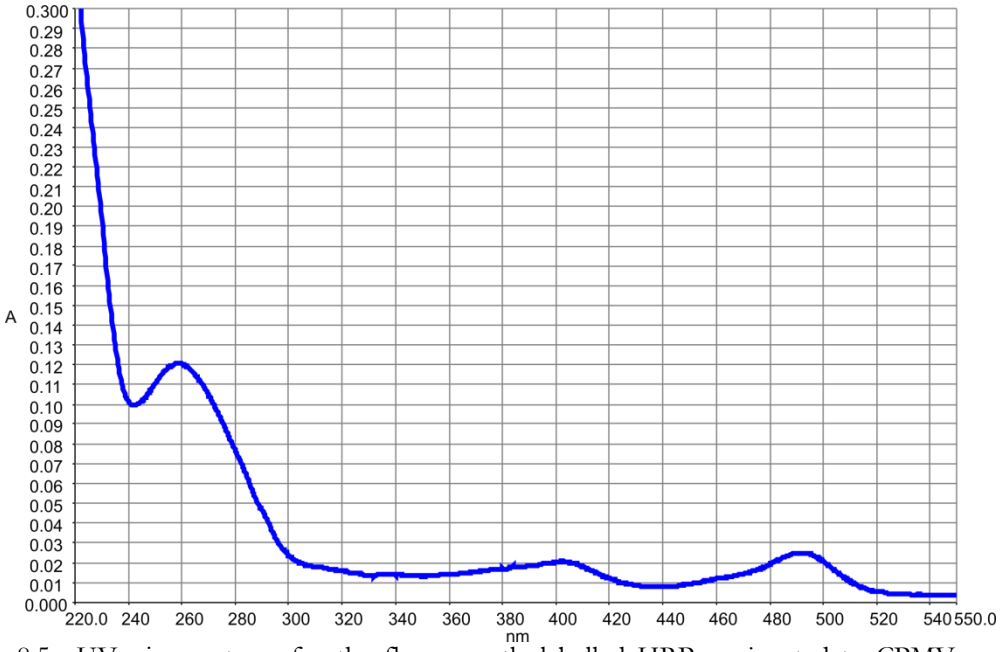

Figure 8.5– UV–vis spectrum for the fluorescently labelled HRP conjugated to CPMV particles. The number of dyes per virus was determined to be 32 dyes per virus while there are 2 ± 0.45 dyes per enzyme as calculated according to the manufacturer's instruction. This equates to 14 ± 3 enzymes per virus.

The TEM images for $^{HRP–ADH}$CPMV Figure 8.6–A revealed intact, monodisperse, CPMV particles of *ca.* 38.5 ± 0.5 nm in diameter, which is in agreement with the measured particles of ~ 40 ± 0.3 nm by DLS, Figure 8.6–B. This confirms that the particles are modified and that the increase in the particle size of ~ 10 nm corresponds to the expected particle size with the enzyme bound to the exterior of the particles. Furthermore, TEM was used to detect the remaining aldehyde groups on the $^{HRP–ADH}$CPMV by staining with $AgNO_3$ as shown in Figure 8.7–A. It has been reported that the silver staining technique (also known as Tollens' reagent) can be used for selective staining of exposed polysaccharides in the cell wall. The specificity of this staining is dependent on the production of aldehyde groups after periodate oxidation of the polysaccharide (Hanker & Giammara, 1983). It is proposed that the remaining unreacted aldehyde groups on the $^{HRP–ADH}$CPMV react with silver nitrate, causing a deposition of silver on specific sites. The pattern observed in Figure 8.7–A does not resemble any patterns obtained from the negative controls as shown in Figure 8.7–B, C and D and that the black dots in Figure 8.7–A (metallic silver) are localized on the spherical particles of the same size of modified virus

particles. This confirms that the oxidised enzyme is coupled to the virus capsid. Metallic silver was not seen on any parts of the grids.

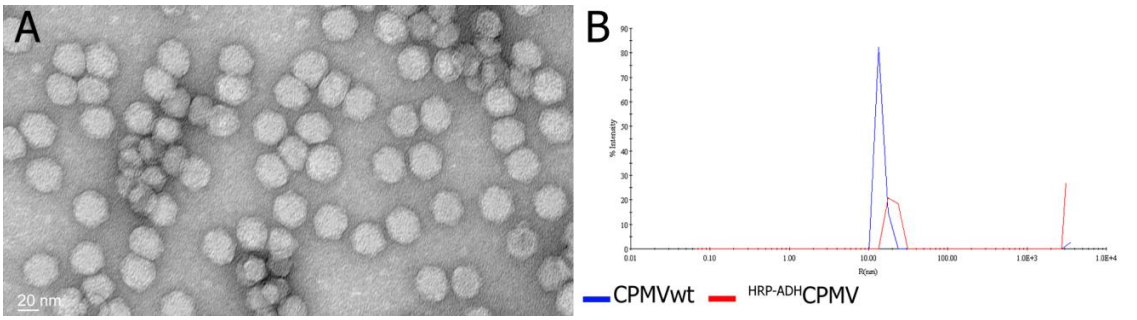

Figure 8.6–TEM image of $^{HRP–ADH}$CPMV particles stained with 2% UA (A) and the corresponding DLS data in (B). Both characterisation methods confirmed independently the successful coupling of HRP to the virus capsid and shows particles of ~ 40 nm in diameter.

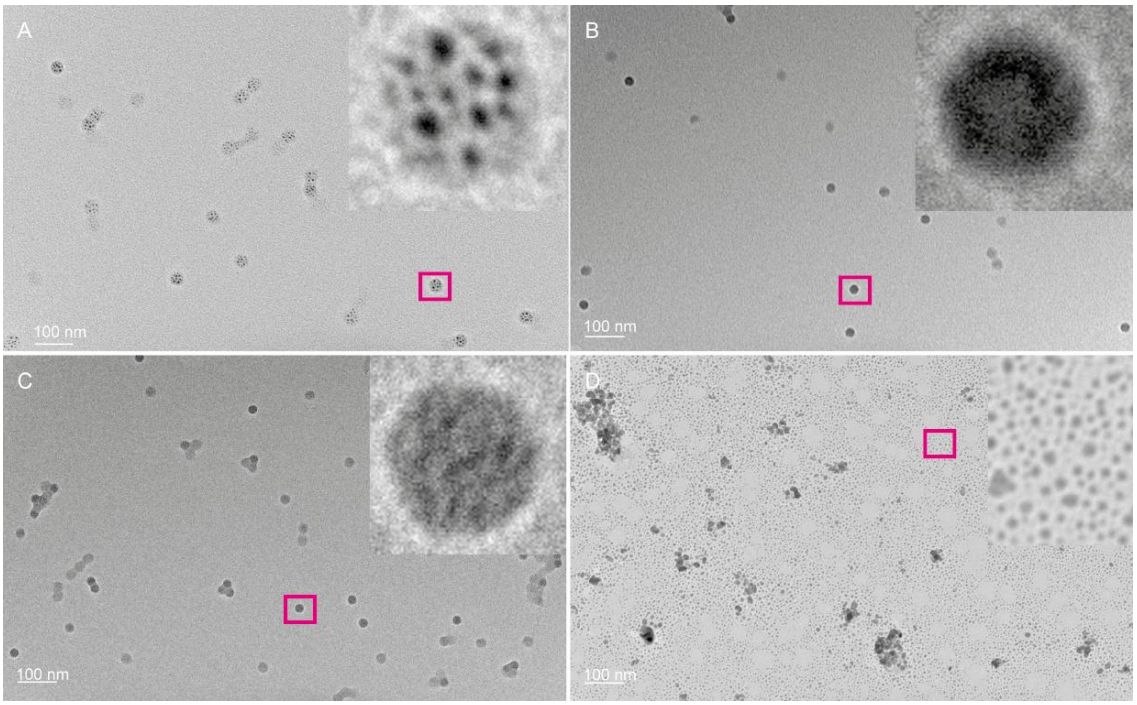

Figure 8.7– TEM images of $^{HRP–ADH}$CPMV particles stained with 1% $AgNO_3$ solution. Particles were washed thoroughly with Milli–Q water after deposition on TEM grids and after the addition of 5–10 µl of 1% $AgNO_3$ solution. (A) $^{HRP–ADH}$CPMV particles; inset confirms the localization of the metallic silver on the virus capsid; (B) CPMVwt; (C) $^{NHS–ester}$CPMV; and (D) free HRP–ADH. The pattern observed in panel C corresponds to the same size and pattern observed in panel A confirming the successful modification of the virus capsid.

Further, zeta potential for suspensions of the $^{HRP–ADH}$CPMV particles in buffer are considerably more negative than that for CPMVwt, Figure 8.8–A, of *ca.* –(12 ± 1.5) mV. Additionally, $^{NHS–ester}$CPMV, as a positive control, has a zeta potential value of –(19.5 ± 1.2) mV Figure 8.8–B. Zeta potential values of –(36 ± 2.1) mV for $^{HRP–ADH}$CPMV are expected since HRP molecules are much smaller than CPMV particles and HRP molecules are composed of charged and uncharged residues. HRP contains 21% carbohydrate according to the PDB data bank (1H58) and 308 amino acid residues in which 60% are hydrophilic and 40% are hydrophobic residues (Veitch, 2004).

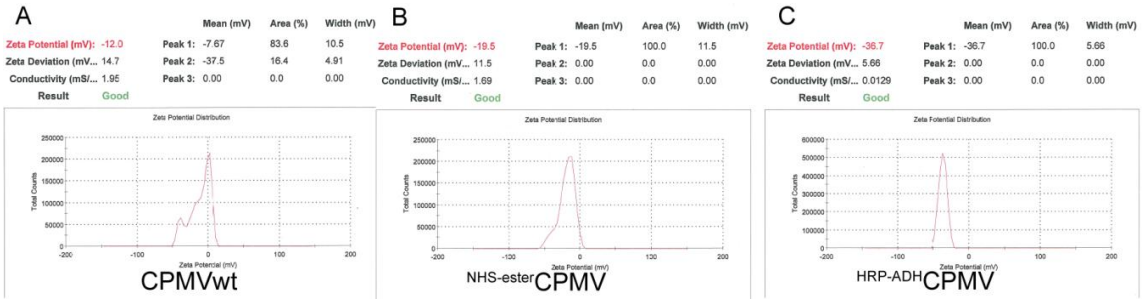

Figure 8.8– Zeta potential measurement of (A) CPMVwt (B) $^{NHS–ester}$CPMV and (C) $^{HRP–ADH}$CPMV particles.

8.3.3 Enzyme quantification

The enzymatic activity of the immobilised HRP was investigated in the presence of H_2O_2 and TMB as substrates. Incubation with $^{HRP–ADH}$CPMV particles resulted in the production of various degrees of blue colour depending on the enzyme concentration; in comparison to CPMVwt particles that did not catalyse a colour change. This confirmed that the immobilised HRP retained their catalytic activity. When the enzymatic activity experiment was repeated on particles stored at 4 ºC for 7 days, approximately the same absorbance was observed suggesting that no structural changes to the HRP particles had occurred during the storage period.

To quantify the number of enzymes coupled to the virus, $^{HRP–ADH}$CPMV calibration curves were obtained using different working standard solutions of free HRP prepared by serial dilution. The HRP concentration was determined independently as explained in section 7.2.2.5. Each enzyme concentration was prepared and used on the same day, 12 activity measurements

for each enzyme concentration were recorded and the absorbance was averaged. The HRP concentration was plotted versus the absorbance of the substrate (TMB) at 450 nm. The data was fitted with linear regression with slope y= 4.208E+05 (R=0.9536). The absorbance recorded at 450 nm for $^{HRP–ADH}$CPMV (treated as unknown) was 0.9069 and from the calibration curve depicted in Figure 8.9, the corresponding HRP concentration was 1.83 µg. By measuring, the concentration of CPMV particles by UV–vis the number of immobilized enzymes was then calculated to be approximately 11±1 per virion. This assumes that HRP activity on the virion is the same as the HRP activity in solution (i.e., no enzymatic activity loss). The data is in agreement with the number of enzyme per virus subsequently calculated from the HRP calibration curve (Figure 8.9).

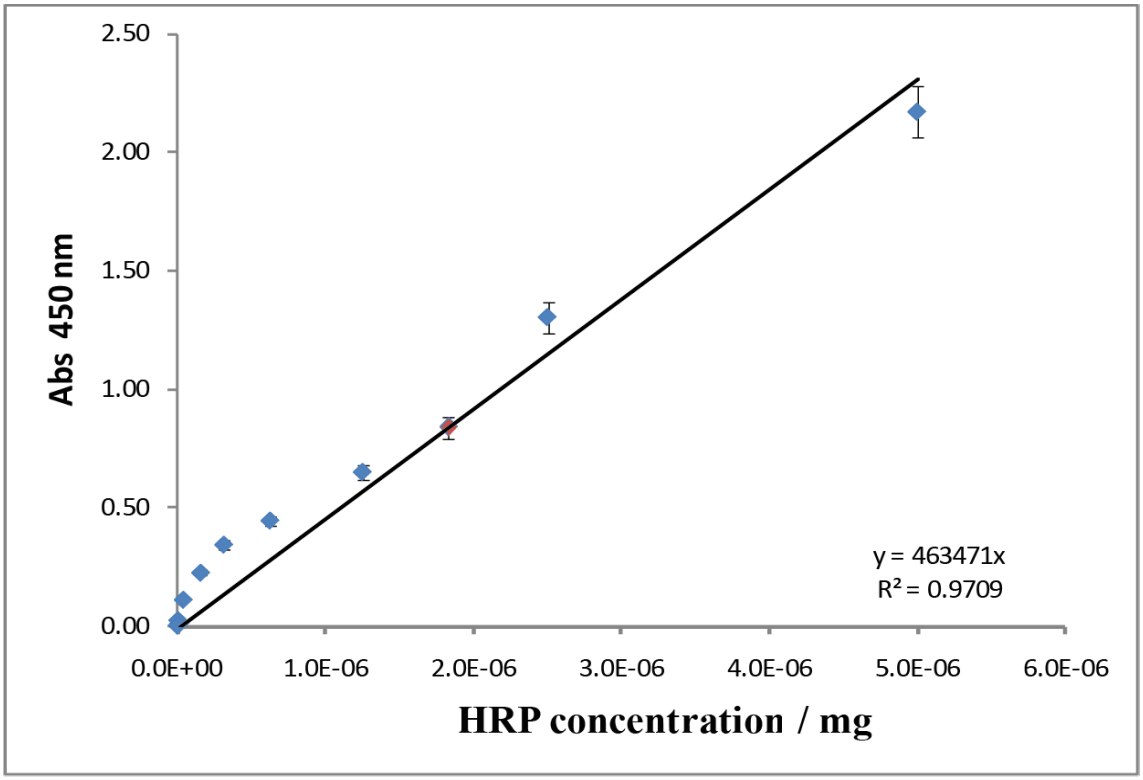

Figure 8.9– Calibration curve plotting known HRP concentrations against their corresponding absorbance at 450 nm. The error bars represent standard deviation. The red point is the absorbance of $^{HRP–ADH}$CPMV at 450 nm used to obtain the HRP concentration.

It was found that the maximum number of enzyme was a third of that expected for theoretical full coverage. If HRP is considered as a solid sphere with a radius of gyration of 2.65 nm, as calculated by molecular dynamics simulation based on its crystal structure (Laberge et al, 2003), then the surface area ($4\pi r^2$) of HRP is approximately 88.24 nm^2 (Silva et al, 2007). Therefore, the area of 11 HRP molecules amount to ca. 970 nm^2 in comparison to 2463 nm^2 for a CPMV particle with a 14 nm radius; the maximum coverage is approximately 28 enzymes per virus. These estimates are not accurate because CPMV is not a perfect sphere and neither is HRP. Therefore, the overall CPMV surface area might not represent the actual available area for enzyme coupling. Furthermore, three assumptions had to be taken into consideration: 1, the immobilised enzymes retained their enzymatic activity without any changes; 2, all immobilised enzymes contribute equally to the overall enzymatic activity detected by TMB; 3, the structural conformation of the enzymes remains the same and the active site is accessible by the substrate, while keeping in mind that access for the substrate maybe more difficult than to free enzymes.

8.3.3.1 $^{GOX–ADH}$CPMV

Glucose oxidase (GOX) from the fungus *Aspergillus niger* is a highly specific enzyme for D–glucose; it is a dimeric protein with a molecular weight of 160 kDa. GOX was selected for the possible development of a selective glucose sensor, which might be useful for blood glucose monitoring. The enzyme was activated via the periodate method as previously described and the ADH linker was added to the enzyme. The integrity of the modified particles was confirmed by agarose gel electrophoresis (Figure 8.10–A) and TEM (Figure 8.10–B). Figure 8.10–A shows an ethidium bromide stained agarose gel of wild–type, a positive control of $^{NHS–ester}$CPMV, $^{GOX–ADH}$CPMV, and $^{GOX–ADH}$CPMV^{Fc6ac} conjugates. According to their migration in an electric field towards the anode, the $^{NHS–ester}$CPMV particles migrate more slowly toward the anode than wild–type and each of the $^{GOX–ADH}$CPMV and $^{GOX–ADH}$CPMV^{Fc6ac}.

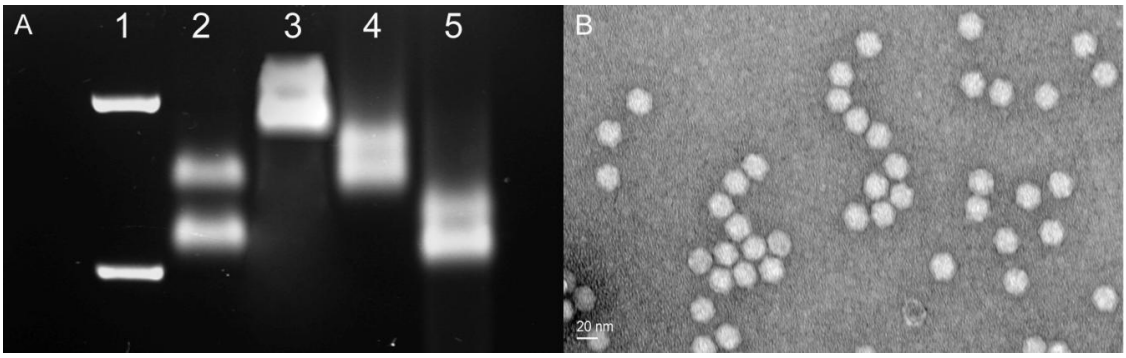

Figure 8.10– Agarose gel (1.2%) electrophoresis of $^{GOX–ADH}$CPMV particles visualised by ethidium bromide staining. Lane1 represents a 1–kbp DNA ladder 2, CPMVwt; 3, $^{NHS–ester}$CPMV; 4, $^{GOX–ADH}$CPMV; 4, $^{GOX–ADH}$CPMV^{Fc6ac} doubly functionalised particles.

SDS–PAGE, Figure 8.11, revealed an extra band on the modified particles of approximately 65–70 kDa, which possibly corresponds to the small coat protein and one monomer of the enzyme.

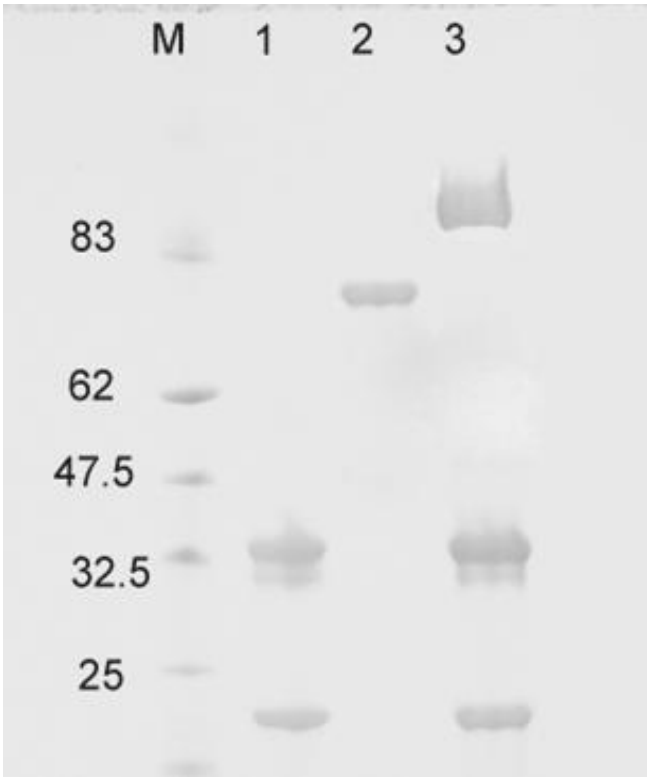

Figure 8.11– SDS–PAGE of $^{GOX–ADH}$CPMV particles. Modified particles were purified on sucrose gradient followed by gel filtration on Sephacryl–S500 column as described. Lane 1, wild–type CPMV; 2, ADH–GOX; and 3, $^{GOX–ADH}$CPMV; M is prestained protein marker. The extra band in $^{GOX–ADH}$CPMV lane may correspond to one enzyme monomer conjugated to the small subunit.

The particle size in buffer as measured by DLS shows an increase in average hydrodynamic diameter to ca. 38 nm following enzyme coupling as shown in Figure 8.12.

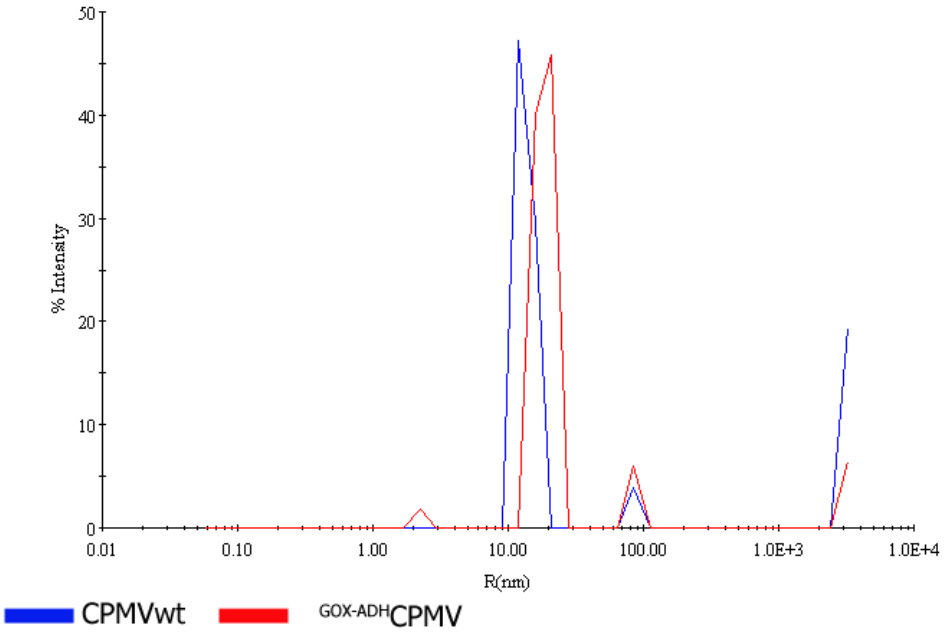

Figure 8.12– DLS data comparing CPMVwt and $^{GOX–ADH}$CPMV.

To quantify the number of enzymes coupled to the virus in $^{GOX–ADH}$CPMV sample, calibration curves were obtained using different standard solutions of free GOX prepared from stock solution. The reactivity was determined photometrically using Amplex Red Glucose/Glucose Oxidase Assay Kit (Invitrogen, cat No A22189) according to the manufacturer's instructions. In the case of Amplex Red assay, the added hydrogen peroxide reacts with 10–acetyl–3,7–dihydroxyphenoxazine (the Amplex Red reagent) in the presence of HRP (provided with the kit) to form the oxidation product resorufin. Resorufin has an absorption peak at approximately 571 nm at a pH of 7.4.

The free GOX concentration was determined from the serial dilution values. Each enzyme concentration was prepared and used on the same day, 12 activity measurements for each enzyme concentration were recorded and the absorbance was deducted from the empty well values and averaged. The GOX concentration was plotted versus the absorbance of the substrate (Amplex Red) at 571 nm. The data was fitted with linear regression with slope y= 0.0852(R^2 = 0.9161). From the absorbance recorded at 571 nm for $^{GOX–ADH}$CPMV (treated as

unknown) and from the calibration curve depicted in Figure 8.13, the corresponding free GOX concentration was 3.598 µg. By comparison to the concentration of CPMV particles by UV–vis (0.0546 mg). The number of immobilized GOX enzymes was found to be approximately 2–3 ±1 per virion. This assumes that GOX activity on the virion equals GOX activity in solution (no enzymatic activity loss).

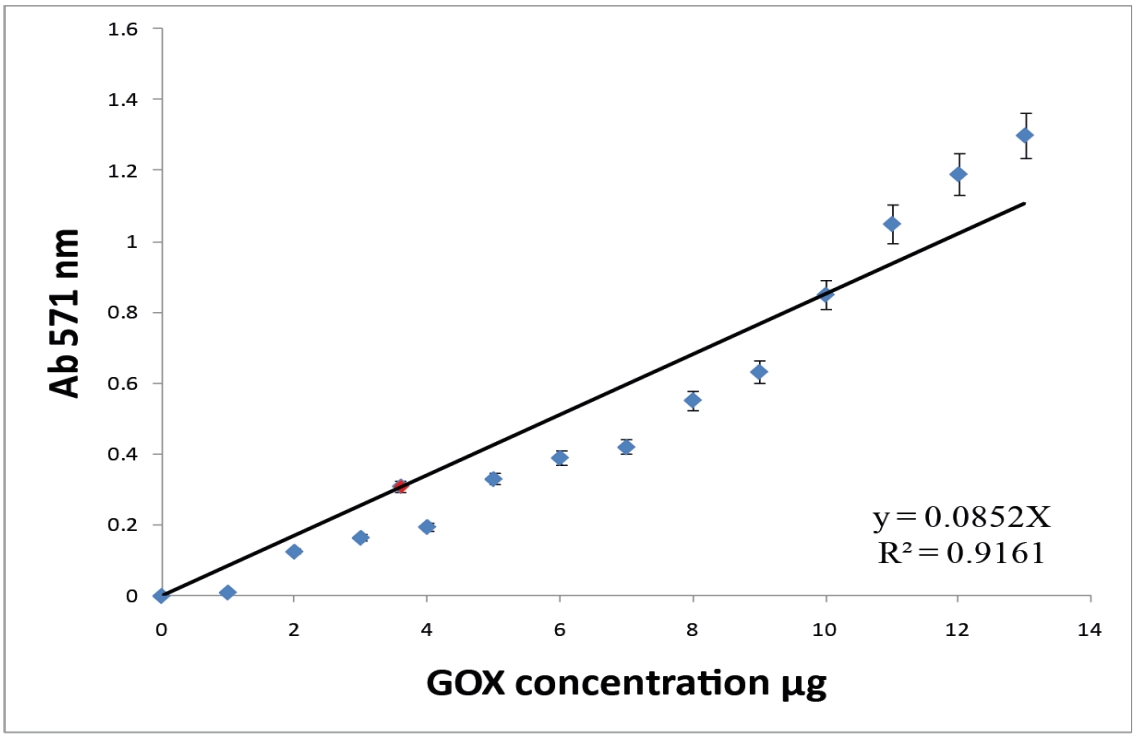

Figure 8.13– Calibration curve plotting known GOX concentrations against their corresponding absorbance at 571 nm. The red point is the absorbance of $^{GOX–ADH}$CPMV at 571 nm used to obtain the GOX concentration

8.3.4 $^{GOX–ADH}$CPMV and electrochemistry studies in solution

The resulting $^{GOX–ADH}$CPMV was characterised by cyclic voltammetry. Covalently coupled ferrocene was used as a redox mediator to increase the electron transfer speed. The amperometric study was conducted in 0.1 M sodium phosphate buffer pH 7.0, the electrochemical cell was set as described in the experimental section. The current response to the glucose concentration change was measured as a consequence of the addition of small aliquots of glucose stock solution. The ferrocene that is coupled to both of the enzyme and the virus previously described in chapter 7 ($^{(Fc6ac)GOX–ADH}$CPMV) particles gave voltammograms consistent with a reversible one–electron redox reaction as shown in Figure 8.14 . The number

of ferrocene was verified as explained at the beginning of this chapter and found to be ~ 400 ± 11 ferrocene per $^{GOX–ADH}$CPMV complex. Under the same reaction conditions, neither free glucose nor glucose oxidase exhibited any observable electrochemistry. Figure 8.14–A shows a voltammogram of $^{(Fc6ac)GOX–ADH}$CPMV in buffer. Upon addition of D–glucose to the solution a remarkable change in the voltammogram occurs as shown in Figure 8.14–B, no standard ferrocene peaks are observed, the increase in the catalytic current corresponding to the increase in the GOX substrate concentration. This is very significant as it shows the ability to exchange electrons between the ferrocene and the enzyme.

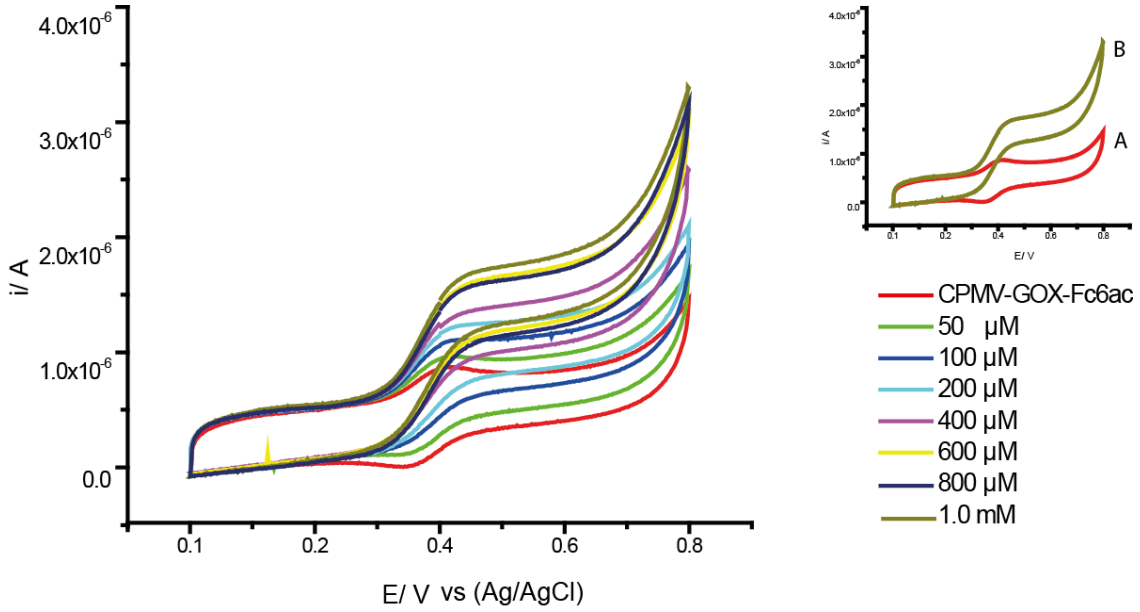

Figure 8.14– Current–potential profiles of $^{(Fc6ac)GOX–ADH}$CPMV suspended in 0.1M sodium phosphate buffer pH 7.0 and 25 °C. The catalytic response of the modified particles upon addition of 50 µM to 1 mM of D–glucose. The scan rate was 100 mV s^{-1}. The inset shows the standard ferrocene signal and the saturated GOX signal and in (B) as for (A), but with the addition of glucose oxidase.

8.4 Conclusions

HRP and GOX were covalently coupled to the CPMV capsid. ^{HRP}CPMV or $^{GOX–ADH}$CPMV particles could be useful building blocks for catalytic devices. The number of enzymes conjugated to the virus capsid was determined to be ~ 11 HRP and 2–3 GOX per virus. Moreover, $^{GOX–ADH}$CPMV showed that the ferrocene/ferrocenium couple can act as an effective

mediator between reduced glucose oxidase and a graphite electrode surface. This needs to be studied further to develop a possible biosensor.

The aim of this section was focused on building on our lab's success in the construction of multilayer assemblies of viral particles on solid surfaces (Steinmetz et al, 2006a; Steinmetz et al, 2006b). The possibility of incorporating ^{Enzymes}CPMV mono/multilayers holds great potential. Therefore, as HRP is involved in many applications such as diagnostic assays (Gosling, 1990), biosensors (Lindgren et al, 2000). These applications take advantage of the immobilization of HRP on a solid support. Therefore, the immobilisation of ^{HRP}CPMV on the solid surface remains the goal to be pursued.

8.5 References:

Basu A, Shrivastav TG, Kariya KP (2003) Preparation of enzyme conjugate through adipic acid dihydrazide as linker and its use in immunoassays. Clin Chem **49:** 1410–1412

Brunel FM, Lewis JD, Destito G, Steinmetz NF, Manchester M, Stuhlmann H, Dawson PE (2010) Hydrazone Ligation Strategy to Assemble Multifunctional Viral Nanoparticles for Cell Imaging and Tumor Targeting. Nano Letters **10:** 1093–1097

Caruso F, Schüler C (2000) Enzyme Multilayers on Colloid Particles: Assembly, Stability, and Enzymatic Activity. Langmuir **16:** 9595–9603

Dunford HB (1979) Peroxidases and Mechanisms of Enzyme Action. Abstr Pap Am Chem S**:** 332–332

Grunes J, Zhu A, Somorjai GA (2003) Catalysis and nanoscience. Chem Commun**:** 2257–2260

Hanker JS, Giammara BI (1983) Principles and Techniques of Electron–Microscopy, Biological Applications, Vol 1, 2nd Edition – Hayat,Ma. Stain Technol **58:** 184–184

Hermanson TG (2008) Bioconjugate Techniques, second edn. London: Academic Press.

Katz E, Willner I (2004) Integrated nanoparticle–biomolecule hybrid systems: synthesis, properties, and applications. Angew Chem Int Ed Engl **43:** 6042–6108

Kvaratskhelia M, Winkel C, Naldrett MT, Thorneley RNF (1999) A novel high activity cationic ascorbate peroxidase from tea (Camellia sinensis) – A class III peroxidase with unusual substrate specificity. J Plant Physiol **154:** 273–282

Laberge M, Huang Q, Schweitzer–Stenner R, Fidy J (2003) The endogenous calcium ions of horseradish peroxidase C are required to maintain the functional nonplanarity of the heme. Biophys J **84:** 2542–2552

Lin Y, Lu F, Tu Y, Ren Z (2004) Glucose Biosensors Based on Carbon Nanotube Nanoelectrode Ensembles. Nano Lett **4:** 191–195

Niemeyer CM (2001) Nanoparticles, proteins, and nucleic acids: Biotechnology meets materials science. Angew Chem–Int Edit **40:** 4128–4158

O'Malley JJ, Weaver JL (1972) Subunit structure of glucose oxidase from Aspergillus niger. Biochemistry **11:** 3527–3532

Pescador P, Katakis I, Toca–Herrera JL, Donath E (2008) Efficiency of a bienzyme sequential reaction system immobilized on polyelectrolyte multilayer–coated colloids. Langmuir **24:** 14108–14114

Steinmetz NF, Calder G, Lomonossoff GP, Evans DJ (2006) Plant Viral Capsids as Nanobuilding Blocks: Construction of Arrays on Solid Supports. Langmuir **22:** 10032–10037

Steinmetz NF, Evans DJ, Lomonossoff GP (2007) Chemical introduction of reactive thiols into a viral nanoscaffold: A method that avoids virus aggregation. Chembiochem **8:** 1131–1136

Veitch NC (2004) Horseradish peroxidase: a modern view of a classic enzyme. Phytochemistry **65:** 249–259

Willner I, Basnar B, Willner B (2007) Nanoparticle–enzyme hybrid systems for nanobiotechnology. FEBS Journal **274:** 302–309

Yáñez–Sedeño P, Pingarrón JM (2005) Gold nanoparticle–based electrochemical biosensors. Anal Bioanal Chem **382:** 884–886

9 Applications of chemical modifications

9.1 Introduction

Nanoparticles are playing a pivotal role in the field of drug delivery because they have the ability to deliver a wide range of drugs with a high potential for specificity to the diseased cells. The potential advantages include high drug payload, improving drug solubility and the ability to introduce ligands for targeted delivery (Petros & DeSimone, 2010; Pokorski et al, 2011).

Chemical bioconjugation has been applied to modify a wide range of biomolecules, including carbohydrates, polysaccharides, nucleic acids, peptides, proteins, antibodies, and viruses. Viruses are used as building blocks by conjugating the desired functional moieties to the surface exposed amino acids, some approaches are currently under investigation for possible nanomedicinal application (Evans, 2008; Evans, 2010; Fischer et al, 2010; Steinmetz, 2010). Virus nanoparticles and chemical modification offers a convenient and simple route to design nanoparticles with multi–functionalities for targeting, imaging, and drug delivery. The size of CPMV virus particles is ideal for a drug carrier; it has been reported that nanoparticles of ~25–30 nm radius are optimal for internalisation via endocytic pathway (Zhang et al, 2009). The relatively acidic environments of endosomal and lysosomal compartments (pH 4.5–5.5) is most often used as the trigger for drug release, mainly by cleavage of hydrozone linkages (Bae et al, 2003; Ulbrich et al, 2004; Ulbrich & Subr, 2004). The development of readily accessible CPMV eVLPs has stimulated interest in using such particles for drug delivery.

9.1.1 Drug coupling and targeting on CPMV

The development of methods for targeting diseased cells with therapeutic molecules, whilst avoiding healthy cells, is an important goal in nanomedicine. The destination–specific delivery of therapeutic moieties will limit the undesired side effects of drugs. Tumour–specific markers and their ligands that specifically recognise receptors over–expressed on diseased cells

have been used (Nanda & St Croix, 2004). CPMV has been identified as having natural specificity toward vimentin (Koudelka et al, 2009). Vimentin was found to have a role in tumour development and progression (Kokkinos et al, 2007) and it is over–expressed in tumour cells (Griffioen et al, 2006). However, some diseased cells express different types of receptors, such as the protein transferrin, integrins or folic acid receptors, on their surface compared to healthy cells. Therefore, different strategies were explored for possible diseased cell targeting.

A peptide derived from VP1 of foot–and–mouth disease virus (FMDV) of a type called A20FMDV2 peptide, with the sequence depicted in Figure 9.1, which was developed by Dr. John Marshall (Centre for Tumour Biology, Institute of Cancer, Barts and the London, Queen Mary's School of Medicine and Dentistry) and co–workers. They have studied FMDV and its binding to cell surface integrins, α5β3, specifically via the RGD motif (DiCara et al, 2008). Integrins are over–expressed on the surface of many types of tumour cells, thus the incorporation of this peptide on to a delivery vehicle could confer tumour–targeting properties. The RGD is a popular targeting sequence and has been chemically attached to CPMV (Sen G. S. et al, 2005) and TMV (Wang et al, 2008). Therefore, chemical modification of virus particles with targeting agents opens the door for the development of "smart bomb" nanocarriers for drug targeting.

Chemical conjugation of the A20FMDV2 peptide offers a very promising approach for the introduction of this targeting peptide to the virus capsid without the need for genetic modification(see chapter 3). The custom–made peptide (Figure 9.1) has cysteine at the C–terminus for attachment to CPMV surface exposed lysines, either by a bifunctional linker (SPDP) or by the EDC/NHS method, and the amino–terminus is blocked with biotin, which enables easy detection. The lysine within the peptide is acetylated (protected) to prevent self–polymerisation.

Figure 9.1– A20FMDV2 peptide sequence for α5β3 integrin targeting. The RGD motif is shown in brown. Ac refers to the acetylated lysine to prevent self polymerisation.

Doxorubicin (Dox) is one of the most well-known chemotherapeutic anticancer drugs. It is a small molecule (MW=545 Da), and is positively charged (pKa 8.4) (Asadishad et al, 2010). Although it kills the cancerous cells by inhibiting the synthesis of nucleic acids within cells, three main problems are encountered with Dox: high toxicity, short lifetime in the body, and low solubility (Yoo & Park, 2004). To overcome the nonspecificity and high toxicity of Dox, many researchers have proposed Dox conjugation to hydrophilic polymers (Mislick et al, 1995). In addition, folic acid has been widely used for targeted drug delivery to cancer cells (Destito et al, 2007; Manchester & Steinmetz, 2009); this is based on the differential expression of folic acid receptors on normal and malignant cancer cells (Lu & Low, 2002). Three approaches to prepare ^{Dox}CPMV and a method for binding folic acid to the virus surface will be described in this Chapter.

9.2 Experimental

Following my synthesis and characterisation of ^{Dox}CPMV, cell uptake studies and cell cultures were conducted in collaboration with Prof. Nicole F. Steinmetz and Dr. Sourabh Shukla; (Department of Biomedical Engineering, Case Western Reserve University, USA).

9.2.1 ^{A20FMDV2}CPMV particles

Carbodiimide EDC/NHS and SPDP methods were used as described in section 2.15 and 2.16, respectively, to generate ^{A20FMDV2}CPMV particles. As has been described in chapter 3. Peptide quantification of ^{A20FMDV2}VLPs$^{cascade\ blue\ dye}$ particles was accomplished as described in section 6.2.15.

9.2.2 $^{Dox–NHS–ester}$CPMV

Surface–exposed carboxylate groups were activated with EDC/NHS, as previously described in section 2.13. The modified particles, after purification, were incubated with 2000 molar excess of Dox–HCl in 20% (v/v) DMSO. The reaction mixture was stirred overnight (16 hours) at 4 °C. Modified particles ($^{Dox–NHS–ester}$CPMV) were eluted through a PD–10 column, fractions collected and concentrated on 100 kDa cut–off columns before being layered onto 5 ml 10–50% sucrose gradient (as described in section 2.14.1). Fractions were collected and dialysed against 10 mM sodium phosphate buffer pH 7.0 for 2–4 days using 100 kDa molecular weight cut–off membranes. The $^{Dox–NHS–ester}$CPMV conjugate concentration was determined by UV–visible spectrophotometry; the yield of $^{Dox–NHS–ester}$CPMV conjugate was between 60–80% based on the initial virus concentration. The number of Dox molecules was determined by measuring the absorbance at 490 nm (extinction coefficient, ε: 13500 M^{-1} cm^{-1}).

9.2.3 $^{Dox–BS3}$CPMV

Bis(sulfosuccinimidyl)suberate (BS^3) is an amine–to–amine crosslinker with a 8–carbon spacer of 11.4 Å in length that contains sulfo–NHS esters at both ends. A 2000 molar excess of freshly prepared aqueous solution of BS^3 was incubated with 1 equivalent of CPMVwt suspended in 20 mM sodium phosphate buffer, 0.15 M NaCl. The reaction was left to proceed at ambient temperature while gently stirring. ^{BS3}CPMV particles were purified on a PD–10 gel filtration column and the eluted fractions were dialysed against 0.1 M sodium phosphate, 0.15 M NaCl; pH 7.2 for 2 days. The modified ^{BS3}CPMV particles were incubated with 2000 molar excess of Dox dissolved in DMSO. The DMSO level was adjusted to 20% (v/v) of the reaction volume. The reaction was left overnight while gently stirring at 4 °C. $^{Dox–BS3}$CPMV particles were purified on 5 ml 10%–50% sucrose gradients as described in section 2.17.1. The fractions containing $^{Dox–BS3}$CPMV were collected and dialysed against 10 mM sodium phosphate buffer for 2–4 days using 100 kDa molecular weight cut–off membranes. The yield of $^{Dox–BS3}$CPMV was 50% relative to the initial CPMV concentration as determined by UV–vis spectrophotometry.

9.2.4 $^{Dox–DTSSP}$CPMV

A homobifunctional sulfo–NHS, dithiobis(sulfosuccinimidyl propionate) (DTSSP) crosslinking agent was used. DTSSP contains an 8–atom spacer of 12 Å in length. It is symmetrically constructed around a central disulfide group that is cleavable. The reaction scheme is simplified in Figure 9.2. CPMV particles suspended in 0.1M sodium phosphate, 0.15 M NaCl; pH 7.2 was incubated with 2000 molar excess of aqueous DTSSP solution. The reaction was left to proceed for 2 hours at ambient temperature. ^{DTSSP}CPMV particles were purified on a PD–10 gel filtration column and the eluted fractions were dialysed against 0.1 M sodium phosphate, 0.15 M NaCl; pH 7.2 for 2 days. Freshly prepared ^{DTSSP}CPMV particles were incubated with 2000 molar excess of Dox dissolved in DMSO. The DMSO level was adjusted to 20% (v/v) of the reaction volume. The reaction was left overnight while gently stirring at 4 °C. $^{Dox–DTSSP}$CPMV particles were purified on 5 ml 10%–50% sucrose gradients centrifuged as described in section 2.17.1. The fractions containing $^{Dox–DTSSP}$CPMV were collected and dialysed against 10 mM sodium phosphate buffer for 2–5 days using 100 kDa molecular weight cut–off membranes. The yield of $^{Dox–DTSSP}$CPMV was 40–50% relative to the initial CPMV concentration as determined by UV–vis spectrophotometry.

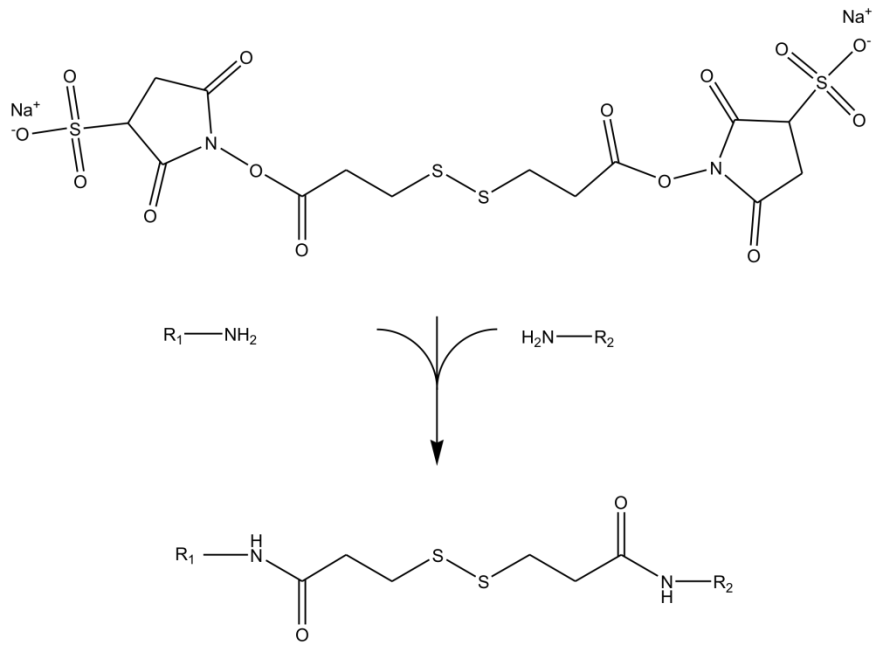

Figure 9.2– DTSSP crosslinking two amine–containing molecules through an amide linkage. R_1 represents the virus and R_2 represents the Dox molecules.

9.2.5 ^{Dox}CPMV quantification

For ^{Dox}CPMV quantification, the extinction coefficient ε_{484} used is 13500 M cm^{-1}.

9.2.6 $^{FA–NHS}$CPMV

Folate N–hydroxysuccinimidyl ester (FA–NHS) was prepared by dissolving folic acid (FA, 1 g) in DMSO. EDC (0.434 g) and NHS (1.151 g) were added to the folic acid solution, the mixture was stirred at room temperature for 2 hours. FA–NHS was then incubated with CPMVwt in a 2000 molar excess, the reaction was left to proceed overnight while gently stirring at 4 °C. The modified $^{FA–NHS}$CPMV particles were purified by gel–filtration over a Sephadex G25 (PD–10 columns) equilibrated with 0.1 M sodium phosphate buffer. The eluted samples were collected and concentrated before being layered on 5 ml 10%–50% sucrose gradients centrifuged as described in section 2.17.1. The fractions containing $^{FA–NHS}$CPMV were collected and dialysed against 10 mM sodium phosphate buffer for 24 hours using 100 kDa molecular weight cut–off membranes. The yield of $^{FA–NHS}$CPMV was 60% relative to the initial CPMV concentration as determined by UV–vis spectrophotometry.

9.2.7 $^{FA–NHS}$CPMV quantification

$^{FA–NHS}$CPMV in 10 mM sodium phosphate buffer pH 7 was reacted with a 2000 molar excess of NHS ester–activated amine specific dye, DyLight488, in DMSO. The DMSO level was adjusted to 20% (v/v) and the reaction left to proceed at 4 °C overnight while gently stirring. The doubly functionalised particles ($^{FA–NHS}$CPMV^{DyLight488}) were purified on a PD–10 column equilibrated with 10 mM sodium phosphate buffer pH 7.0, and eluted samples were concentrated on 100 kDa cut–off columns before being layered onto 5 ml 10%–50% sucrose gradients as described in section 2.17.1. The eluted fractions were collected and dialysed against 10 mM sodium phosphate buffer pH 7.0 for 3 days, changing buffer every 12 hours. After further concentration on 100 kDa cut–off columns, the number of free reactive lysines was calculated to be ~ 165 ± 8 per virion. This equates to approximately 75 FA moieties being bound to each CPMV virus particle or about one FA molecule per asymmetric unit.

9.2.8 $^{Dox–NHS–ester}$CPMV^{FA}

Folic acid was conjugated to pre–modified $^{Dox–NHS–ester}$CPMV particles using the EDC/NHS method. A 2000 molar excess of folic acid was incubated with 2000 molar excess of EDC and 4000 molar excess of sulfo–NHS to 1 molar equivalent of CPMVwt, the reaction was left to proceed while gently stirring at ambient temperature for 2 hours. The mixture was then incubated with 1 molar excess of (5 mg ml^{-1}, 1 ml) $^{Dox–NHS–ester}$CPMV particles overnight at 4 °C. The doubly modified particles ($^{Dox–NHS–ester}$CPMV^{FA}) were concentrated on 100 kDa cut–off columns and layered onto 5 ml 10–50% sucrose gradients as described in section 2.17.1. Fractions were collected and further dialysed on 100 kDa membranes for 24 hours. The $^{Dox–NHS–ester}$CPMV^{FA} conjugate concentration was determined by UV–vis spectrophotometry; the yield of the conjugated particles was between 70–90% based on the initial virus concentration. Modified particles were characterised by agarose gel electrophoresis, TEM and ZP.

9.3 Results and discussion

9.3.1 Attachment of targeting molecules

Successful peptide coupling was monitored using agarose gel electrophoresis (Figure 9.3). When stained with ethidium bromide a fluorescent intensity from a band of different mobility to CPMVwt and to the positive control samples, $^{NHS–ester}$CPMV and ^{SPDP}CPMV, was observed, suggesting that the CPMV surface has been modified by the coupling of A20FMDV2. Two approaches have been adopted to couple the peptide (A20FMDV2) to the CPMV surface, either by using SPDP as described in section 2.16 or alternatively for simplicity, as described in section 6.2.14, a one–step reaction to form a thioester bond. Figure 9.3–A shows results from the SPDP coupling approach and Figure 9.3–B using the EDC approach. When the gel is stained with Coomassie blue no changes in the band position in comparison to the ethidium bromide staining was observed (data not shown), this is consistent with the virus protein surface being modified with the A20FMDV2 peptide.

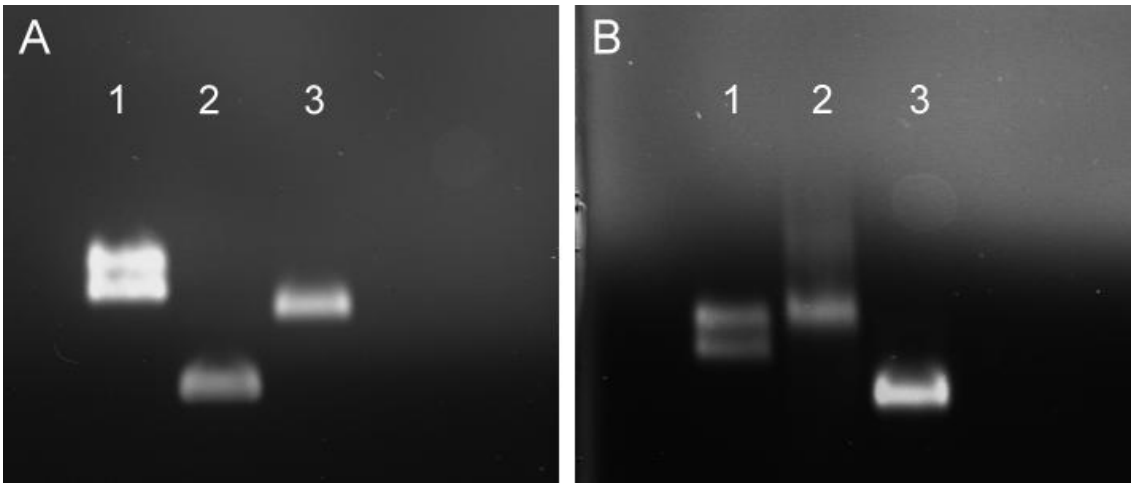

Figure 9.3– 1.2% agarose gel electrophoresis for ^{A20FMDV2}CPMV particles stained with ethidium bromide. (A) SPDP approach; Lane 1, CPMVwt; 2, ^{SPDP}CPMV; 3, ^{A20FMDV2}CPMV, and (B) EDC/NHS approach; Lane 1, CPMVwt; 2, $^{NHS-ester}$CPMV; 3, $^{A20FMDV2-NHS-ester}$CPMV.

Furthermore, TEM confirmed the integrity of the ^{A20FMDV2}CPMV particles. Incubating the $^{A20FMDV2-NHS-ester}$CPMV particles with ^{Streptavidin}AuNP nanoparticles resulted in partial decoration of $^{A20FMDV2-NHS-ester}$CPMV particles with gold nanoparticles (AuNP) due to the presence of biotin on the peptide as shown in Figure 9.4. The number of AuNP per virus is not an accurate representation of the number of peptides being coupled to the virus capsid but it is confirmation of the peptide presence.

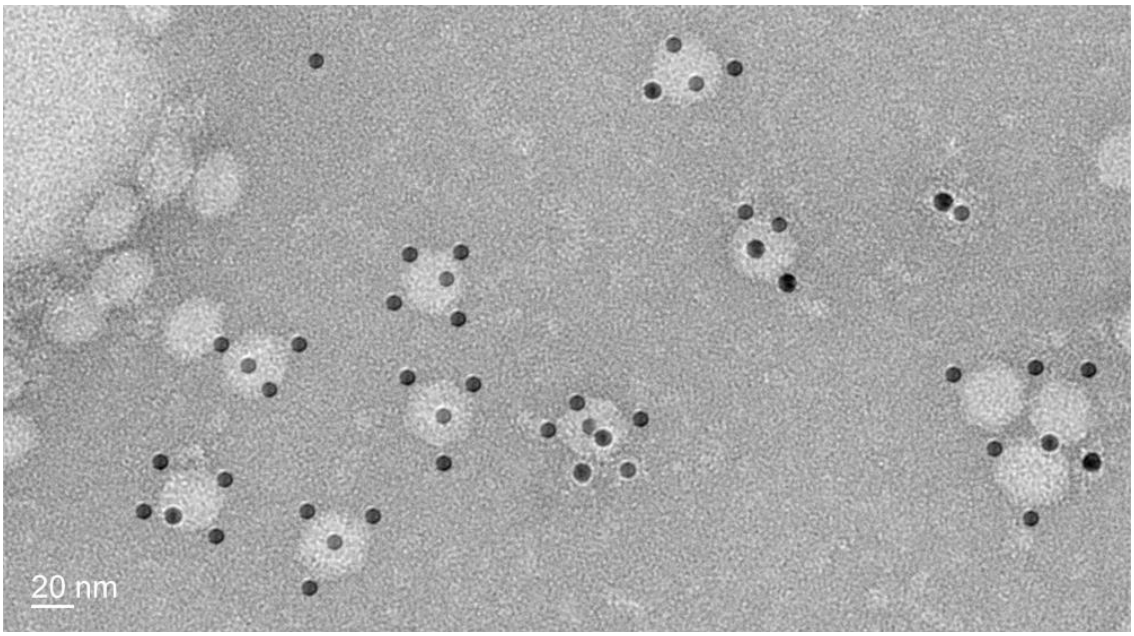

Figure 9.4– Stained TEM image of $^{A20FMDV2-NHS-ester}$CPMV particles. The black spheres are ^{Streptavidin}AuNP attached to the virus capsid as a confirmation of the presence of the peptide but this is not quantitative.

The number of peptides per particle was determined for $^{A20FMDV2–EDC}$CPMV as described in section 6.2.15. The doubly–functionalised particles ^{A20FMDV2}CPMV$^{cascade\ blue\ dye}$ were rigorously purified. The number of remaining reactive carboxylates was calculated from the absorbance of the dye at λ_{399} and ε = 27000 M^{-1} cm^{-1}, to be ~90–105 ± 6 per virion. This equates to approximately 40–50 peptides being bound to each CPMV particle similar results obtained with ^{A20FMDV2}VLPs. Moreover, a control experiment was conducted with unmodified CPMV and cascade blue dye and the number of dyes was found to be ~140–150 dye per virus, this is almost full coverage of all surface accessible carboxylates.

The second approach, which was explored for targeting, is the use of folic acid (FA). It has been shown that the uptake of FA into cells is mediated by the folate receptor (FR), and binding of FA to FR initiates receptor mediated endocytosis and internalisation of FA (Destito et al, 2007; Rijnboutt et al, 1996). For example, FA has been used for targeting strategies such as; the functionalisation of liposomes (Stephenson et al, 2004; Zhao & Lee, 2004).

Plant viruses generally lack the inherent ability to target human or mammalian cells. Therefore, the ability to modify the virus capsid to carry anticancer drug and seek its target as well as evading the immune system. This makes CPMV capsid an ideal template to carry the multi functionalities to the diseased cell. To this end, FA moieties were bound to each CPMV virus particle in addition to the anticancer drug. Furthermore, the ability to bind PEG molecules on the same particle will be something to be explored further in the future for the reduction of immunogenicity against the particles.

The number of FA molecules attached to the virions was determined spectrophotometrically for the $^{FA–NHS}$CPMV^{DyLight488} particles. The number of dyes was calculated to be ~ 165 ± 8 per virion. This equates to approximately 75 FA moieties being bound to each CPMV virus particle or 1 FA molecule per asymmetric unit. This is within the range of previously published data (Destito et al, 2007). The doubly–functionalised $^{FA–NHS}$CPMV^{Dox} particles are developed for both targeting and drug delivery. Particles are currently still under investigation.

9.3.2 Chemical conjugation of doxorubicin

The surface–exposed amino acid groups can be used as anchoring points to modify CPMV particles with drug molecules. Here, the anti–tumour drug Dox was bound covalently to the surface exposed carboxylates on the virus capsid.

9.3.3 Conjugation of doxorubicin to CPMV capsid

Dox has two major functional groups in its structure, a primary amine group and a primary hydroxyl group. Both can be utilised for conjugation to the CPMV capsid. Herein, only the amine group has been exploited for coupling. The conjugation schemes using EDC/NHS or BS^3 linker are illustrated in Figure 9.5. The CPMV particles were further modified with folic acid to demonstrate the ability to introduce a targeting agent as well as drug moieties on the same particle.

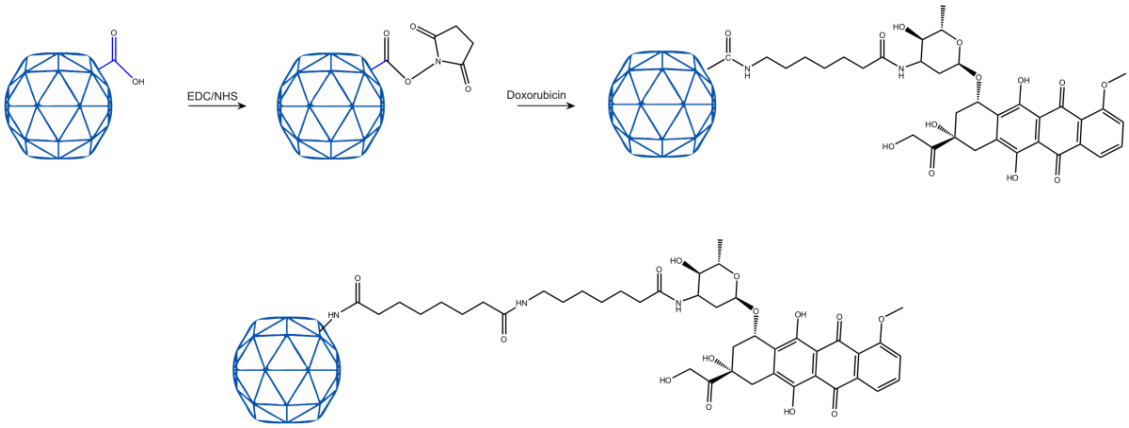

Figure 9.5– Illustration of the chemical coupling of Dox to the CPMV capsid. Carboxylate groups on the virus capsid were activated with EDC/NHS followed by Dox coupling. Alternatively, BS^3 was used to extend the spacer length between Dox and the virus capsid.

9.3.4 ^{Dox}CPMV characterisation

Successful Dox coupling was monitored using agarose gel electrophoresis (Figure 9.6–A), unstained agarose gel shows a fluorescent intensity from a band of different mobility to free Dox which migrated to the cathode, while $^{Dox–NHS–ester}$CPMV had moved in the opposite

direction. This suggests that the $^{Dox–NHS–ester}$CPMV surface has been modified, with the Dox moieties being bound to the virus capsid. Furthermore, staining the gel with ethidium bromide revealed a different mobility of the bands in comparison to positive ($^{NHS–ester}$CPMV) and negative (CPMVwt) controls as shown in Figure 9.6–B. In addition, staining with Coomassie blue confirmed the presence and modification of the coat protein. This is consistent with the particles being modified with both the drug and the targeting agent (Figure 9.6–C). Furthermore, after rigorous purification, $^{Dox–NHS–ester}$CPMV particles have a raspberry colouring, arising from bound Dox. $^{Dox–BS3}$CPMV was characterised in the same way.

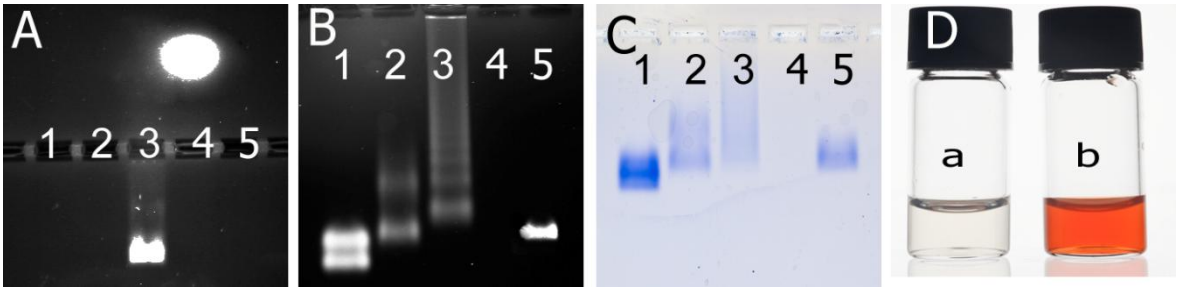

Figure 9.6– Native 1.2% agarose gel electrophoresis (A) unstained; (B) ethidium bromide stained; (C) Coomassie blue stained and (D) is a camera image of $^{Dox–NHS–ester}$CPMV particles, (a), image of CPMVwt and (b), $^{Dox–NHS–ester}$CPMV particles. Lane 1, CPMVwt; 2, $^{NHS–ester}$CPMV; 3, $^{Dox–NHS–ester}$CPMV conjugate; 4, free Dox; 5, doubly functionalised $^{Dox–NHS–ester}$CPMV^{FA} particles.

The number of Dox molecules per virus particle was determined for both coupling approaches to evaluate the effect of the longer linker length on the Dox coupling. The functionalised particles were purified rigorously and the number of Dox molecules was determined by measuring the absorbance at 484 nm (extinction coefficient, ε_{484}: 13500 M^{-1} cm^{-1}). From the absorbance spectrum (Figure 9.7), the number of Dox molecules were calculated to be ~ 30 ± 3 per virion using the EDC/NHS coupling method and 42 ± 5 using BS^3 as a linker. It is expected that the length of the linker will have some affect on the number of Dox moieties coupled to the virus. The number of Dox moieties coupled to the virus surface was slightly higher using BS^3 as a linker. This is possibly to do with the efficiency of coupling due to the stability of the linker in aqueous solution. It has been suggested that coupling with BS^3 generates a hydrophilic–region, which might play a role in the increased number of Dox

molecules bound to the virus capsid (Hermanson, 2008) in comparison to the EDC/NHS approach.

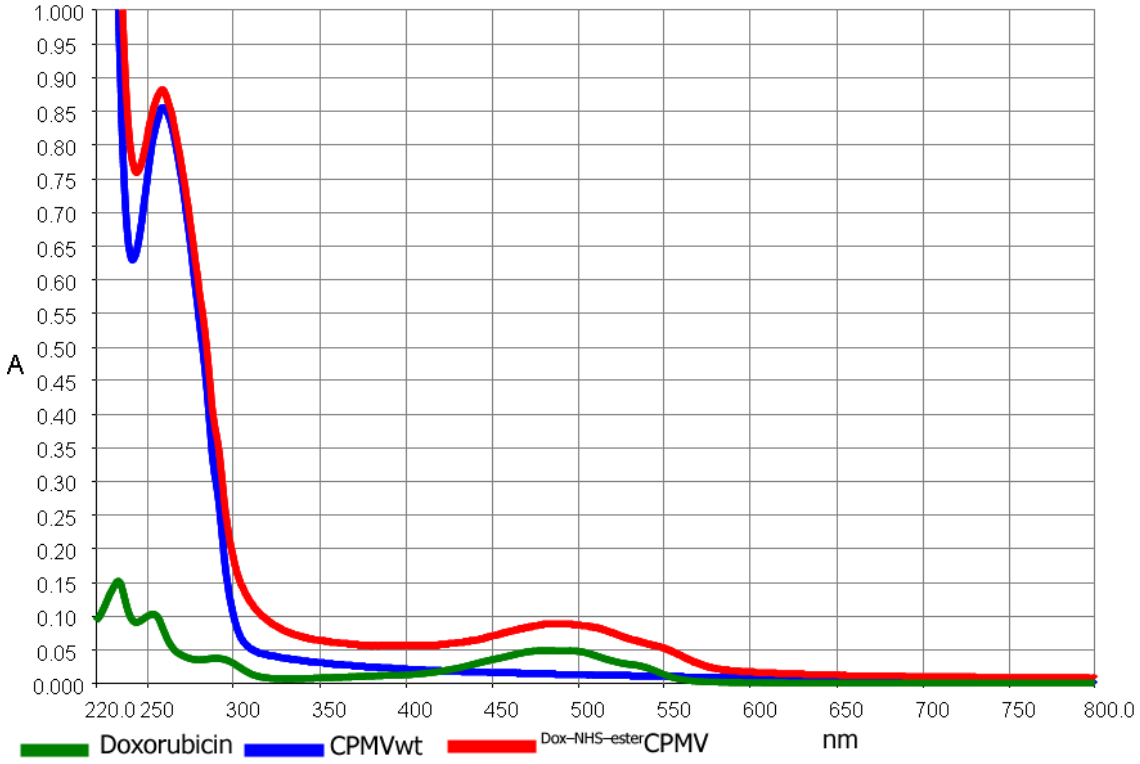

Figure 9.7– UV–visible spectrum of $^{Dox–NHS–ester}$CPMV particles. CPMVwt (blue line), free Dox (green line) and $^{Dox–NHS–ester}$CPMV (red line) using the EDC/NHS approach. The number of Dox bound to the virus capsid was 30 ± 3 per virus.

For drug nanocarriers, the size and the stability are important properties that might influence their *in vivo* performance. In this case, the size and size distribution of $^{Dox–NHS–ester}$CPMV conjugates were examined by DLS (Figure 9.8). The particle size distribution was found to be monodisperse with a polydispersity index of 14.5 %; the particle size increased by 2.2 nm compared to CPMVwt.

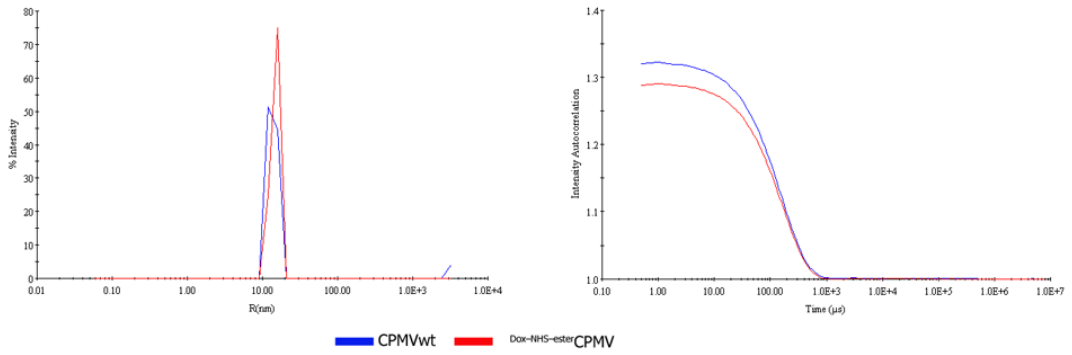

Figure 9.8– DLS data comparing CPMVwt and $^{\text{Dox–NHS–ester}}$CPMV.

The size and morphology of the $^{\text{Dox–NHS–ester}}$CPMV particles were evaluated further by TEM. (Figure 9.9), $^{\text{Dox–NHS–ester}}$CPMV particles are monodisperse with an average diameter of 32 nm. The particles tend to aggregate within 10 days of preparation, which makes it crucial to prepare fresh particles for subsequent experiments.

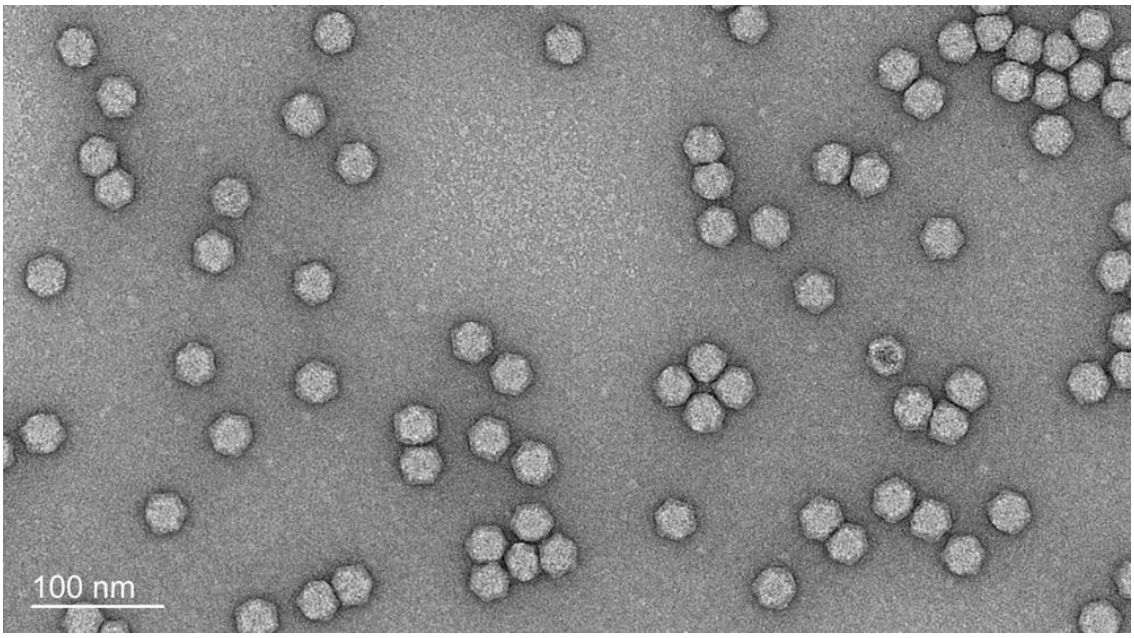

Figure 9.9– Stained TEM image of $^{\text{Dox–NHS–ester}}$CPMV particles.

The zeta potential for suspensions of $^{\text{Dox–NHS–ester}}$CPMV particles in buffer are considerably more negative at –38.1 ± 1.5 mV than that of CPMVwt , of *ca.* – 12 mV and –

14.8 mV for the $^{NHS–ester}$CPMV particles, and show that the modified particles have good colloidal stability and no propensity to aggregate.

The cellular uptake of $^{Dox–NHS–ester}$CPMV and confocal microscopy studies were conducted in collaboration with Prof. Nicole F. Steinmetz and Dr. Sourabh Shukla; (Department of Biomedical Engineering, Case Western Reserve University, USA). The preliminary results of confocal microscopy confirmed the uptake of $^{Dox–NHS–ester}$CPMV by Hela cell lines. However, the fluorescence was not concentrated in the nuclei but in many bright small spots in the cytoplasm Figure 9.10. This is an indication that the $^{Dox–NHS–ester}$CPMV are not falling apart in the lysosomes and therefore Dox molecules are not reaching the nucleus. Disappointingly, the uptake and cell viability of $^{Dox–NHS–ester}$CPMV suggested that this is not an efficient delivery system for cancer chemotherapy. Therefore, another approach was attempted using $^{Dox–DTSSP}$CPMV, which relies on the *in vivo* cleavage of the disulfide bond linking Dox to the virus capsid. This is currently being evaluated and the preliminary results indicate this approach has great potential.

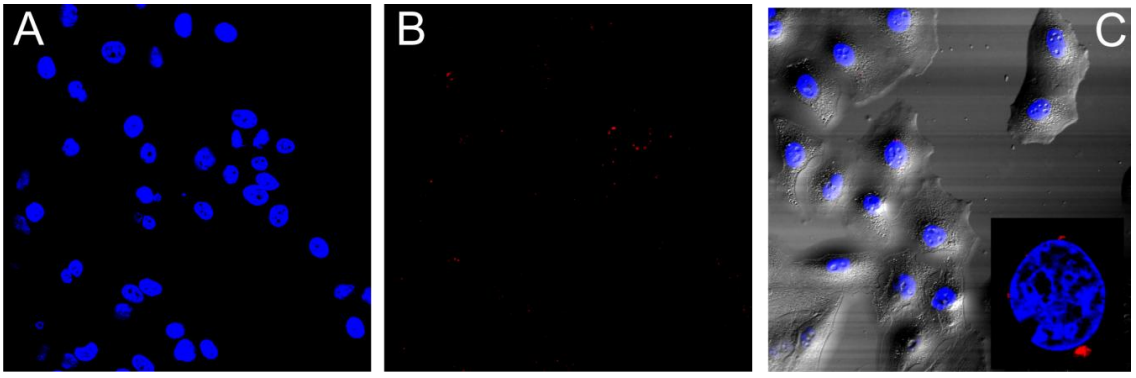

Figure 9.10– Fluorescence analysis of $^{Dox–NHS–ester}$CPMV in Hela cells after 24 hours. (A) Hela cells in the absence of $^{Dox–NHS–ester}$CPMV (B) $^{Dox–NHS–ester}$CPMV (C) $^{Dox–NHS–ester}$CPMV incubation with Hela cells. $^{Dox–NHS–ester}$CPMV was mainly detected in the cytoplasmic and outside the nucleus suggesting. Dr. Sourabh Shukla (Department of Biomedical Engineering, Case Western Reserve University, USA) took the images.

9.4 Conclusion

This chapter investigated the use of CPMV capsid as a scaffold for drug delivery and targeting. A20FMDV peptide was successfully coupled to both CPMV wt and CPMV eVLPs capsid; some work is still needed to fully study this process. Preliminary cell studies on ^{FMDV}CPMV particles are currently under investigation by (Prof. John F. Marshall Institute of Cancer, Centre for Tumour Biology, Barts and the London Queen Mary's School of Medicine and Dentistry, London). The chemical modification of the virus capsid with Dox was attempted to generate a high–payload, targeted, delivery agent for anticancer drugs. Fluorescence imaging showed $^{Dox–NHS–ester}$CPMV can be internalized by Hela cancer cells. Free doxorubicin distributed mainly into the nucleus and cytoplasm of cells, while $^{Dox–NHS–ester}$CPMV was localized around the nucleus, suggesting the conjugated doxorubicin was taken up by endocytosis. However, relying on the virus disassembly was not the right choice in this case. Alternative methods are currently being tested. CPMV properties demonstrate that the attachment of targeting peptides and other agents can be accomplished in geometrically regular structures. The ordered array can be presented to the target cell surface to maximise the probability of endocytosis.

9.5 References

Asadishad B, Vossoughi M, Alemzadeh I (2010) Folate–Receptor–Targeted Delivery of Doxorubicin Using Polyethylene Glycol–Functionalized Gold Nanoparticles. *Industrial & Engineering Chemistry Research* **49:** 1958–1963

Bae Y, Fukushima S, Harada A, Kataoka K (2003) Design of environment–sensitive supramolecular assemblies for intracellular drug delivery: polymeric micelles that are responsive to intracellular pH change. *Angew Chem Int Ed Engl* **42:** 4640–4643

Destito G, Schneemann A, Manchester M (2009) Biomedical nanotechnology using virus–based nanoparticles. *Curr Top Microbiol Immunol* **327:** 95–122

Destito G, Yeh R, Rae CS, Finn MG, Manchester M (2007) Folic acid–mediated targeting of cowpea mosaic virus particles to tumor cells. *Chemistry & Biology* **14:** 1152–1162

DiCara D, Burman A, Clark S, Berryman S, Howard MJ, Hart IR, Marshall JF, Jackson T (2008) Foot–and–mouth disease virus forms a highly stable, EDTA–resistant complex with its principal receptor, integrin alpha v beta 6: Implications for infectiousness. *J Virol* **82:** 1537–1546

Evans DJ (2008) The bionanoscience of plant viruses: templates and synthons for new materials. *Journal of Materials Chemistry* **18:** 3746–3754

Evans DJ (2010) Bionanoscience at the plant virus–inorganic chemistry interface. *Inorganica Chimica Acta* **363:** 1070–1076

Fischer R, Steinmetz NF, Mertens ME, Taurog RE, Johnson JE, Commandeur U, Manchester M (2010) Potato Virus X as a Novel Platform for Potential Biomedical Applications. *Nano Letters* **10:** 305–312

Griffioen AW, van Beijnum JR, Dings RP, van der Linden E, Zwaans BMM, Ramaekers FCS, Mayo KH (2006) Gene expression of tumor angiogenesis dissected: specific targeting of colon cancer angiogenic vasculature. *Blood* **108:** 2339–2348

Hermanson TG (2008) *Bioconjugate Techniques*, second edn. London: Academic Press.

Kokkinos MI, Wafai R, Wong MK, Newgreen DF, Thompson EW, Waltham M (2007) Vimentin and epithelial–mesenchymal transition in human breast cancer – Observations in vitro and in vivo. *Cells Tissues Organs* **185:** 191–203

Koudelka KJ, Destito G, Plummer EM, Trauger SA, Siuzdak G, Manchester M (2009) Endothelial Targeting of Cowpea Mosaic Virus (CPMV) via Surface Vimentin. *Plos Pathog* **5**

Lu W, Xiong C, Zhang G, Huang Q, Zhang R, Zhang JZ, Li C (2009) Targeted photothermal ablation of murine melanomas with melanocyte–stimulating hormone analog–conjugated hollow gold nanospheres. *Clin Cancer Res* **15:** 876–886

Lu YJ, Low PS (2002) Folate–mediated delivery of macromolecular anticancer therapeutic agents. *Advanced Drug Delivery Reviews* **54:** 675–693

Manchester M, Singh P (2006) Virus–based nanoparticles (VNPs): platform technologies for diagnostic imaging. *Advanced drug delivery reviews* **58:** 1505–1522

Manchester M, Steinmetz NF. (2009) Viruses and nanotechnology. *Current Topics in Microbiology and Immunology,*. Springer Berlin Heidelberg, Berlin, Heidelberg.

Mislick KA, Baldeschwieler JD, Kayyem JF, Meade TJ (1995) Transfection of Folate–Polylysine DNA Complexes – Evidence for Lysosomal Delivery. *Bioconjugate Chemistry* **6:** 512–515

Nanda A, St Croix B (2004) Tumor endothelial markers: new targets for cancer therapy. *Curr Opin Oncol* **16:** 44–49

Petros RA, DeSimone JM (2010) Strategies in the design of nanoparticles for therapeutic applications. *Nat Rev Drug Discov* **9:** 615–627

Pokorski JK, Breitenkamp K, Liepold LO, Qazi S, Finn MG (2011) Functional Virus–Based Polymer–Protein Nanoparticles by Atom Transfer Radical Polymerization. *Journal of the American Chemical Society* **133:** 9242–9245

Rijnboutt S, Jansen G, Posthuma G, Hynes JB, Schornagel JH, Strous GJ (1996) Endocytosis of GPI–linked membrane folate receptor–alpha. *J Cell Biol* **132:** 35–47

Sen G. S., Kuzelka J, Singh P, Lewis WG, Manchester M, Finn MG (2005) Accelerated bioorthogonal conjugation: A practical method for the Ligation of diverse functional molecules to a polyvalent virus scaffold. *Bioconjugate Chemistry* **16:** 1572–1579

Stephenson SM, Low PS, Lee RJ (2004) Folate receptor–mediated targeting of liposomal drugs to cancer cells. *Methods Enzymol* **387:** 33–50

Ulbrich K, Etrych T, Chytil P, Pechar M, Jelinkova M, Rihova B (2004) Polymeric anticancer drugs with pH–controlled activation. *Int J Pharm* **277:** 63–72

Ulbrich K, Subr V (2004) Polymeric anticancer drugs with pH–controlled activation. *Adv Drug Deliv Rev* **56:** 1023–1050

Wang Q, Kaltgrad E, Lin TW, Johnson JE, Finn MG (2002a) Natural supramolecular building blocks: Wild–type cowpea mosaic virus. *Chemistry & Biology* **9:** 805–811

Wang Q, Lin T, Johnson JE, Finn MG (2002b) Natural supramolecular building blocks: Cysteine–added mutants of cowpea mosaic virus. *Chem Biol* **9:** 813–819

Yoo HS, Park TG (2004) Folate–receptor–targeted delivery of doxorubicin nano–aggregates stabilized by doxorubicin–PEG–folate conjugate. *Journal of Controlled Release* **100:** 247–256

Zhang S, Li J, Lykotrafitis G, Bao G, Suresh S (2009) Size–Dependent Endocytosis of Nanoparticles. *Advanced Materials* **21:** 419–424

Zhang Y, Yang M, Portney NG, Cui DX, Budak G, Ozbay E, Ozkan M, Ozkan CS (2008) Zeta potential: a surface electrical characteristic to probe the interaction of nanoparticles with normal and cancer human breast epithelial cells. *Biomed Microdevices* **10:** 321–328

Zhao XB, Lee RJ (2004) Tumor–selective targeted delivery of genes and antisense Oligodeoxyribonucleotides via the folate receptor. *Advanced Drug Delivery Reviews* **56:** 1193–1204

10 Conclusions and future work

The overall aim of this thesis was to develop the potential uses of CPMV as a naturally occurring nanoparticle. I started my research by building on previous knowledge regarding the addressability of amino acids on the exterior of the virus. I have extended these addressability studies and demonstrated that the length of the linker plays a role in the number of ferrocene moieties bound to the virus. Additionally, the thesis explores various moieties (ferrocenes, dyes, enzymes, peptides and drug molecules) that could be coupled to the virus exterior capsid to generate desired nanoparticles.

CPMVwt has been utilised as a template for mineralization process using peptides generated by phage–display–peptide library to initiate the nucleation on the virus surface. The chemical coupling of such peptides was favoured over complicated genetic modification approaches that were discussed in this thesis; the same method was used to couple FMDV for use as a therapeutic targeting agent. Besides, these approaches proved to be general to any modifiable surface. As proof of principle, MWCNT was mineralized with CoPt, which generated monodisperse coating. The process was scalable and generated particles with a size that one normally difficult to be obtained by any other methods. Studying the properties of the particles was difficult and although some collaborations were established they were not always fruitful.

To further advance our knowledge in understanding the control and the specificity of the peptides discussed above, CPMV particles were chemically modified to carry a higher negative charge than CPMVwt. It was later utilised as a template for mineralization with cobalt and iron oxide. The magnetic properties of iron oxide–CPMV were established and the particles were further modified as proof of concept. This approach is very simple and it does not require the need of expensive peptides to generate monodisperse metallic nanoshells.

The metallization of CPMV particles using the electrostatic adsorption of palladium anions to the surface exposed lysines and upon reduction to generate Pd^0–CPMV which acted as template for the subsequent metal deposition from solution in the absence of an external electrical current. This approach was also successful in generating monodisperse metallic nanoparticles. The

metallization process provided some control over the thickness of the metallic layer based on the incubation times.

CPMV was further used as a template for the deposition of an ultra-thin layer of polycation (^{PA}CPMV) that was further incubated with gold hydroxide to generate Au–CPMV particles. This was the only successful approach I have tried to generate Au–CPMV particles. The particles were monodisperse and were further modified with thiolated moieties. Surprisingly, the incubation of ^{PA}CPMV particles with citrate capped AuNPs. This reaction resulted in tightly packed, beautiful, self–assembled, tessellated–spheres. All of the control experiments showed that the polycation is essential for this assembly. The control over the size of Au–CPMV nanoparticles was controlled by the amount of gold solution added. The properties of Au–CPMV nanoparticles need to be studied further and developed to produce photothermal agents.

During my studies, our group developed and successfully generated for the first time CPMV eVLPs. Therefore, I have extended the use of CPMV eVLPs as nanocontainers for the synthesis of highly monodisperse cobalt and iron oxide within the eVLPs. The properties were investigated for eVLPs$_{\text{iron oxide}}$ and the magnetic properties were confirmed. While writing this thesis I am still working toward measuring the thermal measurements of VLPs$_{\text{iron oxide}}$ and developing the particles for possible hyperthermia treatment. This work is still on–going.

Furthermore, CPMV eVLPs were explored as nanocontainers to package small dye molecules and drug molecules. The layer–by–layer approach to assemble alternating polycation and polyanion layers onto the VLPs$_{\text{drug}}$ was explored. The polyelectrolytes were selected specifically to be pH– and salt–sensitive in order to explore the use of CPMV eVLPs for controlled drug release. VLPs$_{\text{gemcitabine}}$ was explored for its fluorescent properties. There is still a lot of work to do on this and to further develop the cisplatin anticancer drug/eVLP system. The drug charge and size might be very useful in maximising the payload delivered to diseased cells. Furthermore, the $^{\text{Polyelectrolyte}}$VLPs could be further functionalised with targeting or imaging agents.

It was proposed that immobilisation studies of VNPs on electrode surfaces might be achievable using CPMVwt. The stability of ferrocene, accessibility to a wide range of derivatives and its electrochemical reversibility made it an ideal moiety for possible applications in

nanoelectronics. The immobilisation of ^{Ferrocene}CPMV on different electrode materials was reported in this thesis. Ferrocene immobilisation on SAMs did not affect the electrochemical properties of ferrocene or its stability. However, ^{Ferrocene}CPMV immobilisation was a challenge, the reproducibility was a big issue using this approach. Although I think, the virus may act as an insulator and prevent electron hopping I was not able to prove this. Some further work is still needed to confirm or defy this assumption. Furthermore, it was confirmed that by increasing the spacer length between the ferrocene moieties and the virus a decrease in the amount of the covalently bound moieties was observed. Different chemistries were explored to generate ^{Enzyme}CPMV nanoparticles. Two enzymes (HRP and GOX) were selected as proof of principle. Quantifying the number of the active enzymes coupled to the capsid was tricky but successful and took almost the first two years of my PhD. I will be pursing this work for the coming few months of my remaining time at JIC.

Additionally, ^{Ferrocene}CPMV^{GOX} was investigated as a possible approach to generate digitalised glucose sensing devices. In such systems, ferrocene generally acts as a mediator and the GOX enzyme interacts with the substrate. During the electrochemical detection of glucose using ^{Ferrocene}CPMV^{GOX} particles in solution, glucose binds to the active site of the immobilized enzyme, which induces an increase in catalytic current, resulted in a measurable shift in the redox potential, and alters the current intensity of the Fc/Fc^{+} redox couple. The preliminary results indicated that the detection of the analyte (glucose) sensitive and the detection of minor differences in electrode potential are possible. In light of the sensory approach for ^{Ferrocene}CPMV^{GOX} it is obvious that this system represents one useful platform for the design of digitalised sensors and is required to be pursued further.

The potential applications of the chemically modified CPMV particles to carry multivalent functionalities are of great potential in developing CPMV as a drug carrier and delivery agent. I demonstrated that CPMVwt could be functionalised with anticancer drugs (e.g. Doxorubicin) and be functionalised with targeting agents. ^{Dox}CPMV delivery potential is being investigated at the time of writing this thesis with Prof. Nicole Steinmetz.

To conclude, VNPs have proven to be valuable scaffolds for the construction of desired new materials with precise positioning and control, and CPMV, in particular, is an excellent template of choice to be developed further in the field of bionanoscience.

Appendix